



**HAL**  
open science

# Analysis of high-frequency/high-amplitude acoustic field effects on coaxial injection: application to liquid rocket engines

Antonio Ficuciello

► **To cite this version:**

Antonio Ficuciello. Analysis of high-frequency/high-amplitude acoustic field effects on coaxial injection: application to liquid rocket engines. Acoustics [physics.class-ph]. Normandie Université, 2017. English. NNT: 2017NORMR106 . tel-01743848

**HAL Id: tel-01743848**

**<https://theses.hal.science/tel-01743848>**

Submitted on 26 Mar 2018

**HAL** is a multi-disciplinary open access archive for the deposit and dissemination of scientific research documents, whether they are published or not. The documents may come from teaching and research institutions in France or abroad, or from public or private research centers.

L'archive ouverte pluridisciplinaire **HAL**, est destinée au dépôt et à la diffusion de documents scientifiques de niveau recherche, publiés ou non, émanant des établissements d'enseignement et de recherche français ou étrangers, des laboratoires publics ou privés.



Normandie Université

## THÈSE

**Pour obtenir le diplôme de doctorat**

**Spécialité Physique Energétique**

**Préparée au sein de l'Université de Rouen Normandie**

**Analysis of high frequency/high amplitude acoustic field effects on coaxial injection: application to liquid rocket engines**

**Présentée et soutenue par  
Antonio FICUCIELLO**

**Thèse soutenue publiquement le 08 juin 2017  
devant le jury composé de**

M. Sébastien CANDEL	Professeur Emérite, EM2C, CentraleSupélec, Châtenay-Malabry	Rapporteur
M. Laurent GICQUEL	Ingénieur de Recherche, Docteur-HDR, CERFACS, Toulouse	Rapporteur
M. Michael OSCHWALD	Professeur, Head of Rocket Propulsion Department, DLR, Germany	Examineur
M. Julien REVEILLON	Professeur, CORIA, Université de Rouen Normandie	Examineur
M. Luc-Henry DOREY	Ingénieur de Recherche, Docteur, ONERA, Châtillon	Examineur
Mme Marie THERON	Ingénieur R&D, Docteur, DLA/SDT/EPM, CNES, Paris	Examinatrice
Mme Françoise BAILLOT	Professeure, CORIA, Université de Rouen Normandie	Directrice de thèse
M. Jean-Bernard BLAISOT	Maître de Conférences-HDR, CORIA, Université de Rouen Normandie	Codirecteur de thèse

**Thèse dirigée par Françoise BAILLOT, Professeure des Universités et Jean-Bernard BLAISOT, Maître de Conférences-HDR, Université de Rouen Normandie**



# Acknowledgments

First, I would like to express my gratitude to my two supervisors Prof. Françoise Baillot and Dr. Jean-Bernard Blaisot. Their precious advice, guidance and constant encouragement have been crucial for me in the achievement of my PhD, and I will always be indebted to them. I am also extremely grateful to Dr. Christine Richard for helping me with the huge number of equations that have been derived for this thesis. Her support and kindness have been extremely important to me.

It was a great pleasure being part of such a wonderful team.

I would also like to thank Dr. Marie Théron and the CNES R&D program for funding this research project.

I am extremely thankful to all the members of the administrative staff, of the IT department, of the workshop and of the métrologie and instrumentation team of CORIA. Their outstanding work makes things much easier for everybody and contributes to the amazing ambience which can be found in the laboratory.

I would like to thank the jury members who dedicated part of their precious time to my thesis. I am extremely thankful to Prof. Sébastien Candé and Dr. Laurent Gicquel for their in depth review of my work, and to Prof. Michael Oswald, Prof. Julien Revellion and Dr. Luc-henry Dorey for their precious comments and suggestions.

I am also deeply indebted to all my colleagues and friends: Manu, Andres, Thành, Fred, Stan, Chanisa, Lila, Erwan, Felix, Javier, Abou, Marcos, *Stephano*, Lorenzo, Cédric, Damien. They have been like a family and made my life wonderful in Rouen. They are probably the best result of my PhD and I will always keep with me a lot of good memories. I hope we will keep in touch in the future.

To conclude, I would like to express my deepest gratitude to the most important people in my life: my parents, my sister Martina and my lovely girlfriend Silvia. This PhD, all that I have achieved so far, and everything that I will do in life is dedicated to you. Your sacrifices, support, encouragement make anything possible.



# Abstract

The context of this work relies to high frequency combustion instabilities in Liquid Rocket Engines (LRE). The present research focuses on the effects of high amplitude transverse acoustic fields on non-reactive coaxial injection. The acoustic response of injection domes is found to be dependent on the local properties of the acoustic field in the injection cavity. The modification of the atomization process, induced by the acoustic field, has been analyzed in single and multi-injection configurations. Experiments were performed from low to high Weber number atomization regimes. Three phenomena are observed: jet flattening, improvement of the atomization process and deviation. The combination of these phenomena in multi-injection configurations leads to a droplet clustering phenomenon. In the presence of combustion, such a clustering could lead to non-uniform heat release rate which can trigger or sustain combustion instabilities. A theoretical model based on non-linear acoustics has been developed, providing general expressions of radiation pressure and resulting radiation force, for spherical and cylindrical objects in standing and progressive wave field. The model has been successfully used to interpret and quantify experimental observations in liquid/gas, trans-critical/super-critical and gas/gas configurations and showed that the Helmholtz number  $\alpha$  characterizing the acoustic field and the density ratio  $\eta$  characterizing the two media are two parameters of importance. The major conclusions are that the observed phenomena can be interpreted as resulting from non-linear acoustics, the key feature being the density ratio. It is claimed that the layer separating the two media, seen as an interface, does not need to be restricted only to a liquid/gas interface.

**Keywords:** combustion instability, high amplitude, transverse mode, coaxial injection, atomization, acoustics, nonlinear effects, radiation pressure, rocket engines.

# Résumé

Le contexte de ce travail repose sur l'étude des instabilités de combustion au sein des moteurs fusées à propergols liquides. Cette étude se concentre sur les effets des champs acoustiques transverses de haute amplitudes sur l'injection coaxiale en conditions non-réactives. La réponse acoustique du système d'injection est dépendante des propriétés locales du champ acoustique dans la cavité d'injection. La modification du processus d'atomisation, induit par le champ acoustique, a été analysée dans des configurations simples et multi-injection. Des expériences ont été menées pour des régimes d'atomisation de faibles et hauts nombres de Weber. Trois phénomènes ont été observés: un aplatissement du jet, une amélioration du processus d'atomisation et la déviation du système liquide. La combinaison de ces trois phénomènes en configuration multi-injection résulte en un phénomène de regroupement de gouttes. En présence de combustion, un tel regroupement pourrait mener à un dégagement de chaleur non-uniforme susceptible de déclencher ou d'entretenir des instabilités de combustion. Un modèle théorique basé sur les équations d'acoustique non-linéaire a été développé pour donner les expressions générales de pression de radiation et de forces de radiations résultantes appliqué aux objets sphériques et cylindriques en champ stationnaire ou progressif. Le modèle a été utilisé pour interpréter et quantifier les observations expérimentales en configurations liquide/gaz, trans-critique/super-critique et gaz/gaz, et a permis de montrer que le nombre de Helmholtz qui caractérise le champ acoustique, et le rapport de densité qui caractérise les deux milieux, sont deux paramètres cruciaux. Les principales conclusions montrent que le phénomène observé peut être interprété comme résultant de l'acoustique non-linéaire, dont le paramètre clé étant le ratio de densité. Cela exige que la couche séparant les deux milieux, vue comme une interface, ne doive pas être réduite uniquement à une interface liquide/gaz.

**Mot-clés:** instabilité de combustion, haute amplitude, mode transverse, injection coaxiale, atomisation, acoustique, effets non-linéaires, pression de radiation, moteurs-fusées.

# List of Conference Papers

**A. Ficuciello**, J-B. Blaisot, F. Baillot, C. Richard and M. Théron, *Response of coaxial air-assisted liquid jets in an acoustic field: atomization and droplet clustering*, In the 13<sup>th</sup> Triennial International Conference on Liquid Atomization and Spray Systems, Tainan, Taiwan (August 23-27, 2015).

**A. Ficuciello**, J-B. Blaisot, F. Baillot, C. Richard and M. Théron, *Acoustic response of a feeding system to high-frequency transverse acoustic fields*, In the International Symposium on Thermoacoustic Instabilities in Gas Turbine and Rocket Engines: Industry meets Academia, Munich, Germany (May 30 - June 02, 2016).

**A. Ficuciello**, F. Baillot, J-B. Blaisot, C. Richard and M. Théron, *High Amplitude Acoustic Field Effects on Air-Assisted Liquid Jets*, 52<sup>th</sup> AIAA/SAE/ASEE Joint Propulsion Conference & Exhibit, AIAA Paper No. 2016-5085, Salt Lake City, USA (25 - 27 July, 2016).

**A. Ficuciello**, J-B. Blaisot, F. Baillot, C. Richard and M. Théron, *Multi-injection system response to high-amplitude acoustic perturbations*, In the 13<sup>th</sup> International Conference on Liquid Atomization and Spray Systems (Poster), Brighton, UK (2016).

# List of Journal Papers

**A. Ficuciello**, J-B. Blaisot, F. Baillot, C. Richard, *Investigation of air-assisted sprays submitted to high frequency transverse acoustic fields: droplet clustering*, Physics of Fluids **29**, 067103 (2017); doi:10.1063/1.4985202.

**A. Ficuciello**, J-B. Blaisot, F. Baillot, C. Richard and M. Théron, *Acoustic response of a feeding system to high-frequency transverse acoustic fields*, International Journal of Spray and Combustion Dynamics, Vol. 9 (4), pp. 217-229 (2017); doi:10.1177/1756827717735300.

F. Baillot and J-B. Blaisot, **A. Ficuciello** and C. Richard, *On the radiation pressure and radiation force on a sphere or on a cylinder in an acoustic field*, (writing).



# Contents

<b>Acknowledgments</b>	<b>3</b>
<b>1 Introduction</b>	<b>17</b>
1.1 Overview of Combustion Instabilities . . . . .	17
1.1.1 Combustion Instabilities Classification . . . . .	18
1.1.2 Fundamental Processes . . . . .	21
1.2 LRE Injection System . . . . .	23
1.3 Combustion Instabilities in LRE: Representative Works in the Area . . . . .	25
1.4 Thesis Objectives . . . . .	31
1.5 Thesis Structure . . . . .	32
<b>I Experimental Setup</b>	<b>35</b>
<b>2 TAC-Spray: Transverse Acoustic Cavity for Spray</b>	<b>37</b>
2.1 Acoustic Resonant Cavity . . . . .	37
2.1.1 Pressure Measurements and Signals Generation . . . . .	39
2.1.2 Cavity Acoustic Field . . . . .	41
2.1.2.1 Acoustic Pressure Profiles . . . . .	42
2.1.2.2 Acoustic Pressure Signals at PAN and VAN . . . . .	44
2.1.2.3 Acoustic Pressure at PAN . . . . .	45
2.2 Injection System . . . . .	46
2.2.1 Coaxial Injector . . . . .	46
2.2.2 Injection Domes . . . . .	48
2.2.2.1 Gas Dome Design . . . . .	49
2.2.2.2 Gas Dome Frequency Response to White Noise Excitation . . . . .	53
2.2.2.3 Liquid Dome Design . . . . .	54
2.2.3 Air and Water Supply System . . . . .	57

<b>3</b>	<b>Measurements Techniques</b>	<b>59</b>
3.1	High Speed Back-light Visualization . . . . .	59
3.2	Droplet Size Measurement by Image Processing . . . . .	65
3.3	Laser Doppler Velocimetry (LDV) . . . . .	71
<b>II</b>	<b>Acoustic Effects Upstream and Downstream the Injection</b>	<b>77</b>
<b>4</b>	<b>Upstream effects: Domes' Acoustic Response</b>	<b>79</b>
4.1	Introduction . . . . .	79
4.2	Gas Dome Response . . . . .	80
4.3	Liquid Dome Response . . . . .	90
4.4	Summary of Results . . . . .	92
<b>5</b>	<b>Downstream effects: Atomization Process response</b>	<b>97</b>
5.1	Introduction . . . . .	97
5.2	Single Injector Response . . . . .	98
5.2.1	Flattening . . . . .	98
5.2.1.1	Jet Thickness Evolution . . . . .	101
5.2.1.2	Flattening Threshold . . . . .	104
5.2.2	Atomization Process Improvement . . . . .	106
5.2.3	Deviation . . . . .	110
5.2.3.1	Low Weber Number Atomization Regimes . . . . .	110
5.2.3.2	High Weber Number Atomization Regimes . . . . .	113
5.2.3.3	Deviation as a function of $\tilde{z}$ . . . . .	116
5.3	Multi-point Injection Configuration . . . . .	119
5.3.1	Without Injection Domes . . . . .	119
5.3.2	With Injection Domes . . . . .	123
5.4	Implementation of Droplet Size and Gas Velocity Measurements Techniques	125
5.4.1	Quantification of Deviation for: $We_g > 400$ , $Re_l = 6602$ , $J = 5.1$ . . . . .	126
5.4.2	Droplet Size Characterization . . . . .	128
5.4.3	Gas Velocity Field Characterization by LDV . . . . .	131
5.4.3.1	Without Acoustics . . . . .	132
5.4.3.2	With Acoustics . . . . .	137
5.5	Summary of Results . . . . .	145

<b>III</b>	<b>Modeling</b>	<b>149</b>
<b>6</b>	<b>Nonlinear Acoustic Theory</b>	<b>151</b>
6.1	Introduction . . . . .	151
6.2	Acoustic Radiation Pressure and Radiation Force Equations . . . . .	152
6.3	Cylindrical Objects . . . . .	155
6.3.1	General Expressions . . . . .	155
6.3.1.1	Velocity Potential Expression . . . . .	155
6.3.1.2	Expressions for the Radiation Pressure and its Contributions: $p_\zeta$ , $p_\phi$ and $p_q$ . . . . .	158
6.3.1.3	Coefficients of the Expressions for Standing and Progressive Waves . . . . .	159
6.3.1.4	Dimensionless Expressions . . . . .	160
6.3.2	Convergence Analysis: Truncated Expressions of the Radiation Pressure and Resulting Force . . . . .	161
6.3.3	Small Objects Approximation ( $\alpha \ll 1$ ) . . . . .	164
6.3.3.1	Approximate Expressions for a Standing Wave . . . . .	167
6.3.3.2	Approximate Expressions for a Progressive Wave . . . . .	168
6.3.3.3	Comparison Between General Expressions $p^*$ and $F^*$ and Approximate Solutions $\tilde{p}^*$ and $\tilde{F}^*$ . . . . .	169
6.3.3.4	Contribution of $\tilde{p}_\zeta^*$ , $\tilde{p}_\phi^*$ and $\tilde{p}_q^*$ to $\tilde{p}^*$ for both waves . . . . .	170
6.3.3.5	Asymptotic Approximate Expressions for both Standing and Progressive Waves . . . . .	175
6.3.3.6	Influence of $\eta$ . . . . .	175
6.4	Spherical Objects . . . . .	179
6.4.1	General Expressions . . . . .	180
6.4.2	Truncated expressions . . . . .	183
6.4.3	Small Objects Approximation ( $\alpha \ll 1$ ) . . . . .	184
6.4.3.1	Approximate Expressions for a Standing Wave . . . . .	185
6.4.3.2	Approximate Expressions for a Progressive Wave . . . . .	186
6.4.3.3	Dimensionless Expressions Analysis . . . . .	186
6.4.3.4	Contribution of $\tilde{p}_\zeta^*$ , $\tilde{p}_\phi^*$ and $\tilde{p}_q^*$ to $\tilde{p}^*$ for both waves . . . . .	188
6.4.3.5	Asymptotic Approximate Expressions for $\eta \rightarrow 0$ and $\eta \rightarrow \infty$ . . . . .	190
6.4.3.6	Influence of $\eta$ . . . . .	191
6.5	Most important equations . . . . .	195

6.6	Comparison Between the Nonlinear Quantities in the Presence of Cylindrical and Spherical Objects . . . . .	196
<b>7</b>	<b>Analysis of Observed Phenomena on the Basis of the Theoretical Model</b>	<b>199</b>
7.1	Introduction . . . . .	199
7.2	Interpretation of the Liquid/Gas Results by Means of the Nonlinear Acoustic Model . . . . .	201
7.2.1	Flattening Onset Threshold . . . . .	202
7.2.2	Deviation Angle . . . . .	206
7.2.3	Unsteady Jet Displacement . . . . .	209
7.3	Generalization of the model in the absence of surface tension phenomena .	210
7.3.1	Trans-critical/super-critical conditions (small $\eta$ ) . . . . .	211
7.3.2	Gas/gas conditions (large $\eta$ ) . . . . .	214
7.4	Concluding Remarks . . . . .	216
<b>IV</b>	<b>Conclusion and Perspectives</b>	<b>219</b>
<b>8</b>	<b>Conclusion and Perspectives</b>	<b>221</b>
8.1	General Conclusions . . . . .	221
8.2	Perspectives . . . . .	226
	<b>Bibliography</b>	<b>227</b>
	<b>Appendices</b>	<b>239</b>
	<b>Appendix A - Vibration Tests</b>	<b>241</b>
	<b>Appendix B - Resonant Cavity Eigenmodes</b>	<b>244</b>
	<b>Appendix C - Injection Domes Technical Sketches</b>	<b>246</b>
	<b>Appendix D - Gas dome signal plots</b>	<b>247</b>
	<b>Appendix E - High Speed Visualization Minimum Images Analysis</b>	<b>250</b>

# Nomenclature

## Acronyms

<i>a.a.</i>	acoustic axis
<i>GD</i>	gas dome
<i>IAN</i>	intensity anti-node
<i>LD</i>	liquid dome
<i>LDV</i>	laser doppler velocimetry
<i>LRE</i>	liquid rocket engine
<i>h.r.r.</i>	heat release rate
<i>PAN</i>	pressure anti-node
<i>PT</i>	pressure transducer
<i>PW</i>	progressive wave
<i>SD</i>	Gaussian standard deviation
<i>SW</i>	standing wave
<i>VAN</i>	velocity anti-node

## Greek Symbols

$\alpha$	Helmholtz number $\alpha = ka$
$\gamma$	jet deviation angle
$\Delta p_{Lap}$	Laplace pressure drop
$\Delta p_{rad}$	radiation pressure distribution
$\Delta p_{rad}^{\%}$	radiation pressure distribution corresponding to $p_{\%}$
$\delta t$	hyperbolic tangent function parameter defining the smoothness of the descending function
$\delta t_{ramp}$	acoustic signal ramp duration
$\zeta$	local coordinate normal to the jet
$\eta$	ratio of the medium density over the object density
$\theta$	angle (polar or spherical) coordinate
$\mu_h$	mean value of the Gaussian spatial distribution calculated on the entire image height
$\tilde{\mu}_h$	$\mu_h/w_{im}$
$\mu(z)$	mean value of the Gaussian spatial distribution calculated in a horizontal slice (barycenter $z$ ) of the image
$\tilde{\mu}(\tilde{z})$	$\mu(z)/w_{im}$
$\nu$	kinematic viscosity

$\sigma$	liquid surface tension
$\rho$	density
$\rho_0$	medium density
$\rho_1$	object density
$\omega$	angular frequency

### Roman Symbols

$D_g$	injector maximum exit diameter
$D_l$	injector post exit diameter
$d_j$	liquid dome connection diameter
$d_{or}$	gas dome orifice diameter
$d\widetilde{Th}$	difference in between the initial jet diameter and the jet thickness before atomization
$e$	injector gas annular gap width
$\vec{F}_{rad}$	resulting radiation force
$f(i)$	discrete droplet location probability density function per normalized width $\Delta w/w_{im}$
$h_{im}$	image height
$J$	momentum flux ratio
$L_{inj}$	injector length
$L_j$	liquid dome connection length
$m$	number of spatial classes by which the width of an image is divided
$m_{air}^{max}$	maximum single injector mass flow rate considered in GD response analysis
$\tilde{m}_{air}$	single injector mass flow reduced by $m_{air}^{max}$
$N$	total number of objects $\sum_{k=1}^m N_d(k)$
$N_d$	droplet number distribution
$N_d(i)$	number of objects in class i
$N_d^{max}$	maximum of the droplet distribution $N_d$
$\tilde{N}_d$	normalized droplet number distribution, $N_d/N^{max}$
$\tilde{N}_d(i)$	normalized number of droplets in the class i, $N_d(i)/N^{max}$
$p_a$	0-to-peak pressure amplitude at the pressure antinode
$p_{a,pp}$	peak-to-peak pressure amplitude at the pressure antinode
$p_{. \%}$	acoustic pressure amplitude leading to a decrease in the round jet thickness by .% at most
$p_{th}$	acoustic pressure amplitude threshold triggering flattening onset
$Re_l$	liquid Reynolds number
$r_o$	jet radius at the measurement location
$r_{inj}$	liquid injector post radius
$s$	number of terms kept in a truncated sum
$t$	time
$t_o$	instant at which the hyperbolic tangent function presents the inflection point

$\widetilde{Th}$	jet thickness reduced by $D_l$
$\widetilde{Th}_f$	final flattened thickness of the jet before atomization occurrence
$\vec{U}$	bulk velocity
$\vec{W}$	liquid column weight
$w_{im}$	image width
$We_g$	gaseous Weber number
$x$	horizontal cartesian coordinate normal to the incident wave
$\tilde{x}$	non-dimensional coordinate
$y$	horizontal cartesian coordinate along the incident wave
$\tilde{y}$	non-dimensional coordinate
$z$	descending vertical coordinate
$\tilde{z}_\gamma$	vertical coordinate with which the deviation angle $\gamma$ is calculated
$\tilde{z}_{max}$	vertical distance from the injection plane for which the jet deviation is maximum
$\tilde{z}$	non-dimensional coordinate

**Superscripts or Subscripts**

0	without acoustics
<i>ac</i>	with acoustics
<i>g</i>	gas
<i>l</i>	liquid
<i>th</i>	threshold



# Chapter 1

## Introduction

### 1.1 Overview of Combustion Instabilities

Combustion instabilities were first observed in the late 1930s in both solid and liquid propellant rocket engines [1, 2] and roughly at the same time in the Soviet Union and in the United States. Since then, combustion instabilities have been encountered in almost all new propulsion system development programs also concerning afterburners and ramjets; and recently, they have also become a serious problem in the development of gas turbines [3] in which the new strategies for reducing emission of pollutants, as lowering the average temperature at which primary combustion occurs, makes combustion less stable and tend to encourage the excitation of oscillations.

Due to the extremely high density of energy released in a volume having relatively low losses, liquid rocket engines are among the systems the most affected by combustion instabilities. A very representative example is the Apollo program. During the 1960s this program motivated a large amount of research in the domain because of the presence of the astronauts. More than 7 years of research, involving more than 2000 full-scale tests were necessary to develop the final engine (a comprehensive review of the subject has been presented in 1993 by Oefelein and Yang [4]). Experience gained during this period formed the basis for developing the Space Shuttle main engine. In 1972 a first effort to assemble a reference report on liquid rocket engine (LRE) combustion instabilities was concluded in the United States from a series of NASA and AIR FORCE sponsored research programs which resulted in the publication of the NASA SP-194 [5]. In 1995 a second reference text intended as an extension of the NASA SP-194 was published in the U.S. by Yang and Anderson [6] followed by another publication in 2007 containing information about the testing and development practices for treating liquid rocket combustion instability

problems in Russia covering more than 50 years of research and edited by Dranovsky, Yang, Culick and Talley [7].

In Europe a significant program has been supported since 1981 as a consequence of the flight failure of an Ariane 4 vehicle due to combustion instability in the first-stage Viking motor. In 2001 the Ariane 5 flight v142 failed to place a satellite into the right orbit. In that case it was the upper-stage Aestus engine that developed combustion instability, leading to the failure of the mission. The Ariane program justified research efforts in the combustion instability domain and in 2001 a French-German collaboration between space agencies, industries and research laboratories was initiated with the objective to provide a better understanding of the phenomenon. The program designated as "Rocket Engine Stability iniTiative" (REST) was initiated by the CNES and DLR in collaboration with research laboratories and industrial partners. The program is currently undergoing.

In a way or another, combustion instabilities have been under continuous investigation and progress made in any one of the systems is fundamental to understanding and treating combustion instabilities in other sorts of system. However, despite the great effort expended on the problem during the last 80 years, our understanding of instability mechanisms is limited and new rocket engines can still be plagued by it. We still need to improve our knowledge about what drives combustion instabilities and how to prevent them; additional investigation is required to provide reliable predictions for practical designs.

### 1.1.1 Combustion Instabilities Classification

Combustion process in liquid rocket combustors is never perfectly steady. Pressure, temperature and velocity fluctuations are always present in the thrust chamber, since a very high energy density is released in a small confined volume where relatively low losses occur. If peak-to-peak pressure fluctuations in the combustion chamber remain below 5% of the main chamber pressure, the engine exhibit what is called "smooth" combustion; whereas if pressure fluctuations exceed this percentage, without a discernible periodicity, the engine exhibit the so-called "rough combustion" [8] . In some conditions pressure fluctuations can interact with engine structure, natural frequencies of the feeding system or with the acoustic resonant modes of the combustion chamber, resulting in periodic fluctuations which can be amplified by a small fraction of the energy released by the combustion process. This phenomenon is referred as combustion instabilities.

Combustion instabilities in liquid rocket engines can be classified in several ways.

According to Barrère and Williams [9] three main classes can be identified, by considering the size of the components involved in the instability process:

- System instabilities : involve the entire system, by an interaction between the process taking place in the chamber, the propellant feed system and also the vehicle structure by means of the thrust fluctuations. In this class can be mentioned the well-known POGO or "chugging" instabilities [1].
- Combustion chamber instabilities : also known as thermo-acoustic instabilities, are characterized by the propagation of the acoustic waves in the combustion chamber.
- Intrinsic instabilities : involve only the reactants, depending on the combustion kinetics but not on the chamber properties. The characteristic combustion times being very short the frequency spectrum of these instabilities is very high.

The first type of instabilities are called low frequency (LF) instabilities, characterized by pressure fluctuations in the 10 to 400 Hz range. The second type is instead characterized by pressure fluctuations at higher frequencies, going from some hundreds of Hz to some kHz; they are called high frequency (HF) instabilities. High frequency instabilities tend to be the most damaging and the most difficult to eliminate. They result from the coupling of the fluctuating heat release rate (h.r.r) with the acoustic field in general relying on the combustion chamber's eigenmodes. In the case of cylindrical chambers, eigenmodes can be classified into longitudinal modes, in the direction of the combustion chamber axis, and azimuthal or radial modes oriented perpendicularly to the chamber axis (see Figure 1.1).

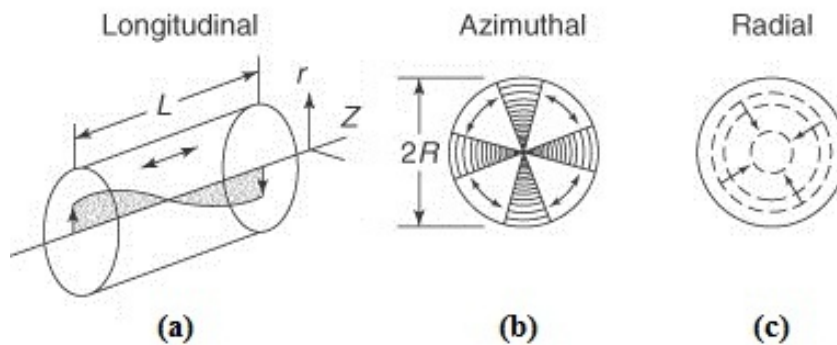


Figure 1.1: Fundamental (a) longitudinal, (b) azimuthal and (c) radial modes of a cylindrical chamber.

Longitudinal modes characterizing liquid rocket instabilities can be progressive or standing waves. Azimuthal modes coming from the counterbalance of two progressive

waves of equal pressure amplitude result in standing waves. Azimuthal modes described by spinning or traveling waves can rotate in the clockwise or counterclockwise. A combination of longitudinal and transverse (azimuthal and/or radial) modes can also be found in real combustion chambers leading to more complicated three-dimensional modes' structures.

Among the different types of combustion instabilities, high frequency azimuthal (spinning or standing) mode instabilities are considered as the most harmful for the operations of liquid rocket engines and unfortunately are the most commonly found in their current development [8]. Instantaneous pressure peaks roughly twice of the chamber pressure under stable operations can be attained and heat release rate (h.r.r.) can increase up to 10 times. Injection head and chamber walls can be seriously damaged (see Figure 1.2) leading to the failure of the mission. It is thus clear that in order to ensure launch vehicles safe operations, high frequency instabilities must be understood and minimized.

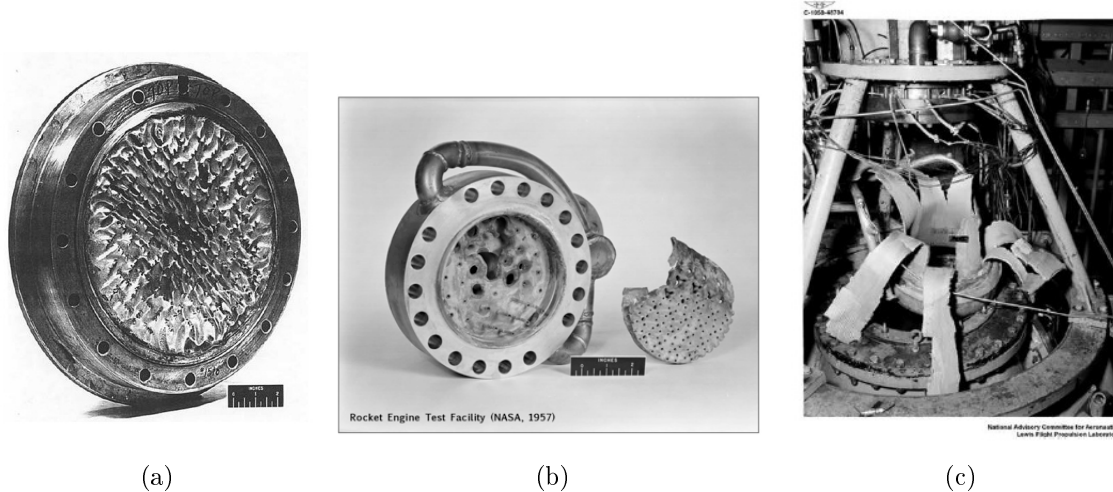


Figure 1.2: Three examples of liquid rocket engines damaged by high frequency combustion instabilities: (a) injection head damaged; (b) engine partially destroyed (NASA) (c) engine exploded during start-up (NASA).

Passive countermeasures are usually adopted to reduce high-frequency instabilities within the combustion chamber. These countermeasures include: injector face baffles, acoustic energy absorption cavities or combustion chamber liners. Once the engine design is fixed it is tested over a wide range of operating condition in order to verify its stability. Rating test guidelines have been released in the U.S. by the Chemical Propulsion Information Agency (CPIA) [10, 11]. According to these guidelines, if the engine suffers sustained, organized oscillations with peak-to-peak amplitudes greater than 10% of the chamber pressure, the engine is classified as unstable.

The amount of tests necessary to prove engine stability has been greatly reduced

since the development of the F-1 engine of the Apollo program thanks to the scientific community upgraded knowledge.

### 1.1.2 Fundamental Processes

In the 1950s Crocco provided a first heuristic approach (the  $n-\tau$  model) to high-frequency instabilities modeling. This approach did not take into account the fine physical processes occurring in the chamber, and postulated that pressure fluctuations could affect the mass flow rates, and thus the heat release rate [12, 13]. The model was later refined and developed into the well known "Sensitive Time-Lag Theory" [14]; it was then validated experimentally for both longitudinal [15] and transverse instabilities [16]. Despite many years of research since the elaboration of the  $n-\tau$  model, there is still a lack of knowledge in the fundamentals of the combustion instability mechanisms. The main problem comes from the numerous involved processes and sub-processes, as well as from the complexity of their potential interactions. Since the sub-processes that occur in between the injection and the chemical reactions are dependent on the pressure and aerodynamics of the combustion chamber, a feedback mechanism able to amplify the natural acoustic modes of a combustion chamber may be encountered [17]. Thus, even small perturbations can be amplified, leading very quickly to high amplitude fluctuations. The feedback loop through which instabilities can be amplified is shown in Figure 1.3. It involves combustion, acoustics and fluid dynamics which rely on many physical or chemical processes. The combustion process is characterized by heat release rate fluctuations and flame/flame interactions which can generate acoustic fluctuations. Acoustics can excite chamber eigenmodes; the complex boundary conditions and the coupling between the chamber and other cavities of the system can result in a modulation of the flow dynamics. The flow field modulation affects injection, atomization, vaporization and turbulence which may lead to flame fluctuations.

The injection system and the combustion chamber are designed to control the conversion of liquid propellants into product gases in order to have uniform distribution of heat release rate. However, the feedback can induce the modification or the modulation of one or more processes inducing unsteady fluctuations of the heat release rate. According to the Rayleigh criterion [18], if the heat release rate fluctuations are in-phase with pressure oscillations, resonant interaction between combustion and acoustic field is possible. This condition is necessary but not sufficient. Indeed, the acoustic energy equation indicates that the amount of acoustic energy of a system increases in time if the source term coming

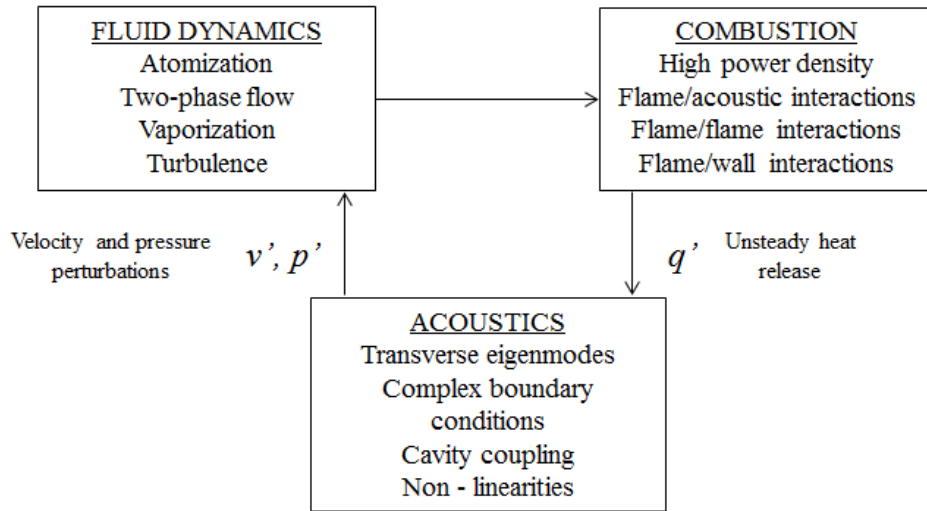


Figure 1.3: A schematic representation of the thermo-acoustic feedback loop involving fluid dynamics, combustion and acoustics and associated sub-processes.

from the coupling ( $p'q'$ ) is greater than the acoustic energy flux and the damping.

The main issue is thus to determine which processes (among those taking place in a combustion chamber), in which hierarchical order, and by means of which mechanisms they can drive the instability process [19]. The feedback mechanisms are commonly sub-classified into two classes: intrinsic and injection-coupled mechanisms. In the injection-coupled mechanism the acoustic fluctuations in the combustion chamber interact with the natural frequencies of the injection system, causing flow-rate fluctuations which contribute significantly to the acoustic pressure amplification. This type of mechanism is usually responsible of low frequency instabilities, but it can also occur in high frequency instabilities [17, 20]. The intrinsic mechanism implies that only the processes taking place after propellant injection, are responsible for the pressure fluctuation amplification in the chamber. This kind of mechanism is considered as a driving mechanism for high frequency instabilities [5].

Although full-scale tests are preferable to investigate engine stability they are expensive, and it is not always easy to perform measurements inside an actual rocket engine. When modification are needed the engine development is delayed, and its cost is strongly augmented. For this reason sub-scale or lab-scale devices are fundamental in order, not only to increase our knowledge in such a complicated field, but also to provide low-order models able to be implemented in numerical simulations. Self-sustained thermo-acoustic instabilities are difficult to be reproduced and investigated in laboratory due to the large complexity of mechanisms involved [1]. For this reason, the different steps describing

instability loops are analyzed separately. In particular, the impact of acoustics on flow dynamics, with or without combustion, is studied by imposing an external acoustic forcing. One of the key elements that must be taken into account is the very high level of acoustic fluctuations existing in those unstable environments, since phenomena observed are directly dependent on this level. Producing high level acoustic fields in laboratory remains a true challenge so that only a few studies are found in the literature; even fewer concern coaxial jet configurations, which are, however, widely used in liquid rocket engines. In these kinds of propulsion systems, propellants are usually in a trans or super-critical phase during steady state operative conditions. However, during the early transient phase, the oxidant can remain in the liquid phase, resulting in a liquid jet surrounded by a coaxial gaseous flow of fuel [21, 22, 23]. Atomization determines droplet size and spatial distribution, influencing the vaporization process which has a direct impact on combustion instability [24, 25]. Since the operating conditions of a given engine can be rendered stable or unstable by a slight injector modification [26], it is clear that the impact of acoustics on the atomization process is of crucial importance. Investigating the response of fluid-systems to acoustic forcing, with and without combustion, is thus essential to understand which processes are involved in the feedback mechanism, how they interact and how energy is transferred to the acoustic field.

## 1.2 LRE Injection System

The purpose of the injection system is to introduce the flow of liquid propellants into the combustion chamber in order to control their conversion into combustion gases at high temperature and pressure [6]. The function of the injector in this sense is of primary importance since it has to atomize the liquid (break up into small droplets), distribute and mix the propellants in order to obtain a proportioned mixture of fuel and oxidizer, with propellant mass flow and composition as uniform as possible over the chamber cross section [8]. Many different types of injection elements exist, each of them presents advantages and drawbacks having strong impact on LRE performance. Most common injectors can be basically classified into three classes: impinging, pintle and coaxial. Simplified cross-section schematics of these types of injectors are reported in Figure 1.4. Based on the propellant injection phase, it is then possible to further distinguish between liquid/liquid or gas/liquid injectors.

Impinging injectors (see Figure 1.4(a)) are commonly used with oxygen-hydrocarbon and storable propellants [8, 27]. The ducts are made with a certain angle with respect

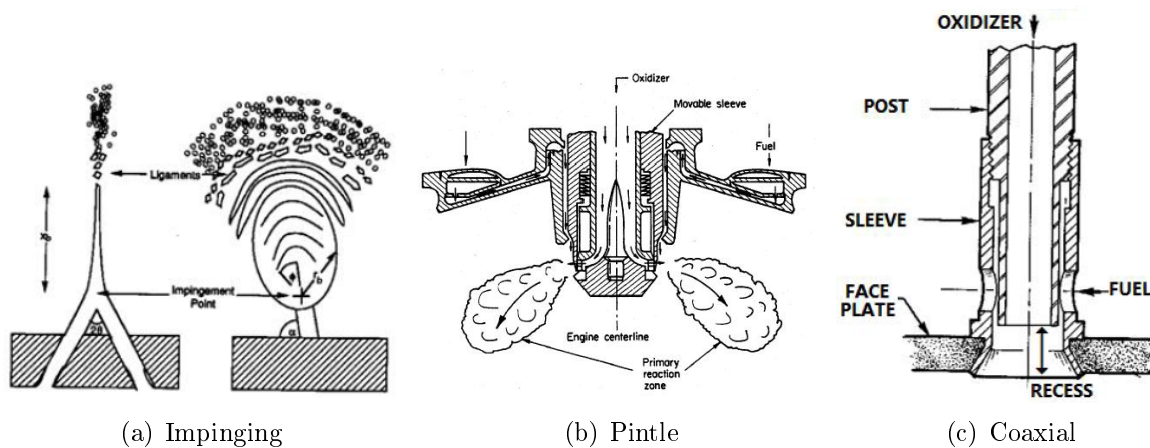


Figure 1.4: Cross-section schematics of most common types of injectors in LRE: (a) impinging; (b) pintle and (c) shear-coaxial.

to the injector plate in order to obtain the propellants impingement. Impingement forms thin liquid fans and aids atomization of the liquids into ligaments and then into droplets. Several configurations with 2 and up to 5 jets can be found and impact can be induced between jets of the same propellant (like impinging) or between the two propellants (unlike impinging). This type of injector presents good atomization and mixing characteristics associated with low fabrication costs. However, there is still a lack of basic knowledge regarding the fundamental atomization mechanisms of impinging jets and their subsequent mixing and combustion processes [28]. Pintle or throttleable injectors (see Figure 1.4(b)) have been used in the lunar descent module engine and currently in the Merlin engine designed by SpaceX. They are basically used in engines in which thrust must be controlled. One of the biggest advantages is the relatively low sensitivity to combustion instability. The third class of injectors is represented by coaxial injectors in which one of the propellant, usually the oxidizer in the liquid phase, is injected in the central tube (oxidizer post), while the gaseous fuel is injected in the coaxial annular channel. Atomization is achieved by the development of a shear layer resulting from the strong velocity difference between the two propellants, with the gas injected at a higher velocity than the liquid. If one of the two fluids is injected with a tangential velocity component the injector is called swirl-coaxial. This solution can be frequently find in Russian engines like the RD-180. When both propellants are injected parallel to the injector axis the injector is called shear-coaxial (see Figure 1.4(c)). This kind of injector is widely used in liquid rocket engines with cryogenic propellants like liquid oxygen (LOX) and gaseous hydrogen. Most of the U.S. and European rocket engines use shear-coaxial injectors. It is the case of the Space Shuttle main engine (SSME) or the Ariane 5 Vulcain engine.

Combustion chambers of liquid rocket engines are usually feed with a large number of injectors, which can go from a few dozens to some hundreds as shown in the F-1 engine view presented in Figure 1.5. Each injector must provide the same injection conditions, in order to ensure proper oxidizer/fuel mixing ratio and uniform distribution of propellant in the combustion chamber. Figure 1.6 presents an exploded view of the F-1 engine in which the fuel inlet manifold and the oxidizer dome are visible. The dome and the manifold are designed to ensure homogeneous distribution of propellants.



Figure 1.5: Detail on an F-1 engine injector plate at the forward end of the nozzle.

The geometry of the feeding system depends on the architecture of the engine. The injectors represent a connection between the combustor dynamics and the feeding system, and even if they are usually designed with a pressure drop (15 -20 %) to avoid any acoustic coupling, thermo-acoustic instabilities may occur as a result of the coupling of the acoustic eigenmodes of the dome/manifold with those of the combustion chamber. This mechanism is known as *injection-coupled* mechanism. It can cause mass flow-rate fluctuations able to significantly contribute to the process of acoustic pressure oscillation amplification.

### 1.3 Combustion Instabilities in LRE: Representative Works in the Area

In this section a review of the research activities dedicated to the investigation of high frequency combustion instability in Liquid Rocket Engine (LRE) is given. Particular attention is paid to those works concerning the interaction between acoustic fields and

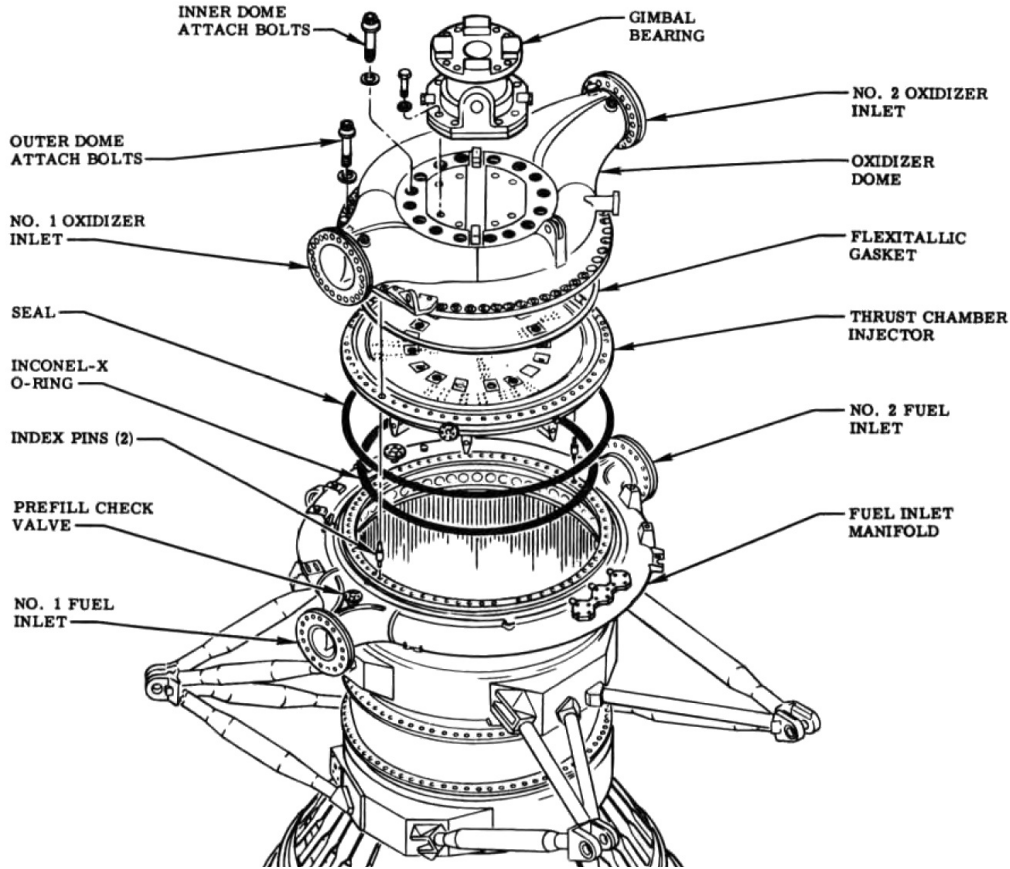


Figure 1.6: F-1 injection head exploded view.

injection processes.

Since the first postulation of the  $n - \tau$  model a large amount of research activities concerning high-frequency instabilities have focused on the characterization of injection flows in cold-flow or reacting conditions. One of the first investigation concerning the effects of an external acoustic forcing on fluid injection was conducted by Miesse [29]. A free water jet was submitted to transverse and longitudinal acoustic perturbation. It was shown that transverse waves, more than longitudinal ones, induced a modification of the jet structure in particular reducing the length of the continuous liquid core. In 1965 Heidmann experimentally investigated a liquid oxygen jet combusting in a gaseous hydrogen atmosphere under the effects of a spinning transverse mode [30, 31]. He observed that the jet atomization and vaporization processes were affected by the acoustic field and their modification affected the heat release rate. Evidence of the connection between atomization/vaporization and high-frequency instabilities led the scientific community to conduct theoretical analysis of droplet vaporization under the effects of a transverse

acoustic field: the general conclusion was that acoustic forcing diminished the vaporization time [32, 33, 34]. Experimental investigation on a LOx/H<sub>2</sub> engine configuration in the 1960s highlighted a link between engine stability and the injected hydrogen temperature. It was later explained that decreasing the temperature induced a decrease in the injection velocity, which affected the jet dynamics. Lower injection velocities caused liquid jet to be more sensitive to chamber pressure fluctuations resulting in flow-rate fluctuations. This suggested that for sufficiently low H<sub>2</sub> temperature injection-coupled feedback mechanism could lead to high-frequency instabilities [35]. In 1969 Heidmann and Groeneweg [36] identified the injection-chamber acoustic coupling as a driving mechanism for high-frequency instabilities and demonstrated that pressure fluctuations might be suppressed through appropriate acoustic design of the manifold.

These works together with many other early works in the field of high-frequency combustion instability in LRE were included in the already cited NASA SP-194 [5]. This report has been long considered to cover all engineering requirements for liquid rocket engines development. In the 1990s, in the U.S. the advanced launch system (ALS) [37] program renewed the community interest in the investigation of the instability phenomenon. In 1991 Hoover *et al.* investigated the effects of an acoustic field on a free water jet, in sub-critical conditions [38]. Acoustic field amplitudes were produced up to 165 dB and a jet flattening process was observed perpendicularly to the acoustic axis. They proposed an explanation for the flattening based on the impact of two opposite transverse gas flows. However, the two flow configurations they compared did not fall in the same range of Weber numbers. So, even though the authors found similar tendencies, the results suggest that the physical mechanisms involved in the flattening of the jet are quite different in the two experiments. Extensive investigation of non-reacting flow responses to a transverse acoustic field was also performed at the Air Force Research Laboratory (AFRL) for sound pressure levels (SPL) up to 180 dB. Chehroudi and Talley [39] dedicated the attention on a free liquid jet of nitrogen introduced into a chamber at room temperature, under sub and super-critical pressures. They observed a jet flattening, with greater effects for low nitrogen flow rates and lower chamber pressures. The experimental set-up was then modified to investigate LN<sub>2</sub>/GN<sub>2</sub> co-axial flows [40, 41]. The liquid jet was observed to assume a sinusoidal shape under transverse acoustic field. The group then systematically investigated the response of a coaxial jet of nitrogen to such an acoustic field under sub-critical, trans-critical and super-critical conditions, focusing on the intact liquid core length reduction [42, 43, 44]. The jet under trans-critical conditions located at a velocity anti-node showed a fluctuation of the core length with a maximum reduction of the inner

core length of about 90 %. This reduction was thought to enhance mixing; based on these observations (and other ones concerning impinging jets behavior [27]) Chehroudi proposed a feedback-mechanism for the high-frequency instability driving process [45].

A research group at the University of Maryland conducted experiments on coaxial  $GO_2/GH_2$  flame subjected to a transverse acoustic forcing [46, 47]. It was shown that small acoustic disturbances could be amplified by flame-acoustic coupling under certain conditions, leading to the modulation of the h.r.r. fluctuations and that baroclinic torque could play a role in triggering flame acoustic interactions [48].

A research group at Purdue University undertook investigation of combustion instabilities from both experimental and numerical points of view and research activities are currently ongoing. The CVRC (Continuously Variable Resonance Combustor) test bench operating at Maurice Zucrow Laboratory is used to study longitudinal instabilities. Instability is reproduced by using a historically unstable injector to excite the resonance mode of a cylindrical combustor [49]. Variations in the oxidizer post length have been proven to strongly affect the combustor stability [50, 51, 52, 53]. Experimental results, in particular concerning phase shift between acoustic pressure and heat release rate fluctuations, were used to develop a reduced order model for high frequency instability prediction, based on linearized Euler equation [54, 55, 56] and served as database to develop simulations which were able to reproduce spontaneous instability of the system [57, 58]. The same approach concerning the excitation of the combustor eigenmodes through an unstable element was used to study transverse instability in a rectangular chamber using methane and oxygen [59, 60, 61, 62, 63].

Parallel to these activities a large research program was initiated in Europe as a consequence of the destruction of the Ariane 4 launcher in 1980 and the failure of the Ariane 5 flight V510 in 2001. These two episodes served to remind that the knowledge in the field of LRE combustion instability was still limited and that further investigation was still necessary.

At DLR several experimental and numerical studies have been dedicated to characterize coaxial jets, in both non-reactive and reactive conditions [64, 65, 66], and to investigate high-frequency combustion instabilities in sub-scale and lab-scale rocket models [67]. The Common Research Combustor (CRC), developed in the framework of the REST initiative, is a lab-scale motor dedicated to studying flame-acoustic interaction. A siren is used to modulate a secondary nozzle and to excite combustor eigenmodes. The position of the secondary nozzle could be varied at a number of angular position around the side wall in a way that either the pressure or the velocity anti-node could be aligned with the flame. By

using high-speed OH\* imaging, it was observed that h.r.r. fluctuations were the strongest at the pressure anti-node [68, 69]. Further investigations on the CRC highlighted how the characterization of the acoustic modes of the injection system/chamber was important in the interpretation of experimental results [70, 71]. In parallel a numerical study on the same experimental set-up also revealed the role played by the coupling of the acoustic cavities on the resonance frequencies [72].

The experimental principle of the CRC was extended to more representative conditions with the development of Combustor H (BKH). In this configuration five coaxial injectors, operating with  $LOx/H_2$ , are clustered in a rectangular combustor. As in the CRC acoustic, BKH is excited with a rotating wheel modulating the flows at the exhaust nozzle. Shadowgraph imaging revealed significant response of the  $LOx$  core to transverse instability. As acoustic amplitude was increased a decrease of the intact core length was observed, due to accelerated breakup and mixing [73, 74]. The BKH was also used to investigate the phenomenon of injection-chamber coupling [75, 76]. The use of acoustic baffle in the  $H_2$  manifold was necessary in that case to reduce acoustic coupling.

Recently, the impact of acoustic coupling between the injection system and the combustion chamber has been also investigated in another sub-scale model combustor at DLR: the research Combustor D or BKD. The BKD is a sub-scale rocket combustor which presents, under certain operating conditions, spontaneous high-frequency instabilities with amplitudes greater than 20% of the mean chamber pressure (peak-to-peak). Experiments indicated that the 1T chamber mode could be excited if the  $LOx$  post resonance frequency coincides with that of the 1T mode. Emissivity flame response showed dominant frequencies corresponding to  $LOx$  post acoustic resonance frequencies [77, 78]. Combustion instabilities in the BKD combustor have been also object of numerical simulations [79] based on high-performance Large-Eddy Simulation in combination with computational acoustics. By triggering instabilities in the chamber they were able to obtain limit cycles and acoustic activity in the injection domes that successfully compared with experiments.

Combustion instability and jet acoustic interaction were also the subject of a large research program in France. The Multi Injector Combustor (MIC) is a lab-scale combustor operating at the Mascotte test bench at ONERA [80, 81, 82] in collaboration with the EM2C laboratory. It was developed especially for high frequency combustion instability research and it can work with three or five coaxial injectors (initially conceived for  $LOx/H_2$  it was later adapted for  $LOx/CH_4$ ). Acoustic modes of the chamber can be excited with a rotating toothed wheel which modulates the exhaust nozzle flow. Experiments indicated

that injector-injector interaction may play a role in driving instabilities. A significant modification of the flame structure was shown, with an increase in the spreading angle leading the neighboring flames to overlap [83]. At the same time the French group of the EM2C laboratory simulated the interaction between flame and acoustics [84, 85] to reproduce the MIC experiments. Simulations provided flame responses similar to those observed experimentally. In the case of a trans-critical round jet of nitrogen submitted to a transverse acoustic field [86], they obtained a jet flattening at the intensity anti-node and an oscillating motion in the direction of the acoustic axis. Flattening was ascribed to the presence of low pressure regions on jet sides where the pressure drop was attributed to a behavior explained by the unsteady Bernoulli theorem. In order to produce greater acoustic perturbation, the MIC was then modified with the addition of the Very High Amplitude Modulator (VHAM), an excitation system composed by two parallel exhaust nozzles alternatively excited with a toothed wheel. The new experimental setup was used to investigate the response of five cryogenic coaxial jet flames, in sub-critical and trans-critical regimes, under high-frequency transverse acoustic field [87, 88]. It was shown that, provided that the acoustic level was high enough in the combustion chamber, the flame length and the atomization process were modified by acoustic forcing in the vicinity of velocity anti-nodes. In some conditions, a flame flattening or an asymmetry in the flame distribution were observed. These observations are coherent with those found in other works focusing on non-reactive flows.

In the framework of the REST research program, investigation of non-reactive coaxial jet response submitted to high amplitude high frequency acoustic field were also undertaken at the CORIA laboratory [89, 90, 91]. The research activities have pointed out how an acoustic field with a sufficiently high amplitude ( $< 165$  dB) can drastically affect the behavior of an air-assisted water jet. Flattening of the jet was observed at the velocity anti-node for low Weber atomization regimes and the threshold for the flattening onset was calculated [90]. Deviation from the vertical axis at the intensity anti-node was observed for droplets placed under the roof. No quantification of high Weber atomization regimes response was provided. The typical response of the low Weber number jets to the transverse acoustic field at the velocity and intensity anti-nodes was ascribed to nonlinear acoustic effects, which could not be neglected for high acoustic amplitudes. In particular, the local radiation pressure [92] distribution and the resulting radiation pressure force were thought to explain the jet behavior. Preliminary calculation of radiation pressure for spherical objects were performed in order to identify a threshold for the flattening phenomenon [90]. The mathematical derivation of such quantities was carried out based

on the work of King [93]. The group also investigated the effects of a transverse acoustic field on premixed flames [94, 95]. Responses similar to those obtained for non-reactive flows were quantified (flattening and deviation), showing that non-linear acoustic effects observed in liquid/gas jets could also be effective in gas/gas systems.

## 1.4 Thesis Objectives

The literature survey presented in the previous section indicates that interaction between acoustics and injection process is a subject always present in the research programs on HF combustion instabilities. Although reacting flows should be studied, in conditions as close as possible to operating conditions, past researches have revealed that investigation of non-reactive flows offers important insight into the fundamental involved mechanisms. However, a limited number of works has been dedicated to the response of non-reactive flows to acoustics, and only a few involving acoustic levels comparable with those typical of combustion instabilities in liquid rocket engines. Several measurements could be made in such conditions, which would help to better understand the behavior of sprays under high/amplitude pressure fluctuations. Moreover, experimental data could be used to develop or validate numerical tools for combustion instability prediction. The aim of the research activity presented in this thesis is to contribute to fill this gap, providing experimental data, and also a theoretical model for the explanation of the phenomena observed. The research has been funded by the CNES R&D program, in the framework of the activity of the French-German research group REST. The study is based on one of the three branches of the loop presented in Figure 1.3, and focuses on the interaction between fluid dynamics and acoustics. The objective is to improve the knowledge of the effects of high-amplitude high-frequency acoustic fields on non-reactive coaxial injection, by facing three aspects of the problem.

The first aspect concerns the acoustic response of an expressly designed injection system represented by a liquid injection dome and a gas injection dome. A parametric investigation is performed in order to characterize the sensitivity of the system to some of its key geometrical features, and to identify which dome configuration may facilitate the acoustic coupling with the main chamber.

The second part of the research is dedicated to the investigation of the response of a coaxial jet to acoustic perturbations. The objective is to quantify the effects of high-amplitude/high-frequency acoustic fields on high Weber atomization regimes and to identify and quantify the parameters characteristic of the jet response. Jet response has been

systematically investigated for several injection locations in order to submit the jet to all possible acoustic conditions. Atomization regimes from Rayleigh axi-symmetric to fiber one have been considered. Single-injector and three-injector configuration have been investigated. In the case of the three-injector configuration experiments were carried out with and without injection domes. Responses at low Weber number atomization regimes are used to: identify the nonlinear effects responsible for the changes induced by acoustics; interpret the response of high Weber number atomization regimes; explain how acoustics can affect the droplet spatial distribution in the chamber.

The first and third points are strongly related to the development of the theoretical model based on nonlinear acoustics introduced by Baillot *et al.* [90] to describe the jet response. By combining experimental results and theoretical development it is demonstrated that all phenomena observed at low Weber number regimes can be ascribed to non-linear acoustics and that the same mechanisms also affect high Weber number atomization regimes. This also leads to a new interpretation of super-critical jet response and also for reactive flows [94, 95] and thus improve the knowledge of the thermo-acoustic feedback mechanisms responsible for the trigger and sustain of combustion instabilities.

## 1.5 Thesis Structure

The thesis is organized in three parts.

The first part is dedicated to the description of the experimental setup and measurement techniques. The TAC-Spray test rig is presented in Chapter 2. The acoustic resonant cavity and the forced acoustic field are described in section 2.1. The injection system is described in section 2.2. Details of the coaxial injector geometry and of the injection domes are given in this section. Measurement techniques are presented in Chapter 3: high-speed back-light visualization technique is introduced in section 3.1; droplet size measurement by image processing is described in section 3.2 and Laser Doppler Velocimetry (LDV) for gas velocity field characterization is presented in section 3.3.

Experimental results are discussed in the second part. Chapter 4 is dedicated to the characterization of the injection domes' acoustic response. The response of the atomization process to the acoustic field is reported in Chapter 5. Single injector configuration is discussed in section 5.2 whereas multi-point injection configuration is presented in section 5.3. Preliminary results concerning droplet size and gas velocity field measurements are reported in section 5.4.

The third part focuses on the theoretical model. Acoustic nonlinear theory is in-

roduced in Chapter 6. Fundamental equations for acoustic radiation pressure and the resulting radiation force are derived in section 6.2. Specific expressions are obtained for cylindrical and spherical objects. In Chapter 7 the phenomena observed experimentally are interpreted on the basis of the theoretical model.

The concluding remarks and perspectives for future development are given in Chapter 8.

Complementary results and information can be found in the appendices. Appendix A reports the results of the vibration test campaign, which has been carried out to improve the experimental setup configuration. In Appendix B the influence of the loudspeaker duct length on the resonant cavity eigenmodes is discussed by reporting numerical results. In Appendix C technical sketches concerning the injection domes are reported. Appendix D shows an example of high-speed visualization post-processing for flow visualization.



# Part I

## Experimental Setup



## Chapter 2

# TAC-Spray: Transverse Acoustic Cavity for Spray

*The experimental activities described in this thesis have been carried out at the CORIA laboratory on the test bench called **Transverse Acoustic Cavity for Spray** or TAC-Spray. The experimental setup is composed of a main resonant cavity in which a high-amplitude high-frequency acoustic field is produced and the injection system. Characteristics of the main resonant cavity and of the generated acoustic field are discussed in section 2.1. The injection system is presented in section 2.2: the injector geometry and injection domes are introduced in subsections 2.2.1 and 2.2.2, respectively. Air and water supply system is described in section 2.2.3.*

### 2.1 Acoustic Resonant Cavity

The experimental setup is composed of a semi-open resonant cavity represented in Figure 2.1 inside which an acoustic field is forced. The aim is to reproduce acoustic fluctuation amplitudes similar to those that can be found in a real LRE combustion chamber when it experiences high frequency combustion instability. The resonant cavity consists of two parallel vertical walls made of steel, a roof and a floor, both made of PVC. The distance between the two vertical walls is indicated as  $L_c$ , the width of the walls is  $W_c$  and the total cavity height (the distance in between the roof and the floor) is  $H_c$ . In the reference frame  $\vec{x}$  represents the horizontal direction parallel to the cavity walls;  $\vec{y}$  represents the direction perpendicular to the walls and parallel to the acoustic axis (*a.a.*) while  $\vec{z}$  is the vertical descending direction. The origin  $O$  of the reference frame is taken at the top center of the cavity, i.e. at the center of the roof's inner surface.

Two square ( $W_c/4 \times W_c/4$ ) optical access windows are located on the vertical walls (one on each side). A pair of Beyma CP850Nd compression drivers is placed on each vertical plate as shown in Figure 2.1(b).

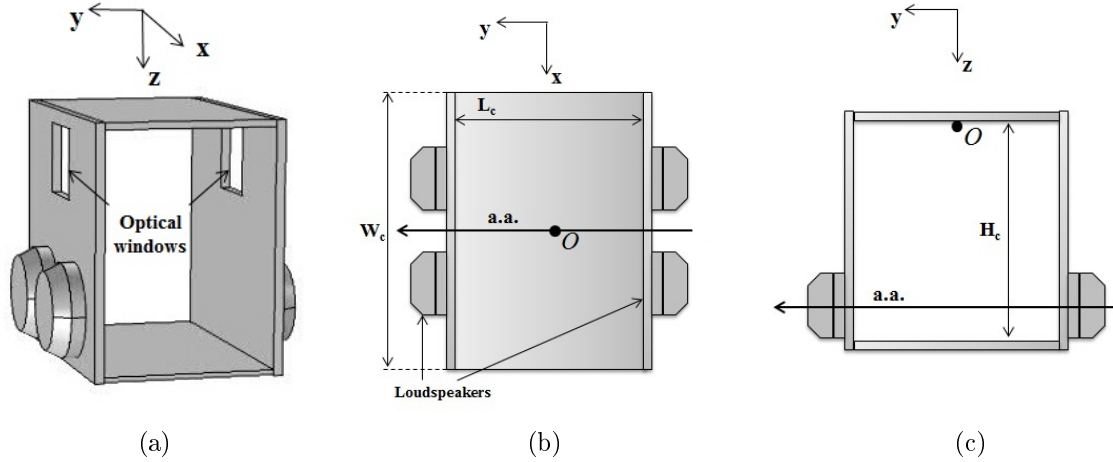


Figure 2.1: Experimental test-rig: (a) acoustic semi-open resonant cavity; (b) acoustic cavity upper-side view; (c) acoustic cavity front-side view.

Compression drivers are used at the limit of their capacity, in order to reach the highest amplitude pressure fluctuations in the resonant cavity. To avoid premature deformation or breaking of the titanium diaphragm inside the loudspeakers the maximum level are reached progressively and maintained for a short period. The typical input signal envelop is composed of a ramp of length  $\delta t_{ramp}$  raising from 0 to the maximum signal amplitude, a constant part at the maximum amplitude and a decreasing ramp from the maximum to 0. Each part lasts 300 ms. In order to ensure compression drivers internal coil cooling, an interval of at least 10-15 minutes must be considered in between two consecutive tests. The maximum voltage that loudspeakers can sustain with this protocol is of 48 VRMS. Using an amplifier with a gain of + 32 dB the signal generated must not exceed 1400 mVRMS. Before amplification the signal is filtered with a high-pass filter with a crossover frequency of 500 Hz to avoid compression drivers damaging.

Acoustic pressure can attain a maximum peak-to-peak amplitude of 12000 Pa. For this reason the entire system is placed in an acoustically isolated room provided with several passages for electric cables and pipes.

The strong acoustic fields produced in the main cavity induce also, as a secondary effect, mechanical vibrations on the cavity structure which are transmitted to all components directly connected with it. Vibrations of strong intensity could induce undesired vibrations of the injector bodies affecting measurements. Thus an aluminum structure

has been placed around the main cavity in order to reduce the vibrations transmitted to the injection domes. The entire injection system is placed on the top of the main resonant cavity and sustained by this expressly designed structure which support also feeding lines, valves, mass flow meters and it can be used also as a support for the camera when needed. Measurements of the mechanical vibrations transmitted to the domes before and after the structure installation confirm the reduction of transmission. Details concerning the support structure and the mechanical vibration measurements can be found in Appendix A.

### 2.1.1 Pressure Measurements and Signals Generation

Acoustic measurements have been performed using high frequency pressure transducers and microphones. Two Brüel & Kjær microphones type 2670 have been used to characterize the acoustic field inside the main resonant cavity without flow in the first part of the research. Signal acquisition was done through the OROS36 Multianalyzer recorder and a dedicated software (NVGate).

The experimental setup was then modified to allow injection through two injection domes (see section 2.2.2). The previous acquisition system was replaced and experiments were managed through a LabVIEW interface and the National Instruments CompactDAQ-9178 (NI cDAQ) system. The LabVIEW interface was developed in order to automate the signal generation, the acoustic field acquisition and the synchronization with the cameras when required. Three NI modules were used in the cDAQ (see Figure 2.2):

- NI 9263: for analog signals generation, used to generate the electric signal sent to the loudspeakers and the TTL signals for synchronization;
- NI 9215: analog module for signal acquisition. It is used to check the amplitude and the shape of the electric signal generated for the loudspeakers and to check the synchronization;
- NI 9234 IEPE: for analog signal acquisition, used for acoustic pressure measurements from PCB high frequency pressure transducers;

Three types of PCB high frequencies pressure transducers were used to characterize the acoustic response of injection domes and to measure the acoustic pressure reference in the cavity. These transducers allow measurements in both gas and liquid media and can be easily installed through their clump nut (which is not possible with Brüel & Kjær microphones type 2670).

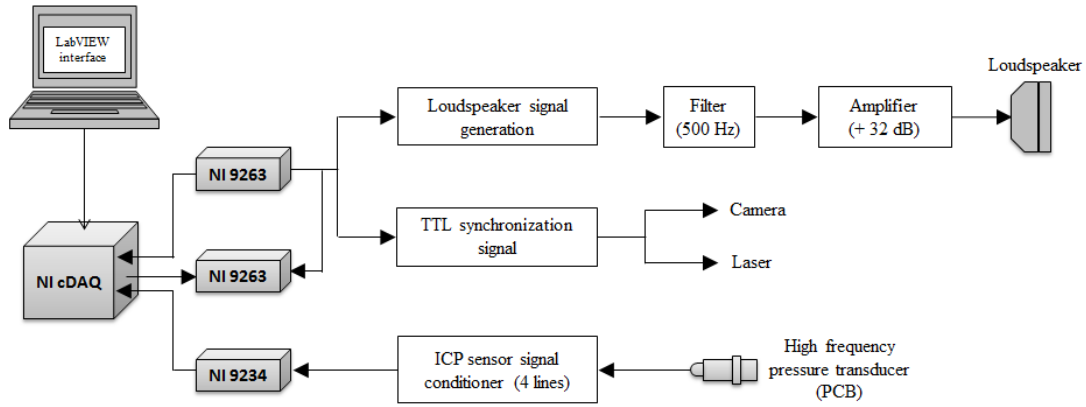


Figure 2.2: Schematic of the system for the generation and acquisition of signals.

- PCB 106B51 for the measurement of the reference pressure in the main cavity;
- PCB 106 (x4) for the measurement of the reference pressure in the main cavity and the acoustic pressure inside the gas dome (see subsection 2.2.2.1);
- PCB 113B28 (x2) for the measurement of the acoustic pressure inside the liquid dome (see subsection 2.2.2.3).

A 4-channel ICP sensor signal conditioner model 482C54 was used to provide the necessary current excitation to the PCB transducers.

An example of acoustic pressure signal measurement in the resonant cavity is shown in Figure 2.3. Acoustic field produced inside the resonant cavity follows the envelope of the loudspeaker input signal with the amplitude of fluctuations increasing from 0 to  $p_{a,pp}$  then a plateau at  $p_{a,pp}$  and finally a decreasing ramp from  $p_{a,pp}$  to 0.

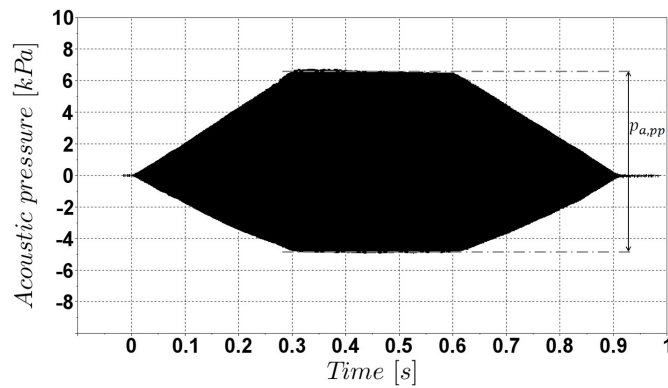


Figure 2.3: Example of raw acoustic pressure signal measurement ( $x = y = z = 0$ ,  $f = 1000 \text{ Hz}$ ).

The peak-to-peak amplitude of the acoustic pressure presents a maximum at the beginning of the plateau and then slightly decreases. This is due to the compression drivers which cannot generate exactly the same amplitude during the entire plateau. To avoid overestimation of the effective acoustic field to which the jet is submitted, peak-to-peak amplitude is calculated from signal histogram. Figure 2.4 represents a typical signal post-treatment. Figure 2.4(a) shows the signal histogram from which the peak-to-peak amplitude  $p_{a,pp}$  is calculated; Figure 2.4(b) represents the signal Power Spectral Density (PSD) plot.

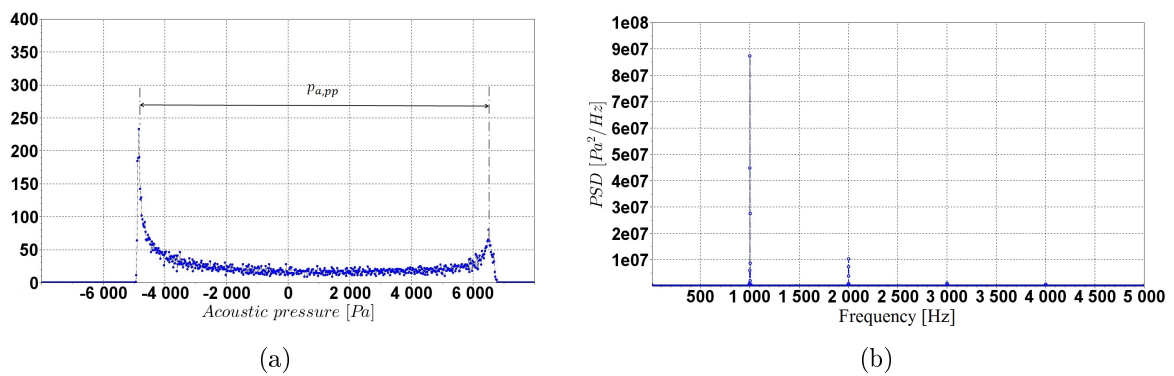


Figure 2.4: Example of acoustic signal post-processing: (a) signal amplitude calculation; (b) power spectral density plot ( $x = y = z = 0$ ,  $f = 1000 \text{ Hz}$ ).

In the following, the peak-to-peak value  $p_{a,pp}$  at PAN will be considered as the reference acoustic pressure for the tests.

## 2.1.2 Cavity Acoustic Field

The size of the cavity and the location of the loudspeakers have been chosen in order to maximize the amplitude of the acoustic field and in order to produce an acoustic field inside the resonant cavity that can be identified, at first approximation, as a planar standing wave in the  $\vec{y}$  direction corresponding to the 2<sup>nd</sup> transverse mode (2T) of the cavity.

In the previous works [89, 90] the acoustic resonant cavity was provided with only two loudspeakers that were placed in the upper side of the vertical walls (close to the roof) at their center ( $x = 0$ ). With such a configuration peak-to-peak acoustic pressure amplitudes up to  $\approx 5000 \text{ Pa}$  could be produced. In order to increase the acoustic levels the experimental setup evolution was studied. The number of loudspeakers was increased from 2 to 4 (two on each wall) at the same distance from the roof. The vertical position

was then varied and the configuration adopted in the present work was found to be the one providing the highest acoustic levels, which can be as high as 12000 Pa (peak-to-peak amplitude). Simulations, with the Acoustics module of COMSOL Multiphysics, have been used as support to the design phase. The Acoustics module is an optional package that extends the COMSOL environment and presents functionality optimized for the analysis of acoustics and vibration problems. For analysis of the main resonant cavity simulations have been performed with the *Acoustic-Solid Interaction, Frequency domain* interface, which combine the *Pressure acoustics* and the *Solid Mechanics* interface. The Helmholtz equation is solved in the frequency domain to obtain the acoustic pressure  $p$ . Cavity walls, roof and wall are treated as rigid walls (i.e. zero normal acoustic-velocity fluctuations). The loudspeakers are modeled as circular surfaces and a normal acceleration at the frequency  $f = 1000 \text{ Hz}$  is imposed as boundary condition. The entire system is then placed in a larger domain simulating the environment and to allow wave propagation through out the open sides of the cavity.

Figure 2.5 shows the resonant cavity acoustic field simulated in the injection plane ( $x = 0$ ) for the current configuration in which the loudspeakers are closer to the floor than the previous configuration. The acoustic field in the upper half part of the cavity corresponds with a good approximation to the 2T mode of the cavity.

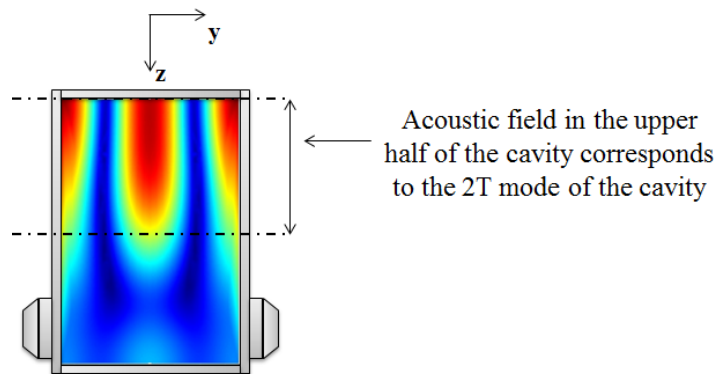


Figure 2.5: Resonant cavity numerical acoustic field.

### 2.1.2.1 Acoustic Pressure Profiles

Measurements inside the resonant cavity confirm simulations presented in Figure 2.5. Figure 2.6 represents the horizontal and vertical acoustic field experimental profiles in the injection plane ( $x = 0$ ) compared with simulations. The horizontal profile in Figure 2.6(b) shows the acoustic field profile in the region close to the injector exit plane ( $z \approx D_l$ ).

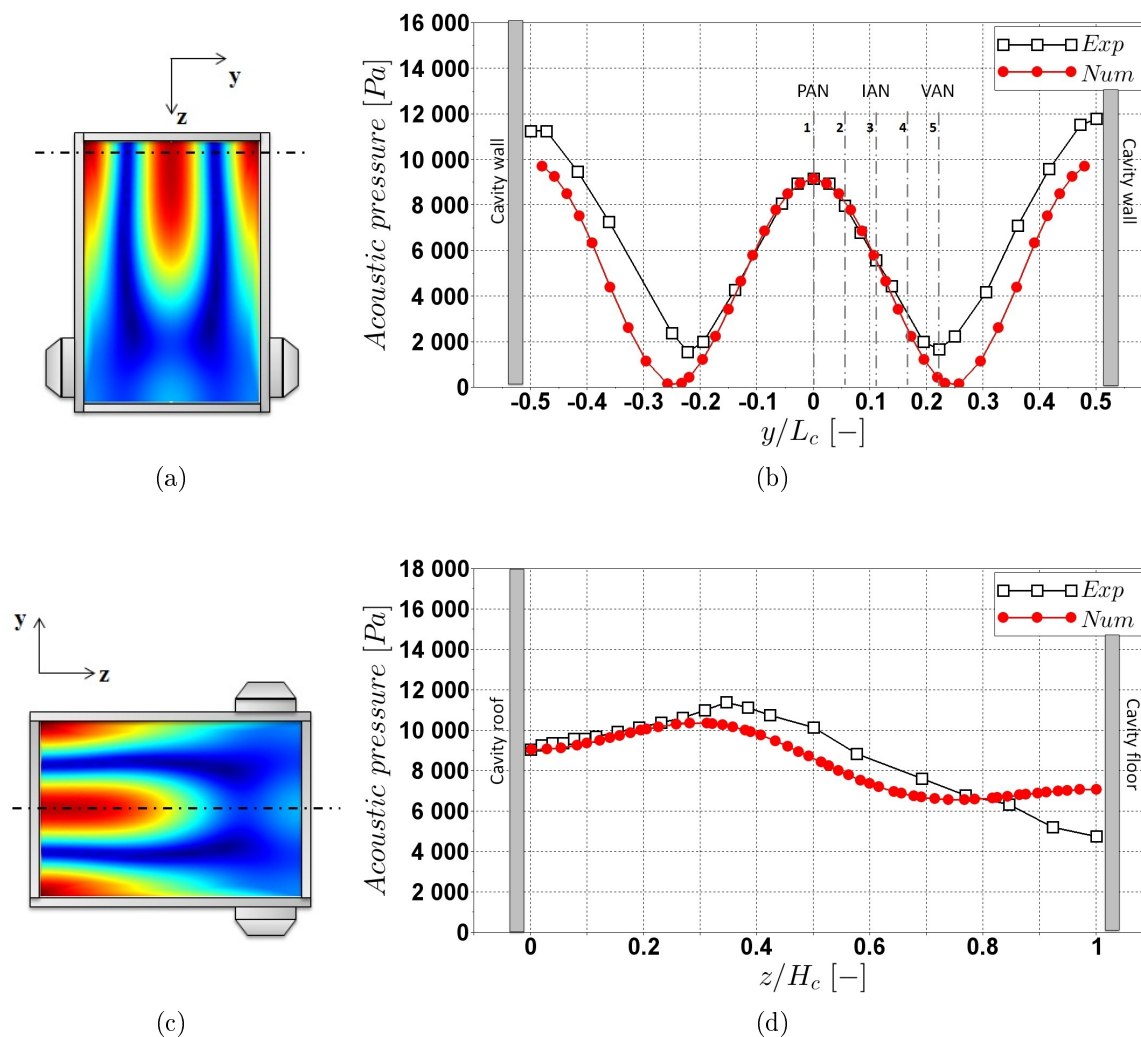


Figure 2.6: Comparison between experimental and numerical acoustic field: (b) horizontal profile ( $x = 0$ ) and acoustic reference locations along the acoustic axis *a.a.* (1=PAN,  $y/L_c = 0$ ; 2=PAN-IAN,  $y/L_c = 1/16$ ; 3=IAN,  $y/L_c = 1/8$ ; 4=IAN-VAN,  $y/L_c = 3/16$ ; 5=VAN,  $y/L_c = 1/4$ ); (d) vertical profile at  $x = y = 0$ ; .

The jet can be submitted to different conditions in terms of acoustic pressure and velocity fluctuations, depending on its position in the cavity. Five locations of interest along the  $y$ -direction (parallel to the direction of *a.a.*) are specified, representative of all possible acoustic conditions to which the jet can be submitted: the pressure anti-node (PAN); the intensity anti-node (IAN), the velocity anti-node (VAN); the position PAN-IAN at equal distances between the pressure and intensity anti-nodes, and the position IAN-VAN between the intensity and velocity anti-nodes. IAN is the location where acoustic flux per unit surface in the  $\vec{y}$  direction is maximum, the acoustic flux being defined as the product between the acoustic pressure and the acoustic velocity  $u_a(y, t)$ . The maximum

acoustic pressure fluctuations are reached at the pressure anti-nodes. Figure 2.6(d) shows the vertical profile measured at the pressure anti-node (PAN). It can be seen that the acoustic pressure does not vary much in almost the first half of the cavity height, thus the jet can be considered submitted to a quasi-uniform acoustic field in the vertical direction.

In the vicinity of the two velocity anti-nodes (around  $y/L_c = 1/4$ ) the acoustic pressure fluctuation presents two minima. Experiments indicated that pressure amplitudes at VAN are in between 20 – 30% of those at PAN. Pressure amplitude is not null at the velocity anti-nodes because the cavity is open on two sides which causes acoustic losses and because cavity walls do not provide perfect reflecting boundary conditions. As a consequence of the non-perfect reflection a phase shift between the incident and reflected progressive wave can result. The acoustic pressure in the vicinity of the velocity anti-nodes can be considered as the superimposition of a stationary and a progressive wave of the same frequency as shown by Lespinasse [95]. This model is also able to reproduce the phase shift between the pressure antinode and the positions in the vicinity of the velocity antinode, which experiments were found to vary continuously across VAN from  $-\pi$  to  $\pi$ .

### 2.1.2.2 Acoustic Pressure Signals at PAN and VAN

Figure 2.7 shows the acoustic pressure signals measured at PAN (see Figure 2.7(a)) and VAN (see Figure 2.7(b)) and their respective power spectral density plots (see Figure 2.7(c) and 2.7(d)). Measurements are taken at  $x = 0$  at the forcing frequency of  $f=1015$  Hz. In Figure 2.7(a) and 2.7(b) raw signals are compared with signals filtered at 1015 Hz<sup>a</sup> (black solid line) and 2030 Hz<sup>b</sup> (black dashed line).

The raw signal recorded at PAN (see blue line Figure 2.7(a)) is non-symmetric and presents a quasi-sinusoidal shape at the forcing frequency of 1015 Hz (see Figure 2.7(c)). The deformation is due to nonlinear distortion caused by the harmonics of the forcing frequency (see peaks at 2030 Hz and 3045 Hz in the spectrum of Figure 2.7(c)); which however present energy densities at least one order of magnitude lower than that at 1015 Hz. The peak-to-peak amplitude of the raw signal is 10900 Pa, which corresponds to 174.7 dB, whereas the amplitude of the signal filtered at 1015 Hz is 10120 Pa, which corresponds to 174 dB. At VAN the signal is much more distorted (see red line in Figure 2.7(b)) and the power spectral density plot shows two peaks of similar amplitudes (see Figure 2.7(d)). The main peak is represented by the first harmonic, i.e. 2030 Hz,

---

<sup>a</sup>Signals are filtered with a Scilab pass band digital filter with a lower cut-off frequency of 950 Hz and an upper cut-off frequency of 1100 Hz.

<sup>b</sup>Signals are filtered with a Scilab pass band digital filter with a lower cut-off frequency of 1950 Hz and an upper cut-off frequency of 2100 Hz.

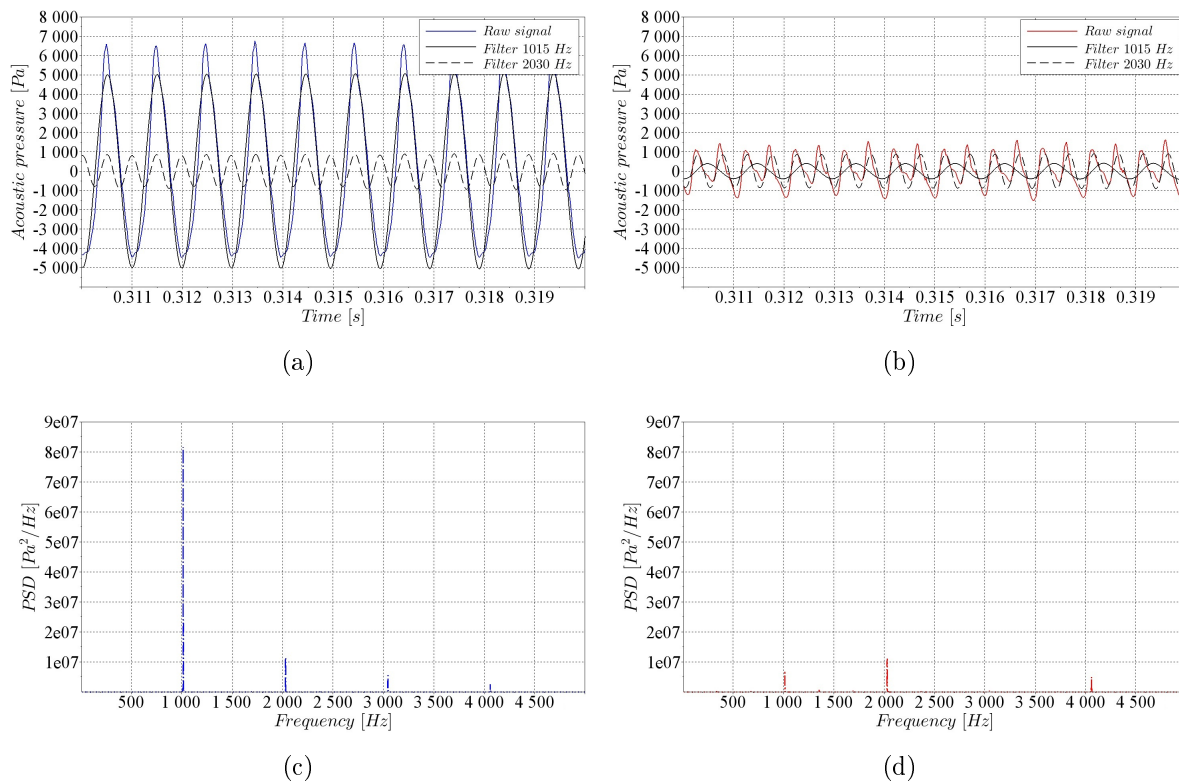


Figure 2.7: Acoustic signal measurements and power spectral density plots for (a-c) PAN and (b-d) VAN for  $f = 1015 \text{ Hz}$  ( $x = 0$ ).

which presents the same energy density as that observed at PAN. The second peak is the fundamental frequency, i.e. 1015 Hz. In this case energy density is one order of magnitude lower than that measured at PAN. The spectra suggest the presence of secondary standing wave corresponding to the 4T mode of the cavity superimposed onto the 2T mode. The 4T mode presents five pressure anti-nodes. Two of them correspond in space to the velocity anti-nodes of the 2T mode. Signal filtering at 2030 Hz indicated that the amplitude of the corresponding wave is around 1600 Pa (see Figure 2.7(a) and 2.7(b)), which further explains the residual pressure fluctuations at VAN (see Figure 2.6(b)).

### 2.1.2.3 Acoustic Pressure at PAN

The acoustic pressure at PAN ( $p_{a,pp}$ ) depends on the amplitude of the loudspeakers' input signal and on the resonant conditions. Figure 2.8(a) shows  $p_{a,pp}$  at PAN as a function of the voltage mVRMS of the signal generated with the LabVIEW interface (before amplification) for a frequency of 1015 Hz. It can be seen that  $p_{a,pp}$  increases almost linearly with the signal generated; 1400 mVRMS is the maximum value that loudspeakers

can sustain (see section 2.1). The value of  $p_{a,pp}$  also varies as a function of the forcing frequency, as shown in Figure 2.8(b). In this case the maximum of  $p_{a,pp}$  is attained around 1015 Hz. Before testing, the forcing frequency was adjusted around 1000 Hz in order to find conditions at which loudspeakers provided the desired resonant condition and the maximum value of acoustic pressure at PAN was reached.

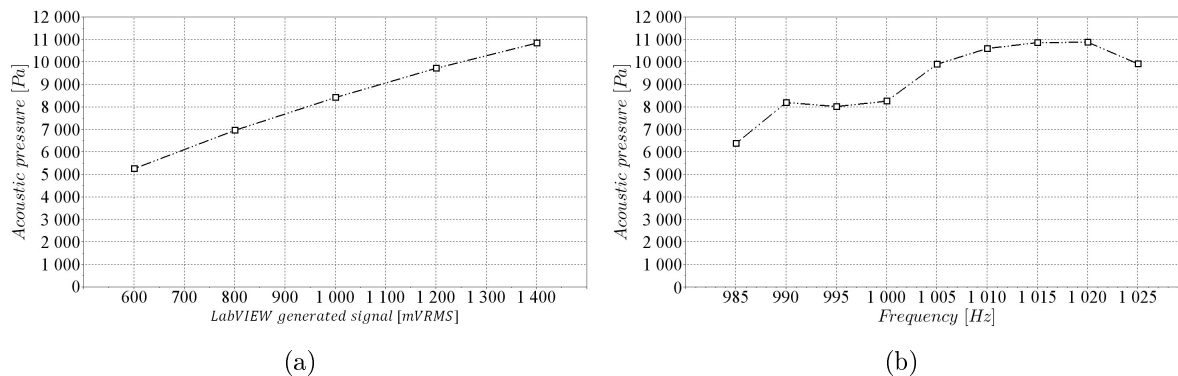


Figure 2.8: Acoustic pressure signal amplitude at PAN ( $x = 0$ ) as a function of: (a) the forcing frequency.

## 2.2 Injection System

### 2.2.1 Coaxial Injector

The injector considered in the present work belongs to the family of the shear-coaxial injectors (see Figure 1.4). A cross-section schematic of the injector used is presented in Figure 2.9. The liquid is injected in the central post tube while the gas flows from the two side inlets through the external coaxial channel. The liquid is water, and the gas flowing around the liquid jet is air (air-assisted liquid jet). A close-up view of the injector exit is shown on the right side of the picture. The exit diameter of the liquid post is indicated as  $D_l$  and the overall exit diameter is  $D_g$ , whereas  $e$  is the thickness of the gas annular gap.

The liquid post presents a divergent at the exit and no recess zone is made. The geometry is similar to that of the injector used in the previous work [89, 90], except for the injector body length and the diverging angle.

Injection conditions will be indicated by three non-dimensional numbers: the gaseous Weber number  $We_g$  [96, 97], the liquid Reynolds number  $Re_l$ , and the momentum flux

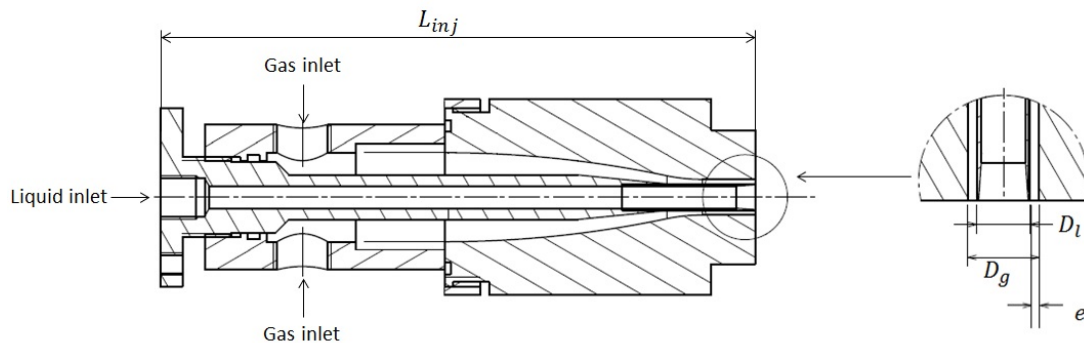


Figure 2.9: Schematic of the coaxial injector used in the experiments and close-up view of the injector exit.

ratio  $J$ . They are expressed as follows:

$$We_g = \frac{\rho_g U_g^2 D_l}{\sigma_l} \quad Re_l = \frac{D_l U_l}{\nu_l} \quad J = \frac{\rho_g U_g^2}{\rho_l U_l^2} \quad (2.1)$$

where  $\rho_g$  and  $U_g$  are the density and the bulk velocity of the gas while  $\rho_l$ ,  $U_l$ ,  $\sigma_l$  and  $\nu_l$  are respectively the density, bulk velocity, surface tension and kinematic viscosity of the liquid at standard conditions.

Depending on the injection conditions different atomization regimes can be identified [89, 96, 98]. Figure 2.10 shows five atomization regimes characteristic of air-assisted liquid jet disruption modes: Rayleigh axi-symmetric ( $We_g = 9$ ;  $Re_l = 2500$ , see Figure 2.10(a)); Rayleigh non-symmetric ( $We_g = 40$ ;  $Re_l = 3000$ , see Figure 2.10(b)); Shear break-up ( $We_g = 60$ ;  $Re_l = 2900$ , see Figure 2.10(c)); Membrane ( $We_g = 129$ ;  $Re_l = 3200$ , see Figure 2.10(d)) and Fiber ( $We_g = 224$ ;  $Re_l = 3200$ , see Figure 2.10(e)).

In the present work several flow conditions have been investigated ( $9 < We_g < 600$ ,  $1000 < Re_l < 6600$ ) covering all atomization regimes previously cited, ranging from Rayleigh axi-symmetric regime to fiber type regime.

In the following atomization regimes characterized by  $We_g < 100$  will be indicated as *low Weber* number atomization regimes, whereas atomization regimes with  $We_g > 100$  will be indicated as *high Weber* number atomization regimes. A specific injection condition with  $We_g = 519$ ,  $Re_l = 6600$ ,  $J = 5.1$  has been also selected in order to investigate the response of a jet more representative of actual injection conditions in a liquid rocket engine and it will be indicated as T-LRE in the following. Experimental results concerning this specific test conditions are used for validation of numerical tools developed at ONERA as object of a scientific collaboration in the framework of the REST group.

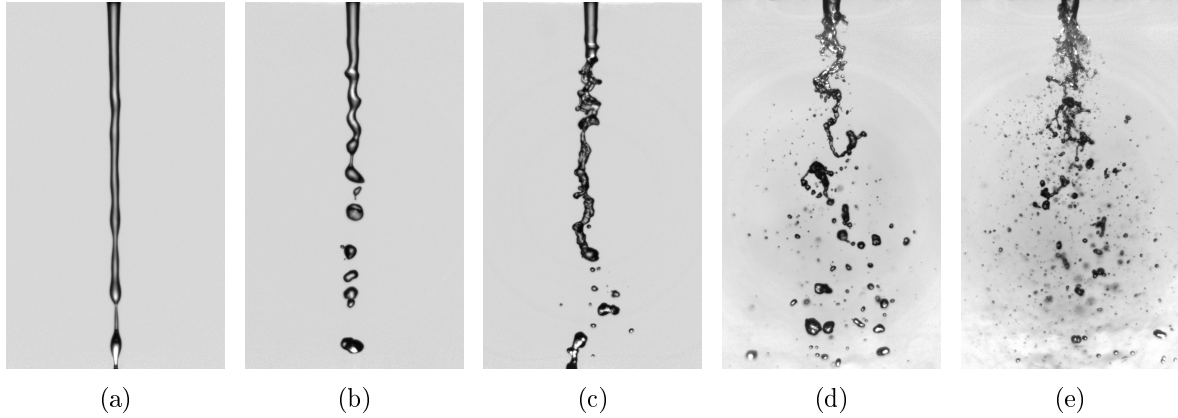


Figure 2.10: Examples of liquid jet atomization regimes obtained with the coaxial injector studied: (a) Rayleigh axi-symmetric ( $We_g = 9$ ;  $Re_l = 2500$ ); (b) Rayleigh non-symmetric ( $We_g = 40$ ;  $Re_l = 3000$ ); shear break-up ( $We_g = 60$ ;  $Re_l = 2900$ ); membrane ( $We_g = 129$ ;  $Re_l = 3200$ ) and fiber ( $We_g = 224$ ;  $Re_l = 3200$ ).

Up to three injectors can be placed simultaneously on the cavity roof in order to simulate multi-point injection systems. The conditions of temperature and pressure of the cavity where the injection takes place are those of the ambient. Injectors placed in the acoustic cavity have their exit plane coincident with the inner surface of the roof. Multi-point injection tests were performed with independent feeding lines for the three injectors connected or not with the injection domes. In the following a specific test conditions represented by  $We_g = 190$ ,  $Re_l = 2000$  will be considered as representative of high Weber atomization regimes. Multi-point injection tests (with and without injection domes) and gas velocity measurements were made for these specific injection conditions.

## 2.2.2 Injection Domes

The characterization of the acoustic response of the injection domes represents one of the objectives of this work. To do that, two variable-size injection domes were designed and built. In this way it has been possible to investigate how acoustic produced in the resonant cavity could propagate upstream through out the injectors and interact with the resonant modes of the feeding system. The entire system is conceived in such a way that several design parameters can be modified to investigate their influence on the acoustic coupling. A numerical parametric analysis was performed with the Acoustics module of COMSOL Multiphysics<sup>®</sup> in order to determine the geometries (size and shape) of the two injection domes. The Eigenfrequency study type of the *Pressure Acoustics* interface, in which the Helmholtz equation is solved in the frequency domain without source terms,

has been used. The acoustic pressure  $p$  is the only variable of the problem. Figure 2.11 presents the two numerical domains and the parameters considered in the analysis. More details concerning domes geometries and schematics can be found in Appendix C. These geometries have been used to calculate the domes' eigenmodes. The boundary conditions imposed at the injectors' exit plane are those of an open boundary ( $p = 0$ ) while all other surfaces are treated as rigid walls (i.e. zero normal acoustic-velocity fluctuations); no mass flow rate is considered in the simulations.

Domes' size and also size of the connection components between the domes and the injectors allow varying domes' eigenfrequencies,  $f_{m,n,p}$  around the frequency of the acoustic field forced in the main cavity, i.e.  $1 \text{ kHz}$ . Here  $m$ ,  $n$  and  $p$  indicate the number of nodes respectively in the direction  $\vec{x}$ ,  $\vec{y}$  and  $\vec{z}$ . Determination of the geometries and sizes of the two domes was based on the fact that the cavities should have been provided with movable parts and based on geometrical and manufacturing process constraints.

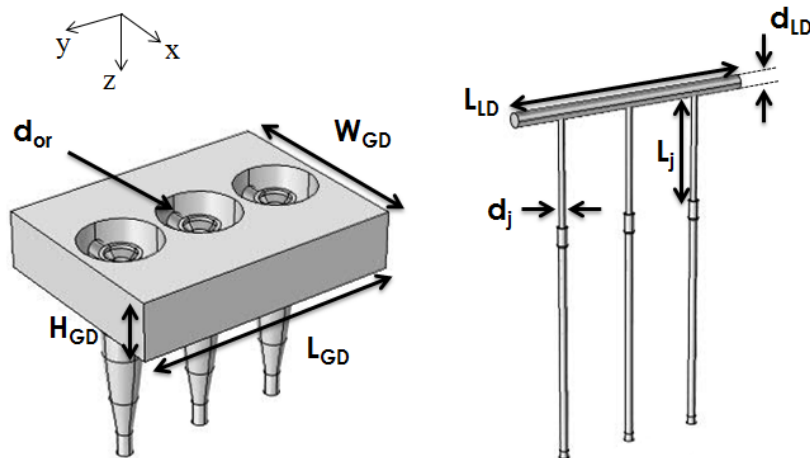


Figure 2.11: Gas dome  $GD$  (left side) and liquid dome  $LD$  (right side) internal domains considered in numerical simulations (COMSOL Multiphysics<sup>®</sup>).

### 2.2.2.1 Gas Dome Design

The gas dome presents a rectangular section and encloses a part of the three injector bodies (see Figure 2.12). The gas is injected into the dome through out the four gas inlets placed on the dome sides which are parallel to the injectors line (see Figure 2.12(a)). Figure 2.12(b) shows a cut of the domain along the injectors axes. The internal injector geometry presented in Figure 2.9 is taken into account in the simulations. Gas then enters into the injectors through out two diametrically opposite inlets of injector bodies

(see Figure 2.9). The diameter of the inlet orifices  $d_{or}$  can be changed by replacing the internal inserts which are shown in Figure 2.12(c). Three inlet orifice diameters have been tested: 0.375, 0.75 and 1.125 (diameters are scaled with the total injector exit diameter  $D_g$ , see Figure 2.9). The length  $L_{GD}$  and the height  $H_{GD}$  of the dome have been fixed since simulations indicated that the dome width  $W_{GD}$  was the parameter that the most strongly affects the resonant modes of interest. Two pistons (see Figure 2.12(a)) have been placed on the same surfaces of the gas inlets in order to vary the dome size  $W_{GD}$ . The smallest gas dome volume will be indicated in the following as  $GD0$  and the biggest one as  $GD8$ . The dome sizes scale linearly with their indexes, which means that  $GD8 - GD6 = GD4 - GD2$ .

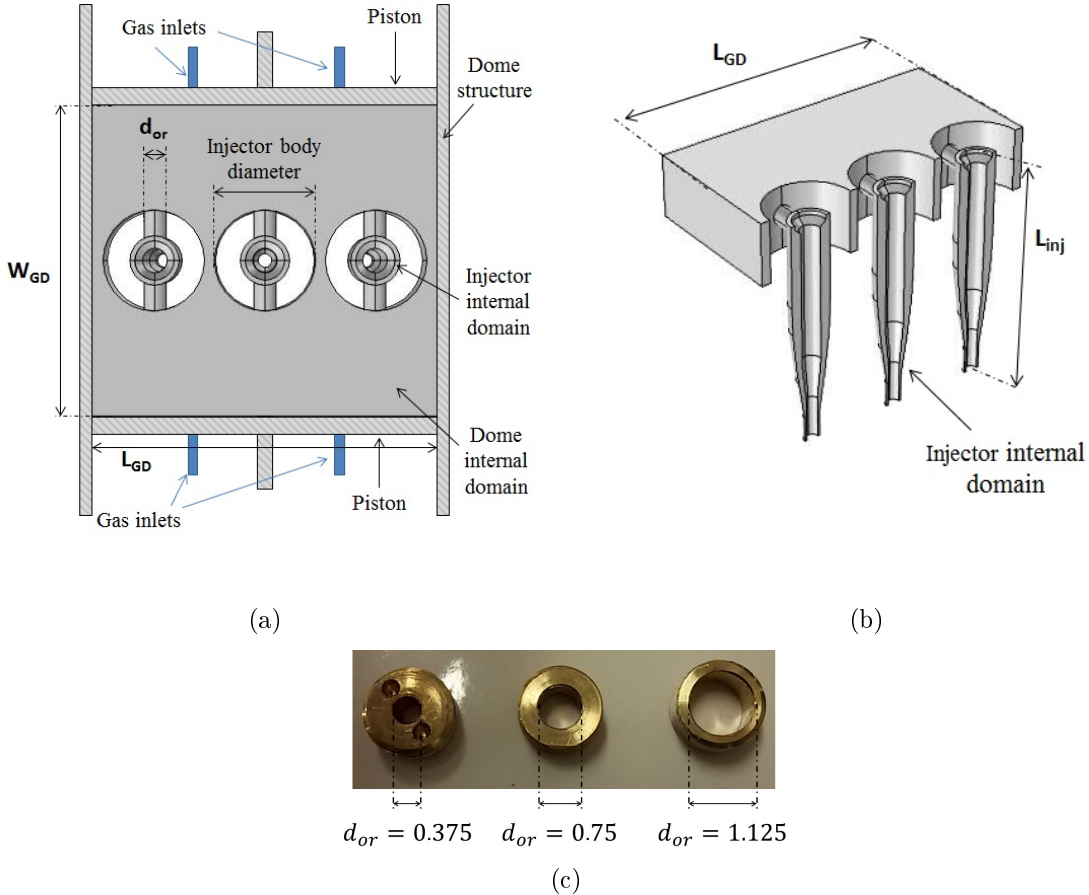


Figure 2.12: (a) Gas dome upper view; (b) half gas dome side view (c) orifice internal inserts  $d_{or}$ .

Figures 2.13(a) and 2.13(b) represent the real part of the complex pressure amplitude distribution of the mode shapes GD-A, GD-B and GD-C of the three eigenfrequencies

around 1 *kHz*. These results are provided by the simulations for  $d_{or} = 1.125$ , respectively for *GD0* and *GD8*. Characterization of numerical mode shapes is given as a function of reduced coordinates:  $\tilde{x}_g = x/W_{GD8}$  and  $\tilde{y}_g = y/L_{GD}$ . Envelope profiles of pressure amplitudes along  $\tilde{x}_g$  and  $\tilde{y}_g$  are reported in Figures 2.13(c) and 2.13(d). These profiles are calculated at the gas dome mid-height ( $H_{GD}/2$ ) for  $\tilde{y}_g = 0.16$  and  $\tilde{x}_g = 0.11$  respectively (see Figure 2.13(a) and 2.13(b)). Numerical acoustic pressure distributions for GD-A indicate that, in the vertical planes  $\tilde{y}_g = constant$ , all points are in-phase (see Figure 2.13(a)) and acoustic pressure has a maximum at  $\tilde{x}_g = 0$  and decreases toward the dome boundaries at  $\tilde{x}_g = \pm 0.5$  (see Figure 2.13(c)). The vertical symmetry plane  $\tilde{y} = 0$  is the nodal plane (see Figure 2.13(d)),  $f_{0,1,0}$ . Acoustic pressure amplitudes decreases by increasing the dome size from *GD0* to *GD8*.

An example of the influence of the dome size on the mode frequencies is shown in Figure 2.14 for  $d_{or} = 1.125$ . Calculations indicate that eigenfrequency associated with mode GD-A increases from 950 to 1005 Hz by increasing the dome size from *GD0* to *GD8*. Mode GD-B presents a spatial structure similar to that of GD-A along the  $\tilde{x}_g$ -axis (see Figure 2.13(c)). In every plane  $\tilde{z}_g = constant$  two nodal lines parallel to  $\tilde{x}_g$  are identified,  $f_{0,2,0}$  (see Figure 2.13(d)). In both plots curves corresponding to *GD0*, *GD4* and *GD8* are superimposed. Increasing the dome size does not affect the associated eigenfrequency, which varies between 1040 and 1050 Hz (see Figure 2.14).

The third mode, named GD-C changes its shape as the dome size is increased. For *GD0*, *GD2* and *GD4* all points in the dome cavity are in phase (see Figure 2.13(a)) and the dome acts as a Helmholtz resonator,  $f_{0,0,0}$ . For *GD6* and *GD8* two nodal lines appear in the  $\tilde{y}_g$ -direction,  $f_{2,0,0}$  (see Figure 2.13(b)). In the  $\tilde{x}_g$ -direction, acoustic pressure amplitudes at the pistons' walls, are of the same order of magnitude as those observed for *GD0* (see Figure 2.13(c)). Increasing the dome size from *GD0* to *GD8* produces an associated eigenfrequency which decreases from 1100 Hz to roughly 1040 Hz (see Figure 2.14).

Based on these results the geometry selected has been considered appropriate for the purpose of the investigation and the final manufactured dome is shown in Figure 2.15.

Pressure transducer housing and pistons are also indicated. In the following only pressure transducer locations indicated in the figure will be discussed in order to identify the eigenmode excited experimentally. Each transducer's location is identified by means of the nomenclature indicated in Figure 2.15 (i.e.  $PT_{l0}$ ;  $PT_{c0}$ ;  $PT_{r0}$ ;  $PT_{l1}$ ;  $PT_{l2}$  and  $PT_{l3}$ ). Transducers' positions in the  $\tilde{x}$ - $\tilde{y}$  plane are summarized in Table 2.1. Up to 4 pressure transducers (PCB 106B) can be placed on the gas dome at the same time in order to characterize its acoustic response.

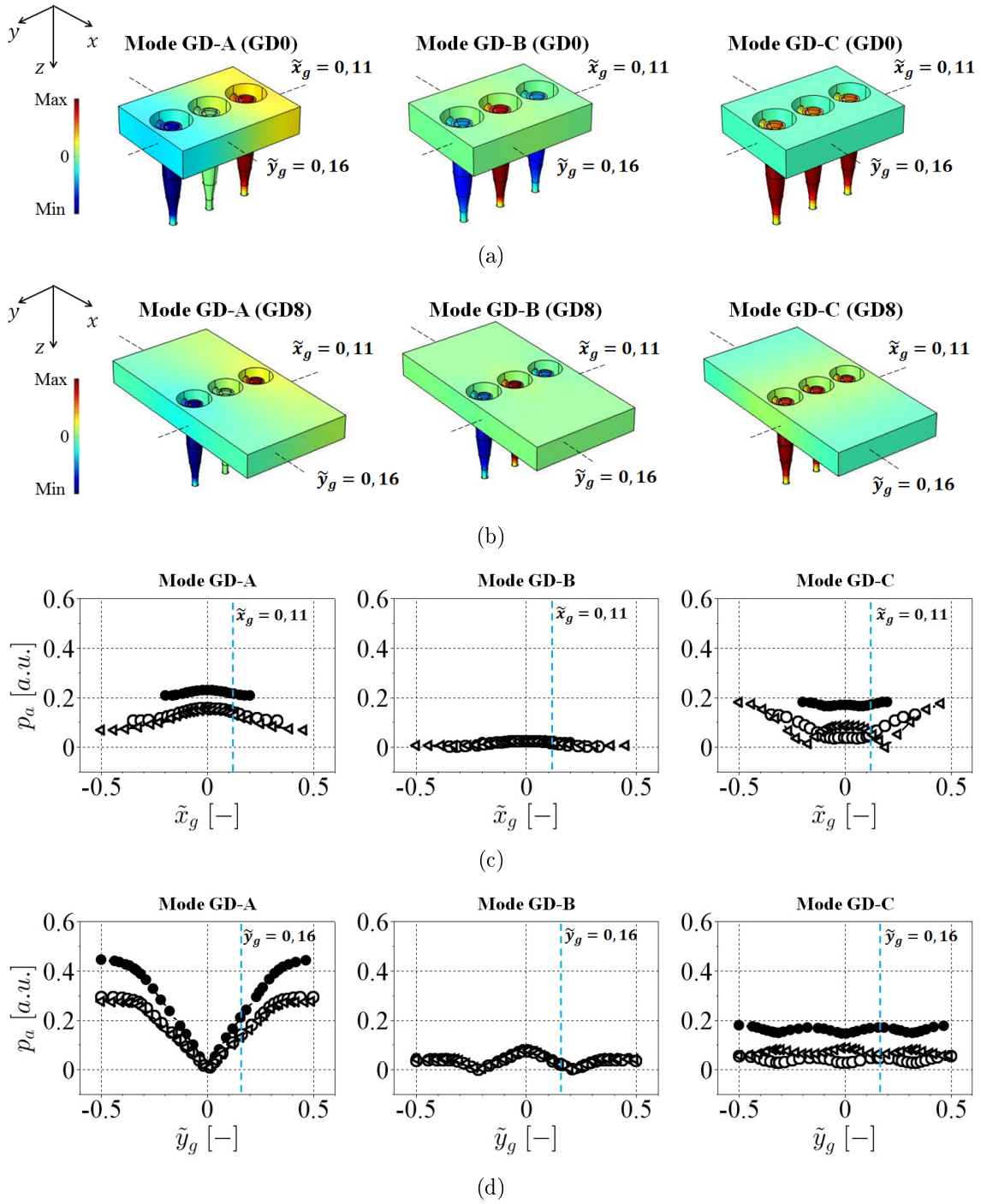


Figure 2.13: Gas dome mode-shapes obtained with COMSOL Multiphysics<sup>®</sup>: (a) real part of the complex pressure amplitude distribution (*GD0*;  $d_{or} = 1.125$ ); (b) real part of the complex pressure amplitude distribution (*GD8*;  $d_{or} = 1.125$ ); (c) envelope profiles of pressure amplitudes at  $\tilde{y}_g = 0,16$  w.r.t.  $\tilde{x}_g = x/W_{GD8}$ ; (d) envelope profiles of pressure amplitudes at  $\tilde{x}_g = 0,11$  w.r.t.  $\tilde{y}_g = y/L_{GD}$ . (● *GD0*; ○ *GD4*; ◁ *GD8*;  $d_{or} = 1.125$ ).

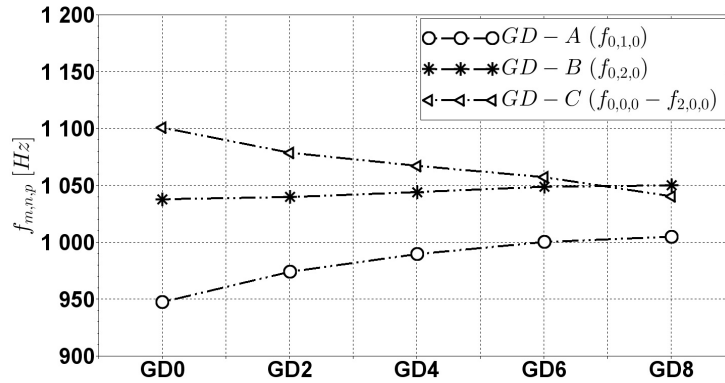


Figure 2.14: Gas dome eigenfrequencies as a function of the dome size ( $d_{or} = 1.125$ ).

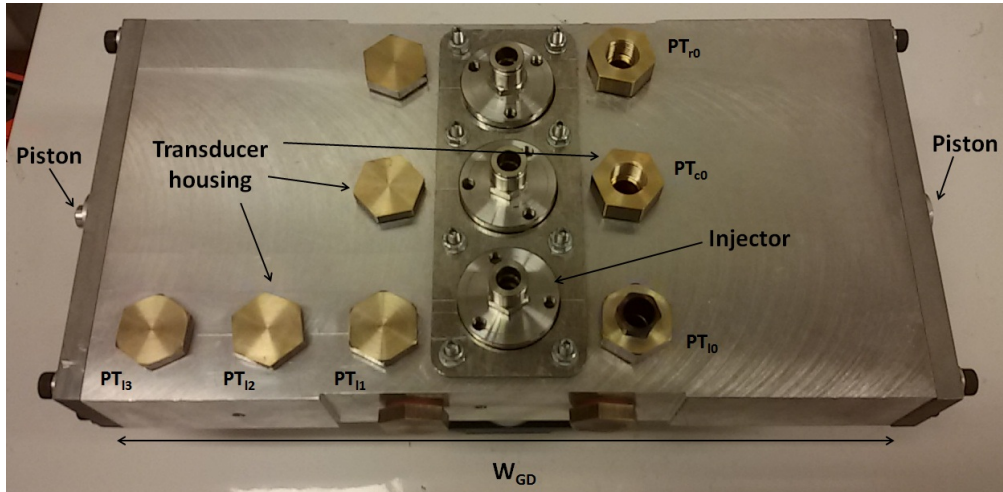


Figure 2.15: Gas dome upper view and pressure transducer locations.

	$PT_{l0}$	$PT_{c0}$	$PT_{r0}$	$PT_{l1}$	$PT_{l2}$	$PT_{l3}$
$\tilde{x}$	-0.17	-0.17	-0.17	0.17	0.32	0.47
$\tilde{y}$	0.39	0	-0.39	0.39	0.39	0.39

Table 2.1: Pressure transducers' positions in the gas dome as functions of the reduced coordinates  $\tilde{x}$  and  $\tilde{y}$ .

### 2.2.2.2 Gas Dome Frequency Response to White Noise Excitation

The frequency response of the gas dome has been investigated experimentally with a procedure similar to that found in the literature for the acoustic characterization of combustion chambers with quarter wave cavities [99]. A white noise signal has been used to excite the dome. The signal generated with a Scilab function is amplified with a gain of

+ 26 dB and sent to a loudspeaker. Dome size has been varied from  $GD0$  to  $GD8$ ; for each dome size the acoustic pressure has been measured with the  $PT_{11}$  pressure transducer (see Figure 2.15). The signal spectrum is then calculated and filtered in between 900 - 1200 Hz in order to focus on the spectrum region around 1000 Hz. Results are shown in Figure 2.16 for  $GD0$  and  $GD8$ .

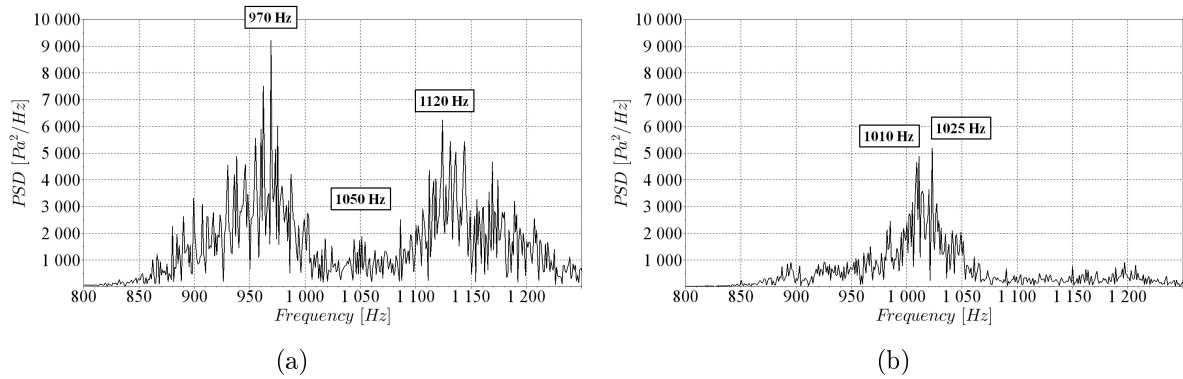


Figure 2.16: Experimental gas dome frequency response to white noise excitation for: (a)  $GD0$  and (b)  $GD8$  ( $d_{or} = 1.125$ ).

By taking into account numerical results reported in Figure 2.14, the three modes GD-A, GD-B and GD-C can be identified in the experimental spectrum of Figure A1(a) at 970 Hz, 1050 Hz and 1120 Hz, respectively. Mode GD-B has very low energy compared with GD-A and GD-C, which is in agreement with Figure 2.13. For  $GD8$  (see Figure A1(b)) the frequencies corresponding to GD-A and GD-C are closer than for  $GD0$ . This narrowing of the spectrum is in agreement with numerical results reported in Figure 2.14, in which eigenfrequencies get closer as gas dome size is increased.

### 2.2.2.3 Liquid Dome Design

The design procedure described in the previous section for the gas dome has been adopted for the *liquid dome* LD (right side in Figure 2.11), and a cylindrical geometry has been chosen. First, the shape of the dome has been selected taking into account injectors body size and manufacturing constraints. Then, the characteristic dimensions have been chosen based on numerical simulations of the liquid dome eigenmodes performed with the Acoustics module of COMSOL. Figure 2.17 shows a side view of the liquid dome in which liquid inlets are indicated.

The diameter of the dome  $d_{LD}$  has been fixed in the analysis, whereas its length  $L_{LD}$  has been selected as the variable parameter, and can be varied by means of two pistons.

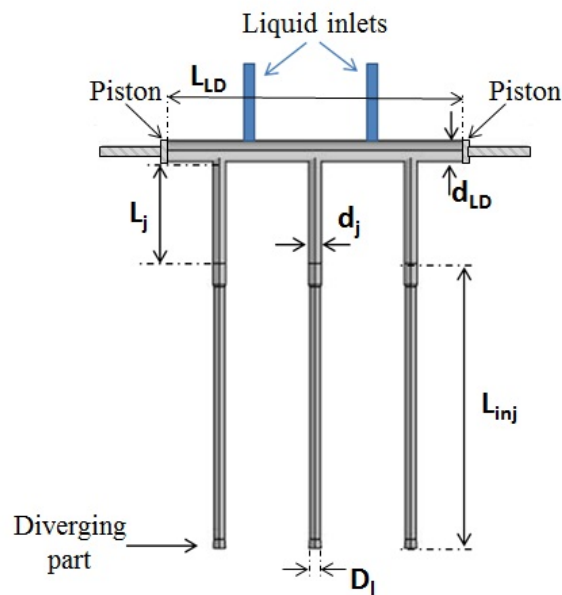


Figure 2.17: Liquid dome numerical domain (side view).

The smallest available liquid dome volume is indicated in the following as  $LD0$  while the largest one as  $LD4$ . The relationship between two consecutive liquid dome sizes is linear, which means that  $LD4 - LD3 = LD1 - LD0$ . The dome is connected to the injectors by three connection junctions. The length  $L_j$  and the diameter  $d_j$  of these junctions are also adjustable parameters. In particular, two connection lengths  $L_j$  of 0.387 and 0.548 and two connection diameters  $d_j$  of 0.67 and 1 have been considered. The values of  $L_j$  and  $d_j$  are scaled with the injector length  $L_{inj}$  and post diameter  $D_l$ , respectively. Figure 2.18 represents the two liquid dome eigenmodes predicted by the simulations that will be considered for the interpretation of the experimental results for which  $L_j = 0.548$  and  $d_j = 0.67$ .

The real part of the complex pressure amplitude distributions are reported in Figure 2.18(a) while the envelope profiles of the pressure amplitude envelope calculated along the liquid dome axis (see Figure 2.18(a);  $\tilde{x}_l = \tilde{z}_l = 0$ ) are reported in Figure 2.18(b). Reduced coordinates considered for the characterization of the eigenmodes in the liquid domes are:  $\tilde{x}_l = x/d_{LD}$ ,  $\tilde{y}_l = y/L_{LD}$  and  $\tilde{z}_l = z/d_{LD}$ . The corresponding eigenfrequencies are shown in Figure 2.19 as functions of the liquid dome size. The eigenfrequency associated to mode LD-A is around 1000 Hz for all dome sizes. When this eigenmode is excited all points in the whole domain are in-phase (see Figure 2.18(a)), with a behavior similar to that of an Helmholtz resonator,  $f_{0,0,0}$ . Mode LD-B is reported here even if its

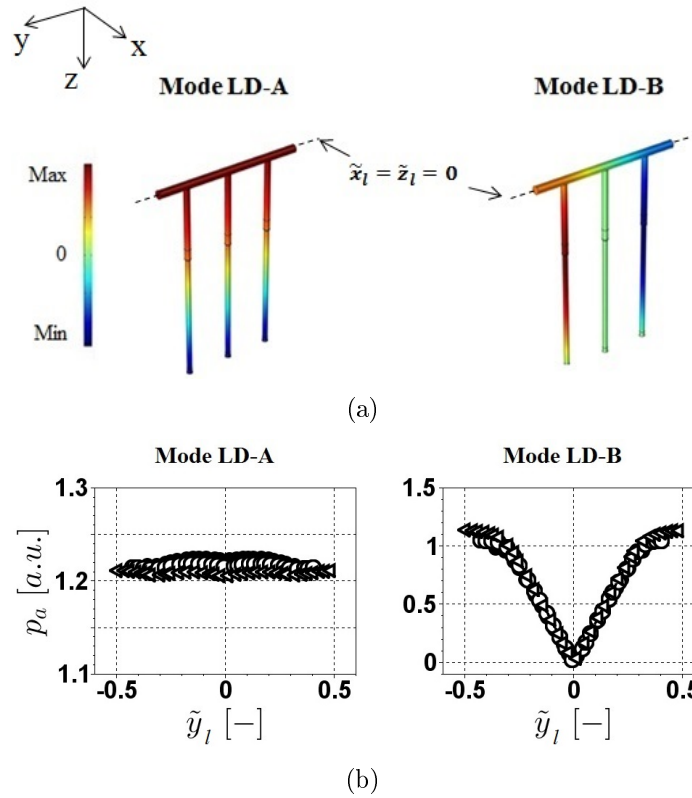


Figure 2.18: Liquid dome mode-shapes (COMSOL Multiphysics<sup>®</sup>): (a) real part of the complex pressure amplitude distribution (LD2); (b) envelope profiles of pressure amplitudes w.r.t.  $\tilde{y}_l = y/L_{GD}$  for  $\bullet$  LD0;  $\circ$  LD2 and  $\triangleleft$  LD4 ( $L_j = 0.548$ ,  $d_j = 0.67$ ).

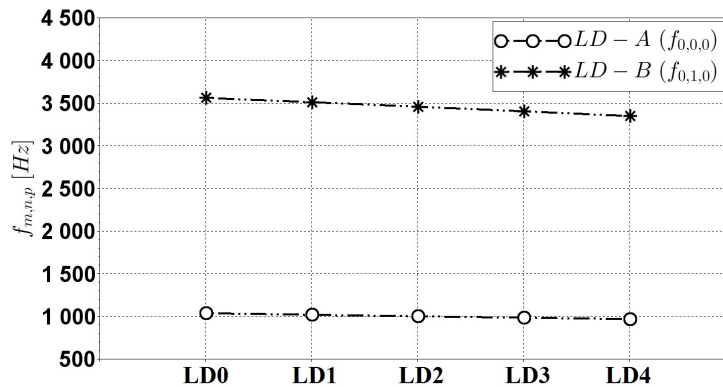


Figure 2.19: Liquid dome eigenfrequencies w.r.t dome length ( $L_j = 0.548$ ,  $d_j = 0.67$ ).

corresponding eigenfrequency is around 3500 Hz, because its spatial structure indicates the presence of a pressure node at the central injector (see Figure 2.18(b)) whilst the two

domes extremities oscillate out-of-phase (see Figure 2.18(a)).

The liquid dome final manufacture is shown in Figure 2.20. Two pressure transducers were installed in the pistons, indicated as  $PT_l$  and  $PT_r$ . Also an exploded view of the right-side piston is reported, in order to show the pressure transducer housing<sup>c</sup>.

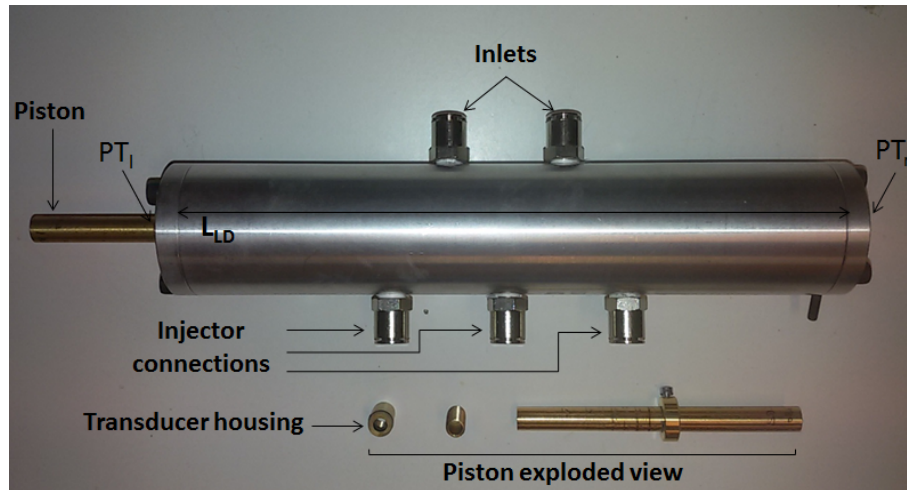


Figure 2.20: Liquid dome side view and piston exploded view.

### 2.2.3 Air and Water Supply System

Figure 2.21 shows a schematic of the supply systems for air and water. Air comes from the building network at the pressure of 8 bar, passes in a pressure regulator valve and goes into the isolated room through one of the pipe passages. It then goes through an on/off valve and then flows into three separated lines, each one provided with a mass flow rate controller (Brooks). Air flowrate can be varied in between 0 and 5 g/s on each line. Water is stored at 3-4 bar in a tank external to the acoustically isolated room. The tank is pressurized with the air coming from the building network. Water goes inside the isolated room, passes through an on/off valve and then flows into three separated lines. Each line is provided with an Oval (model LSF41) flowmeter and a Burkert solenoid valve for mass flow rate regulation. A maximum water flowrate of 100 l/h can be injected in each line. After injection, water is recovered under the resonant cavity floor and discharged through

<sup>c</sup>In the first design two configurations with transducers placed perpendicularly to the dome main axis were tested. Transducers were placed vertically in the upper part or in the lower part of the dome but acoustic measurements did not provide good results. Due to the small diameter of the dome, transducers were never flush mounted, and liquid/gas interfaces could appear giving rise to misleading results. For this reason a new liquid dome was manufactured and the current configuration with pressure transducers installed in the piston and flush mounted in the dome cavity was finally adopted.

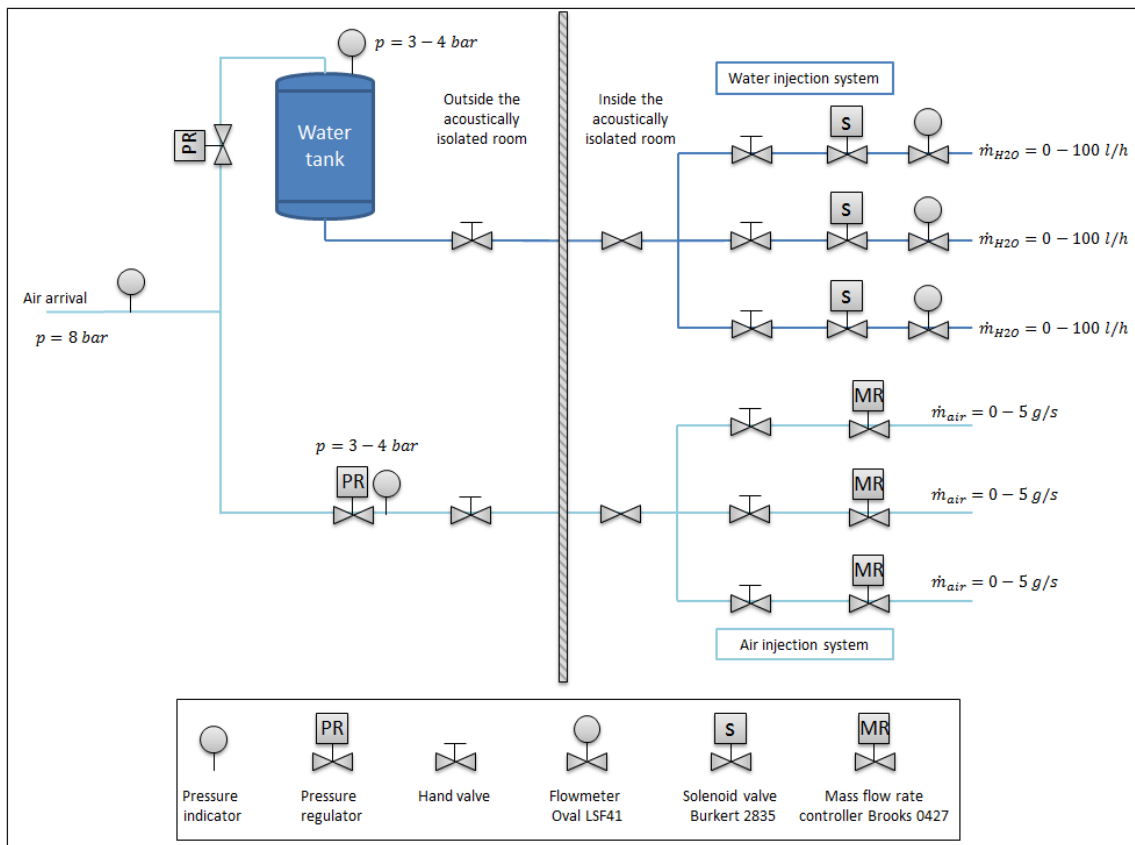


Figure 2.21: Schematic of water and air supply systems.

out a pipe. A dedicated software is used to control the valves and to check and control mass flow rates.

# Chapter 3

## Measurements Techniques

*In this section the measurements techniques adopted for the characterization of the jet response will be described. High speed back-light visualizations technique, which has been used to identify the jet response, is described in section 3.1. Drop size characterization by image processing, performed for a specific case (T-LRE test case), is described in section 3.2. Section 3.3 is dedicated to the Laser Doppler Velocimetry (LDV) technique, chosen to characterize the gas velocity field. Each technique is presented along with post-treatment examples in order to clarify the procedure adopted and facilitate interpretation of results presented in the dedicated chapters.*

### 3.1 High Speed Back-light Visualization

The largest amount of experimental data has been obtained by high-speed back-light visualization image acquisition. This technique consists in placing the object (the liquid jet in the present case) between a continuous diffuse light source and a high-speed camera. Two visualization planes have been considered as shown in Figure 3.1. View *A* provides images in the vertical plane containing the acoustic axis while view *B* provides images in the perpendicular plane. The camera used is a Vision Research Phantom V12 and the light source is a 300W Xenon arc lamp Lot-Oriel LSB530. A diffuser plate is placed in between the light source and the object in order to obtain a homogeneous background (i.e. same grey level on each pixel).

The presence of the object between the light source and the camera causes a local decrease of light transmission and the pixel corresponding to the object shows a lower grey level with respect to the background (see Figure 3.2). The experimental procedure consists in the acquisition of a series of background images without any object (see Figure 3.2(a))

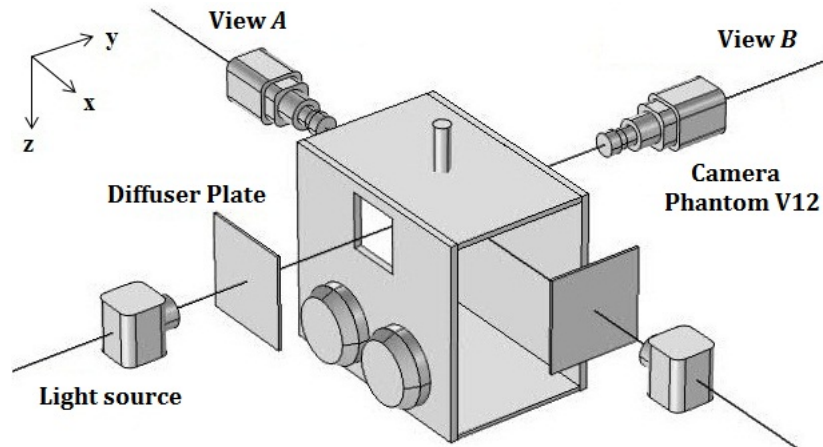


Figure 3.1: Experimental setup for high-speed back-light visualizations.

from which an average background image is obtained.

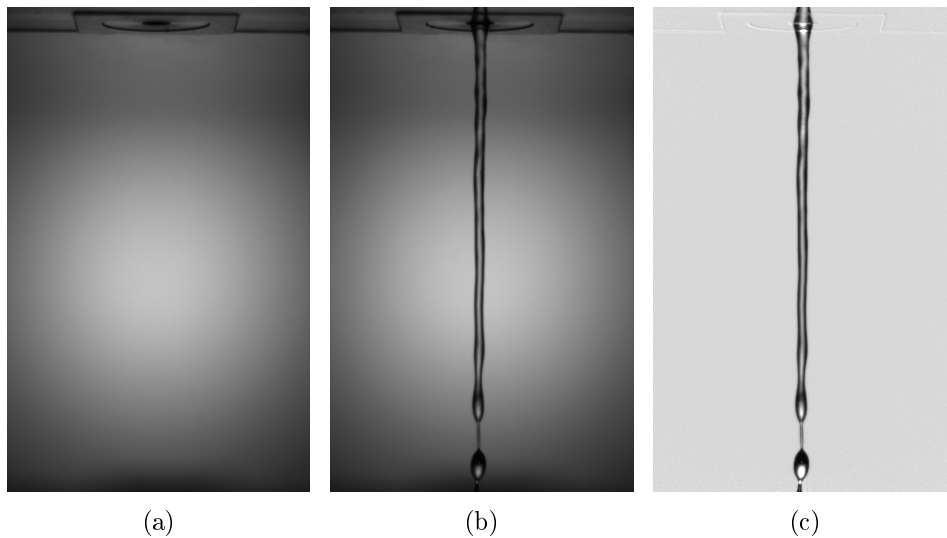


Figure 3.2: High-speed back-light image acquisition samples: (a) background; (b) raw jet image; (c) normalized jet image.

The jet image acquisition is then performed at a frame rate and with a resolution depending on the test configuration. Raw jet images (see Figure 3.2(b)) are then normalized (see Figure 3.2(c)) with the background average image. Image post-processing is performed with home-made software [100] (see Figure 3.3). Single injector test visualizations are usually performed at a frame rate of 6273 fps with a resolution of 800 x 1280 pixels, whereas three-injector visualizations are performed at a frame rate of 6200 fps with a 1024 x 768 pixels image resolution. Normalized images are then converted into two-level images (see Figure 3.3(a)). To do that, a threshold based on grey level must

be chosen. Larger objects are well detected by an image segmentation procedure based on a global grey level threshold fixed at 30% of the grey level dynamic of the current image. For smaller objects or objects with a lower contrast, a segmentation based on a wavelet transform is applied. The Mexican Hat wavelet function is used to compute the second derivative of the Gaussian filtered grey level image and a threshold is applied to the transformed image to detect local concave grey level distributions [100]. All pixels presenting a grey level lower than the global threshold, or in a concave portion of the grey level distribution, will be shown in black (0). They represent the liquid objects like droplets, ligaments and the continuous liquid core. Pixels presenting a grey level higher than the threshold belong to the background and will be represented in white (1). The two-level images are then used to calculate *average* and *minimum* images. Average images, as that represented in Figure 3.3(b), are calculated on a series of images by averaging the grey level pixel by pixel. An example of average images post-processing can be found in Appendix F. These images provide an indication of the spatial region in which the liquid elements are more probable to be found based on the considered image series. In the minimum images each pixel has the minimum grey level over the series (see Figure 3.3(c)) and indicate all pixels in which liquid has been detected at least once (in one image). Figure 3.3(d) represents the same minimum images filtered by a median filter with a structuring element of radius 20 pixels. This value has been selected as a compromise between all images treated.

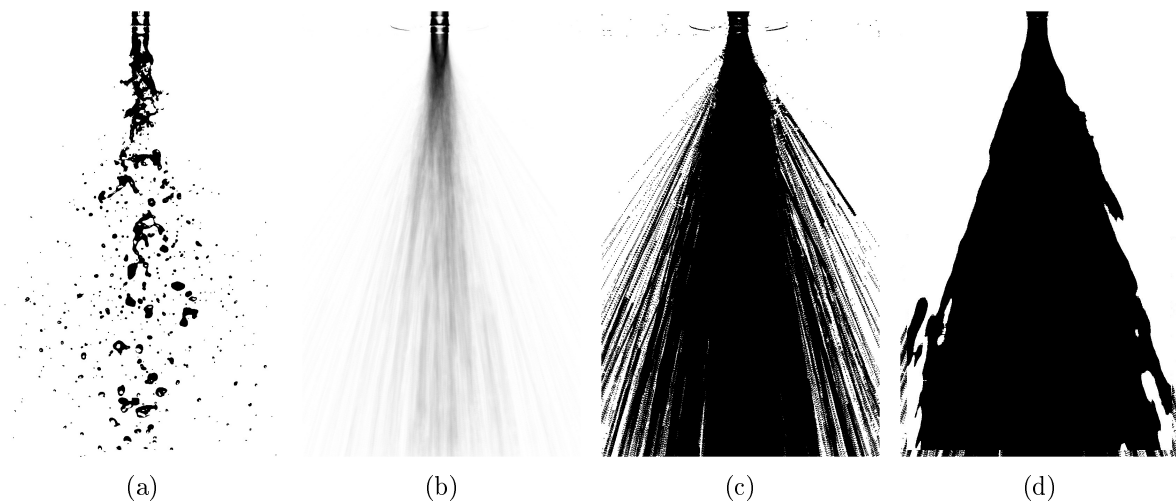


Figure 3.3: Post-processing image examples: (a) two-level image; (b) average image; (c) minimum image, (d) minimum filtered image.

Minimum filtered images are used to calculate the spray cone angle as shown in the example of Figure 3.4(a) and filtering is necessary to avoid those events not statistically

important that could lead to an overestimation of the cone angle. In Figure 3.4(a) the cone angle is defined on the minimum filtered image while in Figure 3.4(b) it is reported on one image of the series.

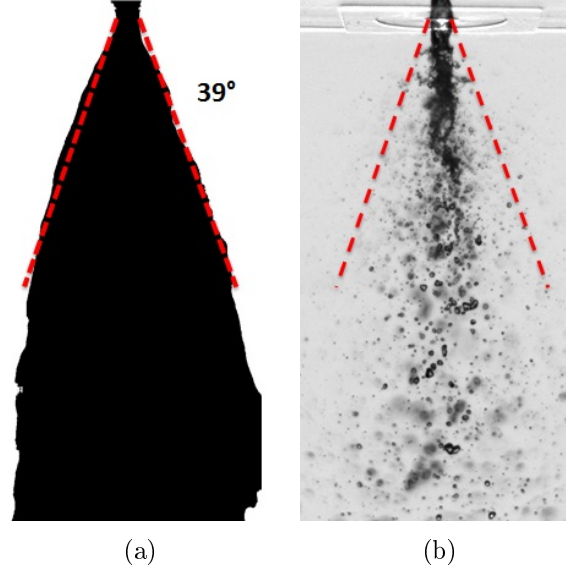


Figure 3.4: Example of cone angle calculated from minimum image (a), and reported on one image of the series (b).

In order to analyse the acoustic effect on the dispersed phase, the droplet spatial distributions in the vertical plane containing *a.a.* and in planes perpendicular to *a.a.*, are investigated by means of image processing performed with home-made software [100]. A sequence of 200 consecutive images selected during the constant envelope part of the acoustic pressure signal (see Figure 2.3) is compared with the case without acoustics. Each image of width  $w_{im}$  is divided into  $m$  spatial classes of the same width  $\Delta w$  (see Figure 3.5).

The discrete droplet location probability density function per normalized class width ( $\Delta w/w_{im}$ ) indicated as  $f(i)$  for class  $i$  is defined by Eq. 3.1.

$$f(i) = \frac{N_d(i)}{\sum_{k=1}^m N_d(k) \Delta w / w_{im}} = \frac{N_d(i)m}{N}. \quad (3.1)$$

where  $N_d(i)$  is the number of objects in the class  $i$  and  $N$  is the total number of objects. In the following, positions will be given in non-dimensional coordinates, i.e.  $\tilde{x} = x/w_{im}$ ,  $\tilde{y} = y/w_{im}$  and  $\tilde{z} = z/h_{im}$ , where  $w_{im}$  and  $h_{im}$  are the image width and height, respectively. Concerning the dispersed phase a morphological criterion [100, 101, 102, 103] has been

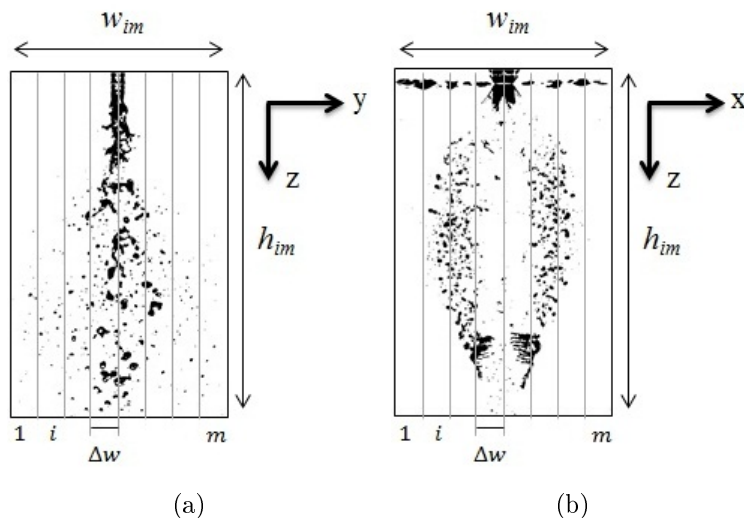


Figure 3.5: Typical examples of output image for (a) view  $A$  and (b) view  $B$ .

applied for the sphericity<sup>a</sup> of the objects ( $S_p \leq 0.6$ ), in order to consider spherical or pseudo-spherical elements with a reduced diameter in the range 0.0025 - 0.25. Droplets diameter is reduced by the injector liquid post exit diameter  $D_l$ .

The error in the  $f(i)$  calculation can be estimated using the propagation of uncertainties theory [104]. Based on Eq. 3.1  $f(i)$  of class  $i$  can be seen as the ratio of two quantities, the number of objects  $N_d(i)$  in the class  $i$  and the total number of objects  $N = \sum_{i=1}^m N_d(i)$ , multiplied by  $m$  the number of classes.

Since  $m$  is fixed, the expression of the relative uncertainty in the  $f(i)$  can be expressed as follows:

$$\frac{\delta f(i)}{f(i)} = \frac{\delta N_d(i)}{\overline{N_d(i)}} + \frac{\delta N}{\overline{N}}. \quad (3.2)$$

Where the overbar indicates mean quantities calculated on a series of  $N$ . The number of object in the class  $i$  is  $N_d(i)$ ; and it is calculated  $N$  times. Thus, it is possible to estimate the mean value of the measurement  $\overline{N_d(i)}$  and its uncertainty  $\delta N_d(i)$  by calculating the standard deviation on the  $N$  measurements. The relative uncertainty in  $N_d(i)$  is then given by  $\delta N_d(i)/\overline{N_d(i)}$ . The same procedure is applied for each class and for the total number of object  $N$  for which the relative uncertainty is  $\delta N/\overline{N}$ . Finally, the relative uncertainty  $\delta f(i)/f(i)$  can be calculated by using Eq. 3.2.

Figure 3.6 represents an example of  $f(i)$  calculation with the relative uncertainty

<sup>a</sup>For an object of surface  $S$  a disk of equivalent surface can be defined. Indicating as  $\Delta S$  the symmetric difference between  $S$  and the surface of the equivalent disk (centered at the barycenter of  $S$ ), the sphericity  $S_p$  is then defined as the ratio between  $\Delta S$  and  $S$ . The value of  $S_p$  ranges from 0 (for a disk, i.e. circular 2D projection) to 2 (in the case of a line).

calculated with the method explained above. Since in each test case the  $f(i)$  are calculated with the same method, the relative uncertainty calculated in one case is used to estimate the error in all the experiments [104].

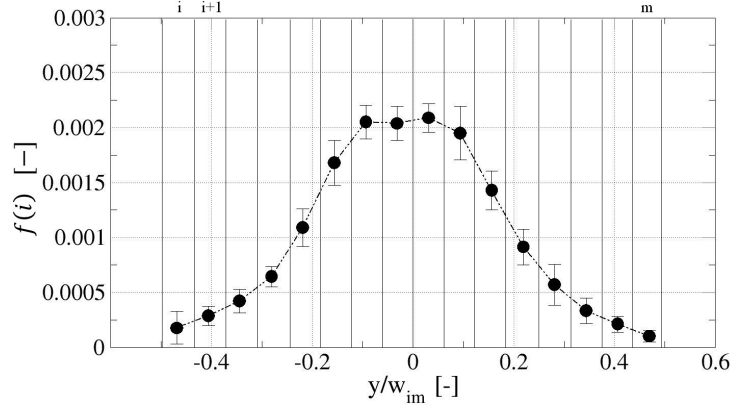


Figure 3.6: An example of  $f(i)$  with indication of the relative uncertainties in the measurements.

All droplet spatial distributions present a bell-shape which can be fitted with a Gaussian function. From the fitting Gaussian function the mean spray position  $\mu_h$  is then calculated. These values are used to quantify the spray deviation in the case of high Weber number atomization regimes. The mean value  $\mu_h$  is calculated considering the entire image, or as a function of the vertical coordinate. In the latter case, the images are subdivided into horizontal slices, and  $f(i)$  is calculated for each of them. Each  $f(i)$  is then fitted with a Gaussian function and the local values of  $\mu(z)$  are calculated. The relative uncertainty in  $\mu_h$  and  $\mu(z)$  are calculated in the same way of that of  $N_d(i)$ .

Still images extracted from the high-speed visualization sequences are used for the calculation of the deviation angle for low Weber number atomization regimes, see Figure 3.7. In each image the two sides of the jet contour are detected and for a fixed vertical coordinate  $z$  the half-distance in between the contour sides represents the jet centerline (in red in Figure 3.7). The jet centerline composed of  $N$  points of coordinates  $(x_i, y_i)$  is then fitted with a linear function of the form  $y_f = A + Bx$  (in blue in Figure 3.7).

The angle  $\gamma$  in between the vertical and the line fitting the jet centerline is calculated as:

$$\gamma = \frac{180}{\pi} \arctan B \pm \delta\gamma. \quad (3.3)$$

The error  $\delta\gamma$  in the estimation of  $\gamma$  is calculated in the same way as for  $f(i)$ . The

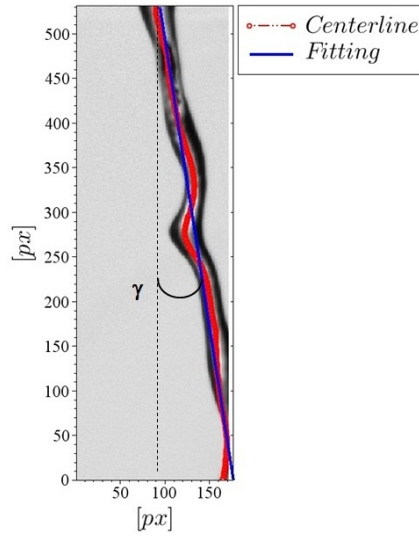


Figure 3.7: Example of jet centerline fitting for deviation angle calculation (– jet centerline, – linear fitting).

uncertainty in the jet centerline position is calculated as:

$$\delta y_j = \sqrt{\frac{1}{N-2} \sum_{i=1}^N (y_i - A - Bx_i)^2}. \quad (3.4)$$

whereas the uncertainty in the calculation of the slope can be deducted using the propagation of uncertainties theory as:

$$\delta B = \delta y_j \sqrt{\frac{N}{\Delta}}. \quad (3.5)$$

where  $\Delta = \sum_{i=1}^N x_i^2 - (\sum_{i=1}^N x_i)^2$ . The uncertainty in  $\gamma$  can be finally calculated as:

$$\delta \gamma = \frac{d\gamma}{dB} \delta B = \frac{180}{\pi} \frac{1}{\sqrt{1+B^2}} \delta B. \quad (3.6)$$

## 3.2 Droplet Size Measurement by Image Processing

In this section the setup, and some of the most important aspects, concerning the droplet size measurements technique by image processing [103] are described. The big advantage of this technique is the ability to quantitatively analyze the liquid element morphology. The imaging setup is in backlight configuration and the objects under consideration are

liquid droplets illuminated by an incoherent light source. Liquid droplet in a spray is a refractive object, whose image is similar to that of an opaque disc, see Figure 3.8(a). Droplets can be thus modeled as opaque or slightly transmitting objects with the object function  $o_g(x, y)$ . The function  $o_g(x, y)$  represents the amount of light transmitted by the object. It is characterized by the contrast coefficient  $\tau$ , and is expressed by:

$$o_g(x, y) = 1 - (1 - \tau)\Pi\left(\frac{\sqrt{x^2 + y^2}}{2a_i}\right) \quad (3.7)$$

where  $a_i = \gamma a_0$  is the radius of the geometric image,  $a_0$  is the object radius,  $\gamma$  is the lateral magnification of the imaging system, and  $\Pi$  is the rectangle function:  $\Pi(t) = 1$  for  $|t| < 0.5$ ;  $\Pi(t) = 0$  otherwise. In an imaging system using a incoherent light source, the

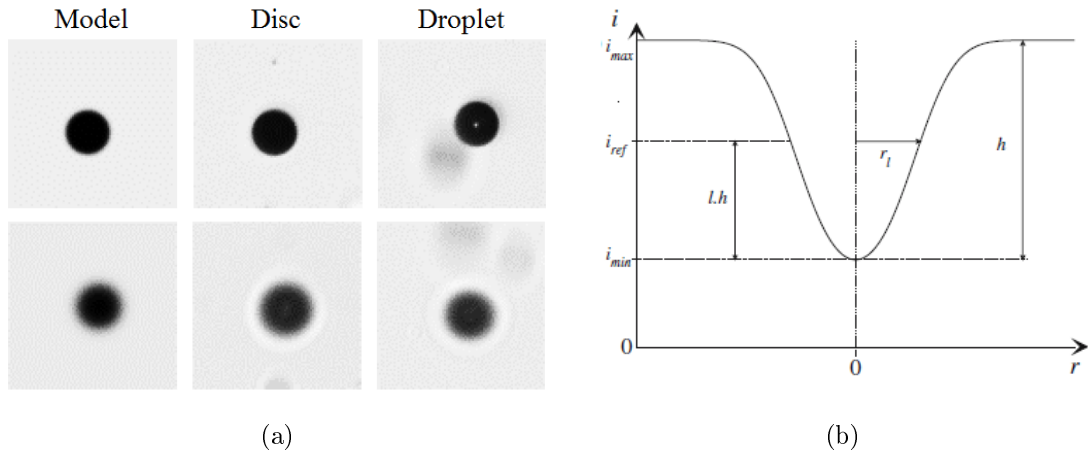


Figure 3.8: (a) Theoretical and experimental normalized images [105], and (b) definition of the relative levels of the theoretical image profile [103].

illumination distribution in the image plane  $i(x, y)$  can be described by the convolution product of the object function  $o_g(x, y)$  and the Point Spread Function (PSF) of the imaging system  $psf(x, y)$  [106]. The PSF of an optical system is defined as the response of the imaging system to an infinitesimally small source point. It is a function of the position of the object with respect to the focus plane, and its width is minimum at the focus plane. The PSF can be represented as a Gaussian function of the kind:

$$psf(x, y) = s_0 \exp\left(\frac{-2(x^2 + y^2)}{\chi^2}\right) \quad (3.8)$$

where  $\chi$  is defined as the PSF half-width. The convolution product between  $o_g(x, y)$  and  $psf(x, y)$  can be then expressed in nondimensional radial coordinates as [103, 107]:

$$\tilde{i}(\tilde{r}) = 1 - 2(1 - \tau) \exp(-\tilde{r}^2) \int_0^{\tilde{a}} \rho \exp(-\rho^2) I_0(2\tilde{r}\rho) d\rho \quad (3.9)$$

where  $\tilde{r} = \sqrt{2}r/\chi$  is the dimensionless radial coordinate,  $\tilde{a} = \sqrt{2}a_i/\chi$  is the dimensionless object radius and  $I_0$  is the modified Bessel function of the first kind. The function  $\tilde{i}$  represents the image grey level profile from which the object diameter is detected (see Figure 3.8(b)). The width of the profile increases when the object diameter increases. For small object width, compared to the PSF width, the image profile present a V-shape, whereas for larger object width (compared to the PSF width) the profile assumes a U-shape [100, 101, 102, 103]. Two image parameters are used to describe the grey level profile. The first one is the image contrast  $C = (i_{max} - i_{min})/(i_{max} + i_{min})$ , where  $i_{min}$  and  $i_{max}$  are respectively the maximum and the minimum levels of  $i(x, y)$ . Images with a low contrast correspond to unfocused objects, or to object widths much smaller than the PSF width. The second parameters is the image half-width  $r_l$  determined at the relative level  $l$  ( $0 < l < 1$ ). A relation between Contrast  $C$ , image half-width  $r_l$  and object radius  $a$  was derived by Blaisot & Yon [103]. Fdida & Blaisot [107] then introduced a depth-of-field criterion based on the estimation of  $\chi$  to calculate droplet size, whatever the droplet out-of-focus position. In practical applications, experimental images are first normalized, then each droplet is individually detected (images are post-processed with home-made software [100]). Parameters ( $C$  and  $r_l$ ) are measured on each normalized droplet image. To characterize droplet shape the *sphericity* morphological parameter defined by Malot & Blaisot [103] is introduced. The sphericity  $S_p$ , is used to quantify the deviation of the droplet shape from the spherical shape (see Figure 3.9). For spherical objects  $S_p = 0$ , whereas  $S_p = 2$  for ligaments. This technique has been applied to characterize the

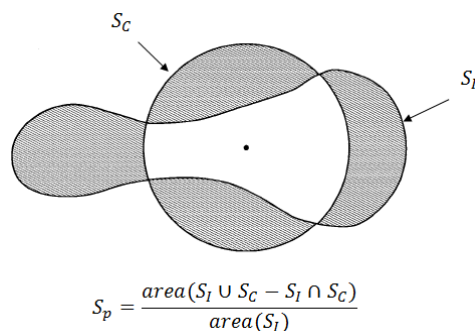


Figure 3.9: Sphericity morphological parameter definition [103].

droplet size distribution for the T-LRE case at IAN ( $We_g > 400$ ,  $Re_l = 6602$ ,  $J = 5.1$ ). The objective is to demonstrate the feasibility of the application of the technique to our experimental setup, in order to produce experimental data to validate numerical simulations (see section 5.4). Measurements have been performed in the vertical plane containing the acoustic axis. The experimental arrangement is shown in Figure 3.10. Two CCD cameras mvBlueCougar-x (Matrix Vision) with a maximum frame rate of 10 Hz (resolution: 2448 x 2050 pixels) have been used simultaneously by introducing a beam splitter. In order to obtain a suitable magnification, an objective with a focal length of 85 mm is used. The distance in between the objective and the camera, due to the presence of the beam splitter, is 25 mm. A Cavitar laser unit and a laser diode generated the illumination for the cameras and the parameters of the laser were controlled through the Cavilux control unit (laser wavelength 640 nm, maximum pulse frequency 100 kHz, minimum pulse duration 20 ns).

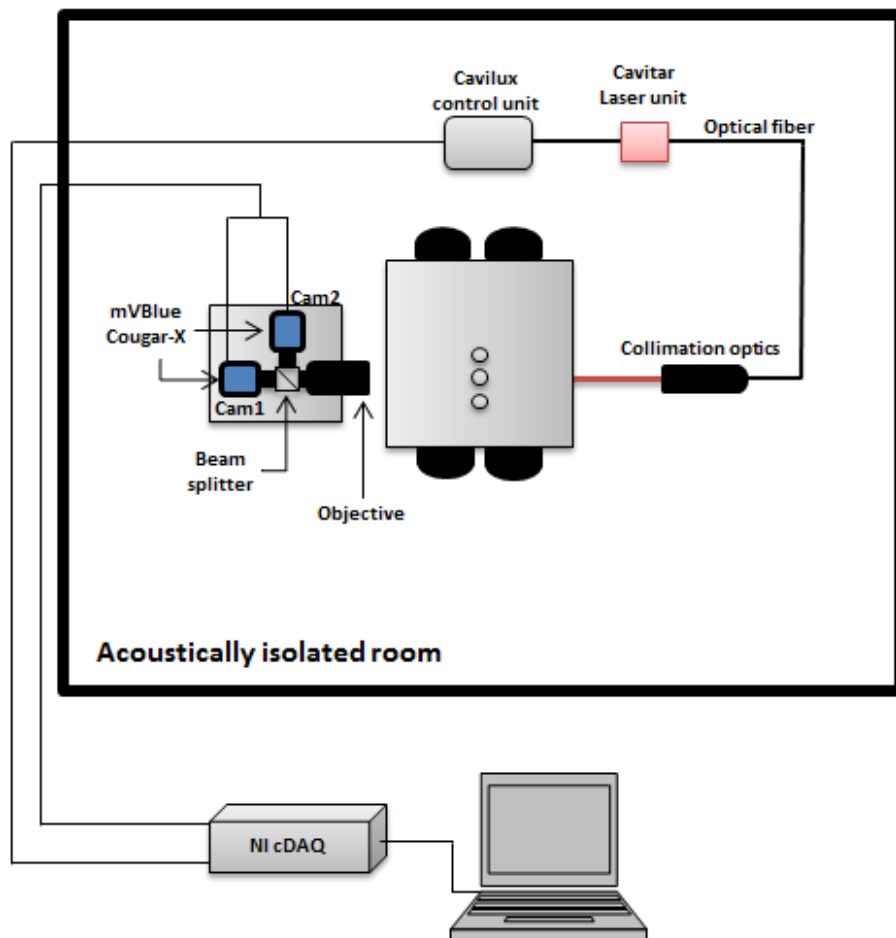


Figure 3.10: Schematic of the experimental setup for droplet size measurement.

The interest of using two camera simultaneously was to double the frame rate in order to increase the number of images acquired in the period in which the spray is submitted to the constant part of the acoustic signal (300 ms) and to reduce the number of tests necessary with acoustics. In order to be able to successfully merge the image sequences acquired with the two cameras it must be ensured that the focus plane is the same and that image post-processing provides the same results in terms of spray characteristics. To ensure the superimposition of the focus planes, the cameras have been installed on two micro-displacement systems. The point spread functions (PSF) [103] half-width  $\chi$  of the two cameras has been calculated by placing an object with a very sharp edge at different locations in the direction perpendicular to the y-z plane (see Figure 3.11). Figure 3.11(a) shows an example of the measurements at the first step of the measurements. The shift between data recorded from the two camera indicated that two focus planes are clearly separated and in this case the two images series could not be compared. After accurate modification of the relative camera position a satisfactory superimposition of the  $\chi$  functions has been obtained as reported in Figure 3.11(b), showing that the superimposition of the two camera focus planes, and thus of the measurement volumes is achieved.

Figure 3.12 shows an example of spray images acquired with the two cameras at the same moment. The first row shows the normalized images while in the second row the same images are reported after conversion into two-level images. The number of objects detected is also reported and a difference of around 2.6 % between the two images is found. This comes from the beam splitter used, which does not perfectly split in half the light emitted from the laser diode. Consequently the image contrasts are not exactly the same which may induce differences in the detection process. A correction in the post-processing has been possible by considering objects with a certain diameter  $3.33 \cdot 10^{-4} < D_{obj}/D_l < 8.33 \cdot 10^{-2}$  and a morphological criterion for the sphericity of the objects  $S_p \leq 0.4$  [101, 102, 103, 100]. In order to have the same measurement volumes on the two camera, and to be not too restrictive in the object detection (for statistical reason) a dimensionless depth-of-focus of about 0.5 has been chosen. For this value, the PSF in Figure 3.11(b) gives a normalized impulse response  $RI/D_l = 2\chi/D_l \approx 0.0083$ . With these parameters the percentage difference in the objects count for the two images shown in Figure 3.12 is reduced to 1.4 %.

The same parameters have been used to compare two identical 60-image series acquired with the two cameras at the same time. The difference in the objects count is around 4.9 %. The percentage differences between the characteristic spray diameters calculated from two series are reported in Table 3.1. Data indicate that images acquired with the

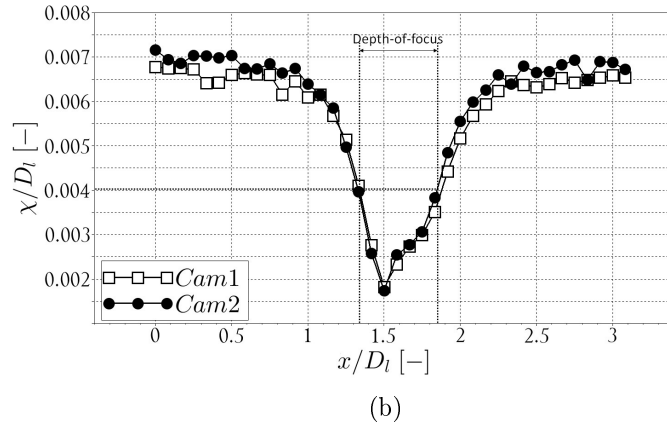
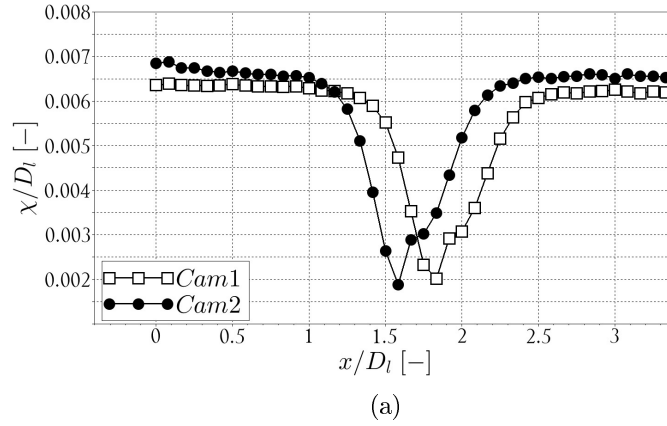


Figure 3.11: PSF for the two mvBlueCougar-x cameras (a) before and (b) after position correction.

two cameras provide similar results in terms of spray characteristics.

Characteristic diameter	Difference %
D30	1.28
D32	1.16
dv0.1	0.34
dv0.5	2.51
dv0.9	0.91

Table 3.1: Percentage difference between the characteristic spray diameters obtained with post-processing of images acquired with the two cameras ( $3.33 \cdot 10^{-4} < D_{obj}/D_l < 8.33 \cdot 10^{-2}$ ,  $RI = 0.05$ ,  $S_p \leq 0.4$ ).

During the experiments with acoustics the two cameras have been triggered alternatively as indicated in Figure 3.13 using a single TTL signal at 10 Hz while the laser unit was triggered at 20 Hz. Cam1 is triggered in mode "raising edge" with the 10 Hz TTL

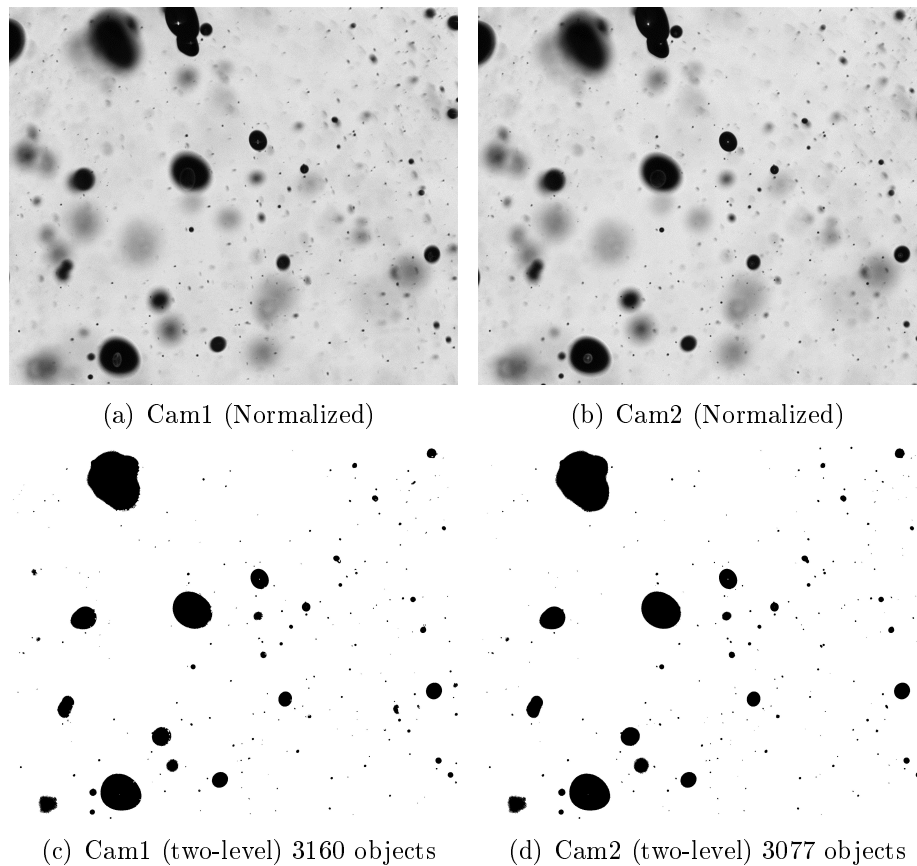


Figure 3.12: Comparison between image acquisition with (a-c) Cam1 and (b-d) Cam2.

signal while Cam2 in "falling edge". The blue and green areas in Figure 3.13 indicate the integration time interval of Cam1 and Cam2 respectively. The images acquired with the two cameras have been gathered to obtain a 120-image series. In this way a sufficient number of images is available with 20 tests to compare with the reference case series without acoustics.

### 3.3 Laser Doppler Velocimetry (LDV)

The characterization of the gas velocity field was carried out using the Laser Doppler Velocimetry (LDV) technique. LDV has been chosen for its non-intrusive nature and for its good temporal and spatial resolution. It relies on the principle that the light, scattered from a particle moving through a measurement volume produced by the intersection of coherent laser beams, will be submitted to a frequency shift proportional to the particle's velocity. The LDV basic configuration (see Figure 3.14) consists of [108]:

- a monochromatic laser, which provides coherent and collimated beams;

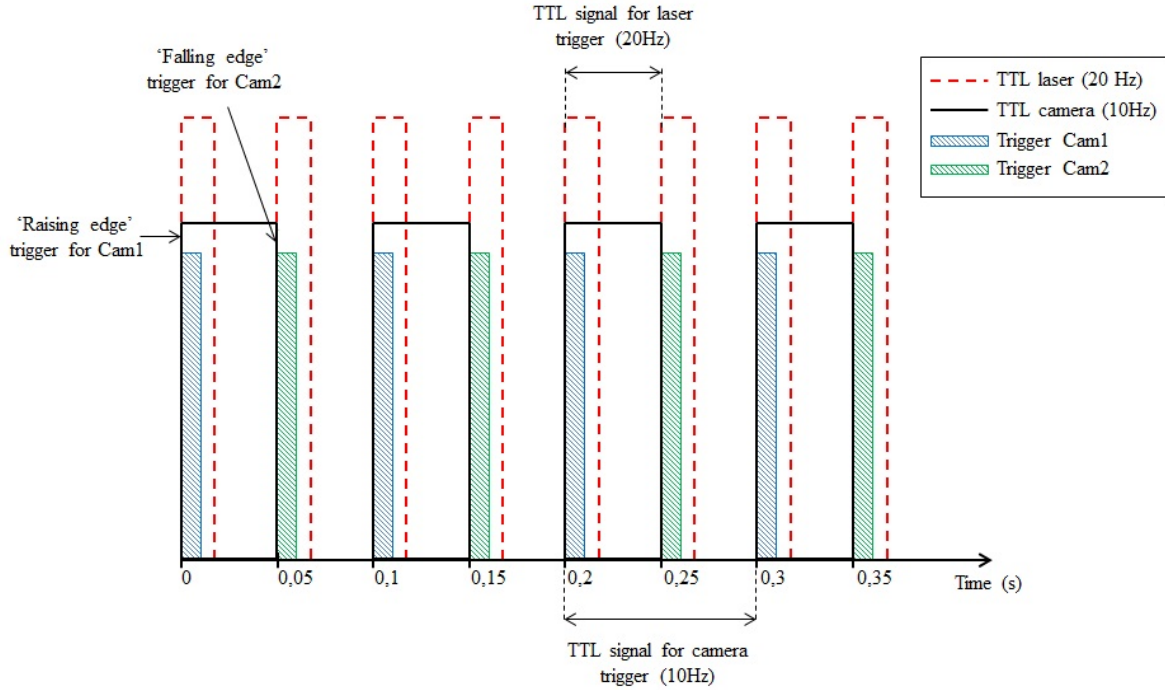


Figure 3.13: Time sequence of TTL signal for cameras trigger (10 Hz) and laser trigger (20 Hz). Cam1 is triggered in mode "raising edge" while Cam2 in mode "falling edge".

- a transmitting optics, which includes a beam splitter, and a focusing lens;
- a receiving optics, which includes a focusing lens and a photomultiplier;
- a signal processor.

This technique requires tracer (or seeding) particles in the fluid (typically the size range of particles is between  $1 \mu m$  and  $10 \mu m$ ). From the single laser beam two laser beams are obtained by means of the beam splitter. The two beams are focused (with a certain angle  $\theta$ ) by a lens to intersect, forming an ellipsoidal measurement volume. In the measurements volume the light intensity is modulated due to interference between the laser beams. The interference produces planes of high light intensity, which are called fringes. The distance between two consecutive fringes  $d_f$  is defined by the wavelength of the laser light and the angle  $\theta$  as  $d_f = \lambda/2 \sin \theta$ . When the particle traverses this fringe patterns the scattered light fluctuates in intensity at a frequency  $f_D$ , called Doppler frequency. The light fluctuation is acquired by a photomultiplier, which produces an electrical current proportional to the light flux, called Doppler burst. The bursts are then processed (filtered and amplified) by the signal processor, which determines the Doppler frequency of each particle. The velocity is then calculated as  $V = d_f f_D$ . In this configuration the direction

of the moving particles cannot be detected. In order to be able to determine the direction of the particle velocity, a bragg cell is used (see Figure 3.14). The bragg cell produces a shift in frequency  $df$  on one of the two beams. Due to the frequency shift between the two laser beams, the diffraction pattern moves at a constant velocity. Two particles moving with the same velocity, but with opposite directions, will produce different frequencies. The measured frequency is thus given by  $F_m = df \pm f_D$ , with the sign depending on the direction of the particle velocity. The particle velocity is finally calculated as  $V = d_f(f_m - df)$ . In some configuration, as the one adopted here, the transmitting and receiving optics are in the same probe (backscatter configuration).

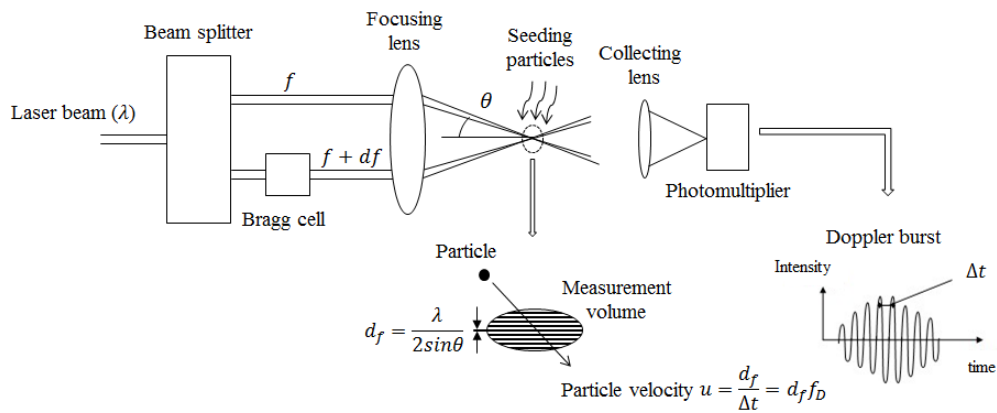


Figure 3.14: LDV principle.

The application of this technique in our experimental setup represented a challenge for three main reasons: the limited space in the experiment room in which dedicated hardware had to be arranged; the development of an air extraction system in the acoustically isolated room to prevent accumulation of seeding particles; the number of test necessary to characterize the flow field with acoustics due to the protocol adopted to prevent loudspeakers damaging (acoustic test duration length is limited to 300 ms to preserve loudspeakers safety, each measured point corresponds to a single test). LDV preliminary measurements have been made for a single jet placed at VAN and IAN at  $We_g = 190$ ,  $Re_l = 2000$  to verify the feasibility of the technique in our experimental setup (see section 5.4). They served as a starting point for future investigations, to produce experimental results for the validation of numerical simulations. The experimental arrangement adopted is shown in Figure 3.15.

An Argon-ion laser was used as a source. Due to limitations in terms of space a configuration in which the transmitting and receiving optics are in the same probe head was used with a focal length of 350 mm and a beam separation of 50 mm. The probe is the

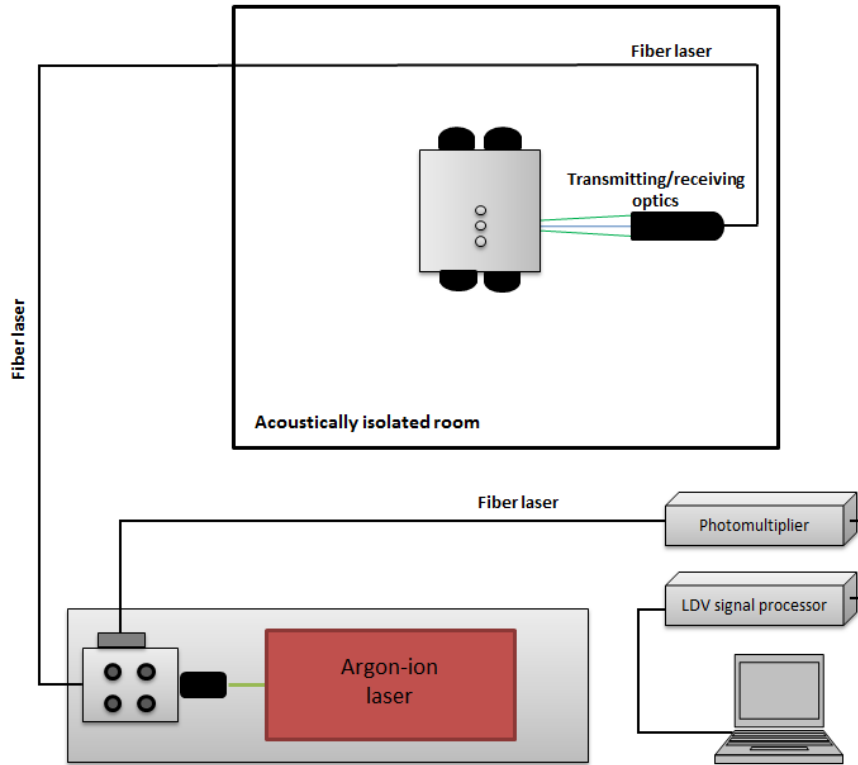


Figure 3.15: Schematic of the LDV experimental setup for gas flow velocity measurements.

only part of the system put inside the acoustically isolated room and it is mounted on a  $3D$  displacement system. From the Argon laser two wavelengths in the visible spectrum (390 to 700 nm) are selected and brought to the probe through a fiber: two blue laser beams ( $\lambda_b = 488 \text{ nm}$ ) used to measure the vertical velocities and two green beams ( $\lambda_g = 514 \text{ nm}$ ) for the measurement of the radial component. The four beams were directed to intersect with an angle  $\theta = 3.94^\circ$  forming an ellipsoidal measurement volume. Data concerning the measurement volume and the fringes are reported in Table 3.2.

Parameter	Value
Measurement volume length (mm)	2.29
Measurement volume height ( $\mu\text{m}$ )	159
Fringe width for $\lambda_b = 488 \text{ nm}$ ( $\mu\text{m}$ )	3.55
Fringe width for $\lambda_g = 514 \text{ nm}$ ( $\mu\text{m}$ )	3.74

Table 3.2: LDV measurement volume parameters.

In order to scatter the light, the flow was seeded with DEHS (Di-Ethylhexyl Sebacic Acid Ester) particles with an average diameter of  $5 \mu\text{m}$ . The Stokes number for a DEHS particle is defined by Eq. 3.10 as the ratio of the characteristic time of the particle inertial

response  $\tau_p$  to the acoustic characteristic time  $\tau_{ac} = 1/f_0$ .

$$S_k = \frac{\tau_p}{\tau_{ac}} = \frac{\rho_p d_p^2}{18\mu_{air}} \frac{1}{1/f_0} \quad (3.10)$$

Here,  $f_0$  is the forcing frequency,  $\rho_p$  and  $d_p$  are the density and characteristic diameter of the DEHS particle and  $\mu_{air}$  is dynamic viscosity of the air. Considering  $\rho_p = 912 \text{ kg/m}^3$  and  $\mu_{air} = 1.81 \cdot 10^{-5} \text{ Pas}$  a Stokes number lower than  $7 \cdot 10^{-2}$  is calculated, which means that particles can be considered as good tracers for the problem in exam. When a DEHS particle crosses the measurement probe, the light scattered by the particles is detected by the photomultipliers (Colorlink), which generates a current proportional to absorbed photon energy, and amplifies that current. The signal is then sent to the LDV signal processor (IFA) which communicates with the computer and the dedicated software. Figure 3.16 shows the local reference system with the sign convention for the radial ( $U_y$ ) and vertical ( $U_z$ ) velocities. Radial (in the  $\tilde{y}$ -direction) and vertical (in the  $\tilde{z}$ -direction) components of the velocity were measured simultaneously at the injector exit plane. The modulus of the velocities is reported in the following reduced with the gas bulk velocity  $U_{g,bulk}$ :  $\tilde{U}_y = U_y/U_{g,bulk}$  and  $\tilde{U}_z = U_z/U_{g,bulk}$ . The injector axis corresponds to  $\tilde{y} = 0$ ,  $\tilde{x} = 0$ . Here, coordinates are reduced with liquid post diameter  $D_l$ :  $\tilde{x} = x/D_l$ ,  $\tilde{y} = y/D_l$  and  $\tilde{z} = z/D_l$ . Measurements were made at a distance  $\tilde{z} = 2e$  from the injection exit plane. With  $e$  being the width of the gas annular gap (see Figure 2.9).

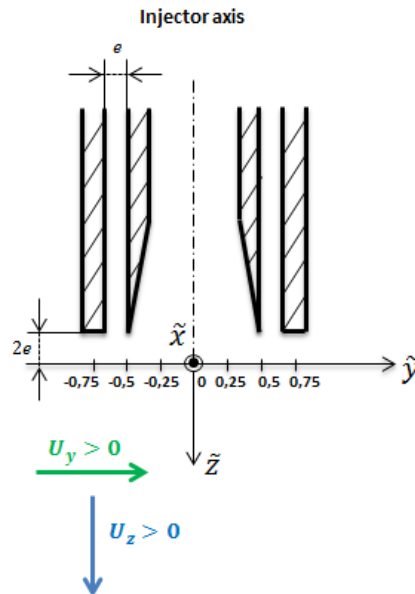


Figure 3.16: Schematic of the local reference system for LDV measurements.

In order to be as close as possible to the injector exit plane the laser probe has been installed with an angle of  $4.5^\circ$  with respect to the horizontal plane. This configuration has been considered by making the hypothesis that the flow presents a negligible tangential velocity. This hypothesis has been experimentally confirmed by a complete velocity cartography of the coaxial jet in the  $\tilde{x} - \tilde{y}$  plane.

Figure 3.17 shows a typical profile in the  $\tilde{y}$  direction of the vertical velocity for  $We_g = 190$  and  $Re_l = 2000$ . Seven tests are shown in the plot to highlight the repeatability of experimental data. In the section dedicated to the experimental results it will be

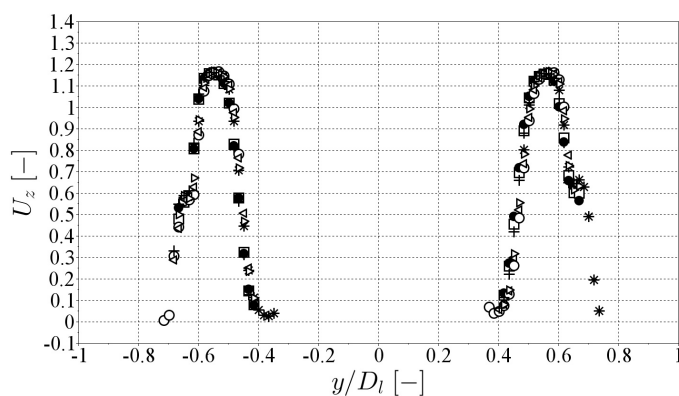


Figure 3.17: Example of LDV accuracy on the vertical velocity measurements for 7 tests without acoustics ( $We_g = 190$  and  $Re_l = 2000$ ).

shown that for the tests with acoustics velocity measurements have been performed for  $-0.6 < \tilde{y} < -0.47$  and  $0.47 < \tilde{y} < 0.6$ . In these intervals (annular flow core) data of the flow without acoustics are highly reproducible, with a detection rate ranging between 12000 and 18000 particles per second.

## Part II

# Acoustic Effects Upstream and Downstream the Injection



# Chapter 4

## Upstream effects: Domes' Acoustic Response

*The two injection domes described in section 2.2.2 have been tested, and their acoustic response is analyzed in this chapter. After a brief introduction explaining the test configurations investigated (section 4.1) the response of the two domes will be discussed separately. Section 4.2 is dedicated to the acoustic response of the gas dome (GD), whereas the liquid dome (LD) will be treated in section 4.3. The last section is dedicated to the general conclusions and remarks (section 4.4).*

### 4.1 Introduction

In this section results of the experimental investigations of the acoustic response of the injection domes will be discussed. The entire injection system assembly is shown in Figure 4.1 along with the main resonant cavity. Three different configurations are shown:

- IAN-VAN-IAN - The central injector exit is placed at the velocity anti-node (VAN) and the two lateral ones at two intensity anti-nodes (IAN), oscillating out-of-phase (non-symmetric excitation conditions);
- PAN-IAN-VAN - The injectors' exits are submitted to different excitation conditions: velocity (VAN), intensity (IAN) and pressure anti-node (PAN) respectively. Acoustic pressure fluctuations in between VAN and PAN are in-phase and the amplitude decreases from PAN to VAN;
- IAN-PAN-IAN - The central injector exit is placed at the pressure anti-node (PAN) where acoustic pressure level is maximum and the two lateral ones at two intensity

anti-nodes (IAN). The three injectors' exits are submitted to in-phase cavity pressure fluctuations symmetrically distributed relatively to the central injector (PAN). The intensity anti-node is defined as the location where the product of the acoustic pressure and velocity fluctuations is maximum in the cavity.

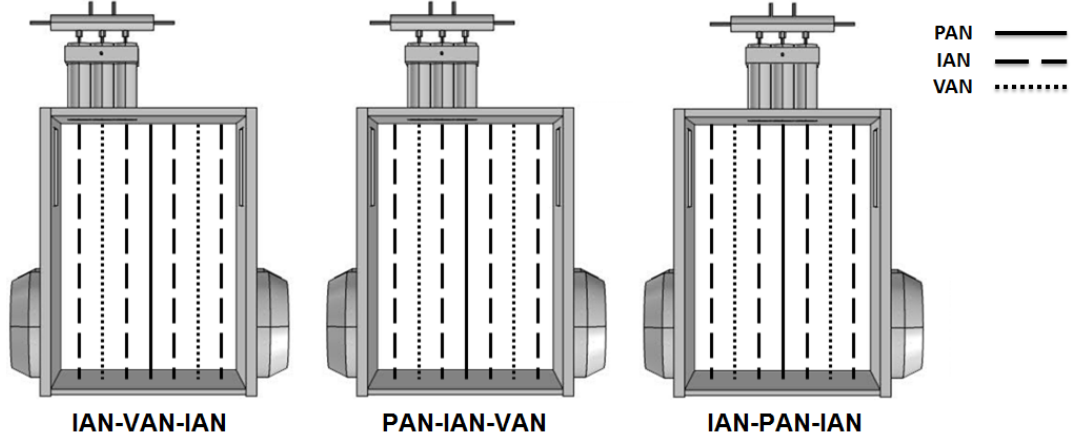


Figure 4.1: Scheme of the injection system placed on the main cavity roof according to three test configurations.

All tests reported here have been performed by forcing the  $2^{nd}$  transverse mode of the main cavity at the frequency of 1 kHz at the maximum available acoustic pressure level corresponds to an amplitude of 12 *kPa* (peak-to-peak acoustic pressure amplitude measured in the cavity).

## 4.2 Gas Dome Response

A total of 180 test configurations were investigated to characterize the acoustic response of the gas dome, combining:

- the geometrical parameters presented in section 2.2.2.1 (domes size, and orifice diameters  $d_{or}$ );
- four air mass flow rates:  $\tilde{m}_{air} = 0 - 0.4 - 0.7 - 1$  (scaled with the largest considered mass flow rate,  $m_{air}^{max}$  corresponding to  $We_g = 190$ );
- the three spatial configurations of the injection system with respect to the acoustic axis indicated in Figure 4.1.

Figure 4.2 represents a schematic of the gas dome in which are reported the pressure transducer locations considered in the analysis and two examples of dome sizes,  $GD0$  and  $GD8$  (see section 2.2.2.1). Pressure transducer  $PT_{l2}$  is only available for dome size greater than  $GD4$ , and  $PT_{l3}$  only for  $GD8$ .

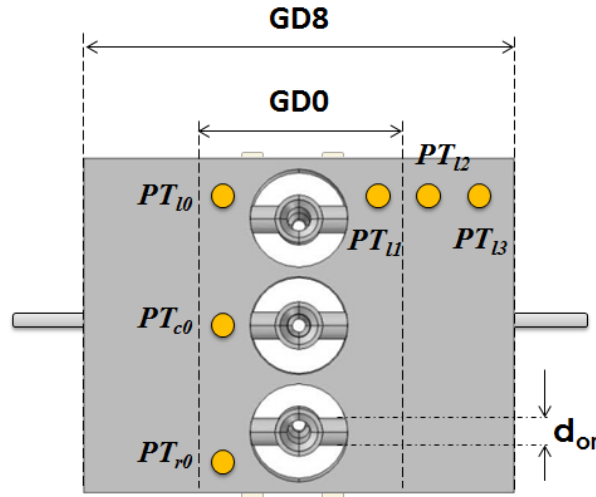


Figure 4.2: Schematic of gas dome and pressure transducer locations.

For all the tested configurations (IAN-VAN-IAN, PAN-IAN-VAN and IAN-PAN-IAN), results indicate that the injection system response is strongly affected by the acoustic conditions imposed at the injectors' outlets and by the design parameters. In all the configurations the acoustic level measured in the gas dome decreases as its size is increased from  $GD0$  to  $GD8$ . Indeed, dome frequency response to a white noise excitation, presented in section 2.2.2.2, indicates that by increasing the dome size the eigenfrequencies of the dome get closer to the forcing frequency. In Figure 2.16 a narrowing of the effective spectrum is noted when the size increases from  $GD0$  to  $GD8$ , in agreement with what found in simulations presented in Figure 2.14. This is accompanied by a crucial decrease in energy density associated with the eigenmodes (see Figure 2.16 in section 2.2.2.2). A decrease of the acoustic pressure amplitude in the gas dome is also observed by increasing the mass flow rate due to an increase of the pressure drop. Similarly, decreasing the orifice diameter  $d_{or}$  also induces an increase in the pressure drop and a lower response.

### IAN-VAN-IAN Configuration

The IAN-VAN-IAN configuration indicates the strongest acoustic response. Some examples of raw pressure signals are presented in Figure 4.3 and Figure D1 of Appendix

D. Figure 4.4 shows the peak-to-peak acoustic pressure amplitudes measured with the

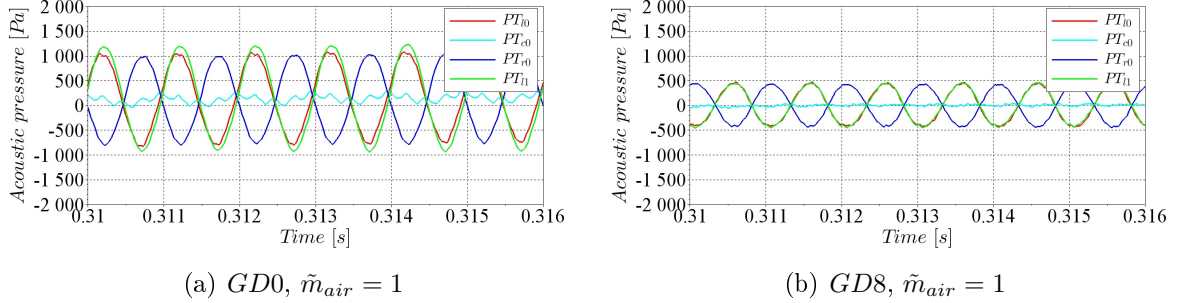


Figure 4.3: Acoustic pressure signal comparison in the gas dome for IAN-VAN-IAN: (a)  $GD0$ ,  $\tilde{m}_{air} = 1$ ; (b)  $GD8$ ,  $\tilde{m}_{air} = 1$  ( $f = 1000 \text{ Hz}$ ;  $p_{a,pp} \approx 12 \text{ kPa}$  at PAN;  $d_{or} = 1.125$ ).

transducers  $PT_{l0}$ ,  $PT_{l0}$ ,  $PT_{l0}$  and  $PT_{l0}$  in the dome. Measurements are reported for four mass flow rates ( $\tilde{m}_{air} = 0 - 0.4 - 0.7 - 1$ ) and for an injector connection diameter  $d_{or} = 1.125$ . A maximum of  $2800 \text{ Pa}$  (peak-to-peak amplitude) is measured without any flow rate (see Figure 4.4(a)), which corresponds to 23% of the acoustic pressure level measured in the main cavity at the pressure anti-node. Increasing the mass flow rate decreases the dome's acoustic response. For the maximum flow rate considered here the acoustic pressure fluctuation amplitude reaches  $2000 \text{ Pa}$ , namely 17% of the acoustic pressure fluctuation amplitude imposed in the main cavity at the pressure anti-node. The three pressure transducer signals  $PT_{l0}$ ,  $PT_{r0}$  and  $PT_{l1}$  have similar acoustic pressure fluctuation amplitudes. Moreover,  $PT_{c0}$  shows a quasi-null signal (see Figure 4.4). Pressure fluctuations of  $PT_{l0}$  and  $PT_{l1}$  are in-phase while  $PT_{l0}$  and  $PT_{r0}$  are always out-of-phase whatever the dome size. All these features are in accordance with the eigenmode GD-A of the gas dome presented in Figure 2.13: all points in vertical planes  $\tilde{y}_g = \text{constant}$  are in-phase (see Figure 2.13(a), 2.13(b) and 2.13(c)) and  $\tilde{y}_g = 0$  is a nodal plane (see Figure 2.13(d)). Acoustic pressure measurements given by transducers  $PT_{l2}$  and  $PT_{l3}$  (see transducer locations reported in Figure 4.2) are shown in Figure 4.5. Results from simulations are also reported for comparison. Simulations in this case are made by considering the dome and the resonant cavity geometries at the frequency of  $1000 \text{ Hz}$  (see section 2.1.2). Results from simulations are scaled with the experimental value of  $PT_{l1}$ . Pressure transducers  $PT_{l2}$  and  $PT_{l3}$  provide complementary information on the acoustic pressure distribution inside the dome. These measurements show a global trend of decrease of the pressure amplitude along  $\tilde{x}_g$ . This is also consistent with mode GD-A in Figure 2.13(a) where coordinates  $\tilde{x}_g = 0.17$ ,  $\tilde{x}_g = 0.32$  and  $\tilde{x}_g = 0.47$  correspond to the locations of  $PT_{l1}$ ,  $PT_{l2}$

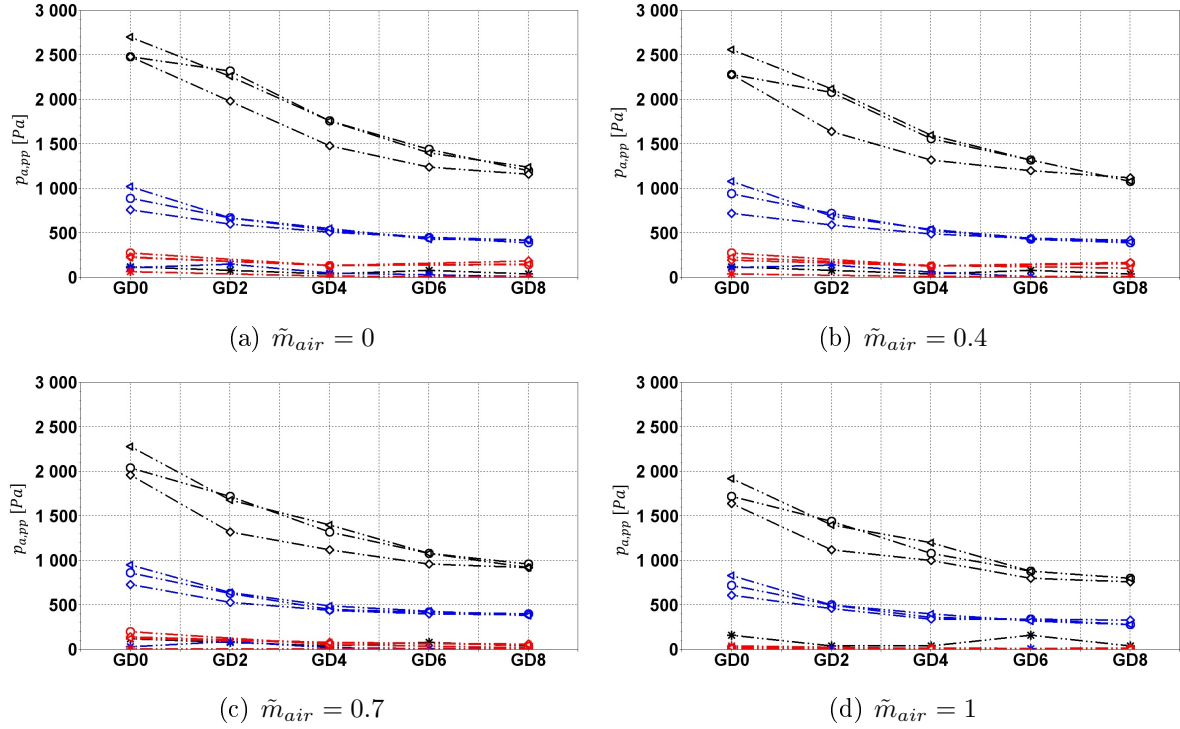


Figure 4.4: Peak-to-peak acoustic pressure measurements in the gas dome as a function of the dome size at IAN-VAN-IAN for: (a)  $\tilde{m}_{air} = 0$ , (b)  $\tilde{m}_{air} = 0.4$ ; (c)  $\tilde{m}_{air} = 0.7$ ; (d)  $\tilde{m}_{air} = 1$  ( $\circ$   $PT_{l0}$ ;  $\star$   $PT_{c0}$ ;  $\diamond$   $PT_{r0}$ ;  $\triangleleft$   $PT_{l1}$ ; red  $d_{or} = 0.375$ ; blue  $d_{or} = 0.75$ ; black  $d_{or} = 1.125$ ).

and  $PT_{l3}$  respectively. Finally Figure 2.13(c) indicates that when dome size is increased, pressure amplitude at a given coordinate  $\tilde{x}_g$  decreases. In combination with the identification of mode GD-A, this indicates that a decrease of the pressure amplitude is likely to occur in the whole dome.

A decrease of the acoustic pressure amplitude in the gas dome is also observed by decreasing the orifice diameter  $d_{or}$ . The influence of the size of  $d_{or}$ , on the acoustic coupling between the gas dome and the main cavity can also be noticed in the phase-shift between the signal of  $PT_{l0}$  and the signals of  $PT_{c0}$ ,  $PT_{r0}$ ,  $PT_{l1}$  and  $PT_{ref}$ , which are reported in Figure 4.6 ( $PT_{ref}$  is the signal of the transducer placed in the main cavity at PAN). With  $d_{or} = 1.125$ , acoustic coupling is facilitated and the phase-shift between  $PT_{l0}$  and  $PT_{ref}$  varies continuously with the dome size. Since the change in the dome size modifies the internal mode shapes, the phase-shift between two spatially-fixed points is affected. The phase-shift inside the gas dome, i.e. between  $PT_{l0}$  and  $PT_{c0}$  also varies from  $45^\circ$  to  $90^\circ$ , due to the modification of the dome's internal mode shapes. The phase difference between velocity and intensity anti-nodes is expected to be different from zero.

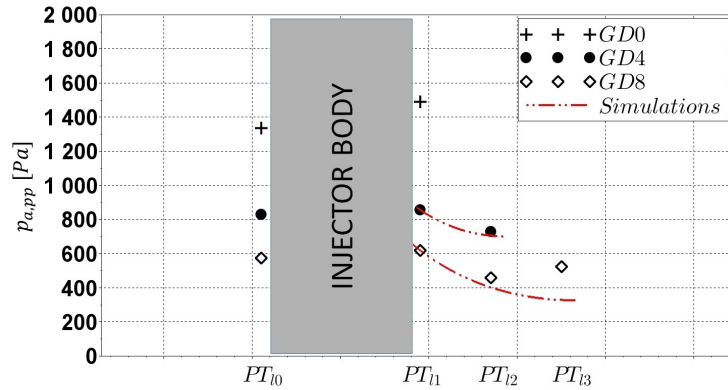


Figure 4.5: Complementary acoustic pressure measurements at IAN-VAN-IAN provided by  $PT_{l_2}$ , and  $PT_{l_3}$  and compared with  $PT_{l_0}$  and  $PT_{l_1}$  (red lines represent simulations, values are scaled with the measurements of  $PT_{l_1}$ ).

Indeed, it was shown by Cáceres *et al.* [109] that in the vicinity of a velocity anti-node of such a transverse acoustic field phase-shift varied continuously from 0 to  $+\pi$ . Thus, in our case the phase difference between velocity and intensity anti-nodes is expected to be different from zero.

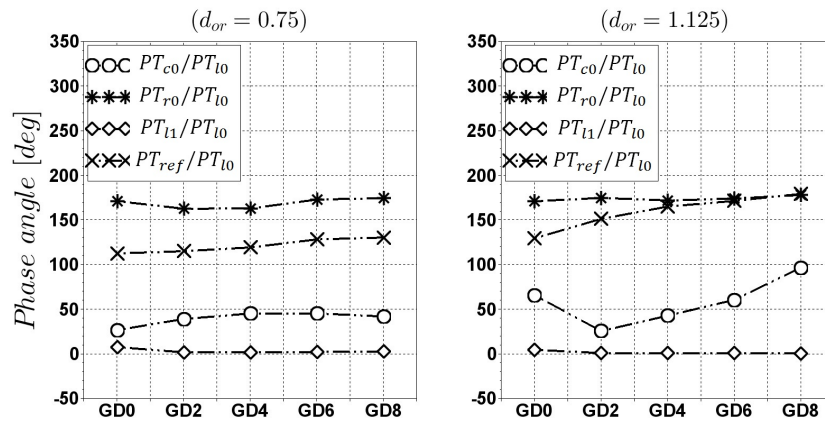


Figure 4.6: Experimental phase-shifts between the  $PT_{l_0}$  signal and  $PT_{c_0}$ ,  $PT_{r_0}$ ,  $PT_{l_1}$  and  $PT_{ref}$  signals as functions of the dome size at IAN-VAN-IAN.

On the contrary, in the presence of a small diameter ( $d_{or} = 0.75$ ), the phase-shifts are independent of the dome size. Indeed, the boundary condition near the orifice is not far from that given by the wall condition; thus, measurement at  $PT_{l_0}$  does not vary with the size of the gas dome. Thus, the mode shapes established in each cavity are not dependent

on each other and the phase-shift between  $PT_{l0}$  and  $PT_{ref}$  remains fixed, as well as the phase shift between  $PT_{l0}$  and  $PT_{c0}$  which is always  $50^\circ$ .

## PAN-IAN-VAN Configuration

At PAN-IAN-VAN the dome is submitted to the largest pressure fluctuation range, due to the presence of both pressure and velocity anti-nodes<sup>a</sup>, at the injectors' exits (see Figure 4.1). Examples of raw pressure signals are shown in Figure 4.7 and Figure D2 of Appendix D).

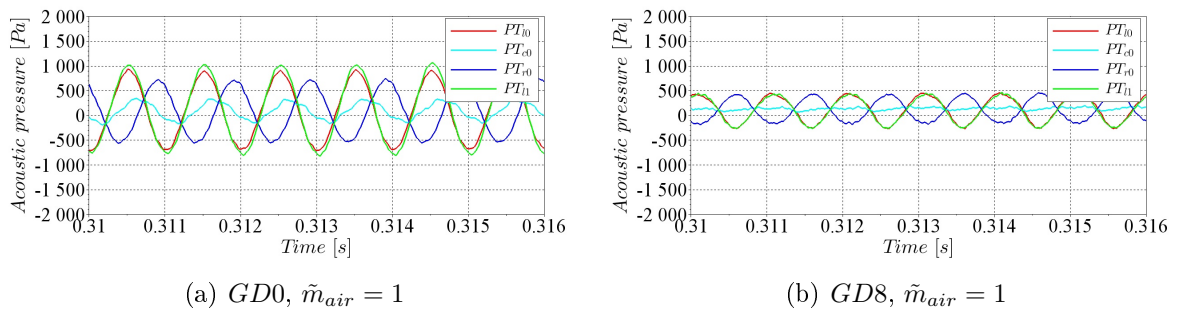


Figure 4.7: Acoustic pressure signal comparison in the gas dome for PAN-IAN-VAN: (a)  $GD0, \tilde{m}_{air} = 1$ ; (b)  $GD8, \tilde{m}_{air} = 1$  ( $f = 1000 \text{ Hz}$ ;  $p_{a,pp} \approx 12 \text{ kPa}$  at PAN;  $d_{or} = 1.125$ ).

The dome response is reported in Figure 4.8 in terms of acoustic pressure amplitude of fluctuations (peak-to-peak values) for  $d_{or} = 1.125$ . Pressure transducer signals  $PT_{l0}$ ,  $PT_{r0}$  and  $PT_{l1}$  present similar amplitudes, which are always higher than that of  $PT_{c0}$  (see Figure 4.8). Also in this configuration, the maximum acoustic response of the injection system is measured for  $GD0$ . It is about  $2500 \text{ Pa}$  without any flow rate (see Figure 4.8(a)) and  $1600 \text{ Pa}$  (see Figure 4.8(d)) with the maximum considered mass flow rate.

<sup>a</sup>With respect to the cavity pressure transducers  $PT_{l0}$ ,  $PT_{c0}$  and  $PT_{r0}$  are respectively at PAN, IAN and VAN.

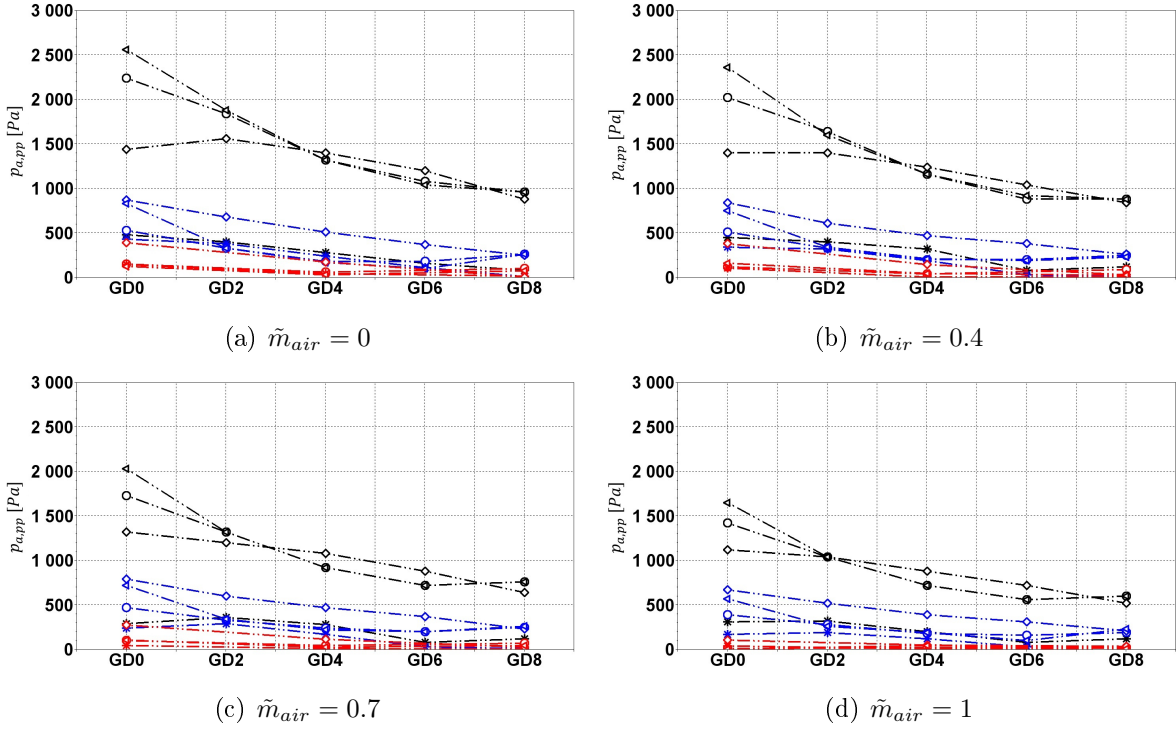


Figure 4.8: Peak-to-peak acoustic pressure measurements in the gas dome as a function of the dome size at PAN-IAN-VAN for: (a)  $\tilde{m}_{air} = 0$ , (b)  $\tilde{m}_{air} = 0.4$ ; (c)  $\tilde{m}_{air} = 0.7$ ; (d)  $\tilde{m}_{air} = 1$  ( $\circ$   $PT_{l0}$ ;  $\star$   $PT_{c0}$ ;  $\diamond$   $PT_{r0}$ ;  $\triangleleft$   $PT_{l1}$ ; red  $d_{or} = 0.375$ ; blue  $d_{or} = 0.75$ ; black  $d_{or} = 1.125$ ).

Figure 4.9 present a comparison between  $PT_{l0}$ ,  $PT_{l1}$ ,  $PT_{l2}$  and  $PT_{l3}$ ; red lines represents simulation of dome response when coupled with the main resonant cavity (results from simulations are scaled with  $PT_{l1}$ ). The acoustic pressure fluctuations inside the dome decrease when the dome's size is increased, which is in agreement with eigenmodes calculations reported in Figure 2.13.

As explained before for the IAN-VAN-IAN configuration in the vicinity of the velocity anti-node phase-shift is expected to vary continuously from 0 to  $+\pi$ . Measurements are thus very sensitive to the position of the pressure transducers, which causes the phase-shifts of  $PT_{l0}$  with  $PT_{c0}$ ,  $PT_{r0}$  and  $PT_{ref}$  to vary with the dome size for both  $d_{or} = 0.75$  and  $d_{or} = 1.125$  (see Figure 4.10). The phase shift plots are presented in Figure 4.10.

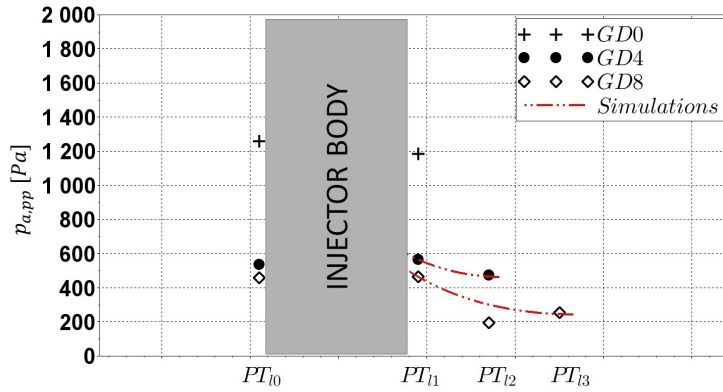


Figure 4.9: (a) Complementary acoustic pressure measurements at PAN-VAN-IAN provided by  $PT_{12}$ , and  $PT_{13}$  and compared with  $PT_{10}$  and  $PT_{11}$  (red lines represent simulations, values are scaled with the measurements of  $PT_{11}$ ).

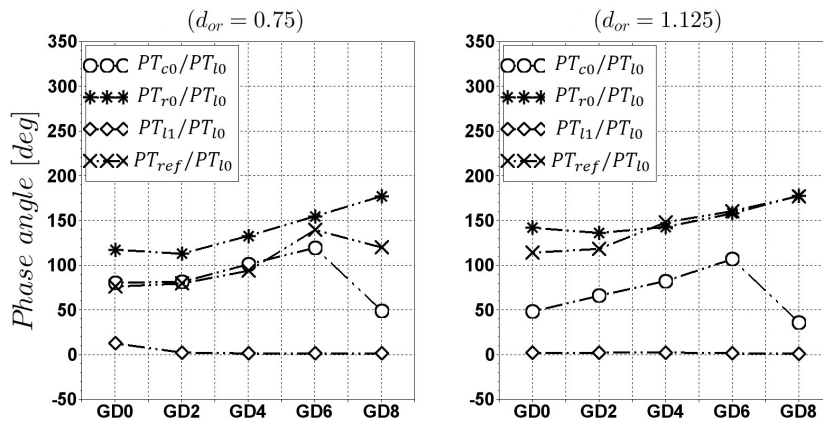


Figure 4.10: Experimental phase-shifts between the  $PT_{10}$  signal and  $PT_{c0}$ ,  $PT_{r0}$ ,  $PT_{11}$  and  $PT_{ref}$  signals as functions of the dome size at PAN-IAN-VAN.

### IAN-PAN-IAN Configuration

The last configuration considered here is the IAN-PAN-IAN which is centered in the cavity (raw pressure signals are presented in Figure 4.11 and Figure D3 of Appendix D).

The three injectors are submitted to in-phase acoustic pressure fluctuations, with amplitude larger than those of the two previous cases, i.e.  $\approx 12 \text{ kPa}$ . Figure 4.12 shows acoustic pressure measurement inside the dome for  $d_{or} = 1.125$ . The acoustic pressure amplitudes measured in the dome are always lower than  $900 \text{ Pa}$ , corresponding to 7.5% of the acoustic pressure amplitude imposed in the main cavity at PAN. Acoustic

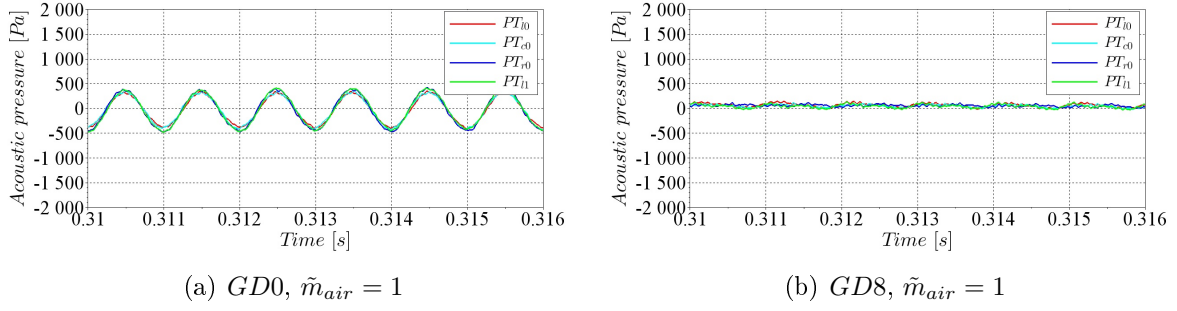


Figure 4.11: Acoustic pressure signal comparison in the gas dome for IAN-PAN-IAN: (a)  $GD0, \tilde{m}_{air} = 1$ ; (b)  $GD8, \tilde{m}_{air} = 1$  ( $f = 1000$  Hz;  $p_{a,pp} \approx 12$  kPa at PAN;  $d_{or} = 1.125$ ).

response is maximum for  $GD0$  and decreases by increasing the dome size. The acoustic conditions imposed at the injectors' exit at IAN-PAN-IAN facilitate the establishment of the GD-C mode (see Figure 2.13 mode GD-C). This is confirmed experimentally by in-phase (see Figure 4.12) and same-amplitude (see Figure 4.12) pressure signals for all pressure transducers in the dome. As observed for the IAN-VAN-IAN configuration, the gas dome is more likely to respond to acoustic excitation for larger junction diameters. For  $d_{or} = 0.75$  phase-shifts are independent from the dome size while for  $d_{or} = 1.125$  they change slightly as dome size is increased.

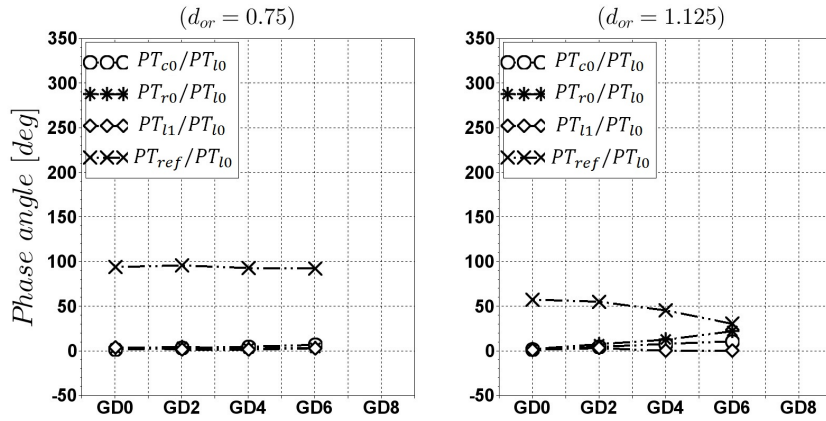


Figure 4.13: Experimental phase-shifts between the  $PT_{10}$  signal and  $PT_{c0}$ ,  $PT_{r0}$ ,  $PT_{l1}$  and  $PT_{ref}$  signals as functions of the dome size at IAN-PAN-IAN.

This slight change is due to the fact that the mode shape changes in this case. Indeed, simulations indicate that, when dome size is increased, the eigenmode changes its mode shape (see Figure 2.13 mode GD-C). A good agreement between pressure amplitudes measured by  $PT_{l1}$ ,  $PT_{l2}$  and  $PT_{l3}$  and those predicted by simulations is shown in

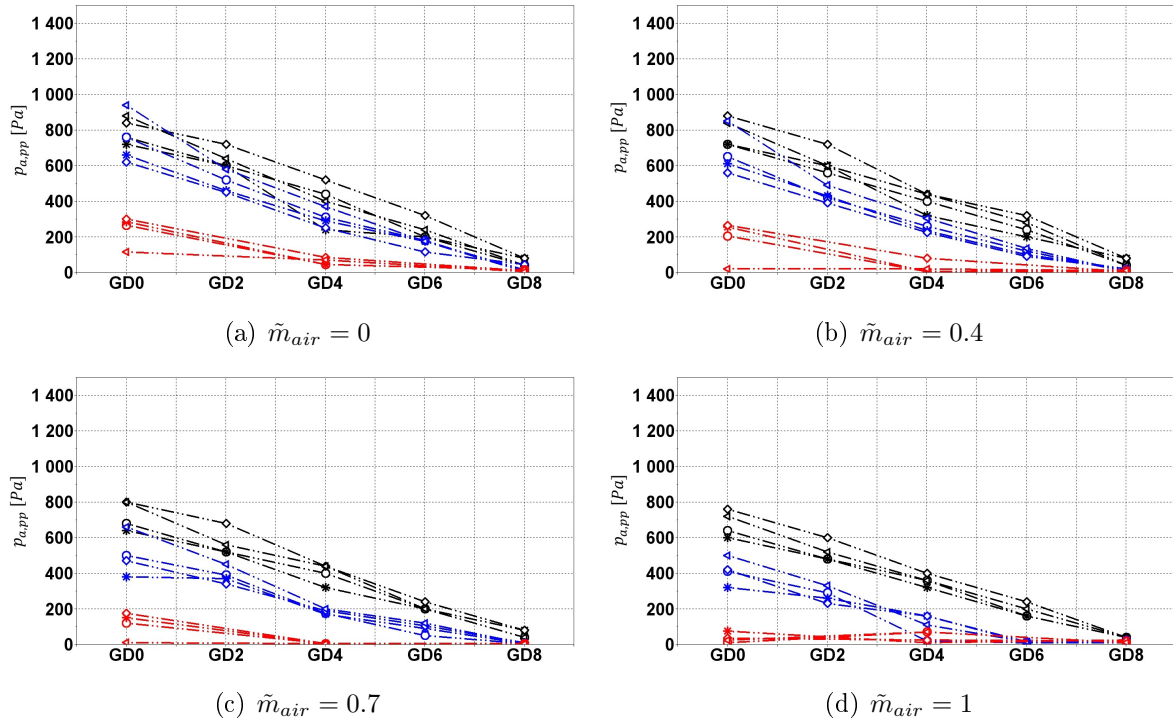


Figure 4.12: Peak-to-peak acoustic pressure measurements in the gas dome as a function of the dome size at IAN-PAN-IAN for: (a)  $\tilde{m}_{air} = 0$ , (b)  $\tilde{m}_{air} = 0.4$ ; (c)  $\tilde{m}_{air} = 0.7$ ; (d)  $\tilde{m}_{air} = 1$  ( $\circ$   $PT_{l0}$ ;  $\star$   $PT_{c0}$ ;  $\diamond$   $PT_{r0}$ ;  $\triangleleft$   $PT_{l1}$ ; red  $d_{or} = 0.375$ ; blue  $d_{or} = 0.75$ ; black  $d_{or} = 1.125$ ).

Figure 4.14. In this case, simulations take into account the main cavity and the gas dome simultaneously. The Helmholtz equation is solved with boundary conditions at the loudspeakers corresponding to a given normal harmonic acceleration fluctuating at the forcing frequency. Black markers represent experimental values as in the two previous cases, the red lines represent numerical simulations for the case of  $GD4$  and  $GD8$ . Numerical curves are scaled by the maximum experimental value of  $PT_{l2}$  and  $PT_{l3}$  respectively for  $GD4$  and  $GD8$ . The appearance of the nodal line is clearly visible at  $GD8$ . Increasing the dome size at IAN-PAN-IAN does not induce a decrease of acoustic pressure fluctuation amplitudes in all points, as it does in the other two configurations. Indeed, pressure amplitude measured with  $PT_{l3}$  at  $GD8$  is higher than the one measured by  $PT_{l0}$  at  $GD0$ , due to the mode shape veering. Acoustic pressure amplitudes detected in the dome are always lower than  $800 Pa$ , which corresponds to 6.7% of the acoustic pressure amplitude imposed in the main cavity at PAN. However, even when the cavity acoustic pressure amplitudes are maximum at IAN-PAN-IAN, the response of the dome in this configuration is always lower than in the other two cases. The fact that the maximum acoustic response

in the dome does not correspond to the maximum acoustic pressure fluctuations in the cavity indicates that the dome acoustics has an important role in the acoustic interaction between the injection system and the main cavity.

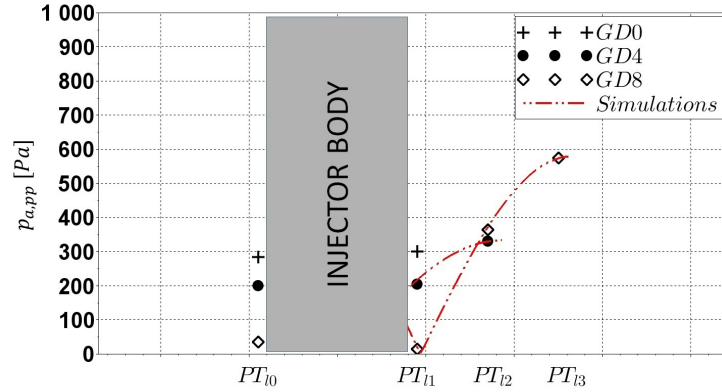


Figure 4.14: Complementary acoustic pressure measurements at IAN-PAN-IAN provided by  $PT_{12}$ , and  $PT_{13}$  and compared with  $PT_{10}$  and  $PT_{11}$  (red lines represent simulations, values are scaled with the measurements of  $PT_{12}$  and  $PT_{13}$  respectively for  $GD4$  and  $GD8$ ).

### 4.3 Liquid Dome Response

The investigation of the liquid dome acoustic response was more challenging than that of the gas dome, due to some difficulties encountered in the positioning of the pressure transducers inside the dome (see section 2.2.2.3). The main problem consisted in having the transducer head completely submerged in the liquid, which is not trivial due to the size of the dome. A pair of transducers smaller than those used in the gas dome were finally installed inside the pistons (see Figure 2.20 in section 2.2.2.3). Thus, only two measurement points were available and both at extremities which did not facilitate the experimental identification of the eigenmodes. On the same basis of what already done with the gas dome a total of 60 test cases was performed, combining:

- the geometrical parameters presented in section 2.2.2.3 (dome size, junction length  $L_j$  and diameter  $d_j$ );
- three spatial configurations of the injection system with respect to the acoustic axis (see Figure 4.1).

Figure 4.15 represents a schematic of the liquid with the locations of the two pressure transducer and two examples of dome sizes,  $LD0$  and  $LD4$ .

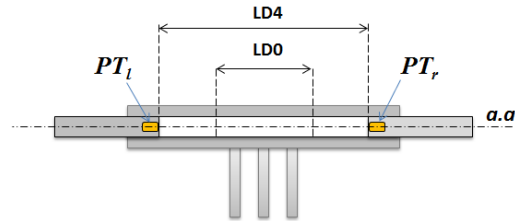


Figure 4.15: Schematic of the liquid dome with pressure transducer locations.

Figure 4.16 shows the amplitudes recorded by  $PT_l$  and  $PT_r$  (presented in the schematic of Figure 4.15) while Figure 4.17 shows the phase-shift between their signals. Both quantities are expressed as functions of the dome size,  $L_j$  and  $d_j$  for the three spatial configurations considered (IAN-VAN-IAN, PAN-IAN-VAN and IAN-PAN-IAN).

- For the IAN-VAN-IAN configuration the liquid dome's acoustic pressure amplitudes are always lower than  $1200 Pa$  (10% of the maximum acoustic pressure in the main cavity at PAN). Changing the junction diameter or length, or the dome size the liquid dome does not present a uniform trend. But for  $L_j = 0.387$  the acoustic pressure measurements of  $PT_l$  continuously decreases with increasing dome size, especially for  $d_j = 1$ . As shown in Figure 4.17(a) the acoustic pressure signals measured with  $PT_l$  and  $PT_r$  tend to be out-of-phase. The phase-shift between transducers suggests an acoustic pressure spatial distribution similar to that of the LD-B mode shape (see Figure 2.18). However, the power spectral density does not present any content around 3500 Hz.

- In the PAN-IAN-VAN configuration the response is more sensitive to the dome size and the acoustic pressure amplitudes decrease with the dome size (see Figure 4.16(b)). A peak is measured for  $LD1$ : it equals  $2000 Pa$  for the shortest junction length and diminishes to  $1200 Pa$  for the longest one. The phase-shift between the transducers ranges between  $40^\circ$  and  $120^\circ$  in Figure 4.17(b), which does not correspond to those of the simple eigenmodes calculated and presented in Figure 2.13.

- For the IAN-PAN-IAN configuration and for  $L_j = 0.387$  acoustic pressure amplitudes (see Figure 4.16(c)) are the lowest and do not exceed  $700 Pa$ . For  $L_j = 0.548$  a stronger response of the liquid dome is obtained. For  $d_j = 0.67$  two peaks are observed for  $LD0$  and  $LD1$ ,  $1600 Pa$  and  $1250 Pa$  respectively. In Figure 4.17(c) the phase shift between left and right transducers indicates that signals are perfectly in-phase for  $d_j = 1$  and  $L_j = 0.387$ , in agreement with the onset of the mode LD-A (see Figure 2.18 mode LD-A).

For  $d_j = 1$  and  $L_j = 0.548$  the response is more complex. For  $d_j = 0.67$  the pressure transducers phase-shift decreases from  $100^\circ$  to  $0^\circ$  for  $L_j = 0.387$  and from  $60^\circ$  to  $0^\circ$  for  $L_j = 0.548$ .

Results indicate that in some conditions the liquid dome can present acoustic pressure fluctuations of the same order of magnitude as that observed in the gas dome. The general tendency is to reduce the acoustic response by increasing the dome size. However, results indicate that the liquid dome's acoustic response is more complex than that of the gas dome since amplitude fluctuations are not affected in a unique manner by the investigation parameters.

## 4.4 Summary of Results

Design procedure described in section 2.2.2 led to the manufacture of the two domes and the experimental investigation of the interaction between a high-amplitude transverse acoustic field and an injection system has been possible. A wide-ranging parametric analysis has been performed and the response of the system has been tested in several configurations. The objective of this investigation was to observe how an injection system could respond to the acoustic pressure fluctuations coming from an instability established in a combustion chamber. Two injection domes, one for the gas and one for the liquid, have been expressly designed in order to investigate the acoustic coupling at the forcing frequency of  $1\text{ kHz}$ . The two domes were used to feed three coaxial injectors similar to those used in liquid rocket engine applications. By changing the position along the acoustic axis, different excitation conditions are imposed on the injection system and thus different mode shapes are excited inside the injection domes. In most of the cases, eigenmode simulations allow the mode shapes excited experimentally to be identified. However in some cases, the response of the domes, particularly the liquid dome, is more complex and direct identification is not possible. The response of the injection system is strongly affected by the acoustic boundary conditions at injector outlets and by all the geometrical parameters considered here.

In all the configurations, the acoustic coupling between the gas dome and the main cavity is weakened by increasing the mass flow rate and the dome size, and by decreasing the diameter of the orifices between the injectors and the gas dome. The only exception is represented by the IAN-PAN-IAN configuration, in which an excessive increase of the dome size causes an increase of the acoustic response. For the IAN-VAN-IAN configuration the boundary conditions imposed at the injector exit plane, in terms of acoustic

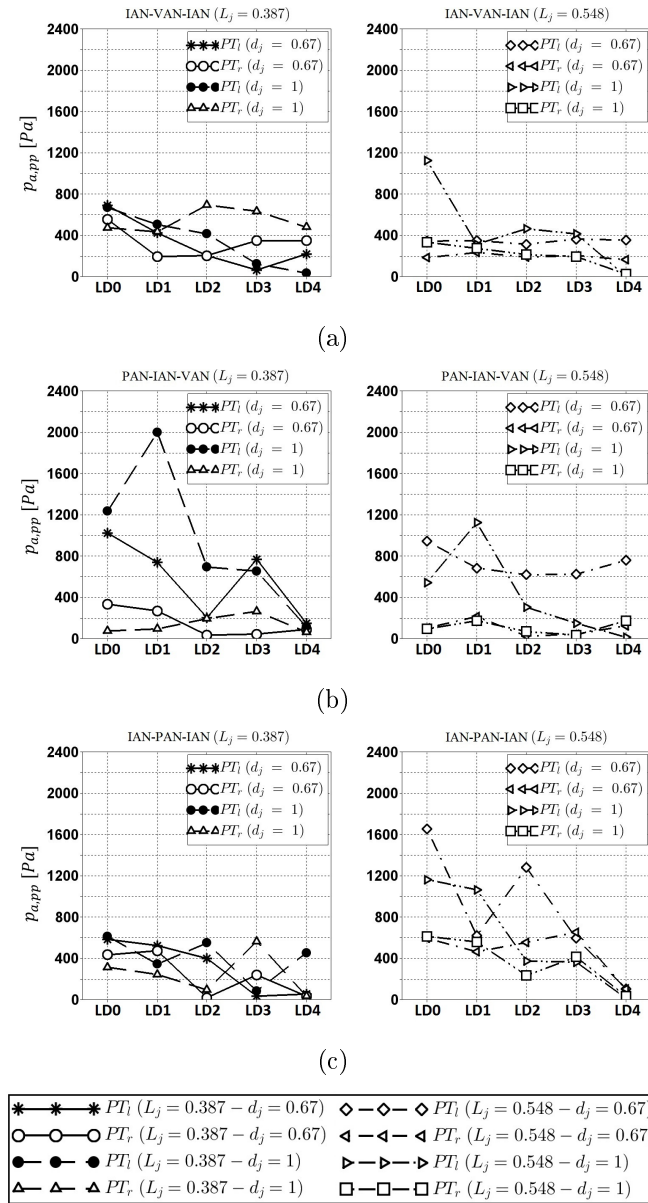
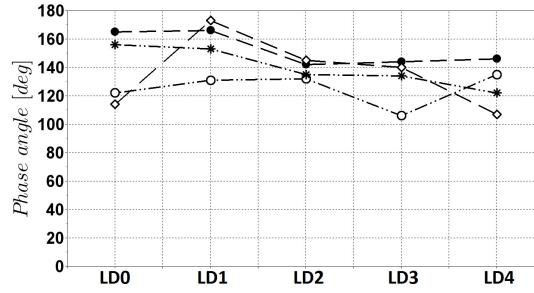


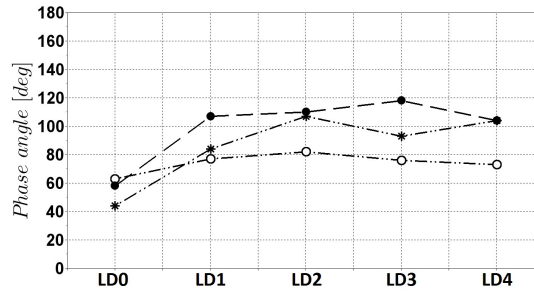
Figure 4.16: Acoustic response of the liquid dome as a function of the dome size at: (a) IAN-VAN-IAN, (b) PAN-IAN-VAN and (c) IAN-PAN-IAN.

pressure amplitudes in the main cavity, are lower than those corresponding to PAN-IAN-VAN and IAN-PAN-IAN configurations. But, the gas dome shows the strongest acoustic response for this configuration. This indicates that the dome acoustics plays a role in the acoustic coupling mechanism between the main cavity and the injection system.

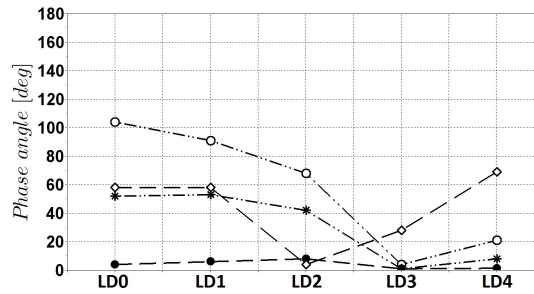
Concerning the liquid dome response, the general tendency is to discourage the acoustic coupling by increasing the dome's size. The liquid dome's response does not seem to be strongly sensitive to the parameters studied here for the IAN-VAN-IAN configuration



(a)



(b)



(c)

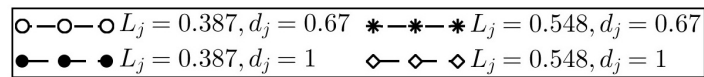


Figure 4.17: Experimental phase-shift between the  $PT_l$  and  $PT_r$  signals as function of the dome size and  $L_j$  at: (a) IAN-VAN-IAN, (b) PAN-IAN-VAN and (c) IAN-PAN-IAN.

except for the acoustic pressure measurement of  $PT_l$  with  $L_j = 0.387$  which continuously decreases with increasing dome size. But, the liquid dome shows a strong acoustic response in some conditions for PAN-IAN-VAN and IAN-PAN-IAN configurations.

The main conclusion is that both liquid and gas domes show a strong response to the transverse acoustic field established in the main cavity. The maximum of acoustic pressure fluctuation amplitudes attains 23% of the amplitudes of the acoustic pressure forced in the main cavity (without mass flow rate). In an actual propulsion system,

such a high level of fluctuations in the injection dome could induce strong mass flow-rate fluctuations. In fact, mass flow-rate fluctuations can contribute significantly to the acoustic fluctuation amplification in the combustion chamber. Moreover, the maximum response of the domes is not observed in the configuration where the injection system is submitted to the highest acoustic pressure fluctuations of the cavity (IAN-PAN-IAN configuration), but rather where the phase-shift conditions can excite a particular dome eigenmode, as in the IAN-VAN-IAN configuration for the gas dome.

Domes' geometries considered here do not replicate actual rocket engine geometries. However, results presented in this study open the path to the definition of general rules that could be used early in design phases, together with numerical simulations, to anticipate and justify the acoustic coupling behavior of domes/main combustion device cavity and represent a starting point for future investigation.



# Chapter 5

## Downstream effects: Atomization Process response

*This section is dedicated to experimental results concerning the effects of the acoustic field on the atomization process. The first part presents the analysis performed through high-speed visualizations (see section 5.1). The single injector response is described for all atomization regimes in section 5.2 by distinguishing three phenomena: flattening, deviation and atomization improvement. Section 5.3 reports results obtained in the three-injector configuration, first without injection domes (section 5.3.1) then with the injection domes (section 5.3.2). In section 5.4 preliminary results concerning droplet size (see subsection 5.4.1) and gas velocity field measurements (see subsection 5.4.3) are shown to demonstrate the feasibility of the techniques chosen. Section 5.5 is dedicated to the general summary and remarks.*

### 5.1 Introduction

One of the main objective of this research activity was the investigation of the response of coaxial jets to high-amplitude pressure fluctuations. Many test conditions were taken into account in order to have a complete characterization of the jet response. The five characteristic injection locations, described in section 2.1, were considered: PAN, PAN-IAN, IAN, IAN-VAN, VAN. These locations cover all the characteristic conditions, in terms of acoustic solicitation, that a jet can find in a standing wave field. Several acoustic levels were tested up to the maximum available, i.e.  $12\text{ kPa}$  (peak-to-peak value measured at PAN). The forcing frequency was adjusted around  $1\text{ kHz}$  depending on ambient conditions. Injection conditions used range from those of the Rayleigh axi-symmetric

regime, up to those of the fiber type regime, which is more representative of actual injection conditions in liquid rocket engine combustion chambers. The investigation of low Weber number atomization response is however fundamental, since atomization regimes such as the Rayleigh axi-symmetric can provide valuable information that are necessary to interpret the behavior of high Weber number atomization regimes.

Single and three-injector test configurations were considered. In the multi-injection configuration, experiments with and without the injection domes have been performed.

Experimental results obtained with the single-injector test configuration allow identifying three main phenomena:

- ***jet flattening***, particularly strong around the velocity anti-nodes. The phenomenon is mainly observed in atomization regimes presenting a long continuous liquid core (low Weber atomization regimes);
- ***atomization process improvement***, observed in the spatial region around the velocity anti-nodes for high Weber number atomization regimes;
- ***jet deviation***, particularly strong around the intensity anti-nodes. It concerns all atomization regimes but its strength decreases while increasing the Weber number.

The knowledge coming from the analysis of single-injector results is then exploited for analyzing the three-injector configuration. Indeed, in multi-injection configurations the combination of the above-mentioned phenomena gives rise to what as been identified as a droplet ***clustering phenomenon***.

## 5.2 Single Injector Response

In this section the response to the acoustic perturbation of a single coaxial jet is investigated via three effects observed experimentally: round jet flattening, atomization process improvement, and jet and spray deviation. One injector is positioned successively at each of the five above-mentioned locations inside the acoustic field. For high Weber number atomization regimes, acoustic effects on the droplet spatial distribution are analyzed in the light of flattening and deviation analysis for low Weber number regimes.

### 5.2.1 Flattening

Experiments on the effects of a transverse acoustic field on free jets [38, 40, 41] and on coaxial jets [89, 90] show the appearance of flattening at a specific location in the

acoustic field, namely at the velocity anti-node (VAN), for sufficiently high acoustic levels. Hoover *et al.* [38] suggested that the flattening could be ascribed to a velocity coupling mechanism similar to the deformation induced by the impact of two opposite transverse gas flows. However, calculation relying on the suggested configuration did not provide results comparable with the experiments. In 2009 Baillot *et al.* [90] proposed a mechanism for the flattening based on nonlinear acoustic effects. A threshold for the onset of the flattening was estimated by means of a calculation based on acoustic field scattered by a spherical object. In light of these results it was decided to analyze the flattening phenomenon, by systematically investigating the different positions inside the acoustic field (including VAN) for a wide range of atomization regimes. The first result is that the phenomenon does not take place exclusively at VAN but in any locations in between VAN and IAN, with a decreasing intensity. The responses of Rayleigh axi-symmetric ( $We_g = 9$ ,  $Re_l = 2500$ ), Rayleigh non symmetric ( $We_g = 40$ ,  $Re_l = 3000$ ) and shear breakup ( $We_g = 60$ ,  $Re_l = 3900$ ) regimes are presented in Figures 5.1 and 5.2. Images were recorded according to views *A* and *B* (see section 3.1) for similar injection conditions. In the case of the Rayleigh axi-symmetric and non-symmetric regimes the flattening and liquid sheet formation are clearly visible around  $t = 0.159s$ . The liquid sheet is subsequently atomized and a spray is formed. For the shear breakup regime, the flattening effect leads to the deformation of a smaller liquid sheet (see Figure 5.2(j)) which is eventually atomized.

Images reported in Figures 5.1 and 5.2 indicate that flattening is limited to a certain portion of the jet not too far from the injector exit plane. At the extremities of the liquid sheet the jet maintains its circular shape. The injector nozzle represents a physical constraint which imposed the circular shape to the jet. This means that the jet cannot be deformed at the very exit of the injector nozzle. However, the constraint imposed by the injector decreases along  $\tilde{z}$ . On the contrary, the interfacial coherence, represented by the Laplace pressure drop, is inversely proportional to the jet radius and increases with  $\tilde{z}^a$ . The competition of these two factors determines the position at which the flattening begins.

---

<sup>a</sup>For low velocity regimes, as those considered here, the jet is accelerated, and the local radius  $r_o(z)$  diminishes with  $\tilde{z}$ . Moreover, the lower the Reynolds number, the more the radius diminishes along the  $\tilde{z}$ -axis.

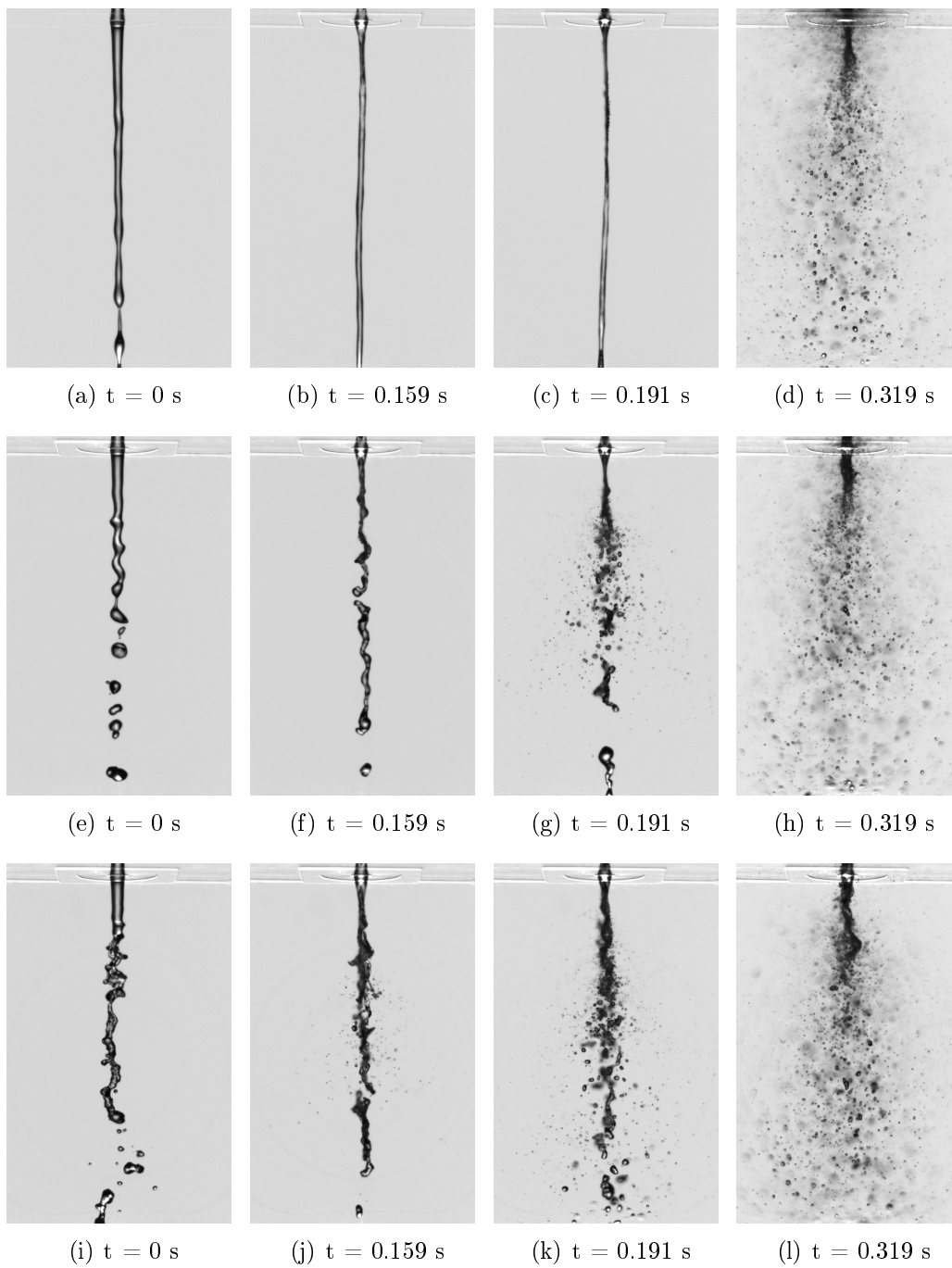


Figure 5.1: View A visualizations of jet response at VAN for: (a-d) Rayleigh axisymmetric ( $We_g = 20$ ,  $Re_l = 1900$ ); (e-h) Rayleigh non-symmetric ( $We_g = 40$ ,  $Re_l = 3000$ ); (i-l) shear break-up ( $We_g = 60$ ,  $Re_l = 3900$ ). Forcing frequency  $f = 1015$  Hz,  $p_{a,pp} = 11800$  Pa.

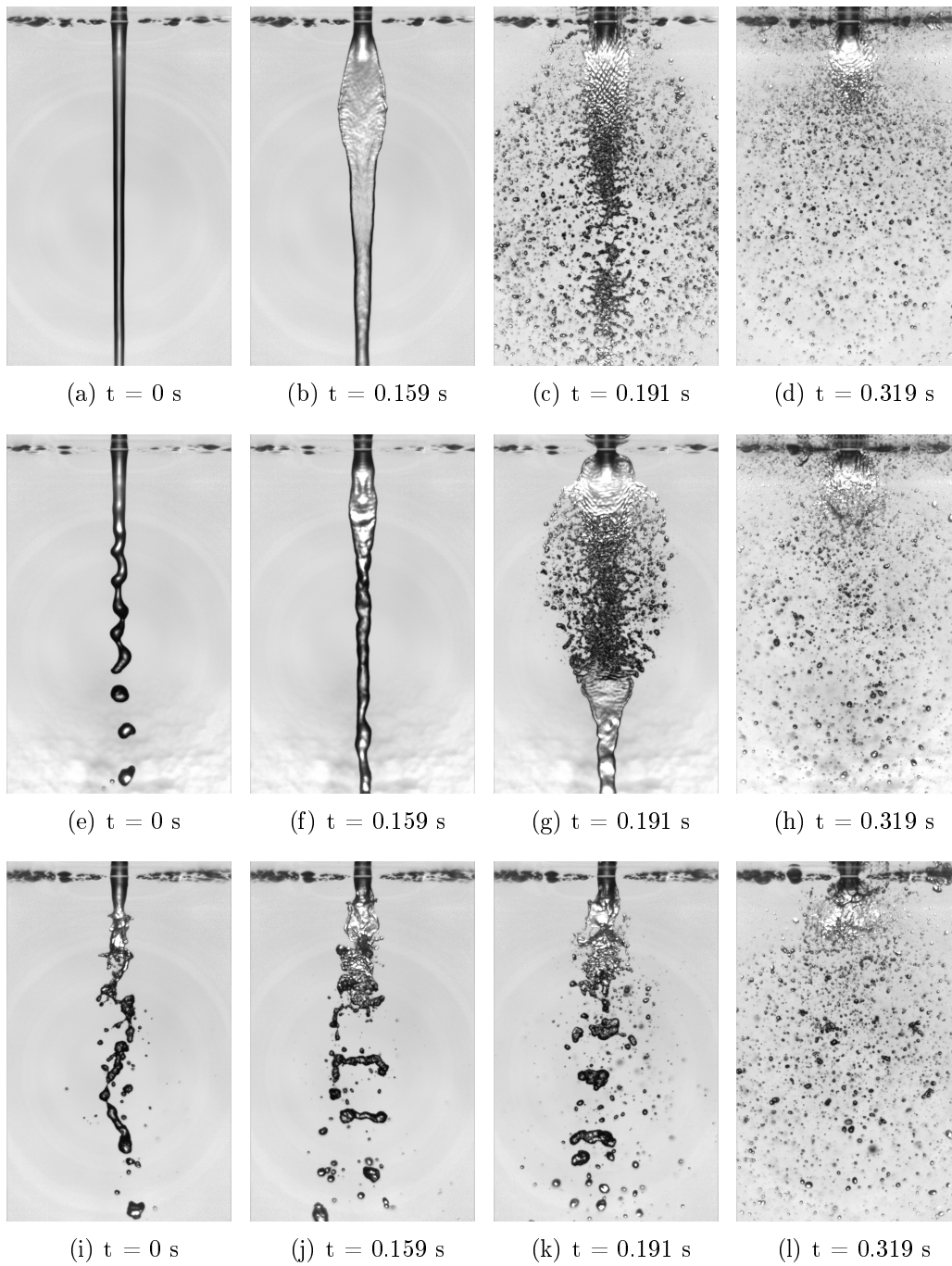


Figure 5.2: View  $B$  visualizations of jet response at VAN for: (a-d) Rayleigh axisymmetric ( $We_g = 9$ ,  $Re_l = 2500$ ); (e-h) Rayleigh non-symmetric ( $We_g = 36$ ,  $Re_l = 2200$ ); (i-l) shear break-up ( $We_g = 80$ ,  $Re_l = 2800$ ). Forcing frequency  $f = 1015$  Hz,  $p_{a,pp} = 11800$  Pa.

### 5.2.1.1 Jet Thickness Evolution

By post-processing the high-speed visualization images an accurate evolution of the jet thickness is obtained as a function of time. The jet thickness  $Th$  can be extracted from

raw images by applying contour detection techniques. Due to its initial shape the Rayleigh axi-symmetric regime is the one that better lends itself to flattening quantification and analysis.

Figure 5.3 shows an example of the complete jet thickness evolution, from flattening to atomization, deduced from high-speed visualizations for a specific location along the jet length,  $\tilde{z} = 3.33$ . The thickness values are reduced by the liquid post exit diameter  $D_l$  ( $\widetilde{Th} = Th/D_l$ ). During the first part of the process the jet thickness is quasi-constant. When acoustic level is high enough to deform the jet, the measured thickness starts to decrease. Then, a steep decrease during flattening and the minimum value represents the thickness of the resulting liquid sheet; after this point the liquid sheet is atomized. The noisy central part in Figure 5.3 is due to the presence of droplets resulting from the sheet atomization. When the acoustics is turned off the jet recover its initial shape, and the original jet thickness is restored.

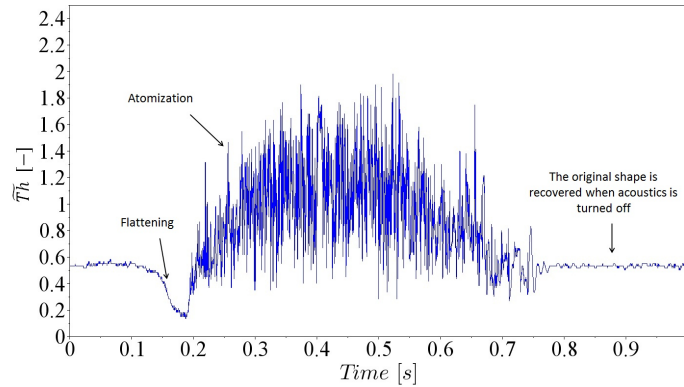


Figure 5.3: Example of jet thickness temporal evolution at VAN for  $\tilde{z} = 0.33$  extracted from high-speed image post-processing (View *A*;  $We_g = 9$ ;  $Re_l = 2000$ ; 1015 Hz;  $p_{a,pp} \approx 12$  kPa).

Jet thickness evolutions as shown in Figure 5.3 are calculated for several vertical locations in between  $1 < \tilde{z} < 12$ . Figure 5.4 shows the jet thickness evolution for some of them. Only the part concerning the flattening is reported here. It can be observed that the evolution of  $\widetilde{Th}$  varies along  $\tilde{z}$ . Indeed, due to the jet acceleration, the jet diameter decreases along  $\tilde{z}$ . Moreover, the larger the distance from the injector exit, the higher the probability to develop instabilities which results in quasi-periodic fluctuations of the jet thickness. To avoid noise in the thickness detection, data are fitted by means of a hyperbolic tangent function, as given by Eq. 5.1:

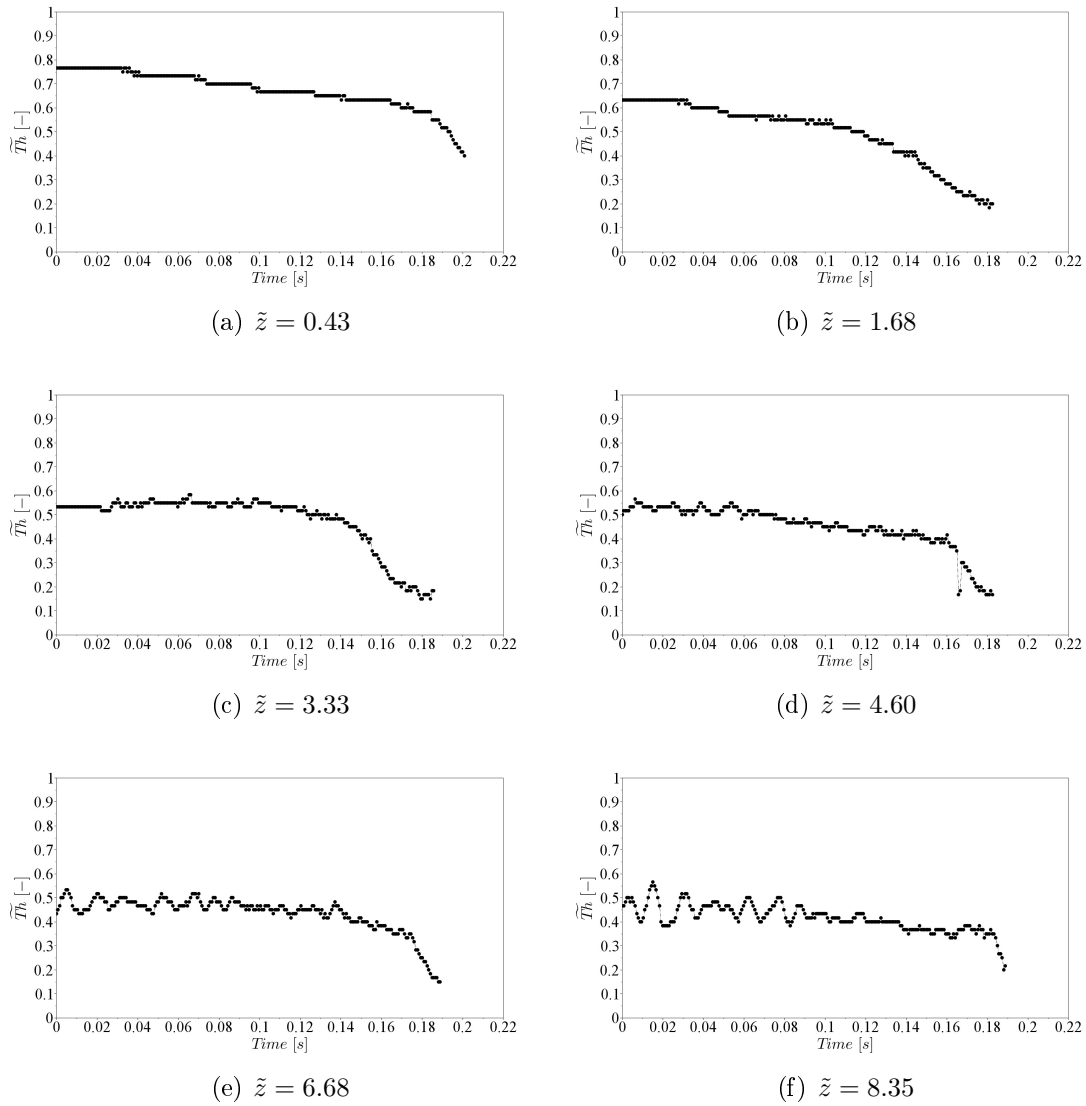


Figure 5.4: Jet thickness time evolution at VAN before atomization for several positions along the vertical axis  $\tilde{z}$  (View A;  $We_g = 9$ ;  $Re_l = 2000$ ; 1015 Hz;  $p_{a,pp} \approx 12$  kPa).

$$\tilde{Th} = \tilde{Th}_f + \frac{d\tilde{Th}}{2} \left[ 1 - \tanh \frac{(t - t_o)}{\delta t} \right]. \quad (5.1)$$

Figure 5.5 shows an example of fitting, for  $\tilde{z} = 3.33$ . The non-dimensional thickness  $\tilde{Th}$  reported here is scaled with  $D_l$ . The parameters  $\tilde{Th}_f$ ,  $d\tilde{Th}$ ,  $t_o$  and  $\delta t$  introduced in Eq. 5.1 are obtained from thickness measurements, see Fig. 5.5. The last fitting function point corresponds to the instant before jet disintegration. At this time the jet presents the minimum thickness, namely  $\tilde{Th}_f$ . Beyond this time the jet atomizes, and its thickness is no longer defined at the measured point.

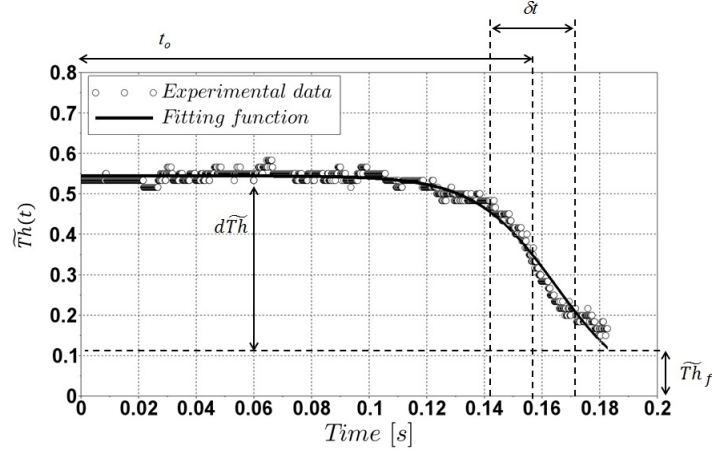


Figure 5.5: Example of jet thickness evolution and its associated fitting curve for a jet in the Rayleigh-axisymmetric regime ( $We_g = 9$ ,  $Re_l = 2000$ ) at VAN,  $p_{a,pp} \approx 12$  kPa, 1 kHz ( $\tilde{z} = 3.33$ ;  $\tilde{T}h_f = 0.1276$ ,  $d\tilde{T}h = 0.4136$ ,  $t_o = 0.1569$  s and  $\delta t = 0.0198$  s).

### 5.2.1.2 Flattening Threshold

The thickness  $\tilde{T}h(t)$  is measured simultaneously with the acoustic field peak-to-peak amplitude  $p_{a,pp}(t)$  at the pressure anti-node. The flattening can be observed gradually and a threshold criterion for its onset can be established. The percentage decrease of the jet thickness for which the flattening phenomenon is considered to begin is fixed at 10%. This value is small enough to consider that the phenomenon is at its very beginning and at the same time the jet is only slightly deformed, which means that its sections can be assumed circular. The corresponding experimental value of the acoustic pressure for which the jet thickness is decreased by 10% is referred as  $p_{10\%}$ . Calculations have been carried out for several locations along  $\tilde{z}$ . An illustration is given here for nine test cases at  $\tilde{z} = 3.33$  and  $\tilde{z} = 5.85$ . The ratio between the initial jet radius  $r_o(\tilde{z})$  and the radius of the injector  $r_{inj}$  is summarized in Table 5.1 along with the value of the maximum acoustic pressure amplitude  $p_{a,pp}$  measured at PAN (peak-to-peak value of the plateau of the signal, see section 2.1.1). Injection conditions are also given in terms of  $We_g$  and  $Re_l$ . The associated values of  $p_{10\%}$  are reported in Figure 5.6.

At  $\tilde{z} = 3.33$  all tests between VAN and IAN-VAN (labeled from 1 to 7 in Table 5.1 and Figure 5.6) present a threshold  $p_{10\%}$  of around 2700 Pa. For tests 3 and 4 corresponding to jets with a larger initial radius (see  $r_o/r_{inj}$  in Table 5.1) obtained by increasing the Reynolds numbers, lower values of the threshold are obtained, 2268 Pa and 2372 Pa respectively. The values of the threshold measured at  $\tilde{z} = 5.85$  are slightly higher than

Test number	Position	$We_g$	$Re_l$	$r_o(\tilde{z} = 3.33)/r_{inj}$	$r_o(\tilde{z} = 5.85)/r_{inj}$	$p_{a,pp}$ [Pa] <sup>a</sup>
1	VAN	9	2000	0.48	0.42	6124
2	VAN	9	2000	0.50	0.44	8379
3	VAN	9	3000	0.72	0.68	10096
4	VAN	9	2700	0.65	0.63	11396
5	VAN	9	2000	0.54	0.48	12277
6	IAN-VAN	6	2000	0.53	0.46	7110
7	IAN-VAN	6	2000	0.54	0.48	12281
8	IAN	6	2000	0.50	0.46	8842
9	IAN	6	2000	0.52	0.48	12283
	PAN-IAN	6	2000	No flattening		
	PAN	6	2000	No flattening		

Table 5.1: Flattening analysis: summary of test case conditions at  $\tilde{z} = 3.33$  and  $\tilde{z} = 5.85$  (<sup>a</sup>Maximum peak-to-peak acoustic pressure amplitude measured at PAN.).

those calculated at  $\tilde{z} = 3.33$ . This is due to the fact that jet radius decreases along  $\tilde{z}$  due to the jet acceleration. The difference is less noticeable for tests 3 and 4. In these two cases, due to the higher values of the Reynolds numbers (see Table 5.1), the jet radius decrease in between the two vertical coordinates is smaller.

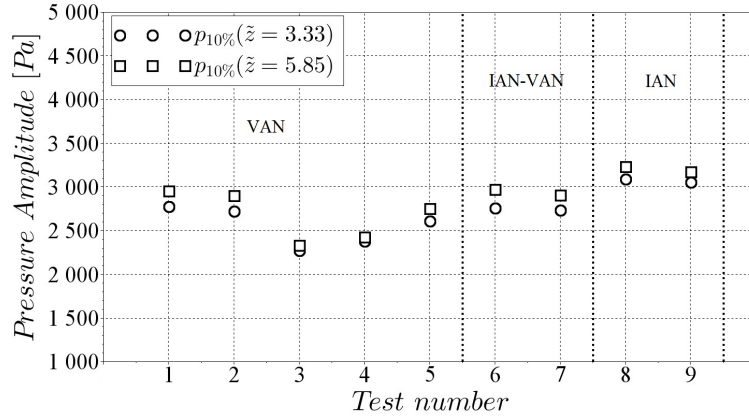


Figure 5.6: Comparison between the values of  $p_{10\%}$  at  $\tilde{z} = 3.33$  and  $\tilde{z} = 5.85$  for the test cases indicated in Table 5.1.

For tests 8 and 9, which correspond to injection at IAN, the threshold  $p_{10\%}$  is around 4000 Pa. High-speed visualizations indicated that at IAN another phenomenon, namely the jet deviation, takes place simultaneously to the flattening. Flattening and deviation compete for the acoustic energy distribution: the acoustic energy is only partially dedicated to the flattening phenomenon while the rest is transferred into the deviation process.

## 5.2.2 Atomization Process Improvement

This section focuses on the consequences of the nonlinear acoustic effects on the atomization efficiency. Discussion concerns atomization regimes at  $We_g \geq 100$  and analysis of the atomization improvement is performed via the quantification of the droplet spatial distribution.

### General response quantification

For high Weber number regimes a spray is already formed without acoustics and jet flattening cannot be detected since the continuous liquid core is very short. However, the radiation pressure acts also on dispersed objects causing droplets deformation and break-up, which modifies the atomization process. Figures 5.7 and 5.8 show images of the spray submitted to acoustics, for two cases of the membrane regime ( $We_g = 129$ ,  $Re_l = 3200$  and  $We_g = 116$ ,  $Re_l = 2800$ ) and two cases of the fiber regime ( $We_g = 224$ ,  $Re_l = 3200$  and  $We_g = 224$ ,  $Re_l = 2800$ ) for which the injector is placed at VAN. In both figures the first row shows the spray in view *A* and the second row shows the spray in view *B*. The spray cone angles are also reported on images at  $t = 0$  s (spray angle without acoustics) and  $t = 0.319$  s (spray angle with acoustics). These angles are determined from minimum images (see first and last columns of Figures 5.7 and 5.8) where each pixel has got the minimum grey level over the image series. In the minimum images black indicates the locations where liquid droplets have passed.

For the membrane regime a drastic modification of the atomization process is observed between  $t = 0$  s and  $t = 0.319$  s, as well on view *A* as on view *B*. A closer observation to what occurs in the vicinity of the nozzle exit clearly shows a flattening of the short liquid core. This is characterized by an increase of the spreading angle in view *B* with a simultaneous increase of the population of small droplets resulting from the atomization of the flattened jet. Without acoustics the cone angle is similar in both views *A* and *B*, while with acoustics a larger cone angle is observed,  $40^\circ$  for view *A* and  $105^\circ$  for view *B*.

For the fiber regime without acoustics the cone angle is around  $40^\circ$  in both directions. In this regime the atomization process modification is not straightforward. A larger increase of the spray angle is observed for view *B* (from  $\approx 40^\circ \approx 80^\circ$ ) than for view *A* (from  $\approx 40^\circ \approx 50^\circ$ ), indicating that even if not clearly visible, a flattening of the remaining ligaments is still possible at such a high Weber number.

Droplet location distributions have been investigated by image analysis [110, 111] to quantify the acoustics effect on the generation and on the spreading of the spray. The

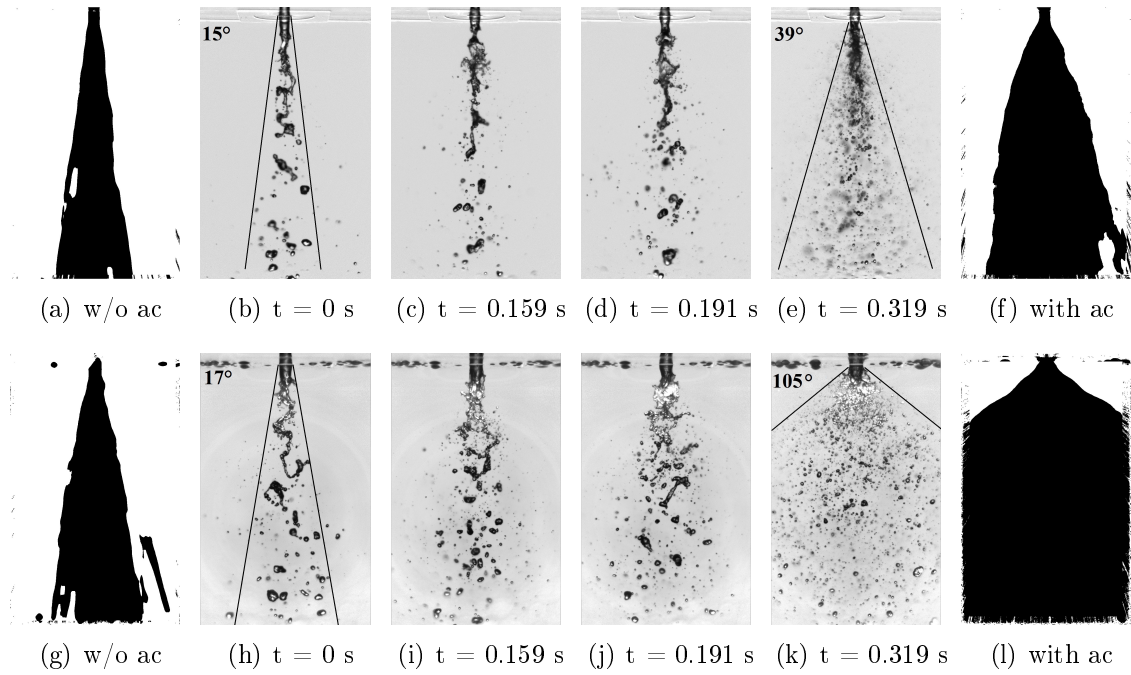


Figure 5.7: Jet response at VAN for the membrane regime: (a-f) view *A*,  $We_g = 129$ ,  $Re_l = 3200$ ; (g-l) view *B*,  $We_g = 116$ ,  $Re_l = 2800$ . Forcing frequency  $f = 1015 \text{ Hz}$ ,  $p_{a,pp} \approx 12 \text{ kPa}$ .

spatial distribution of droplets for the membrane and fiber regimes at VAN are shown in Figure 5.9 for view *A* and *B*. Dash-dotted lines without markers indicate the droplet spatial distribution  $\hat{N}_d^0$  without acoustics, while dash-dotted lines with circular markers correspond to the distribution  $\hat{N}_d^{ac}$  at the maximum acoustic solicitation. Each curve is scaled with respect to the maximum number of object  $N_d^{0,max}$  without acoustics. A higher droplets production is observed for the membrane regime in both views. In view *A*, spatial distributions indicate a concentration of droplets around the injection axis while in view *B* a spreading of the distributions is observed.

The ratio between the integrals of  $\hat{N}_d^{ac}$  and  $\hat{N}_d^0$  representing an assessment of the droplets production ratio  $PR$ , is reported in Table 5.2 for four locations of interest. With acoustics the number of objects is almost doubled in the fiber regime and is 10 times higher in the membrane regime at VAN. If the injector is placed between IAN and VAN a ratio of 7.61 is obtained for the jet in the membrane regime and 1.2 for the fiber regime. At IAN and PAN-IAN this ratio is around 2 for the membrane regime and close to the unity for the fiber case. For these two latter locations the values are underestimated due to the spray deviation which means that a number of the droplets are outside the field of view.

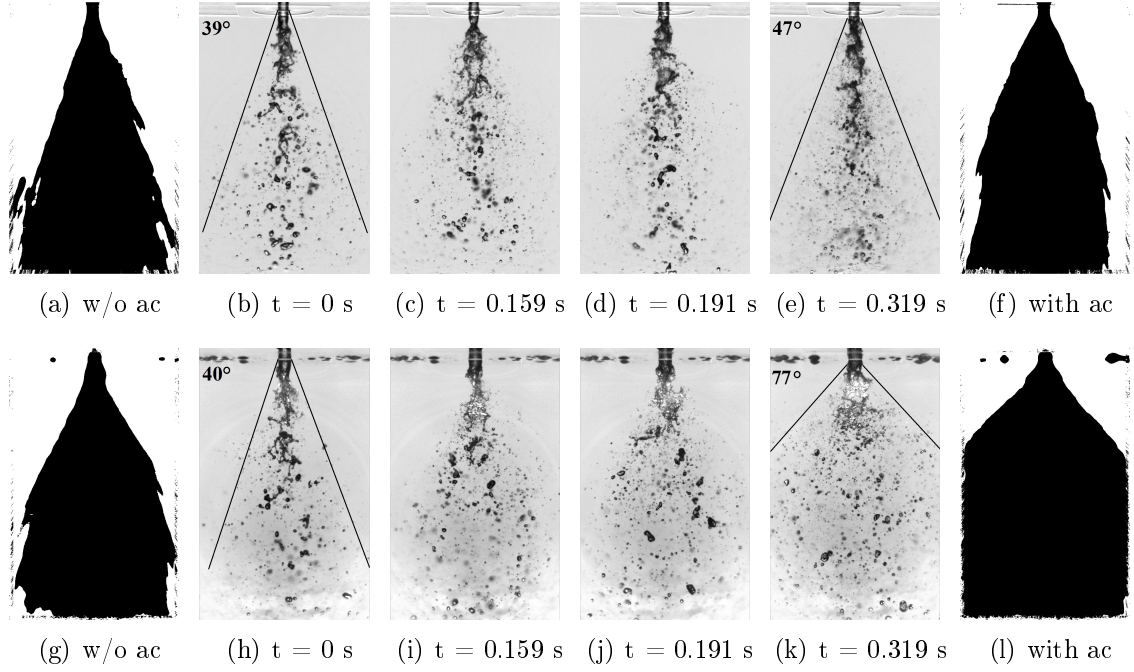


Figure 5.8: Jet response at VAN for the fiber regime: (a-f) view *A*,  $We_g = 224$ ,  $Re_l = 3200$ ; (g-l) view *B*,  $We_g = 224$ ,  $Re_l = 2800$ . Forcing frequency  $f = 1015 \text{ Hz}$ ,  $p_{a,pp} \approx 12 \text{ kPa}$ .

Position	Pr for membrane regime	PR for fiber regime
VAN	9.35	1.76
IAN-VAN	7.61	1.20
IAN <sup>a</sup>	2.21	1.09
PAN-IAN <sup>a</sup>	1.76	0.90

Table 5.2: Droplet production ratio  $PR = \hat{N}_d^{ac} / \hat{N}_d^0$  (<sup>a</sup>  $PR$  is underestimated due to the deviation which brings droplets outside the field of view). View *A*.

### Fiber regime response quantification as a function of droplet size

Figure 5.10 shows the droplet spatial distributions  $\hat{N}_d$  for two classes of droplet diameters in the case of the fiber regime at VAN. The first class (designated as *small droplets*) concerns elements with a reduced diameter in the range 0.0025 - 0.025 while the second one (*big droplets*) involves objects diameters in the range 0.075 - 0.25. Distributions obtained from view *A* are shown in Figure 5.10(a) and Figure 5.10(b) while those from view *B* are reported in Figure 5.10(c) and Figure 5.10(d). Curves in each plot are scaled by the maximum number of objects without acoustics. The Gaussian standard deviation  $SD$  can be considered as an indicator of the spray width.

Small droplets move away from the jet axis as observed in view *A* and *B*. With

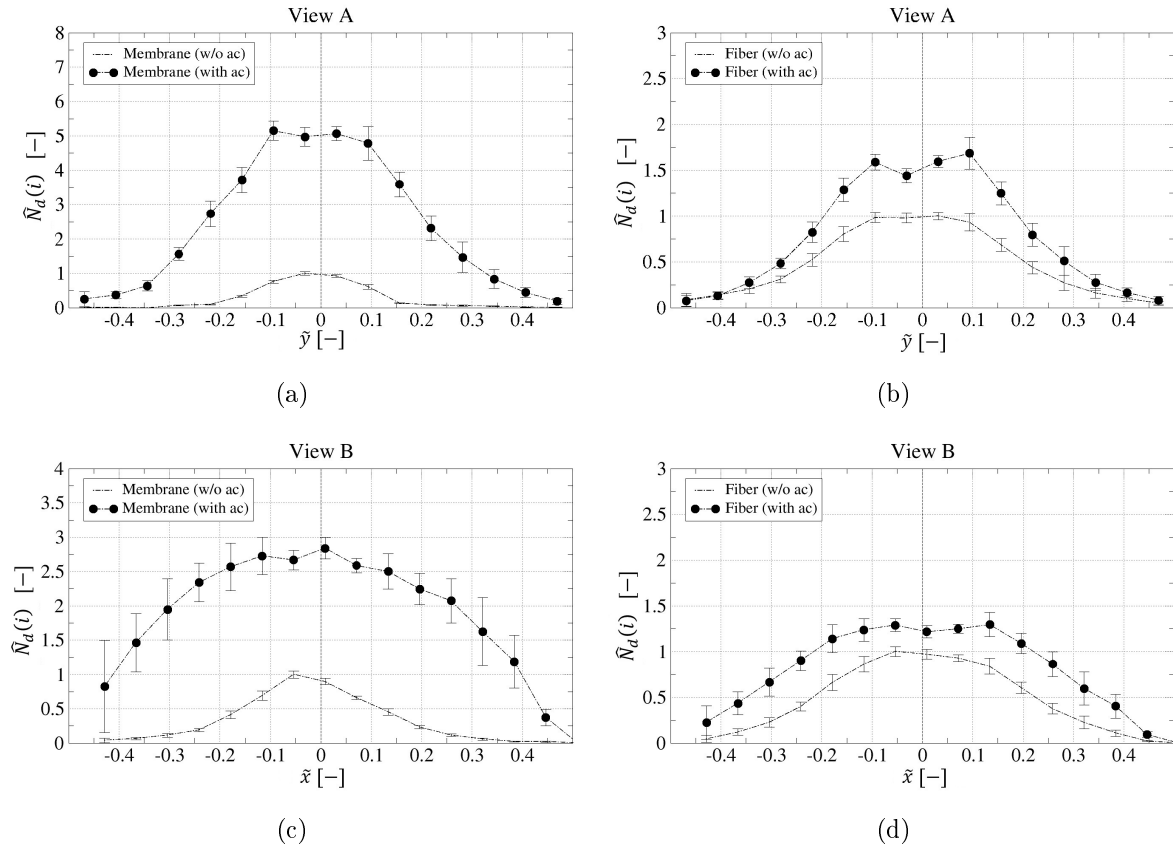


Figure 5.9: Droplet spatial distribution  $\hat{N}_d$  at VAN with ( $\bullet$ ) and without (dash-dotted line) acoustics for: (a) membrane regime,  $We_g = 129$ ,  $Re_l = 3200$ , view *A*; (b) fiber regime,  $We_g = 224$ ,  $Re_l = 3200$ , view *A*; (c) membrane regime,  $We_g = 116$ ,  $Re_l = 2800$ , view *B*; (d) fiber regime,  $We_g = 224$ ,  $Re_l = 2800$ , view *B*. Forcing frequency  $f = 1015$  Hz,  $p_{a,pp} \approx 12000$  Pa.

acoustics  $SD$  increases from 17.2 and 15.8 to 20.2 and 19.5 respectively for the views *A* and *B*. The same behaviour is observed for the big droplets in view *B* for which  $SD$  increases from 11.9 to 19.2 but not for view *A* for which  $SD$  decreases from 11.7 to 9.7. It has already been shown that droplets tend to be merged in VAN under the action of acoustics. In Figure 5.10, VAN corresponds to the image plane of view *B* or to the central axis ( $\tilde{y} = 0$ ) in view *A*. The accumulation of droplets in VAN is particularly significant for big droplets where an increase of drop counting is clearly seen at center of view *A* (see Figure 5.10(b)). Large droplets tend to be trapped in the VAN plane while smaller ones are more likely to be entrained away from the axis by the gas flow and are thus ejected in both views.

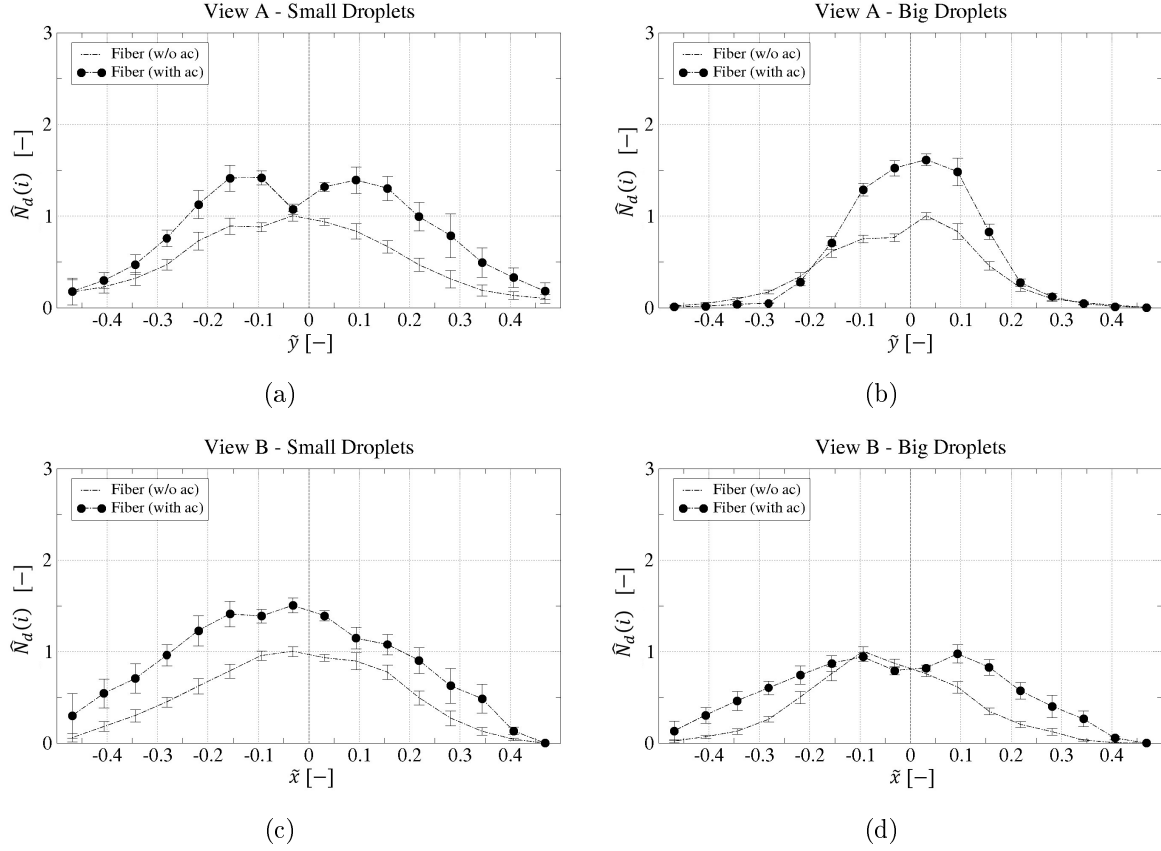


Figure 5.10: Droplet spatial distribution  $\hat{N}_d$  at VAN with ( $\bullet$ ) and without (dash-dotted line) acoustics for the fiber regime  $We_g = 224$ ,  $Re_l \approx 3000$ : (a) *small droplets*, view A; (b) *big droplets*, view A; (c) *small droplets*, view B; (d) *big droplets*, view B. Forcing frequency  $f = 1015$  Hz,  $p_{a,pp} \approx 12$  kPa.

### 5.2.3 Deviation

When the liquid system is far from VAN and PAN it is deviated by the acoustic field toward the nearest VAN. Deviation involves low and high Weber number atomization regimes and both jet and droplets are deviated away from their original trajectories. Low Weber number regimes will be discussed first in order to better visualize the phenomenon, then high Weber regimes will be treated in light of what has been observed for the low Weber regimes.

#### 5.2.3.1 Low Weber Number Atomization Regimes

In the case of Rayleigh axi-symmetric regime, without perturbation, the jet can be considered cylindrical, at first approximation. The deviation is quantified by introducing a deviation angle  $\gamma$ , defined as the angle between the vertical and linear regression of the

jet center-line, evaluated between 0 and  $\tilde{z}_\gamma$ , as indicated in Figure 5.11(d) (see section 3.1 for more details on calculation of the deviation angle). The jet response differs according to the injector position with respect to *a.a.*, as shown in Fig. 5.11.

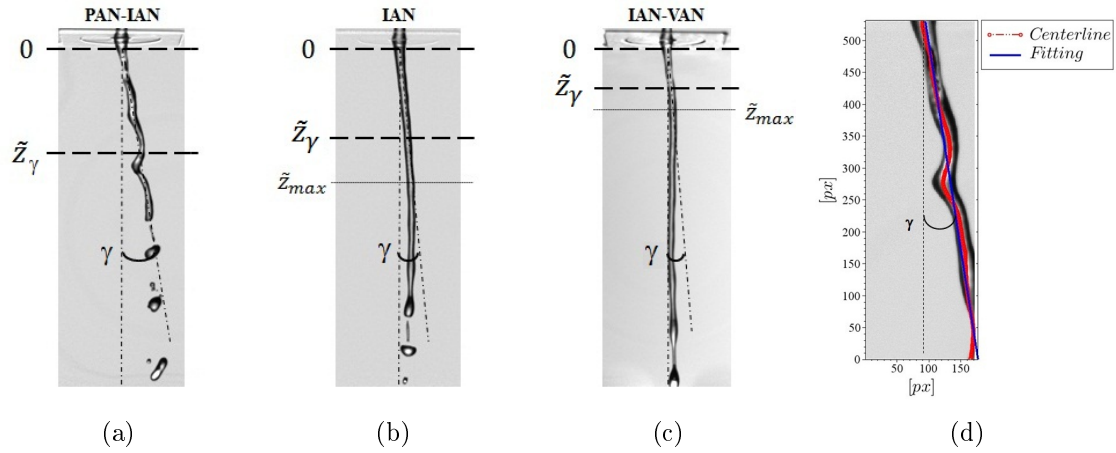


Figure 5.11: Jet deviation at (a) PAN-IAN; (b) IAN; (c) IAN-VAN and (d) example of deviation angle calculation.

### Deviation without flattening

At PAN-IAN a pure deviation is observed. The jet remains cylindrical and the deviation angle is constant through all the jet length (see Figure 5.11(a)). Figure 5.12 shows the evolution of  $\gamma$  for two cases which are indicated by the maximum acoustic levels reached at PAN during the plateau of the acoustic signal: test " $p_{a,pp} = 11870 Pa$ " and test " $p_{a,pp} = 6000 Pa$ ". In both cases,  $\gamma$  increases continuously throughout the ramp and reaches a constant value during the plateau of the acoustic signal. The maximum angle of deviation ( $10^\circ$ ) is observed for the maximum possible amplitude of the acoustic field, i.e.  $p_{a,pp} = 11870 Pa$  measured at PAN. We can conclude that since the flattening phenomenon is totally absent at this location, all the acoustic energy is used to deviate the jet.

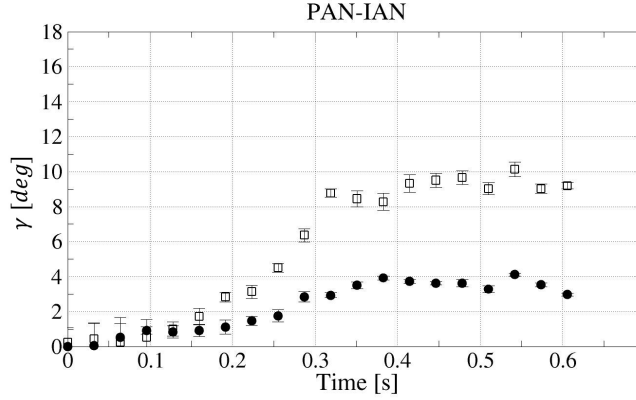


Figure 5.12: Experimental deviation angle for a jet ( $We_g = 9$ ,  $Re_l \approx 2000$ ) placed at PAN-IAN for:  $\square$ , test " $p_{a,pp} = 11870 Pa$ ";  $\bullet$ , test " $p_{a,pp} = 6000 Pa$ ".

### Deviation attenuated by flattening

At IAN and IAN-VAN, deviation and flattening appear simultaneously, and liquid sheet atomization occurs for acoustic levels  $p_{a,pp}$ , measured at PAN, higher than about 5500 Pa. At these locations, part of the acoustic energy is used to flatten the jet, and the liquid surface on which the radiation pressure acts is deformed. It is inferred that due to the liquid surface deformation, the jet response changes along the jet axis and the deviation is no longer uniform (see Figures 5.11(b) and 5.11(c)). The region of the jet close to the injection exit plane is more deviated than the rest of the jet, which remains parallel to the vertical axis. Thus, the jet assumes an arc shape and the point of jet maximum deviation is located at a distance  $\tilde{z}_{max}$  from the injection plane, this distance depending on the injection location. Figures 5.13- 5.14 shows the evolution of  $\gamma$  when the injector is placed at IAN and IAN-VAN. The star-markers represent the instant of atomization. When the amplitude of the acoustic field is not high enough to achieve a total jet flattening, such as  $p_{a,pp} = 3660 Pa$ , the evolution of  $\gamma$  is similar to that observed at PAN-IAN:  $\gamma$  increases continuously throughout the ramp and then reaches a plateau.

At IAN, for test " $p_{a,pp} = 11870 Pa$ ", measured at PAN,  $\gamma$  begins to increase up to  $t = 0.15 s$ . At this time, a transition is observed, during which the jet is also flattened and  $\gamma$  decreases. After the transition  $\gamma$  increases again. For test " $p_{a,pp} = 3660 Pa$ " a certain amount of jet flattening is still present. The transition is less noticeable than in the previous case, and the jet is not atomized. A similar behavior is observed at IAN-VAN (see Fig. 5.14). For test " $p_{a,pp} = 12180 Pa$ ", the transition is observed around  $t = 0.1 s$ , but the sheet is rapidly atomized after this time and  $\gamma$  can no longer be determined. For

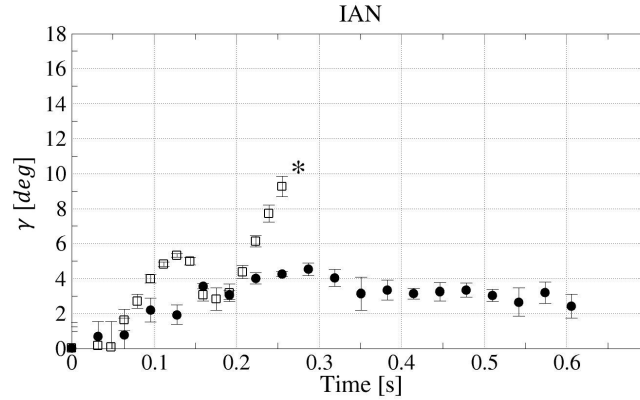


Figure 5.13: Experimental deviation angle for a jet ( $We_g = 9$ ,  $Re_l \approx 2000$ ) placed at IAN for:  $\square$ , test " $p_{a,pp} = 11870 Pa$ ";  $\bullet$ , test " $p_{a,pp} = 3660 Pa$ ".

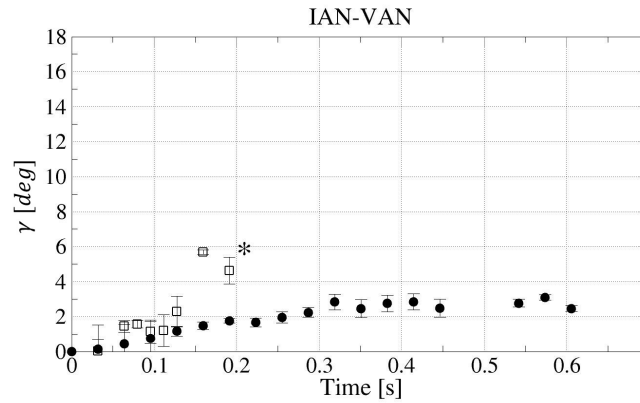


Figure 5.14: Experimental deviation angle for a jet ( $We_g = 9$ ,  $Re_l \approx 2000$ ) placed at IAN-VAN for:  $\square$ , test " $p_{a,pp} = 12180 Pa$ ";  $\bullet$ , test " $p_{a,pp} = 5015 Pa$ ".

test " $p_{a,pp} = 5015 Pa$ ", flattening is less evident. The angle  $\gamma$  constantly increases and reaches a constant value during the plateau of the acoustic signal.

### 5.2.3.2 High Weber Number Atomization Regimes

High Weber number atomization regimes ( $We_g \geq 100$ ) are characterized by a continuous liquid core with a short length and a dispersed phase. Acoustic effects are proved through the analysis of spray deviation which is quantified by comparing the droplet spatial distributions  $f(i)$  (defined by Eq.3.1) with and without acoustics. Figure 5.15 shows  $f(i)$  for the membrane ( $We_g = 100$ ) and the fiber ( $We_g = 220$ ) regimes at IAN and VAN. The dash-dotted lines represent fiber regime  $f(i)$  without acoustics, which is symmetric with respect to the injection axis,  $\tilde{y} = 0$ . A representative case for low Weber regimes with

acoustics (Rayleigh axi-symmetric regime at  $We_g = 20$ ) is also reported for comparison. At IAN all curves are shifted with respect to the case without acoustics indicating liquid accumulation on the right side of the image toward VAN. At VAN (Figure 5.15(e)) all curves are superimposed to the case without acoustics. This is in accordance with the fact that no deviation was observed at this location for low Weber number regimes.

Due to their particular shape the probability density functions can be fitted with a Gaussian function (see section 3.1). The mean value  $\mu_h$  is calculated by considering the droplet spatial distribution  $f(i)$  on the entire image height. Hereafter,  $\mu_h$  is reduced by the image width  $w_{im}$  and indicated as  $\tilde{\mu}_h$ . For each distribution  $\tilde{\mu}_h$  provides a quantification of the spray deviation. Figure 5.16 summarizes the  $f(i)$  mean values for the two cases presented in Figure 5.15 and for the three other locations investigated, IAN-VAN, PAN-IAN and PAN. As expected,  $\tilde{\mu}_h$  depends on the position of the injector along the acoustic axis: it is approximately 0 at PAN and VAN, and maximum at IAN and PAN-IAN, coherently with what observed for  $\gamma$ . It should be mentioned that, for the Rayleigh regime, no data are available at PAN and PAN-IAN since no induced atomization is observed at these particular positions.

The effect of the acoustic pressure level on the deviation of sprays located at IAN is reported in Figure 5.17(a). Three injection conditions are considered: one for membrane atomization regime at  $We_g = 104$ ,  $Re_l = 3900$  and two for fiber regimes at  $We_g = 262$ ,  $Re_l = 3900$  and  $We_g = 225$ ,  $Re_l = 2500$ . As expected, the higher the acoustic pressure level the greater the deviation  $\tilde{\mu}_h$ . When the acoustic pressure level is higher than about 3000-4000 Pa, the spray is deviated and  $\tilde{\mu}_h$  is found to increase non-linearly with the acoustic pressure, according to a quadratic or exponential growth ( $R_{quad}^2 = 0.959$ )<sup>b</sup>.

For amplitudes of the acoustic field lower than 3000-4000 Pa there is no significant deviation. The physical meaning of this pressure threshold can be understood by introducing the acoustic Froude number  $Fr_{ac}$ , defined as the square root of the ratio of the mean acoustic energy of a stationary wave per unit mass  $\varepsilon_{ac} = p_a^2 / (2\rho_g c^2)$  over the gravitational potential energy of the liquid system per unit mass  $\varepsilon_g = \rho_l g D_l$ , calculated on a displacement equal to the initial jet diameter  $D_l$ .

$$Fr_{ac} = \sqrt{\frac{\varepsilon_{ac}}{\rho_l g D_l}} \quad (5.2)$$

As can be seen in Figure 5.17(b) when the Froude number reaches a value of about 1 the spray is deviated, which means that the acoustic potential energy becomes high enough

---

<sup>b</sup>Discrimination between the two kinds of growth would necessitate data for larger pressure amplitudes or larger Froude numbers as seen in the following.

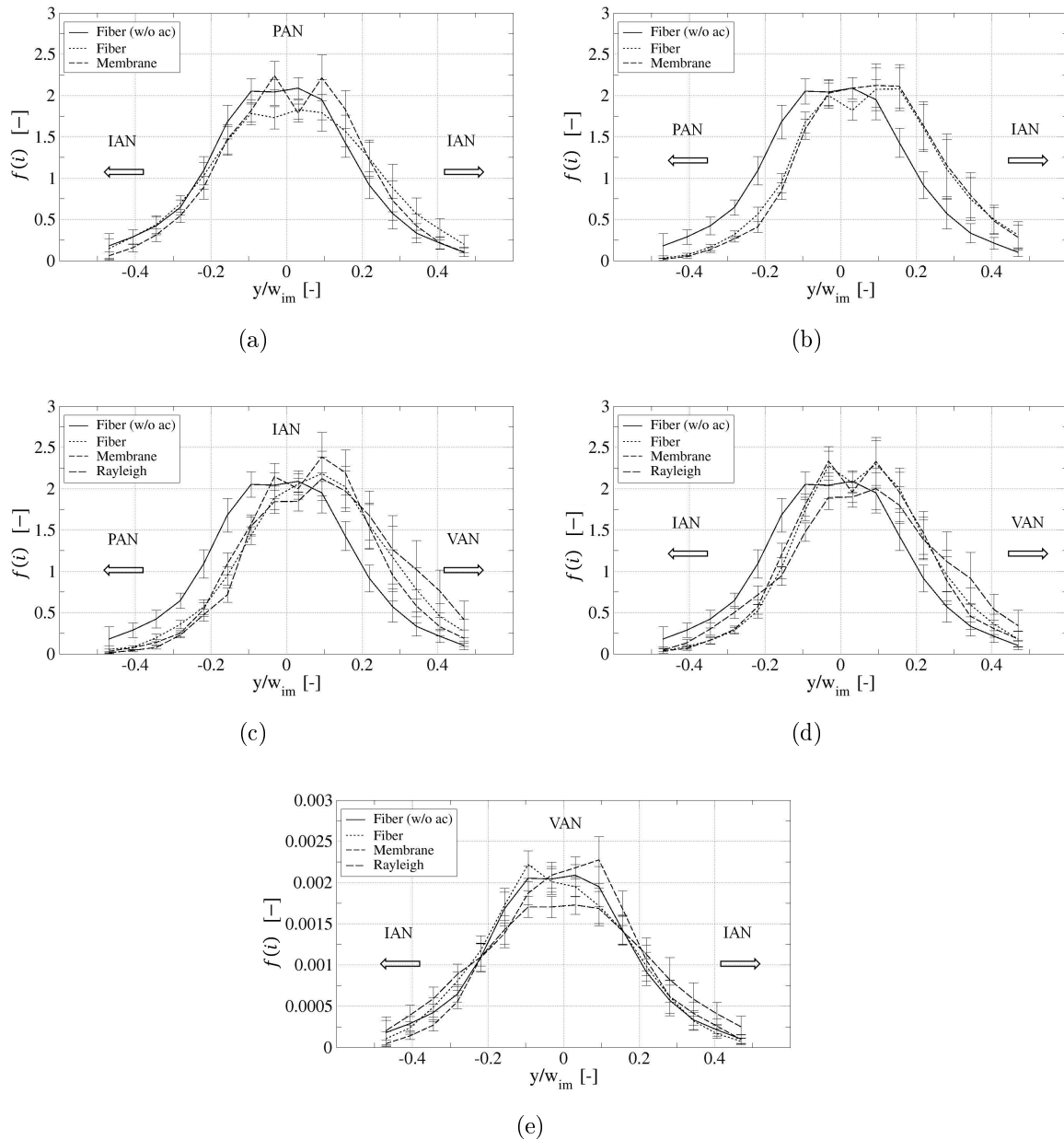


Figure 5.15: Droplet probability density function  $f(i)$  for fiber ( $\cdots$ ); membrane ( $- -$ ) and Rayleigh axi-symmetric ( $- \cdot -$ ) regimes with acoustics ( $p_{a,pp} \approx 12 \text{ kPa}$  at 1 kHz) compared with the fiber regime without acoustics ( $\text{—}$ ) at: (a) PAN; (b) PAN-IAN; (c) IAN; (d) IAN-VAN and (d) VAN.

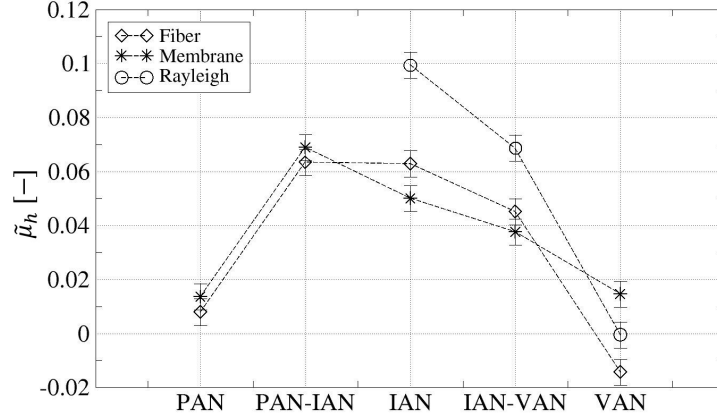


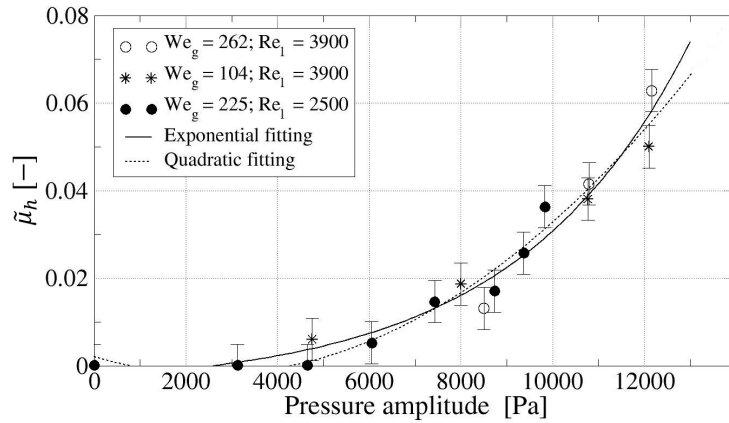
Figure 5.16: Gaussian fitting curve mean value  $\tilde{\mu}_h$  as function of the position along the acoustic axis for:  $\diamond$ , fiber;  $*$ , membrane and  $\circ$ , Rayleigh axi-symmetric regimes ( $p_{a,pp} \approx 12 \text{ kPa}$  at 1 kHz).

to counterbalance the gravitational energy.

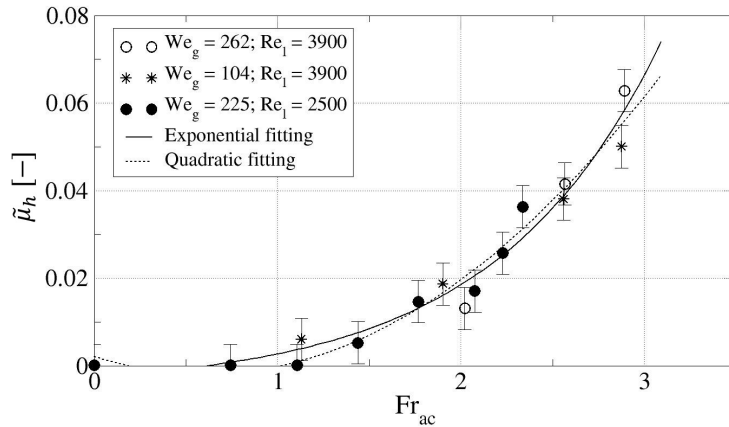
### 5.2.3.3 Deviation as a function of $\tilde{z}$

The whole spray in each image was considered for the calculation of  $\tilde{\mu}_h$  in Figure 5.16 and 5.17(a). To analyse the progress of the spray deviation along the vertical axis, images are subdivided in horizontal slices centered at different locations  $\tilde{z}$  where the local mean value  $\tilde{\mu}(\tilde{z})$  of the Gaussian function used to fit the droplet spatial distribution of each slice is determined. These results are reported in Figure 5.18(a) for the membrane regime and in Figure 5.18(b) for the fiber regime. Whatever the atomization regime, it is clear from these figures that when injection takes place at PAN and at VAN,  $\tilde{\mu}(\tilde{z})$  is almost constant indicating that no deviation occurs<sup>c</sup>. At PAN-IAN and IAN for both regimes and also at IAN-VAN for the fiber regime, the deviation of the spray increases progressively from the injection point toward the nearest VAN location. The maximum deviation determined on the whole spray image that is found to be  $\tilde{\mu}_m = 0.06$  for membrane and fiber regimes at IAN and PAN-IAN. The local maximum deviation is found to be as large as  $\tilde{\mu}(\tilde{z}) \approx 0.1 - 0.12$  at the bottom of the field of view, resulting from a roughly linear increase of the deviation along the vertical axis. For the particular case of the membrane regime at IAN-VAN (Figure 5.18(a)),  $\tilde{\mu}(\tilde{z})$  increases up to the middle of the image and then decreases to zero at the bottom of the field of view. As already observed

<sup>c</sup>In Figure 5.18(b)  $\tilde{\mu}(\tilde{z})$  for VAN measurements are slightly different from zero because there is a small shift between the injector axis and the VAN-axis of the acoustic field. The sign of  $\tilde{\mu}(\tilde{z})$  depends on the side of the shift with respect to the VAN-axis.



(a)



(b)

Figure 5.17: Spray deviation  $\tilde{\mu}_h$  as a function of: (a) acoustic pressure amplitude; (b) acoustic Froude number  $Fr_{ac}$ . Frequency of 1 kHz, injector placed at IAN (exponential fitting curve (—),  $R_{exp}^2 = 0.95954$ ; quadratic fitting curve ( $\cdots$ ),  $R_{quad}^2 = 0.95918$ ).

for the deviation of the cylindrical jet in Rayleigh regime (see section 5.2.3), it seems that spray deviation does not take place everywhere with the same efficiency. The membrane regime is characterized by the presence of large liquid blobs and ligaments that tend to be elongated into thin membranes that finally atomize themselves in very small droplets. At this very point, as observed for the Rayleigh regime, part of the acoustic energy is consumed in liquid blobs flattening, resulting in a less efficient deviation of the spray. This is supported by the strong enhancement of the atomization induced by nonlinear acoustic effect on the spray at this particular position for the membrane regime (see Table 5.2).

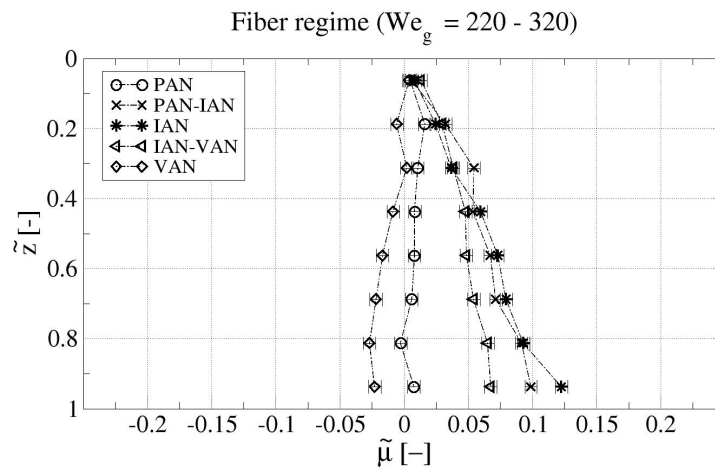
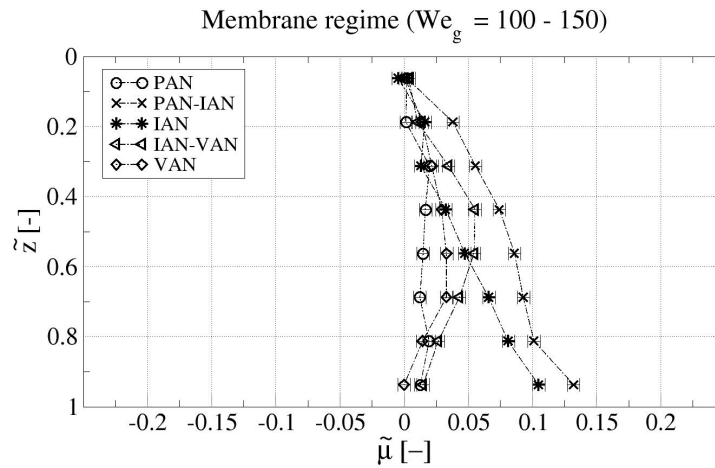


Figure 5.18: Gaussian mean value  $\tilde{\mu}(\tilde{z})$  for (a) membrane and (b) fiber regimes as function of the longitudinal axis at:  $\circ$  , PAN;  $\times$  , PAN-IAN;  $*$  , IAN;  $\triangleleft$  , IAN-VAN;  $\diamond$  , VAN ( $p_{a,pp} \approx 12 \text{ kPa}$  at 1 kHz).

## 5.3 Multi-point Injection Configuration

In a liquid rocket engine hundreds of injectors are used to feed the propellants into the combustion chamber in order to ensure a correctly proportioned mixture of fuel and oxidizer, and uniform mass flow and composition, insofar as possible. The combination of the effects highlighted in the previous sections has been experimentally investigated by placing three injectors in the acoustic cavity. When the injections take place simultaneously, a droplet clustering effect occurs, consecutively to the liquid jet atomization improvement and the deviation generated by the acoustic field. Results reported in this section were obtained from visualizations taken with view *A*. The spatial distributions here are calculated considering objects with a reduced diameter in the range 0.025 - 0.5. At first, injection at low Weber number ( $We_g = 9$ ) is considered, in order to identify crucial features which could be used to interpret response of multi-injection configuration at higher Weber numbers. Response of jets at a higher Weber number ( $We_g = 190$ ) follows.

### 5.3.1 Without Injection Domes

#### Low Weber regime response ( $We_g = 9$ , $Re_l = 2000$ )

In Figure 5.19 three different configurations are presented for three initially identical jets. Each configuration is accompanied by its respective droplet spatial distribution, calculated on the entire image. In Figure 5.19(a) the central jet is placed at PAN and the two lateral ones are both at IAN. The two latter jets are seen to be flattened, atomized and deviated toward the nearest velocity anti-node, while the central jet is unaffected. The deviation is also noted in the spatial distribution plot by the fact that the two distribution maxima are not aligned with the injection axes at IAN.

In the configuration presented in Figure 5.19(b) the injector positions are, from left to right respectively, PAN, IAN and VAN. Droplet spatial distribution indicates that this configuration presents a non symmetric response and droplet clustering is observed in the region around IAN and VAN while an absence of droplets is observed in the plane of the pressure anti-node.

In the last configuration, Figure 5.19(c) injections take place at IAN-VAN-IAN. This configuration exhibits a quasi-symmetric response, all jets are strongly affected by acoustics, and the two lateral ones are deviated toward the central VAN location. The small discrepancies between the right and left sides may results from an asymmetry of the acoustic field (see Figure 2.6(b)).

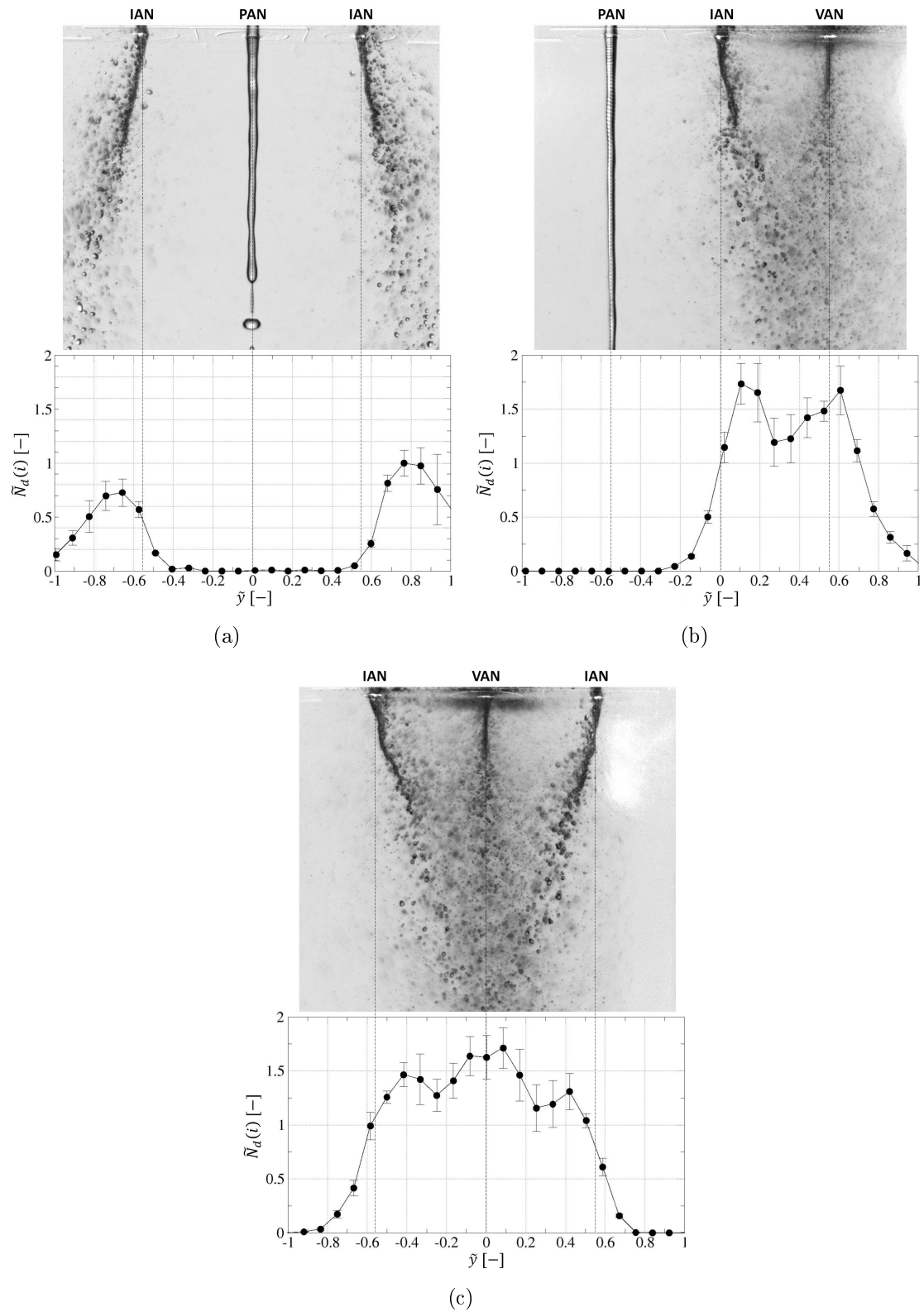


Figure 5.19: Multi-point injection visualization and droplet spatial distribution  $\hat{N}_d$  for low Weber regime at: (a) IAN-PAN-IAN; (b) PAN-IAN-VAN and (c) IAN-VAN-IAN.  $We_g = 9$  and  $Re_l = 2000$ ;  $p_{a,pp} \approx 12 \text{ kPa}$  at 1 kHz (view A).

The corresponding droplet spatial distribution reported presents a bell-shape with a maximum at  $\tilde{y} = 0$  and with practically no droplets along the IAN axes, confirming the clustering effect around VAN. The contribution to the droplet distribution in the vicinity of VAN results from the deviation of the two jets at IAN contrarily to the previous case, which comes from only one IAN-jet. These low Weber number tests allow to clearly visualize the modification of the atomization regime induced by acoustics and the clustering phenomenon. Finally experiments indicate that due to interaction between sprays submitted to such high-level transverse acoustic fields, the region around IAN and VAN is the one with the strongest modification in the atomization regime. In fact, tests with a single injector (see section 5.2) have shown that when the injector is placed at VAN a strong atomization regime improvement takes place and the smallest droplets tend to move away from the injection axis. Thus, they tend to occupy the region around VAN. When the injection takes place at IAN, the modification of the atomization regime is less intense but the droplets are deviated toward VAN. The combination of these two processes causes the present clustering phenomenon in the spatial region around IAN and VAN.

### High Weber regime response ( $We_g = 190$ , $Re_l = 2000$ )

In the light of what is observed at low Weber numbers it is possible to analyze the fiber atomization regime at  $We_g = 190$  and  $Re_l = 2000$ . The same three injection configurations, as reported in Figure 5.19, are considered in Figure 5.20. Each image is divided into 18 classes. The droplet spatial distribution  $\hat{N}_d$  corresponds here to the number of droplets calculated in each class, and reduced by the maximum in the reference case without acoustics (visualizations taken with view  $A$ ). The response is investigated by comparing droplet spatial distributions with acoustics  $\hat{N}_d^{ac}$  and without acoustics  $\hat{N}_d^0$  (see Figure 5.20). The global characteristic behavior observed at low Weber numbers is also found at high Weber numbers, except at PAN where there is no atomization with and without acoustics at low Weber number regimes. Thus, in the vicinity of IAN and VAN similar spatial distribution shapes are found. The droplet spatial distribution for the configuration IAN-PAN-IAN is presented in Figure 5.20(a). At extreme positions, i.e.  $|\tilde{y}| > 0.6$ ,  $\hat{N}_d^{ac}$  is above  $\hat{N}_d^0$  resulting from a deviation in the direction of the velocity antinodes. Moreover, as seen in section 5.2.2, acoustics induces an increase in the droplets number for jet in fiber regimes placed at IAN (Table 5.2 in section 5.2.2). This effect, combined with the interaction of the two lateral sprays with the central one justifies the small accumulation around PAN.

When injection takes place at PAN-IAN-VAN (see Figure 5.20(b)) a strong increment

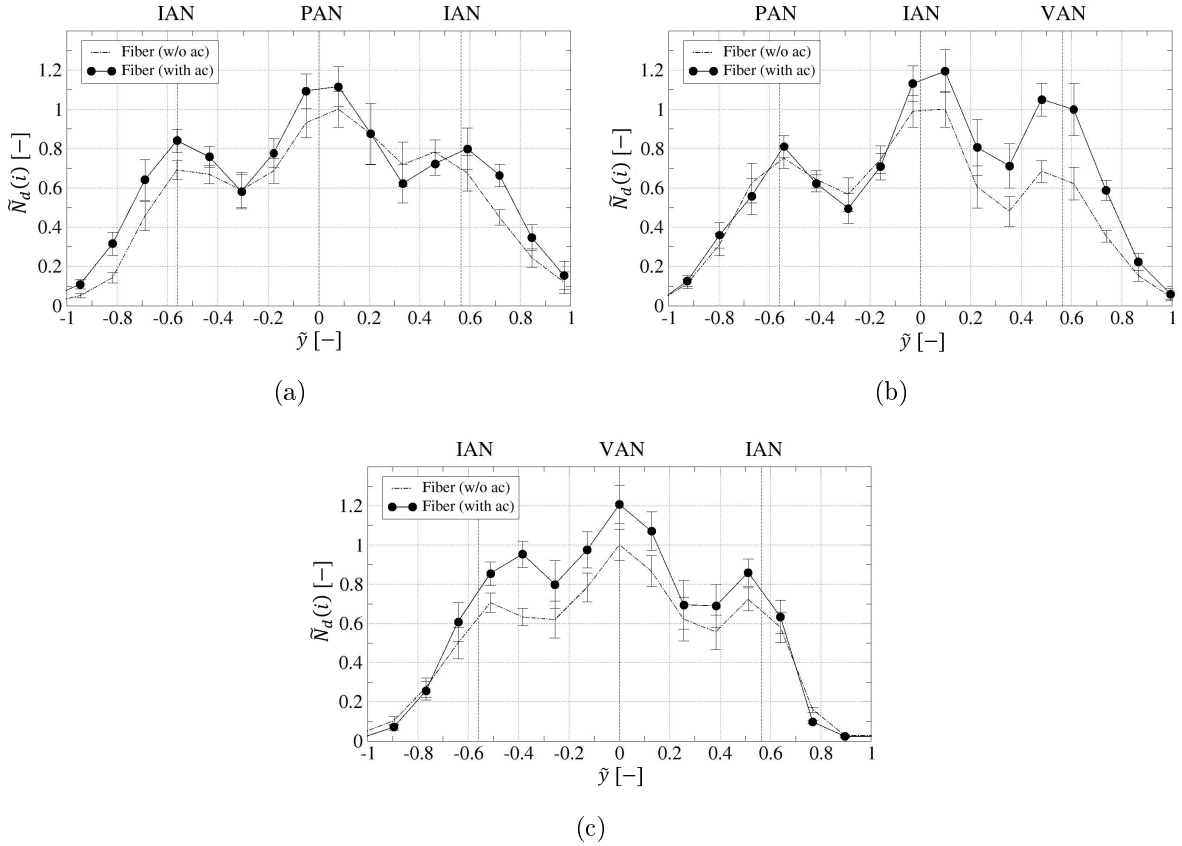


Figure 5.20: Droplet spatial distribution  $\hat{N}_d$  for the fiber atomization regime ( $We_g = 190$ ,  $Re_l = 2000$ ) in multi-point injection test at: (a) IAN-PAN-IAN; (b) PAN-IAN-VAN and (c) IAN-VAN-IAN. Dash-dotted line, no acoustics; ( $\bullet$ ),  $p_{a,pp} \approx 12 \text{ kPa}$  at 1 kHz (view A).

in the number of droplets is observed at IAN and VAN while the production ratio around PAN is almost one. The droplets spatial distribution induced by acoustics is strongly non-symmetric and a clustering in the region between IAN and VAN is measured.

When injection takes place at IAN-VAN-IAN (see Figure 5.20(c)) the two sprays at IAN are deviated toward the central position and a clustering in the region around VAN is quantified. The observed asymmetry, as mentioned above, can be ascribed to the asymmetry of the acoustic field.

Three-point injection tests provide a better insight on the droplet spatial distribution induced by a high amplitude acoustic field even for high Weber number regimes. Similarly to what quantified for the low Weber regimes, experiments confirm that jets in the neighborhood of IAN and VAN, are the most modified. To conclude, the clustering phenomenon results from the combination of deviation and atomization improvement phenomena.

### 5.3.2 With Injection Domes

In the previous section the three-point injection configuration has been discussed in order to highlight the clustering effect. The three injectors were independently fed, thus the response was induced purely by the acoustic induced in the main resonant cavity. However, in Chapter 4 it has been shown that under certain conditions the injection domes, especially the gas dome, can provide a very strong acoustic response. It is thus inferred that such acoustic levels inside the gas dome could provide flow fluctuations which in turns could modify the atomization process and affect the droplet spatial distribution. The maximum acoustic response of the gas dome was measured for  $GD0$  and  $d_{or} = 1.123$ : 800 Pa, 1700 Pa and 2000 Pa respectively for IAN-PAN-IAN, PAN-IAN-VAN and IAN-VAN-IAN (see section 4). These results have been obtained with a mass flow rate corresponding to  $We_g = 190$  (see  $m_{air}^{max}$  in section 4.2). The liquid dome acoustic measurements did not show an uniform trend (see section 4.3). However, the smallest dome size  $LD0$  with the junction  $L_j = 0.548$  with a diameter  $d_j = 1$ , seems to provide in general a strong response (see Figure 4.16 in section 4.3). Results presented in this section have been thus obtained with the following domes' parameters:  $GD0$ ;  $d_{or} = 1.123$  for the gas dome; and  $LD0$ ,  $L_j = 0.548$  and  $d_j = 1$  for the liquid dome.

In Figure 5.21 the non-dimensional droplet spatial distributions  $\hat{N}_d$  for the three-injector configuration without injection domes (—) are compared with those with injection domes (---). Distributions are scaled with the maximum of the distributions without injection domes. At IAN-PAN-IAN (see Figure 5.21(a)), where the gas dome presents the lower acoustic response, the two spatial distributions present similar shapes. At PAN-IAN-VAN (see Figure 5.21(b)) the asymmetry of the distributions with the domes is more marked than that without dome. With an intensification of the droplets clustering in the region between IAN and VAN. At IAN-VAN-IAN (see Figure 5.21(b)), where the gas dome presents the higher acoustic response, a decrease in the droplet counting around VAN is noted.

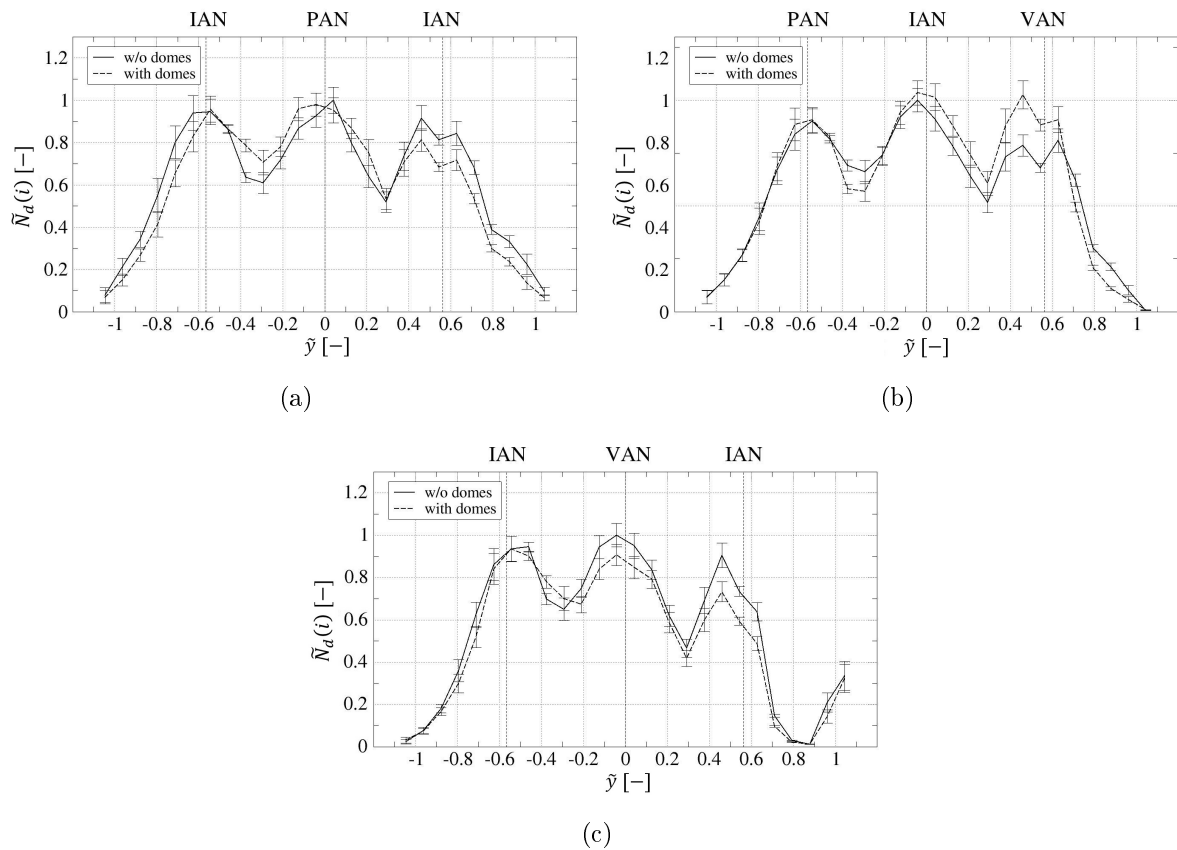


Figure 5.21: Droplet spatial distribution  $\hat{N}_d$  for the fiber atomization regime ( $We_g = 190$ ,  $Re_l = 2000$ ) in multi-point injection test at: (a) IAN-PAN-IAN; (b) PAN-IAN-VAN and (c) IAN-VAN-IAN; without injection domes (—) and with injection domes (---) ( $p_{a,pp} \approx 12$  kPa at 1 kHz;  $GD0$ ;  $d_{or} = 1.123$  for the gas dome; and  $LD0$ ,  $L_j = 0.548$  and  $d_j = 1$  for the liquid dome).

## 5.4 Implementation of Droplet Size and Gas Velocity Measurements Techniques

In the framework of the activities of the REST group a collaboration with the French national aerospace research establishment ONERA has been initiated in order to investigate both, experimentally and numerically, the effects of the acoustic field on the atomization process at injection conditions very close to those typical of liquid rocket engines. The injection conditions chosen are in the fiber regime at high Weber number ( $We_g > 400$ ) with  $Re_l = 6602$  and  $J = 5.1$ . They represent a compromise between the conditions that can be found in a real LRE combustion chamber and those that can be produced in our experimental test bench. The position in the acoustic field selected was IAN, in order to quantify the deviation phenomenon produced by the acoustic perturbation. Our objective is to provide experimental data which will be used to validate numerical simulations. Measurements required concerns spray deviation, droplet size distributions and gas velocity field. The deviation has been quantified by calculating the droplet spatial distribution from high-speed image post-processing. This technique, already used for lower Weber regimes (see Chapter 5), has been used to demonstrate that deviation takes place also in such a high Weber and Reynolds number regimes. The measurement of droplet size and gas velocity represented a challenge due to the experimental setup configuration. Droplet size quantification has been performed by image processing (see section 3.2). Images have been acquired using the experimental setup described in Figure 3.10 in section 3.2, in which two cameras (with a maximum frame rate of 10 Hz) are used simultaneously. The difficulties represented by the application of this technique was due to the number of images required and the protocol adopted to prevent loudspeaker damaging (see section 2.1). Gas field velocity measurements have been performed by Laser Doppler Velocimetry (LDV). The experimental configuration used is that described in section 3.3. The application of this technique in our experimental setup represented a true challenge. The first reason is due to the limited space in the experimental room in which the laser generation system, the probe and the 3-D displacement system had to be arranged. The second problem was the absence of an air extraction system in the acoustically isolated room. The third problem, as for the droplet size characterization, was represented by the protocol adopted to prevent loudspeaker damaging, each measured point corresponds to a single test. LDV preliminary measurements have been made for injection conditions at  $We_g = 190$ ,  $Re_l = 2000$ . The feasibility of these measurements techniques applied to our experimental setup has been demonstrated, and serves as a starting point for future

investigations.

#### 5.4.1 Quantification of Deviation for: $We_g > 400$ , $Re_l = 6602$ , $J = 5.1$ .

High-speed visualizations have been performed at IAN for the following injection conditions:  $We_g > 400$ ,  $Re_l = 6602$  and  $J = 5.1$ . The spray obtained at such injection conditions without acoustics is represented in the left side of Figure 5.22 while the jet submitted to the maximum sollicitation ( $p_{a,pp} \approx 12 \text{ kPa}$  at 1 kHz) of the acoustic field is presented on the right side. A modification of the atomization regime can be observed from the raw images.

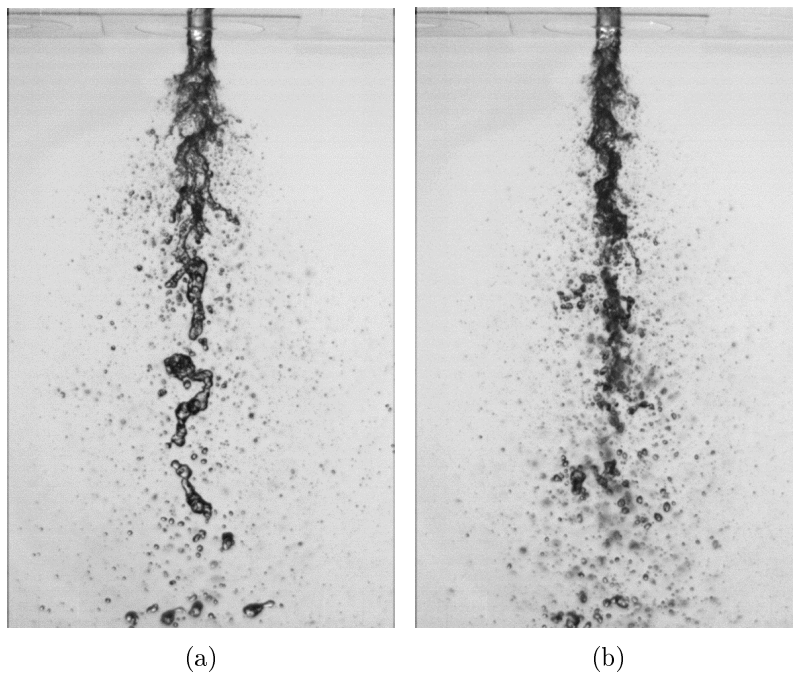


Figure 5.22: Snapshots of the spray (a) without acoustics and (b) during maximum acoustics at IAN ( $We_g > 400$ ,  $Re_l = 6602$ ,  $J = 5.1$ ,  $p_{a,pp} \approx 12 \text{ kPa}$  at 1 kHz).

In order to quantify the deviation of the jet the droplet spatial distribution has been calculated following the same procedure already adopted in section 5.2.3.2.

Image post-processing has been performed on the entire image width and length, considering a sequence of 200 frames. Objects with a reduced diameter in the range 0.003 - 0.3 have been considered (object diameters are reduced by  $D_l$ ). A morphological criterion on the droplet sphericity  $Sp \leq 0.4$  is used. In Figure 5.23 the droplet spatial distribution with acoustics is compared with that of the spray without acoustic perturbation. The

droplet spatial distribution without acoustics is non-symmetric. This can be ascribed to a non-perfect centering of the liquid post with respect to the injection axis, which is noticeable only at very high values of the Weber number. The asymmetry is also present

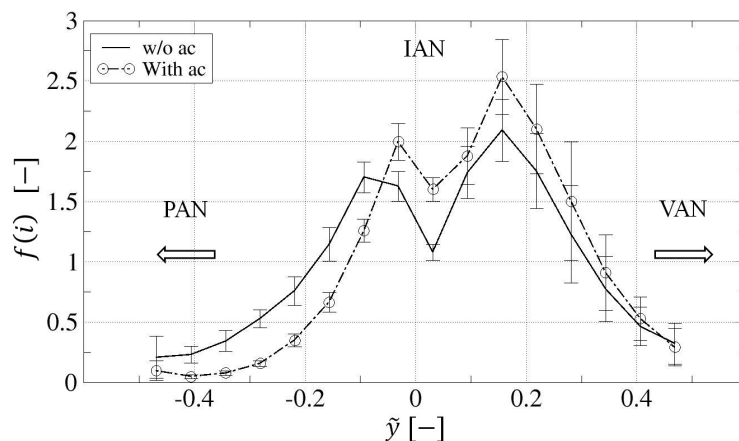


Figure 5.23: Droplet spatial distribution  $f(i)$  for the ONERA test case without acoustics (—) and with acoustics at IAN (—○—) ( $We_g > 400$ ,  $Re_l = 6602$ ,  $J = 5.1$ ,  $p_{a,pp} \approx 12 \text{ kPa}$  at 1 kHz).

in the case with acoustics in which deviation is moreover observed. Deviation is detected in the direction towards the velocity anti-node (right side of the figure) and its strength decreases from left to right. On the left side, i.e. in between PAN and IAN, the two curves are clearly separated due to the deviation which is strong enough to move the droplets toward VAN located on the right side of the image. On the contrary, on the right side, i.e. in between IAN and VAN, the deviation is less intense (see section 5.2.3) and the difference between the two curves is less marked. This result confirms what has been already observed at lower Weber numbers.

As discussed in section 5.2.3.2 the deviation is not constant all along the jet axis. Thus, in order to better characterize the spray deviation images are subdivided into horizontal slices along the vertical axis  $\tilde{z}$ . Results are reported in Figure 5.24. Two classes of objects are considered in order to identify possible differences in the response due to the object diameters:  $0.003 < D_{obj}/D_l < 0.03$  for small objects;  $0.03 < D_{obj}/D_l < 0.3$  for big objects (with  $\phi_d = D_{obj}/D_l$  being the reduced equivalent spherical diameter). The deviation for the entire population ( $0.003 < \phi_d < 0.3$ ) is also reported in the plot. They are compared with the reference case without acoustic for objects with a diameter in the range  $0.003 < \phi_d < 0.3$ . The three distributions with acoustics present similar behaviors and are superimposed; deviation increases linearly from the injector exit plane

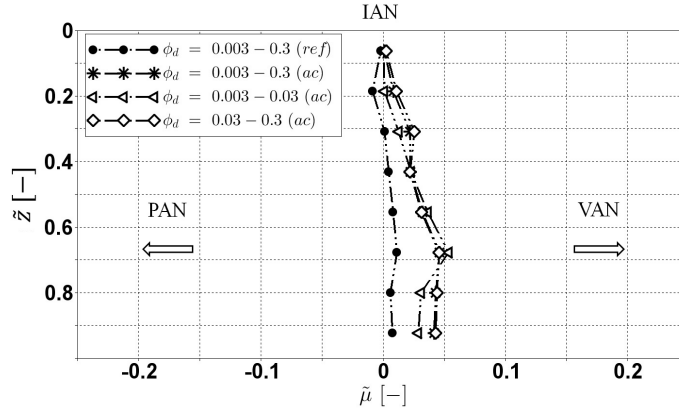


Figure 5.24: Gaussian mean value  $\tilde{\mu}(\tilde{z})$  as a function of  $\tilde{z}$  for: (—)  $\phi_d = 0.003 - 0.3$  (reference values without acoustics); (x)  $\phi_d = 0.003 - 0.3$  (ac); ( $\triangleleft$ )  $\phi_d = 0.003 - 0.03$  (ac) and ( $\diamond$ )  $\phi_d = 0.03 - 0.3$  (ac) ( $We_g > 400$ ,  $Re_l = 6602$ ,  $J = 5.1$ ,  $p_{a,pp} \approx 12$  kPa at 1 kHz).

until  $\tilde{z} = 0.7$ , where it reaches a maximum of roughly  $0.5D_l$ . For  $\tilde{z} > 0.7$  the deviation remains constant.

## 5.4.2 Droplet Size Characterization

Images shown in Figure 5.22 suggest a modification of the atomization regime induced by the acoustic field. Droplet size measurements have been performed in order to investigate modification induced by the acoustic field at IAN for  $We_g > 400$ ,  $Re_l = 6602$  and  $J = 5.1$ . The experimental setup is that described in section 3.2. Two cameras with a maximum frame rate of 10 Hz have been used simultaneously as shown in Figure 5.4.2 in order to reduce the number of tests, and to prevent loudspeaker damaging. A total of 120 images has been acquired during the acoustic solicitation following the procedure explained in section 3.2 (see Figure 3.13). The size of the measurement window is  $1.8D_l \times 1.5D_l$  (resolution: 2448 x 2050 pixels). The coordinates of the center of the measurements window are:  $\tilde{x} = 0$ ,  $\tilde{y} = 0.28D_l$ ;  $\tilde{z} = 15D_l$ . In Figure 5.25 the measurement window position is shown on an image from the high-speed series. This measurement position has been chosen as result of a compromise between numerical calculation needs, and experimental measurement feasibility. It is sufficiently distant from the injection plane to have a sufficient number of objects; and not too close to the liquid core in order to prevent ligaments or blobs to be captured by the images. Objects considered in the post-processing are in the reduced diameter range  $3.33 \cdot 10^{-4} < D_{obj}/D_l < 8.33 \cdot 10^{-2}$  with a sphericity criterion of  $S_p \leq 0.4$ .

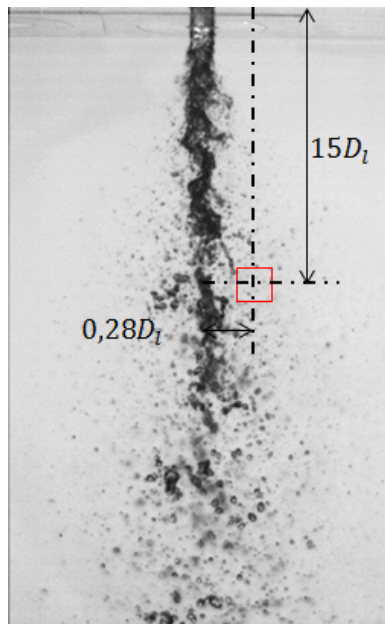


Figure 5.25: Representation of the droplet size measurement window location ( $\tilde{x} = 0$ ,  $\tilde{y} = 0.28D_l$ ;  $\tilde{z} = 15D_l$ ) on an image from the high-speed series (measurement window size:  $1.8D_l \times 1.5D_l$ ).

### Quantification of deviation

The droplet spatial distribution has been calculated on the entire measurement window, in the same way as droplet spatial distributions have been calculated from high-speed visualization images (see section 3.1). Results are shown in Figure 5.26. Without acoustics the droplet spatial distribution is quasi-constant indicating a homogeneous distribution along  $\tilde{y}$  in the measurement window. With acoustics a strong asymmetry in the droplet distribution is observed indicating that the deviation, which has been clearly observed on large scale (see Figure 5.23), is also noticeable at reduced scale. The effects of the deviation are also noticeable in the average number of objects detected per images, which is increase of about 15% with acoustics.

### Droplet size quantification

The same series of images that has been used in the previous section, for the quantification of the deviation, have been used to quantify the droplet size distribution. The numerical distribution  $f_{num}$  has been calculated as follows. Let consider the range of diameters in between the maximum and minimum diameters detected from the images. This range can be divided into  $n$  classes, and for each classes the median diameter  $D_{med}$  can be calculated as the diameter corresponding to half of the distribution in the interval  $n$ . The numerical

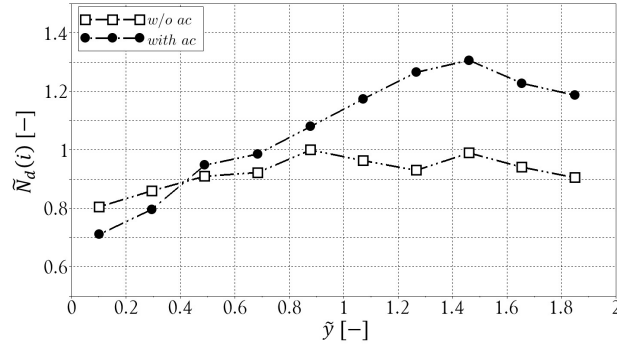


Figure 5.26: Droplet spatial distribution ( $\square$ ) without acoustics and ( $\bullet$ ) with acoustics ( $We_g > 400$ ,  $Re_l = 6602$ ,  $J = 5.1$ ,  $p_{a,pp} \approx 12 \text{ kPa}$  at 1 kHz).

distribution  $f_{num}$  indicates the probability to find objects in a certain diameter interval. The integral of the numerical distribution is equal to 1. The numerical distributions calculated without acoustics and with acoustics are compared in Figure 5.27 as functions of  $D_{med}/D_l$ . They are scaled with the maximum of the numerical distribution without acoustics. The two curves do not present noticeable differences. Moreover, characteristic

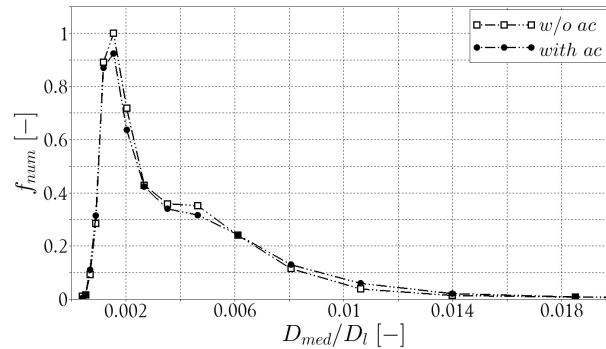


Figure 5.27: Droplet size distribution ( $\square$ ) without acoustics and ( $\bullet$ ) with acoustics ( $We_g > 400$ ,  $Re_l = 6602$ ,  $J = 5.1$ ,  $p_{a,pp} \approx 12 \text{ kPa}$  at 1 kHz).

spray diameters present percentage differences of the same order of magnitude of the technique incertitude ( $< 8\%$ ). Thus, even if a clear translation of the population, due to the deviation has been quantified, no variation of the spray population is observed (in the range of diameters considered). From the statistical point of view, a larger number of images would be necessary to quantify modification of the spray population. In particular for what concerns large droplet diameters, that mainly contribute to the liquid mass distribution in the spray.

### 5.4.3 Gas Velocity Field Characterization by LDV

In this section the local gas velocity field is analyzed by means of the Laser Doppler Velocimetry technique (see section 3.3) in order to highlight modifications induced by the acoustic field. A specific injection condition at high Weber number is considered,  $We_g = 190$   $Re_l = 2000$  at IAN and VAN at the maximum acoustic pressure fluctuations available,  $\approx 12kPa$  peak-to-peak at 1000 Hz. The objective is to demonstrate the feasibility of LDV measurements in our experimental configuration for future applications to injections conditions more representative of those typical of LRE combustion chambers ( $We_g > 400$ ,  $Re_l = 6602$ ,  $J = 5.1$ ).

Both radial and vertical velocities were measured simultaneously without and with acoustics for comparison. The positions considered are the velocity and intensity anti-nodes. Figure 5.28 represents a schematic showing the sign of the reference chosen to specify the velocity vector, and the local reference system.

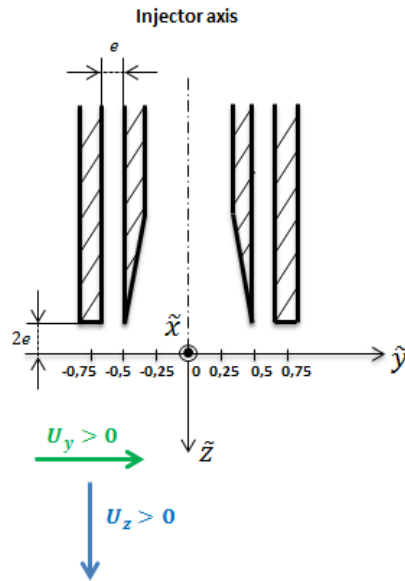


Figure 5.28: Local reference system for Laser Doppler Velocimetry measurements.

The radial velocity is indicated as  $U_y$  while the Vertical velocity is  $U_z$ . The modulus of the velocities is reduced with the gas bulk velocity  $U_{g,bulk}$ :  $\tilde{U}_y = U_y/U_{g,bulk}$  and  $\tilde{U}_z = U_z/U_{g,bulk}$ . Only dimensionless velocities will be provided hereafter. The injector axis corresponds to  $\tilde{y} = 0$ ,  $\tilde{x} = 0$ . Here, coordinate are reduced with liquid post diameter  $D_l$ :  $\tilde{x} = x/D_l$ ,  $\tilde{y} = y/D_l$  and  $\tilde{z} = z/D_l$ . Measurements have been made at a distance from the injector exit plane equal to  $2e$  (where  $e$  is the width of the gas annular gap). Seeding particles of DEHS are injected with the gas flow. For  $\tilde{y} < -0.6$  and  $\tilde{y} > 0.6$  seeding

particles detection rate is close to 0 thus the region of interest is restricted between these two values. Moreover, when the liquid flow is injected, velocity is not measured between  $\tilde{y} = -0.47$  and  $\tilde{y} = 0.47$  in order to prevent damage of the photo multiplier through over-excitation. Measurements reported have been obtained with a detection rate in between 10000 and 18000 particles per second.

### 5.4.3.1 Without Acoustics

#### Without water

First, the gas flow field without liquid injection and without acoustic has been measured. Figures 5.29(b)-5.29(a) show the mean values of the radial and vertical velocities in the horizontal plane  $\tilde{x} - \tilde{y}$  (perpendicular to the direction of the flow), at a distance equal to  $2e$  downstream the injection plane. In Figures 5.29(d)-5.29(c) the mean values of the radial and vertical velocities in the vertical plane  $\tilde{y} - \tilde{z}$  are reported (parallel to the direction of the flow).

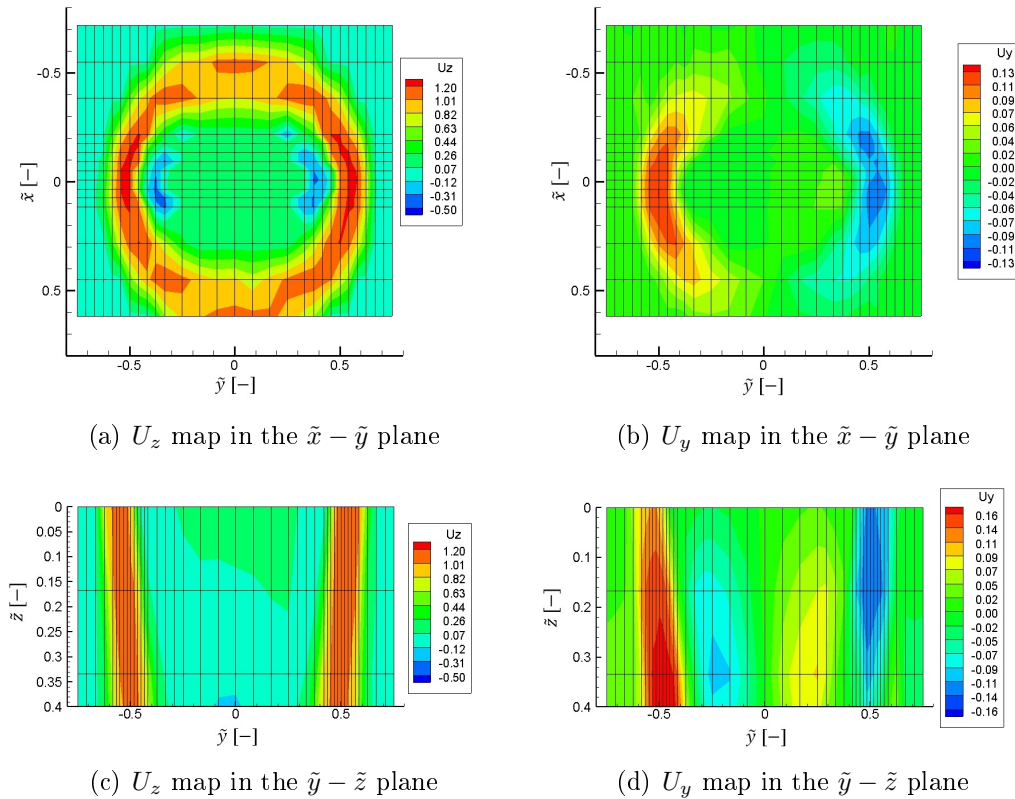


Figure 5.29: Gas velocity characterization in the (a-b)  $\tilde{y} - \tilde{z}$  and (c-d)  $\tilde{x} - \tilde{y}$  planes for  $We_g = 190$  and  $Re_l = 0$  (Without acoustics).

These measurements served also to verify the position of the measurement volume with respect to the injector axis. The grids shown in these plots represent the meshes used for the measurements. The colormaps have been obtained by interpolating the mean velocity values measured in the mesh. Figure 5.30 presents three examples of vertical and radial velocity mean profiles for  $\tilde{x} = -0.04$ ,  $\tilde{x} = 0$  and  $\tilde{x} = 0.04$ , as functions  $\tilde{y}$  axis ( $\tilde{x} = 0$ ;  $\tilde{z} = 2e$ ). Velocity profiles are those typical of annular jets. Both radial and vertical velocity fields show a good axial symmetry<sup>d</sup>. The radial velocities measured around  $\tilde{y} = 0$  are null which indicates that tangential velocity is negligible. The sign of the radial velocities indicates that the co-flow tends to converge toward the injection axis. The vertical velocity field illustrated in Figures 5.29(a)-5.30(a) shows two negative velocity regions in the center zone. They indicate the presence of a recirculation zone, which is due to the absence of the central liquid jet.

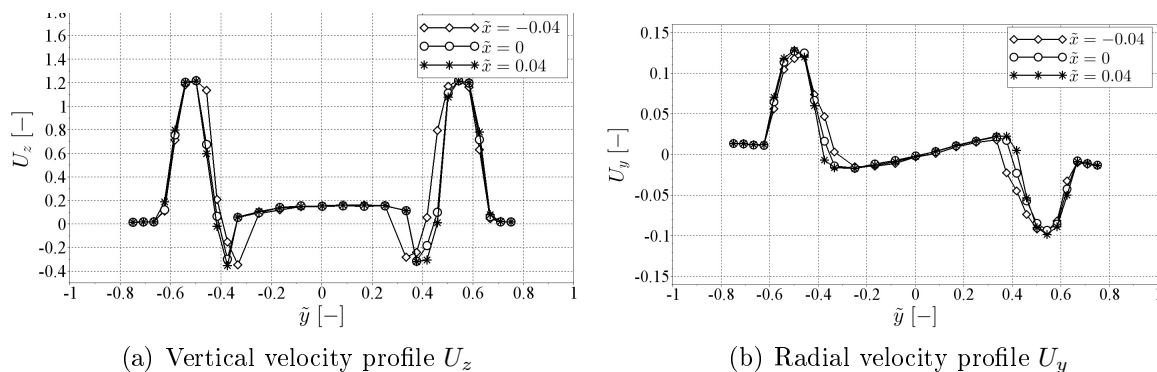


Figure 5.30: Mean values of the (a) radial velocity and (b) vertical velocity profiles for:  $\tilde{x} = -0.04$ ;  $\tilde{x} = 0$ ;  $\tilde{x} = 0.04$  ( $We_g = 190$ ,  $Re_l = 0$  without acoustics).

### With water

Figure 5.31 shows the mean values of the vertical and radial velocities measured with a central liquid jet at  $Re_l = 2000$  as functions of  $\tilde{y}$  ( $\tilde{x} = 0$ ;  $\tilde{z} = 2e$ ). Mean profiles measured without the central jet are also reported for comparison. Velocities profiles present the typical shapes of annular jets. The presence of the central jet reduces the tendency of the gas flow to converge toward the injection axis, leading to a reduction of the radial velocities in the central part of the coaxial flow (in between  $|0.6| < \tilde{y} < |0.5|$ ). The vertical velocities are less affected by the presence of the central liquid jet. Figure 5.32 shows an example of the time series for the vertical (blue) and radial (green) velocity data recorded at  $\tilde{y} = -0.6$  ( $\tilde{x} = 0$ ;  $\tilde{z} = 2e$ ). A well-defined periodicity can be observed in both signals

<sup>d</sup>In order to avoid swirled flow a grid has been put inside the injector.

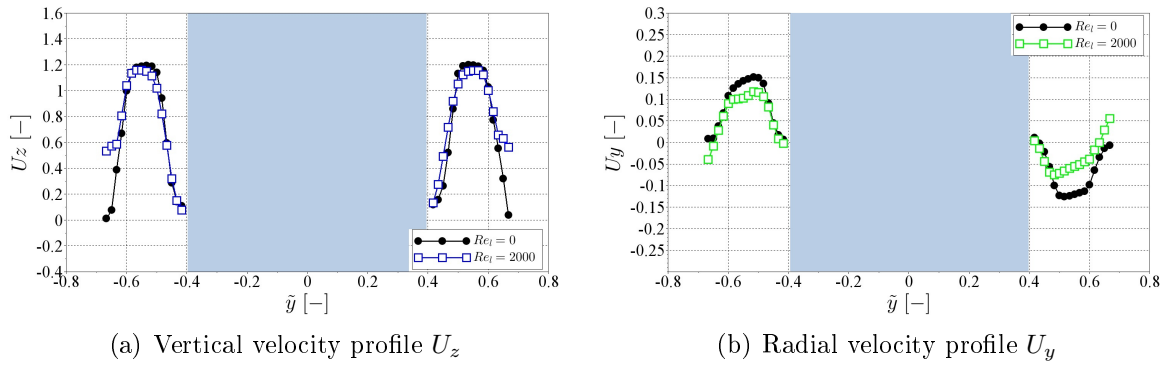


Figure 5.31: Comparison with and without (black) central liquid jet of the mean values of the vertical (blue) and radial (green) velocities as functions of  $\tilde{y}$  ( $\tilde{x} = 0$ ;  $\tilde{z} = 2e$ ).

(a close-up view of the two signals in between  $t = 0.2$  s and  $t = 0.25$  s is shown on the right sides of the images).

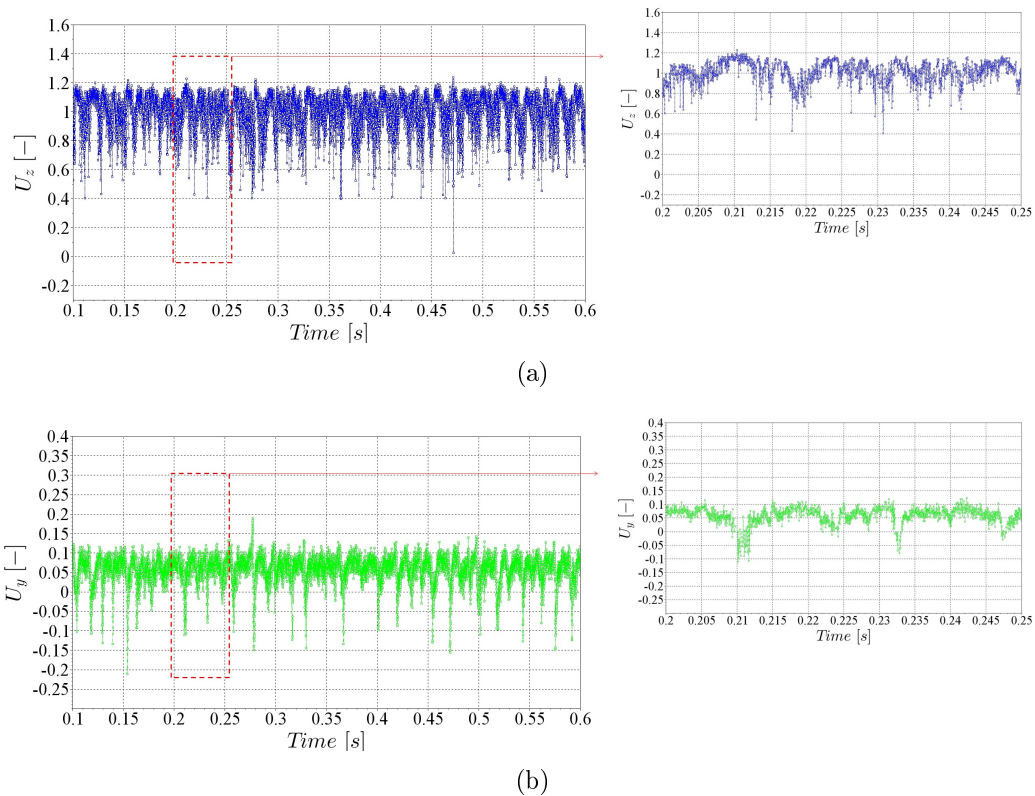


Figure 5.32: Examples of raw data signals for vertical (a) and radial (b) velocities without acoustics ( $\tilde{x} = 0$ ;  $\tilde{y} = -0.6$ ;  $\tilde{z} = 2e$ ;  $We_g = 190$ ,  $Re_t = 2000$ ).

### Power spectral density plots

The power spectral density plots<sup>e</sup> of the time series for  $U_z$  and  $U_y$  velocities are respectively shown in Figures 5.33 and 5.34 for six different locations along the  $\tilde{y}$ -axis:  $\tilde{y} \pm 0.6$ ;  $\pm 0.53$ ;  $\pm 0.47$ . PSD values are reduced with the maximum value of the PSD calcu-

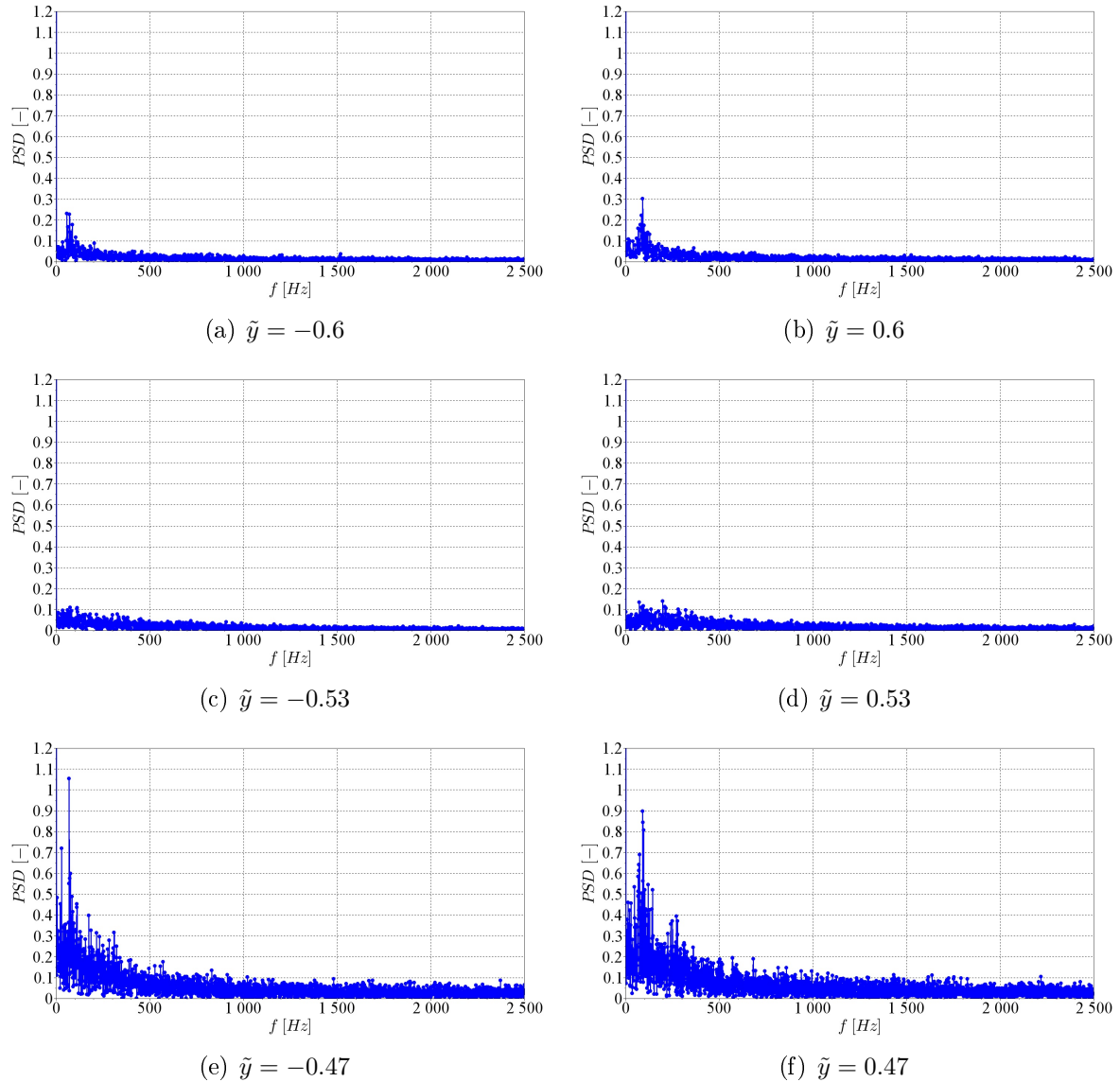


Figure 5.33: PSD of re-sampled signals for vertical velocities without acoustics ( $\tilde{x} = 0$ ;  $\tilde{z} = 2e$ ;  $We_g = 190$ ,  $Re_l = 2000$ ).

lated on  $U_z$ . A characteristic frequency around 90 Hz is observed in the PSD plots of  $U_z$  (see Figures 5.33). The intensity of the PSD associated to this frequency is highest near the liquid/gas interface ( $\tilde{y} = |0.47|$ ). By using the expression  $fp = Uc/40\delta$  proposed by

<sup>e</sup>Since sampling rate is not constant, but due to the particles detection, the raw signals are re-sampled in order to calculate the Fast Fourier Transform and the PSD.

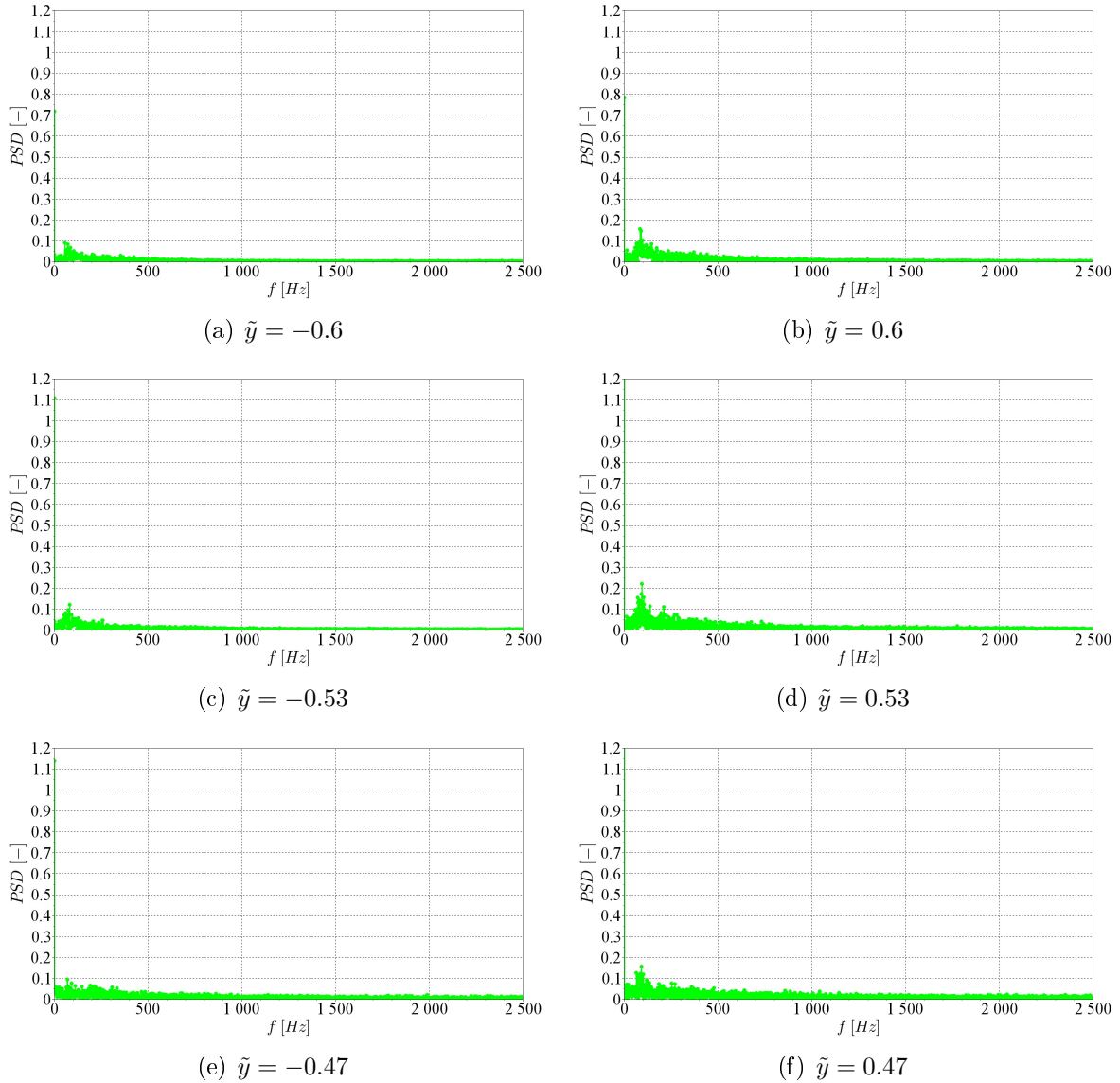


Figure 5.34: PSD of re-sampled signals for radial velocities without acoustics ( $\tilde{x} = 0$ ;  $\tilde{z} = 2e$ ;  $We_g = 190$ ,  $Re_l = 2000$ ).

Marmottant [112] for the frequency of instabilities at the liquid/gas interface, we obtain  $fp \approx 82 \text{ Hz}$  which is of the same order of magnitude of the experimental values. Here  $U_c = U_g(1 - J^{-0.1}) / (1 + \sqrt{\rho_l / \rho_g})$  [89, 112] is the convection velocity, and  $\delta = 0.077D_l$  is the momentum thickness calculated from the vertical velocity profile. This suggests that this frequency may be due to instabilities arising at the liquid/gas interface, which propagate through the gas annular thickness with decreasing intensity, and affect also  $U_y$ . Indeed, the same characteristic frequency is observed in the PSD plots of the radial velocity (see Figures 5.34). The intensity of the PSD peak on  $U_y$  is similar at each coordinate  $\tilde{y}$ , and it is much lower than that calculated for  $U_z$ .

### 5.4.3.2 With Acoustics

In order to investigate the influence of the acoustic field on the gas radial and vertical velocities, LDV measurements have been done on jets at VAN and IAN for the maximum peak-to-peak amplitude of the acoustic pressure measured at PAN, 12000 Pa at 1000 Hz. Measurements have been performed on each side of the coaxial flow focusing on the spatial region where the quantity of seeding particles is larger and thus signal quality is higher ( $\tilde{x} = 0$ ,  $|0.47| < \tilde{y} < |0.6|$ ,  $\tilde{z} = 2e$ ). Injection conditions chosen to verify the feasibility of the LDV measurements in our experimental setup with acoustics are  $We_g = 190$ ,  $Re_l = 2000$ .

#### Injection at VAN

The mean values of the vertical ( $U_z$ ) and radial ( $U_y$ ) velocities measured with acoustics ( $p_{a,pp} = 12000$  Pa peak-to-peak, 1000 Hz) at VAN are compared, in Figure 5.35, with those obtained without acoustics. Their relative RMS values ( $U_{z,rms}$  and  $U_{y,rms}$ ) are also reported in the figure as empty square markers. For what concerns the vertical velocity,

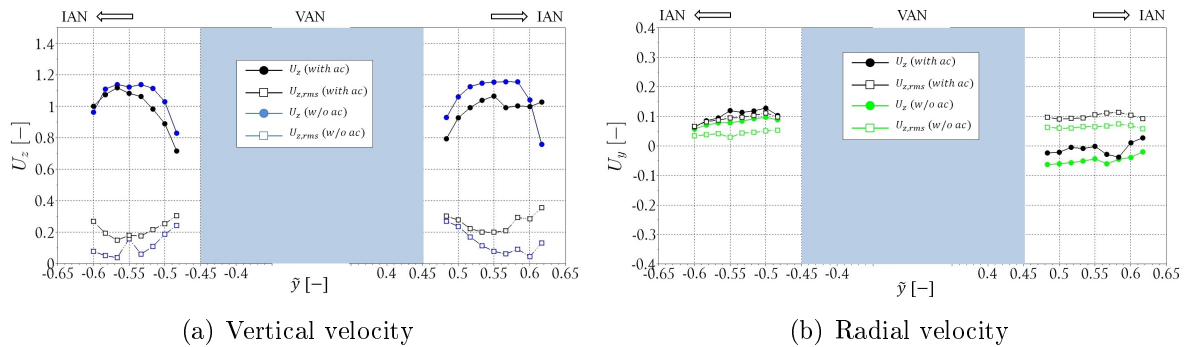


Figure 5.35: Comparison at VAN between mean and RMS values of (a) vertical and (b) radial velocities with and without acoustics as functions of  $\tilde{y}$  ( $\tilde{x} = 0$ ;  $\tilde{z} = 2e$ ;  $We_g = 190$ ,  $Re_l = 2000$ ; with acoustics:  $p_{a,pp} = 12$  kPa,  $f = 1$  kHz).

mean profiles with acoustics are similar to those obtained without acoustics. A reduction of the vertical velocity is noted in the region closer to the injector axis. This modification is symmetrical with respect to the injection axis. The rms values are higher with acoustics. Without acoustics  $U_{z,rms}$  increases from  $\tilde{y} = |0.6|$  to  $\tilde{y} = |0.47|$ . With acoustics the  $U_{z,rms}$  profiles present a minimum in the central part of the gas flow (around  $\tilde{y} = |0.55|$ ) and increases toward the two interfaces gas/gas and liquid/gas. The increase of the rms values at the gas/gas interface is due to the fluctuations imposed by the acoustic field. Radial velocities in between  $|0.47| < \tilde{y} < |0.6|$  present quasi-constant profiles with and without

acoustics, and  $U_y \approx 0$  with acoustics for  $0.47 < \tilde{y} < 0.6$ . Similar profiles were also observed by Lespinasse [95] in the analysis of a premixed flame submitted to acoustics<sup>f</sup>. Rms values of the radial velocity increases with acoustics, attaining roughly one third of the theoretical acoustic velocity amplitude.

### Raw data acquisition signals

Figure 5.36 shows an example time series for the vertical and radial velocity data acquisition signals at VAN ( $We_g = 190$ ,  $Re_l = 2000$ ). Measurements reported in this example have been performed close to the gas/gas interface at  $\tilde{x} = 0$ ,  $\tilde{y} = -0.6$  and  $\tilde{z} = 2e$ . The typical envelop of the acoustic signal (see Figure 2.3) sent to the loudspeakers can be observed. The velocity fluctuations oscillate around their mean values, proportionally to the instantaneous amplitude of the acoustic field. The effect is stronger on the vertical velocity. Close up views (in between  $t = 0.31$  s and  $t = 0.32$  s) of the two signals show fluctuations with the same period as that of the forcing frequency (1000 Hz).

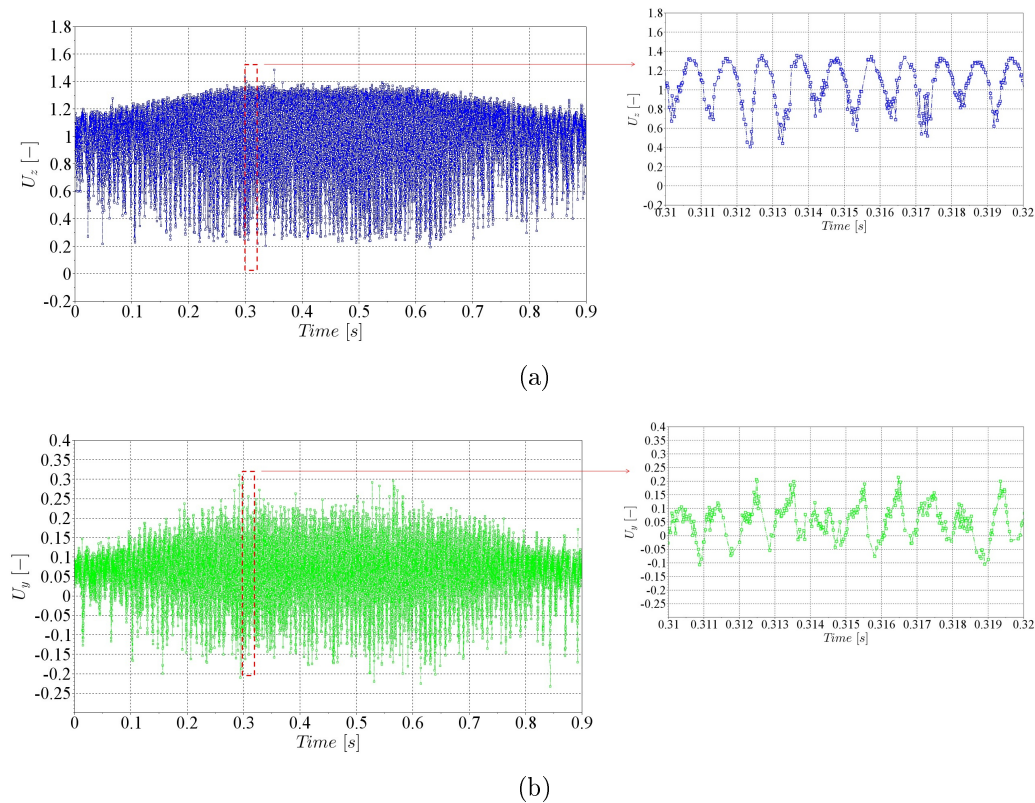


Figure 5.36: Examples of raw data signals for vertical (a) and radial (b) velocities with acoustics at VAN ( $\tilde{x} = 0$ ;  $\tilde{y} = -0.6$ ;  $\tilde{z} = 2e$ ;  $We_g = 190$ ,  $Re_l = 2000$ ;  $p_{a,pp} = 12$  kPa,  $f = 1$  kHz).

<sup>f</sup>Velocity profiles were obtained with Particle Image Velocimetry (PIV) technique. In that case, the entire environment was seeded for the measurements.

### Power spectral density plots

PSD plots of the signals presented in Figure 5.36 are reported in Figures 5.37 and 5.38 along with those calculated at:  $\tilde{y} = 0.6$ ;  $\pm 0.53$ ;  $\pm 0.47$ . A main peak at 1000 Hz is

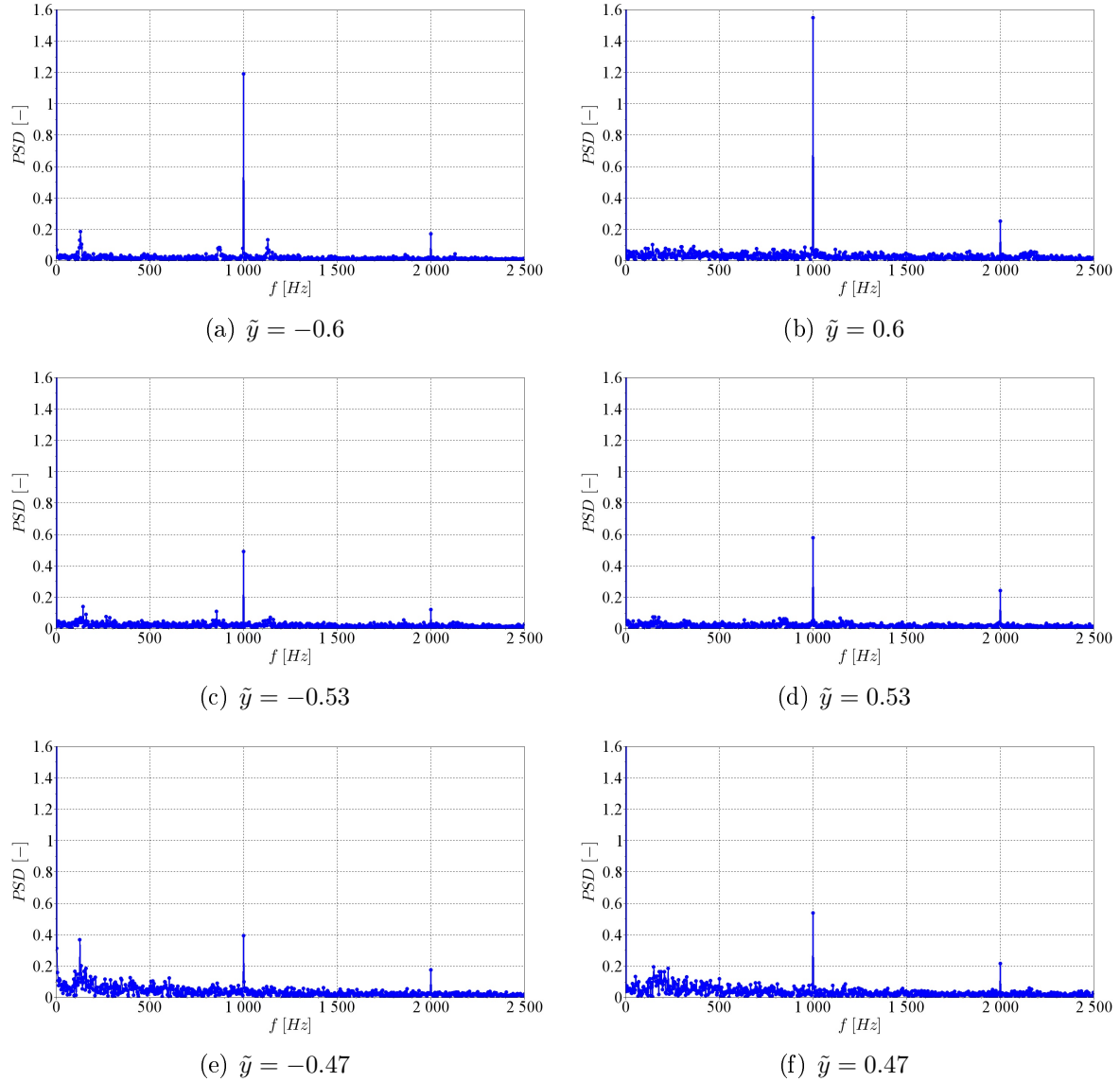


Figure 5.37: PSD of re-sampled signals for vertical velocities with acoustics at VAN( $\tilde{x} = 0$ ;  $\tilde{z} = 2e$ ;  $We_g = 190$ ,  $Re_l = 2000$ ;  $p_{a,pp} = 12$  kPa,  $f = 1$  kHz).

observed in every plot (namely in every measurement location), corresponding to the forcing frequency. For what concerns  $U_z$ , the peak is maximum at the gas/gas interface (see Figures 5.37(a) and 5.37(b)). The intensity of the peak decreases at intermediate positions in the gas annular flow (see Figures 5.37(c) and 5.37(d)) and approaching the liquid/gas interface (see Figures 5.37(e) and 5.37(f)). Two lower peaks are also noted: one at 2000 Hz corresponding to the first harmonic of the main frequency; and one at around

120 Hz. The peak at 120 Hz presents stronger amplitude at the liquid/gas interface (see Figure 5.37(e)) and corresponds to the liquid/gas interface instability discussed in the previous section. The modification of the frequency may result from the effects of the acoustic field on the flow field. PSD plots concerning the radial velocity also present a main peak at 1000 Hz, and two lower peaks at 2000 Hz, and 120 Hz. It is worth noting that the response at VAN is symmetrical with respect to the injector axis (the same behavior is observed on the opposite sides of the coaxial flow).

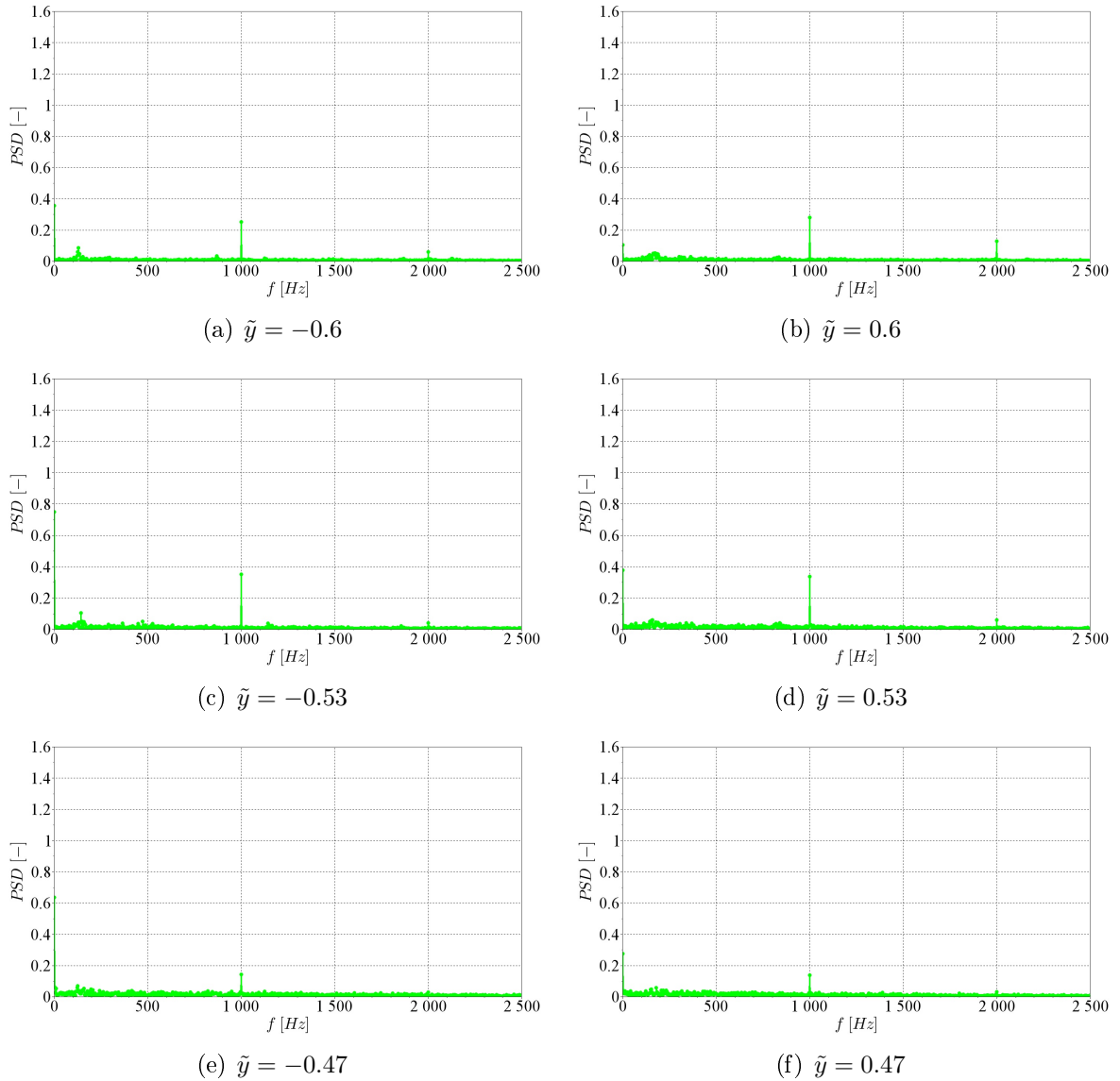


Figure 5.38: PSD of re-sampled signals for radial velocities with acoustics at VAN ( $\tilde{x} = 0$ ;  $\tilde{z} = 2e$ ;  $We_g = 190$ ,  $Re_l = 2000$ ;  $p_{a,pp} = 12 \text{ kPa}$ ,  $f = 1 \text{ kHz}$ ).

## Injection at IAN

The same analysis performed at VAN will be presented in this section for IAN. The mean values of  $U_z$  and  $U_y$  measured with acoustics ( $p_{a,pp} = 12000 Pa$  peak-to-peak, 1000 Hz) at IAN are compared, in Figure 5.39, with those measured without acoustics (rms values  $U_{z,rms}$  and  $U_{y,rms}$  are also reported in the figure as empty markers). Velocity profiles have similar shapes with and without acoustics. However, a non-symmetrical reduction of the mean values of the vertical velocity is noted in Figure 5.39(a). The mean values  $U_z$  on the side close to PAN ( $\tilde{y} < 0$ ) are reduced more than those on the side close to VAN ( $\tilde{y} > 0$ ). The non-symmetrical response is also noticeable in the rms values. In the region close to VAN rms values with and without acoustics are similar. On the contrary, in the side close to PAN the rms measured with acoustics are higher than those measured without acoustics. Mean and rms values of the radial velocity are only slightly affected by acoustics at IAN. Mean values of  $U_y$  are higher with acoustics on the side close to PAN, whereas  $U_y \approx 0$  with acoustics on the side close to VAN.

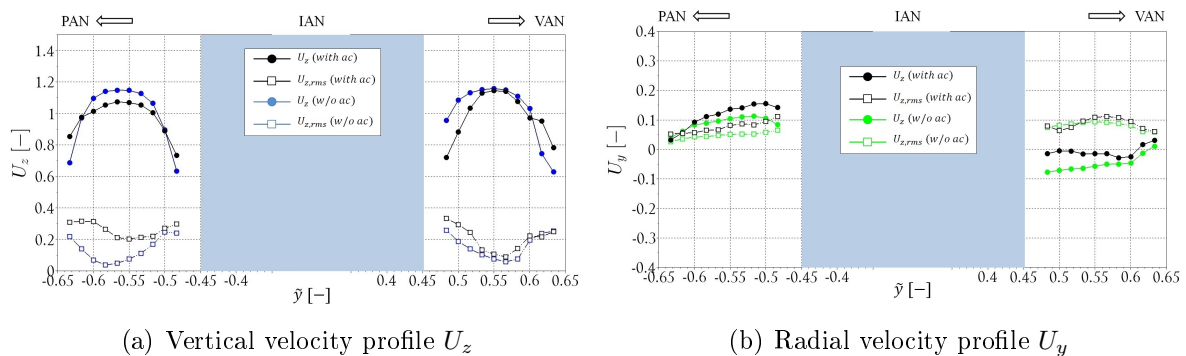


Figure 5.39: Comparison at IAN between mean and RMS values of (a) vertical and (b) radial velocities with and without acoustics as functions of  $\tilde{y}$  ( $\tilde{x} = 0$ ;  $\tilde{z} = 2e$ ;  $We_g = 190$ ,  $Re_l = 2000$ ;  $p_{a,pp} = 12 kPa$ ,  $f = 1$  kHz).

### Raw data acquisition signals

Figure 5.40 shows an example of time series for the vertical and radial velocity data acquisition signals at IAN ( $We_g = 190$ ,  $Re_l = 2000$ ). Measurements reported in this example have been performed close to the gas/gas interface at  $\tilde{x} = 0$ ,  $\tilde{y} = -0.6$  and  $\tilde{z} = 2e$ . Close up views (in between  $t = 0.31$  s and  $t = 0.32$  s) of the two signals are also reported in the figure. The typical envelop of the acoustic signal (see Figure 2.3) sent to the loudspeakers can be observed on  $U_z$ . Instantaneous values of the two velocities oscillate around the mean value with amplitudes of fluctuations proportional to those of the acoustic field. The effects of acoustic modulation are not clearly visible on the radial

velocity.

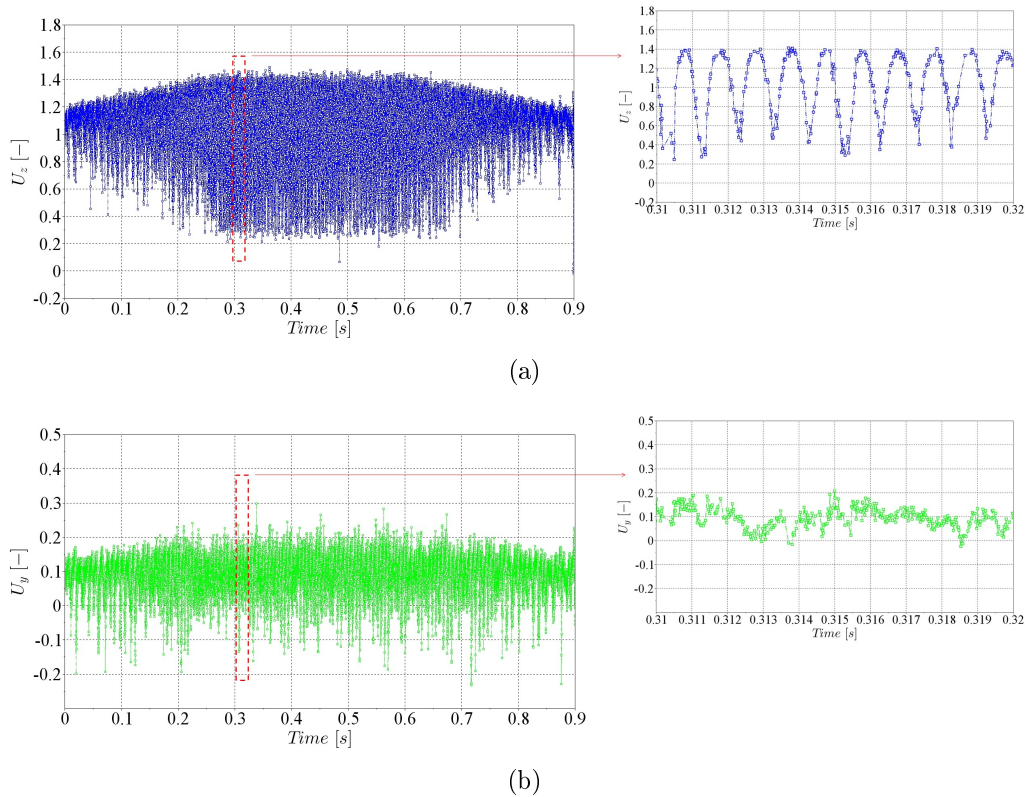


Figure 5.40: Examples of raw data signals for vertical (a) and radial (b) velocities with acoustics at IAN ( $\tilde{x} = 0$ ;  $\tilde{y} = -0.6$ ;  $\tilde{z} = 2e$ ;  $We_g = 190$ ,  $Re_l = 2000$ ;  $p_{a,pp} = 12 \text{ kPa}$ ,  $f = 1 \text{ kHz}$ ).

### Power spectral density plots

PSD plots of signals presented in Figure 5.40 are reported in Figures 5.41 and 5.42. Five more locations are considered for comparison,  $\tilde{y} = 0.6$ ;  $\pm 0.53$ ;  $\pm 47$ . For what concerns vertical velocities  $U_z$ , a main peak at 1000 Hz is noted in all locations. Its amplitude is maximum at the gas/gas interface (see Figures 5.41(a) and decreases by approaching the liquid/gas interface (see Figures 5.41(e) and 5.41(f)). Two lower peaks are also noted: one at 2000 Hz corresponding to first harmonic of the signal; the other one at around 120 Hz. Contrarily to what observed at VAN, the response of the coaxial gas flow at IAN is not symmetric. A stronger response is noted on the PAN side ( $\tilde{y} < 0$ ) than on the VAN side ( $\tilde{y} > 0$ ). As already stated above, radial velocity are less influenced by the acoustics field at IAN. PSD plots in Figures 5.42 present an energy content much lower than that of vertical velocities. The amplitude of the peak at 1000 Hz is one order of magnitude lower than for  $U_z$ , and the strongest response is observed on VAN side for  $U_y$  whereas it is on PAN side for  $U_z$ . This is due to the fact that radial velocity is more sensitive to

acoustic velocity fluctuations, which are maximum at VAN.

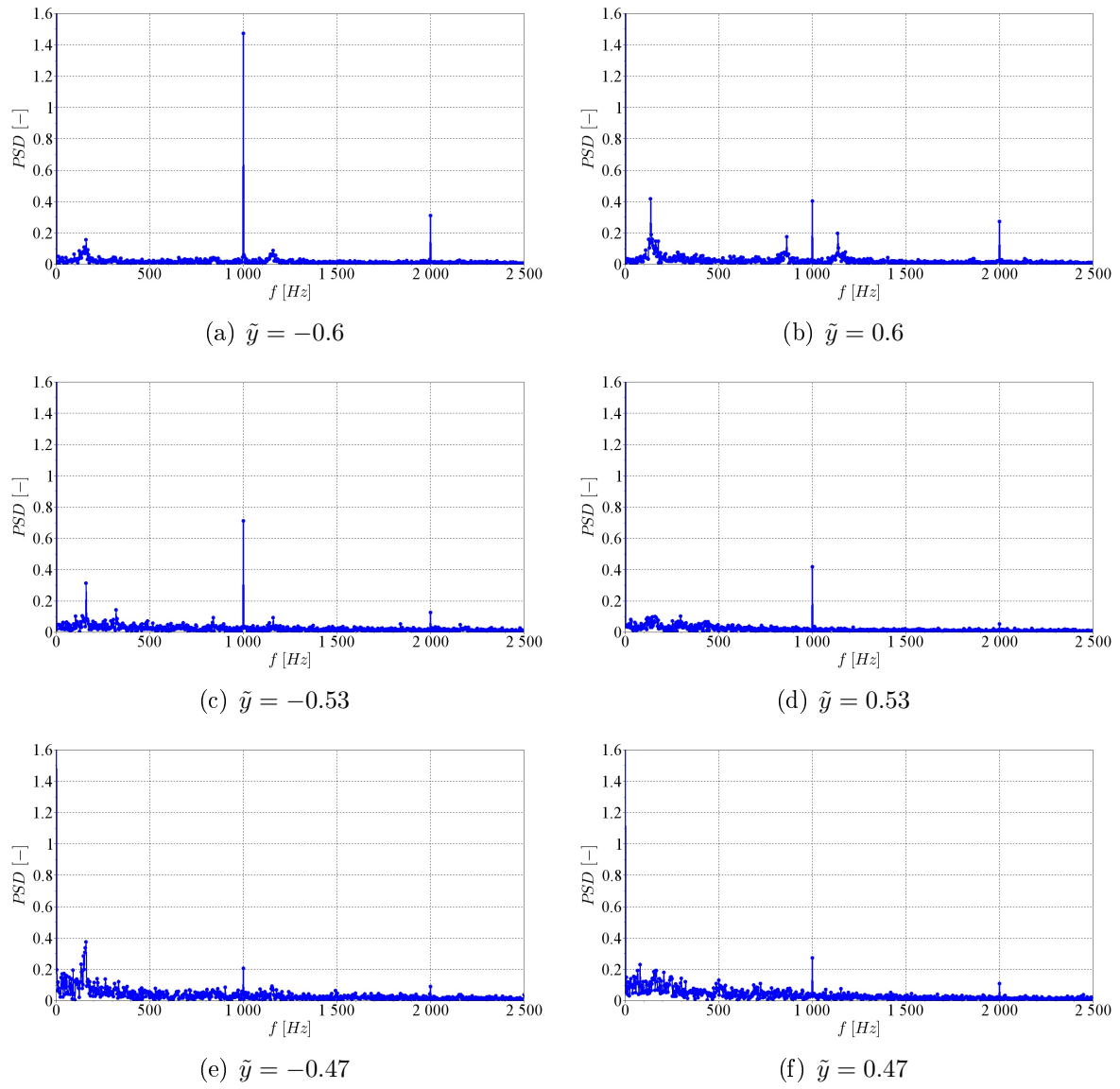


Figure 5.41: PSD of re-sampled signals for vertical velocities with acoustics at IAN ( $\tilde{x} = 0$ ;  $\tilde{z} = 2e$ ;  $We_g = 190$ ,  $Re_l = 2000$ ;  $p_{a,pp} = 12 \text{ kPa}$ ,  $f = 1 \text{ kHz}$ ).

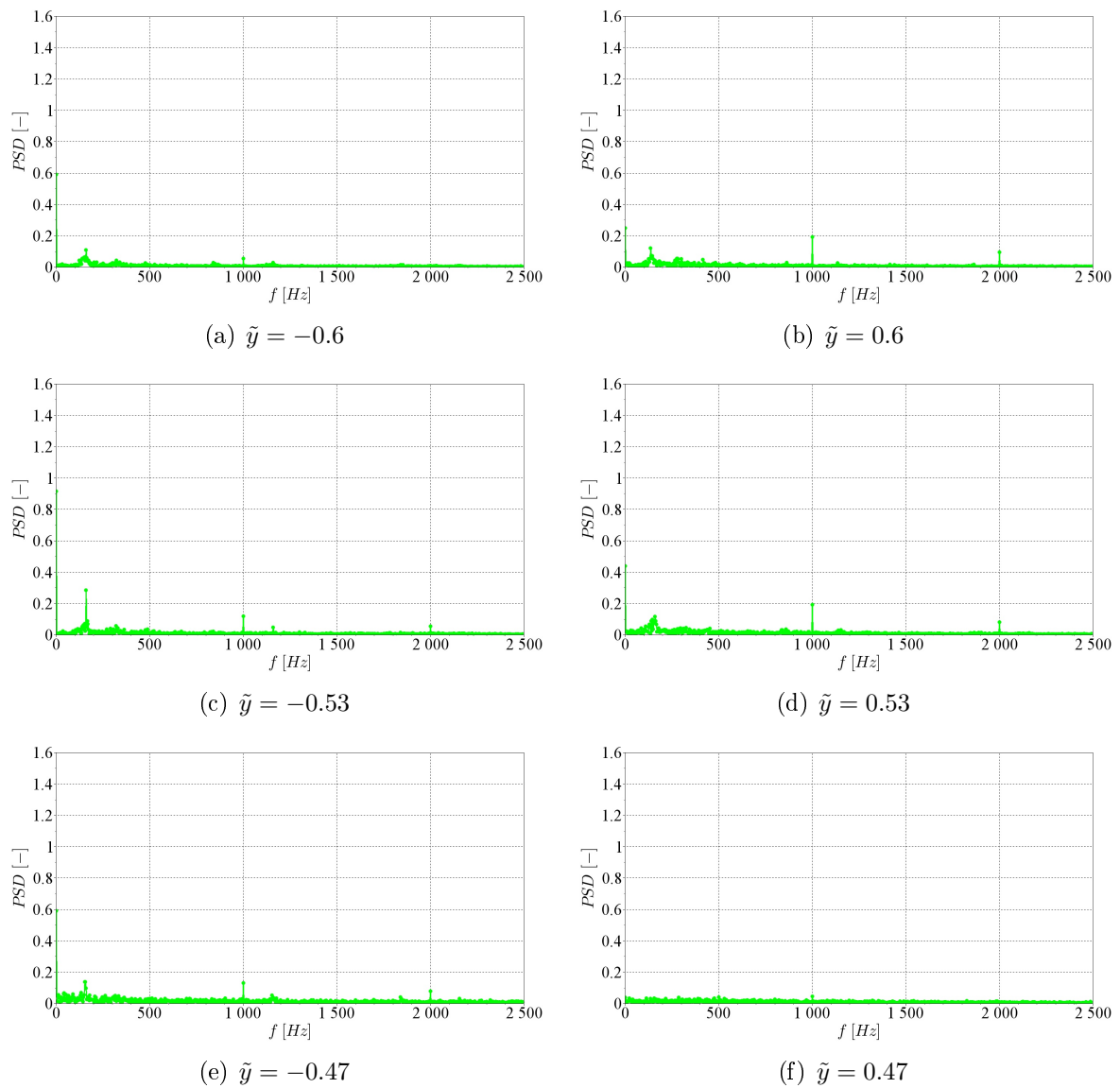


Figure 5.42: PSD of re-sampled signals for radial velocities with acoustics at IAN ( $\tilde{x} = 0$ ;  $\tilde{z} = 2e$ ;  $We_g = 190$ ,  $Re_l = 2000$ ;  $p_{a,pp} = 12 \text{ kPa}$ ,  $f = 1 \text{ kHz}$ ).

## 5.5 Summary of Results

Coaxial air-assisted liquid jet behavior under the effects of high amplitude/high frequency acoustic fields has been experimentally investigated. Several injection conditions and locations with respect to the acoustic field, as well as the influence of the amplitude of the acoustic field, have been taken into account in the experiments. Single injector and multi-point injection tests have been performed with and without the injection domes.

The position of the injector in the acoustic field is demonstrated to be a crucial factor in the jet response. The higher the acoustic amplitude the stronger the system response and the effects observed at low Weber number regimes are demonstrated to take place also at very high Weber numbers.

High-speed visualizations allowed identifying three main phenomena which, depending on the position inside the acoustic field, can take place separately or simultaneously.

The first phenomenon is the flattening of the liquid core in a liquid sheet, in the direction perpendicular to the acoustic axis. Flattening has been observed in low and high Weber number atomization regimes, with decreasing intensity from VAN to IAN. This phenomenon is based on the competition between acoustics and the jet coherence force which is represented by the Laplace's pressure drop. As soon as acoustics is sufficient to overcome the jet coherence force, the flattening is observed. For sufficiently high acoustic levels the liquid sheet is atomized. In the case of low Weber number atomization regimes a threshold, in terms of acoustic pressure, has been identified for the onset of the flattening. By assuming that a jet thickness decrease of 10% could be associated to the beginning of the flattening a mean value of about 2700 Pa has been found for jets placed at VAN and IAN-VAN. Results indicated that for smaller jet diameters higher acoustic energy was necessary to flatten the jet. This confirms that the Laplace's pressure drop competes with acoustics to maintain jet initial shape (in Chapter 7 it will be shown that the existence of a heavy/light interface is at the basis of the observed phenomena). When injection takes place closer to IAN the calculated threshold is higher than that calculated at IAN and VAN-IAN,  $\approx 4000 Pa$ . Indeed, around IAN another phenomenon, namely the jet deviation takes place simultaneously to the flattening. These two phenomena compete for the acoustic energy distribution, which consequently is only partially dedicated to the flattening phenomenon.

The deviation of the liquid system has been observed in all positions between VAN and PAN (these two locations excluded) for low and very high Weber number regimes (see T-LRE test case). For low Weber number regimes the deviation has been quanti-

fied directly from high-speed visualization images. For high Weber number atomization regimes, the droplet spatial distributions have been calculated, from high-speed image series, to determine the spray deviation. The deviation of the spray presents a non-linear growth with the acoustic pressure. No deviation has been observed for acoustic pressure lower than around 3000 - 4000 Pa. This threshold has been physically interpreted by introducing an acoustic Froude number; defined as the square root of the ratio of the mean acoustic energy of a stationary wave per unit mass over the gravitational potential energy of the liquid system per unit mass. The measured values of 3000 - 4000 Pa corresponds to a Froude number of about 1. This means that deviation is possible as soon as the acoustic potential energy becomes high enough to counterbalance the gravitational energy.

The third phenomenon observed in this work is the improvement of the atomization process at high Weber number atomization regimes. Ligaments, liquid blobs and big droplets are broken into smaller droplets with a process similar to the flattening. The phenomenon has its maximum impact at VAN and decreases in strength for jets placed close to PAN, where it is no longer present. For very high Weber number atomization regimes droplets are too small and difficult to broken and thus more acoustic energy is required to modify the atomization regime.

Multi-point injection tests have been also performed at low and high Weber numbers. Low Weber number atomization regime response is used to interpret results at higher Weber numbers. They confirm what has already been observed for single injection experiments. The main result is a droplet-clustering phenomenon in the spatial region between IAN and VAN which results from the combination of deviation and atomization improvement.

In conclusion, experimental results indicates that acoustics can drastically affect the atomization process and affect the droplet spatial distribution. It has been demonstrated that acoustics can enhance the atomization process, which can directly affect the combustion processes, e.g. by augmenting the heat flux to the chamber walls and to the injector exit plane. In multi-point injection configurations such as in liquid rocket engines, a spatial redistribution of the spray can occur in the combustion chamber, leading to droplet clustering between IAN and VAN. The non-uniform distribution of the spray inside the chamber can cause spatial non-homogeneity of the heat release rate.

In the framework of the activities of the REST group a collaboration with the French national aerospace research establishment ONERA has been initiated to investigate the effects of acoustics on the atomization process at injection conditions very close to those typical of liquid rocket engines. The injection conditions chosen were: ( $We_g > 400$ )

with  $Re_l = 6602$  and  $J = 5.1$ . The position in the acoustic field selected was IAN. The deviation has been quantified by calculating the droplet spatial distribution from high-speed image post-processing. Droplet size have been measured by image post-processing. Measurements highlighted the presence of the deviation. However, modifications of the atomization regime could not be quantified. In future applications, for a complete characterization of the spray, measurements should be done at VAN at different vertical and radial locations. Gas velocity field has been measured by LDV at VAN and IAN for  $We_g = 190$  and  $Re_l = 2000$ . Velocity profiles typical of coaxial flows have been calculated. With acoustics both velocities presented a modulation at the forcing frequency, with stronger intensity at the gas/gas interface. A symmetrical response was observed at VAN, where mean vertical velocities are slightly reduced by acoustics. On the contrary the response observed at IAN was non-symmetric. The flow side in between IAN and PAN is the one presenting the stronger response. Velocity rms values are globally higher with acoustics, due to the fluctuations imposed by the acoustic field.

The application of these two techniques in our experimental setup represented a challenge. Preliminary results have been presented to confirm the feasibility of their application in our experimental conditions, and serves as a starting point for future investigations.



Part III

Modeling



# Chapter 6

## Nonlinear Acoustic Theory

*This chapter is dedicated to the development of a theoretical model able to describe the jet responses observed experimentally. The model is based on nonlinear acoustic theory, whose basic concepts are introduced in section 6.1. The general expressions concerning the radiation pressure and the resulting radiation force are introduced in section 6.2. In section 6.3 these expressions are derived for an objects of cylindrical shape. Both standing (SW) and progressive (PW) wave fields will be discussed. Simplified expressions under the hypothesis of small objects, compared to the acoustic wavelength, will be presented in section 6.3.3, and compared with the general expressions. The radiation pressure distribution will be discussed and analyzed as a function of the position of the object in the acoustic field and of the ratio of the medium density over the object density (see section 6.3.3.5). Based on the same procedure, the case of spherical objects is also treated in section 6.4. Results for these two geometries are compared in section 6.6.*

### 6.1 Introduction

In many applications acoustic pressure fluctuations are low enough to interpret the acoustic field and the involved phenomena by means of linear acoustic concepts. Unfortunately, thermo-acoustic instabilities occurring in liquid rocket engines are characterized by pressure fluctuation amplitudes that cannot be approximated as low-amplitude acoustic waves. In such conditions it is necessary to consider finite-amplitude waves and get into the field of nonlinear acoustic equations. Nonlinear acoustics is the portion of physics which studies the behavior of sufficiently powerful acoustic fields [113, 114]. Nonlinear effects induce mean steady phenomena characterized by the time-average of quadratic fluctuations of acoustic quantities. When acoustic waves propagate in a field without obstacles,

a quantity named *acoustic radiation pressure* can be defined as the difference between the time-averaged potential and kinetic acoustic energies per unit volume [92]:

$$p_{rad}^{free} = \frac{\langle p'^2 \rangle}{2\rho_0 c_0^2} - \frac{\rho_0}{2} \langle u'u' \rangle + C \quad (6.1)$$

Here  $C$  is a constant generally equal to zero by assuming that the acoustic wave is damped in an infinite volume;  $p'$  and  $u'$  are respectively the acoustic pressure and velocity fluctuations;  $c_0$  is the speed of sound and  $\rho_0$  is the density of the fluid at rest in the reference state. An object placed in the acoustic field is submitted simultaneously to the incident and scattered acoustic waves whose nonlinear effects must be taken into account. Thus, Eq. 6.1 must be modified to take into account the contribution of both incident and scattered acoustic fields.

Radiation pressure was first studied by Lord Rayleigh as the acoustic counterpart of the pressure induced by an electromagnetic wave. In analogy with the electromagnetism, where the radiation pressure is the pressure experienced by a material surface when it is illuminated by a light wave, the acoustic radiation pressure is the mean excess pressure experienced by an object surface in a sound field. Nowadays, acoustic radiation pressure is used in the field of acoustic levitation [115, 116]. In these applications the *acoustic radiation force*, defined as the integral of the radiation pressure on the object surface, is used to counterbalance the object weight and levitate the object.

Here, the radiation pressure distribution and the resulting radiation force, will be used to interpret and explain the phenomena observed in Chapter 5, namely the flattening and the deviation. In this chapter, the general equations for the acoustic radiation pressure and force will be derived for the case of cylindrical and spherical objects. The same approach used by King [93] and Zhuk [117] for the derivation of the expressions of the radiation force will be adopted. Approximate and asymptotic expressions will be also derived under the approximation of small objects.

## 6.2 Acoustic Radiation Pressure and Radiation Force Equations

Let us consider the case of a compressible and isentropic fluid, for which  $\rho \neq constant$  and the entropy  $s$  is constant ( $ds = 0$ ). The thermodynamic equation in terms of enthalpy  $h$  can be written as:

$$dh = dp/\rho \quad (6.2)$$

Under these hypotheses a general form of the Bernoulli's equation can be obtained as:

$$h = \int \frac{dp}{\rho} = -\frac{1}{2}\vec{v}^2 - \frac{\partial\phi}{\partial t} + C = -\frac{1}{2}(\vec{\nabla}\phi)^2 - \dot{\phi} + C \quad (6.3)$$

where  $\phi$  is the velocity potential defined as  $\vec{v} = \vec{\nabla}\phi$ . The enthalpy  $h$  can be written as the sum of the enthalpy of the reference state  $h_0$  and the fluctuating part  $h'$ ,  $h = h_0 + h'$ , and similarly for the pressure  $p = p_0 + p'$ . Expanding  $h$  in powers of  $p$ , and taking only terms up to second order:

$$h = \left(\frac{\partial h}{\partial p}\right)_s \Big|_0 (p - p_0) - \frac{1}{2} \left(\frac{\partial^2 h}{\partial p^2}\right)_s \Big|_0 (p - p_0)^2 + o(2) \quad (6.4)$$

Since  $\left(\frac{\partial h}{\partial p}\right)_s \Big|_0 = 1/\rho_0$ , and  $p' = p - p_0$  we have:

$$h' = \frac{p'}{\rho_0} - \frac{p'^2}{2\rho_0^2} \left(\frac{\partial \rho}{\partial p}\right)_s = \frac{p'}{\rho_0} - \frac{p'^2}{2c_0^2\rho_0^2} \quad (6.5)$$

Substituting Eq. 6.5 into Eq. 6.3 and omitting the "''" superscript we have:

$$p = -\rho_0\dot{\phi} - \frac{1}{2}\rho_0(\vec{\nabla}\phi)^2 + \frac{\rho_0}{2c_0^2}\dot{\phi}^2 \quad (6.6)$$

By taking into account only second-order quantities, the pressure change in the fluid can be expressed in terms of quantities calculated from the linear sound equations, so that it is not necessary to solve directly the nonlinear equations of motion obtained when terms of higher order are taken into account [92].

Let now consider a rigid object with surface  $S$  free to move in the ideal fluid and subjected to a sound wave field. In this case the object is submitted simultaneously to the incident and scattered acoustic waves, and the velocity potential of the incident wave field  $\phi_i$  as well as the velocity potential of the scattered field  $\phi_r$  must be taken into account. The pressure variation in the fluid is given by Eq. 6.6 [92, 93, 117] where the total velocity potential is now given by  $\phi = \phi_i + \phi_r$ . If the object is free to move under the influence of the acoustic field the derivative of the velocity potential referred to the moving origin is given by the equation:

$$\dot{\phi} = \frac{d\phi}{dt} - \vec{U} \cdot \vec{\nabla}\phi \quad (6.7)$$

where  $\vec{U}$  is the translational displacement velocity.

In the case of harmonic waves of period  $T$ , the radiation pressure  $p_{rad}$  acting on the object surface is obtained as the time average of Eq. 6.6 over one cycle:

$$p_{rad} = \frac{1}{T} \int_0^T \left( -\rho_0 \dot{\phi} - \frac{1}{2} \rho_0 (\overline{\nabla \dot{\phi}})^2 + \frac{\rho_0}{2c^2} \dot{\phi}^2 \right) dt = p_\zeta + p_\phi + p_q \quad (6.8)$$

Eq. 6.8 indicates that expression of  $p_{rad}$  is composed of three terms which can be calculated separately: the time-average volumetric potential energy density  $p_q$ ; the time-average volumetric kinetic energy density  $p_\phi$  and the contribution due to the motion of the object  $p_\zeta$ . It is important to notice that due to the presence of the object the time average of  $\dot{\phi}$  is not zero, and the first term  $p_\zeta$ , expressed in the Lagrangian reference frame, can be simplified as:

$$p_\zeta = \frac{\rho_0}{T} \int_0^T (\vec{U} \cdot \overline{\nabla \dot{\phi}}) dt \quad (6.9)$$

In order to obtain the radiation pressure acting on the object, the three terms  $p_\zeta$ ,  $p_q$  and  $p_\phi$ , as well as the total velocity potential  $\phi = \phi_i + \phi_r$ , have to be determined at the boundary of the object. The expression of  $\phi_i$  depends on the nature of the acoustic field (standing or progressive wave) whereas  $\phi_r$  depends, in addition, on the geometry of the object (e.g. cylinder or sphere). The scattered wave field  $\phi_r$  should be determined by requiring that the boundary condition on the object surface satisfies the equation:

$$\vec{U} \cdot \vec{N} = v_N = \overline{\nabla \dot{\phi}} \cdot \vec{N} \quad (6.10)$$

where  $v_N$  is the component of the fluid velocity along the unit normal  $\vec{N}$ , at any point of the object surface.

The integral of  $p_{rad}$  on the object surface gives rise to a net force called acoustic radiation force  $\vec{F}_{rad}$ .

$$\vec{F}_{rad} = - \iint_S p_{rad} \vec{N} dS \quad (6.11)$$

These equations are valid for both standing and progressive wave fields and for an object of cylindrical or spherical shapes.

## 6.3 Cylindrical Objects

In the work of Boisdron [89] and Baillot *et al.* [90] a first approach in the modeling of liquid jet response to acoustic perturbation by means of nonlinear acoustic equations was performed. The equations considered for  $p_{rad}$  and  $\vec{F}_{rad}$  were those relative to the case of spherical objects. In the case of jets with initial round shape more representative geometries must be considered. For this reason the expressions of the acoustic radiation pressure and force exerted on cylindrical objects (which better represent the case of a liquid jet) will be derived in this section. A similar analysis concerning spherical object can be found in section 6.4.

The case of a cylindrical rigid body submitted to an acoustic field has been treated by Zhuk [117] and by Wu [118] for what concerns progressive and standing waves, respectively. But they focused their approach only on the radiation force expression while no general expressions were given for the radiation pressure. Moreover, no systematic study was performed to characterize the response by means of the driving parameters, leading to an absence of any behavioral interpretation of the model. In this section we will consider an infinite long cylinder with radius  $a$  placed in an harmonic sound field characterized by an angular frequency  $\omega$ . General expressions are derived for both acoustic radiation pressure and resulting force per unit length acting on the cylinder. Specific expressions will be then obtained for plane standing and progressive acoustic waves.

Referring to Figure 6.1 the axis of the unperturbed cylinder coincides with the ascending axis  $z$  of a Cartesian coordinate system  $(x, y, z)$ . The axis  $(O, \vec{y})$ , with  $O$  defined as the origin of any cylinder cross-sections, is parallel to the wave number vector  $\vec{k} = k\vec{y}$  of the incident wave. On the axis  $(O, \vec{y})$ , the points of polar coordinates  $(r = a, \theta = 0)$  and  $(r = a, \theta = \pi)$  are called equatorial points. The perpendicular axis  $(O, \vec{x})$  passes through the two points  $(r = a, \theta = \pi/2)$  and  $(r = a, \theta = 3\pi/2)$ , named pole points.

### 6.3.1 General Expressions

#### 6.3.1.1 Velocity Potential Expression

The velocity potential  $\phi_i$  of the incident wave can be expressed in the associated polar coordinates  $(r, \theta, z)$  as:

$$\phi_i = \sum_{n=0}^{\infty} A e_n K_n J_n(kr) \cos n\theta e^{-i\omega t} \quad (6.12)$$

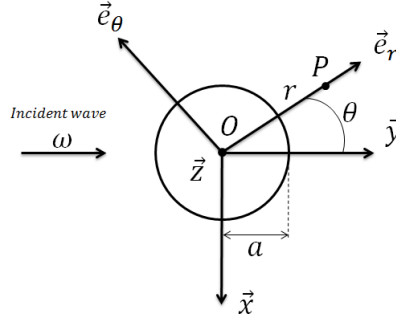


Figure 6.1: Schematic of the coordinate reference frame in a plane perpendicular to the cylinder vertical axis.

where  $A$  is the amplitude of the velocity potential,  $k = \omega/c_0$ , and  $J_n(kr)$  are the cylindrical Bessel functions of the first kind,  $e_n = 2$  for  $n \geq 1$  and  $e_0 = 1$ . The coefficients  $K_n$ , which can be complex numbers, depend on the nature of the sound field, e.g. standing or progressive wave. If  $p_a$  is the maximum pressure amplitude, then  $A$  is equal to  $p_a/\omega\rho_0$ . The velocity potential  $\phi_r$  of the scattered acoustic field can be expressed as follows:

$$\phi_r = \sum_{n=0}^{\infty} A_n H_n^{(1)}(kr) \cos n\theta e^{-i\omega t} \quad (6.13)$$

where  $H_n^{(1)}(kr)$  are the cylindrical Hankel functions of the first kind. The constants  $A_n$  are determined by requiring that the boundary condition on the cylinder surface, derived from Eq. 6.10, satisfies:

$$U \cos \theta = \left. \frac{\partial \phi}{\partial r} \right|_{r=a} \quad (6.14)$$

with  $a$  the cylinder radius. The cylinder translational displacement velocity  $\vec{U}$  is then obtained by applying the momentum equation to the cylinder:

$$m\dot{\vec{U}} = \vec{F} = - \iint_{S_1} p \vec{N} dS_1 \quad (6.15)$$

where  $S_1$  is the cylinder cross-section surface,  $m = \pi a^2 \rho_1$  the mass per unit length of the cylindrical object, and  $\vec{F}$  is the hydrodynamic force acting on the object by unit length. To calculate the displacement velocity  $\vec{U}$  with Eq. 6.15, for  $r = a$ , it is sufficient to keep the first order term of  $p$  in Eq. 6.6 [93, 117]. Since the component of  $\vec{F}$  over  $\vec{x}$  is null<sup>a</sup> then  $\vec{U}$  is given by:

<sup>a</sup>The projection of  $p\vec{N}$  in the x-direction leads to integrals  $\int_0^{2\pi} \cos n\theta \sin \theta d\theta = 0$ .

$$\vec{U} = \frac{\eta}{a} \left[ 2AJ_1(ka)K_1 + A_1H_1^{(1)}(ka) \right] e^{-i\omega t} \vec{y} \quad (6.16)$$

with  $\eta = \rho_0/\rho_1$ . Using Eq. 6.12, 6.13 and 6.16, Eq. 6.14 satisfied at  $r = a$  becomes :

$$\begin{aligned} \frac{\eta}{a} \left[ 2AJ_1(ka)K_1 + A_1H_1^{(1)}(ka) \right] \cos \theta = A \sum_{n=0}^{\infty} e_n k J'_n(ka) K_n \cos n\theta + \\ \sum_{n=0}^{\infty} k A_n H_n^{(1)'}(ka) \cos n\theta \end{aligned} \quad (6.17)$$

By introducing the Helmholtz number  $\alpha = ka$ , the resolution of the previous relationship, for  $n = 1$ , leads to the following coefficient:

$$A_1 = \frac{-Ae_1(J'_1(\alpha) - \frac{\eta}{\alpha}J_1(\alpha))}{H_1^{(1)'}(\alpha) - H_1^{(1)}(\alpha)\frac{\eta}{\alpha}} K_1 = \frac{-Ae_1F_1(\alpha)}{F_1(\alpha) + iG_1(\alpha)} K_1 \quad (6.18)$$

and for  $n \neq 1$ :

$$A_n = -\frac{Ae_n J'_n(\alpha) K_n}{H_n^{(1)'}(\alpha)} = -\frac{Ae_n F_n(\alpha) K_n}{F_n(\alpha) + iG_n(\alpha)} \quad (6.19)$$

with:

$$F_n(\alpha) = \alpha^2 J_{n+1}(\alpha) - n\alpha J_n(\alpha) \quad \text{for } n \neq 1 \quad (6.20a)$$

$$G_n(\alpha) = \alpha^2 Y_{n+1}(\alpha) - n\alpha Y_n(\alpha) \quad \text{for } n \neq 1 \quad (6.20b)$$

$$F_1(\alpha) = \alpha^2 J_2(\alpha) - (1 - \eta)\alpha J_1(\alpha) \quad (6.20c)$$

$$G_1(\alpha) = \alpha^2 Y_2(\alpha) - (1 - \eta)\alpha Y_1(\alpha) \quad (6.20d)$$

Finally the expression of the translational displacement velocity  $\vec{U}$  of the cylinder is given by:

$$\vec{U} = -\frac{\eta}{a\pi} \frac{2Ae_1 i\alpha K_1}{(F_1(\alpha) + iG_1(\alpha))} e^{-i\omega t} \vec{y} \quad (6.21)$$

and the total velocity potential  $\phi$  at  $r = a$  is expressed by:

$$\phi = -\frac{2Ai\alpha}{\pi} \sum_{n=0}^{\infty} e_n \frac{K_n}{F_n(\alpha) + iG_n(\alpha)} \cos n\theta e^{-i\omega t} \quad (6.22)$$

The  $K_n$  coefficients depend on the kind of the considered acoustic field.

### 6.3.1.2 Expressions for the Radiation Pressure and its Contributions: $p_\zeta$ , $p_\phi$ and $p_q$

The three terms in Eq. 6.8 can be now calculated separately:

$$p_\zeta = \rho_0 \frac{\eta^2}{2a^2} (R_1^2 + S_1^2) \cos^2 \theta + \rho_0 \frac{\eta}{2a^2} \left[ \sum_{n=1}^{\infty} n (R_1 R_n + S_1 S_n) \sin n\theta \right] \sin \theta \quad (6.23)$$

$$p_\phi = -\frac{\rho_0}{2} \left[ \frac{\eta^2}{2a^2} (R_1^2 + S_1^2) \cos^2 \theta + \frac{1}{2a^2} \left( \sum_{n=1}^{\infty} n^2 (R_n^2 + S_n^2) \sin^2 n\theta + 2 \sum_{1 \leq n < m \leq \infty} nm (R_n R_m + S_n S_m) \sin n\theta \sin m\theta \right) \right] \quad (6.24)$$

$$p_q = \frac{\rho_0}{4c^2} \omega^2 \left[ \sum_{n=0}^{\infty} (R_n^2 + S_n^2) \cos^2 n\theta + 2 \sum_{0 \leq n < m \leq \infty} (R_n R_m + S_n S_m) \cos n\theta \cos m\theta \right] \quad (6.25)$$

The sum of the three terms provides the radiation pressure  $p_{rad} = p_\zeta + p_\phi + p_q$ :

$$p_{rad} = \rho_0 \frac{\eta^2}{4a^2} (R_1^2 + S_1^2) \cos^2 \theta + \rho_0 \frac{\eta}{2a^2} \left[ \sum_{n=1}^{\infty} n (R_1 R_n + S_1 S_n) \sin n\theta \right] \sin \theta - \frac{1}{2a^2} \left( \sum_{n=1}^{\infty} n^2 (R_n^2 + S_n^2) \sin^2 n\theta + 2 \sum_{1 \leq n < m \leq \infty} nm (R_n R_m + S_n S_m) \sin n\theta \sin m\theta \right) + \frac{\rho_0}{4c^2} \omega^2 \left[ \sum_{n=0}^{\infty} (R_n^2 + S_n^2) \cos^2 n\theta + 2 \sum_{0 \leq n < m \leq \infty} (R_n R_m + S_n S_m) \cos n\theta \cos m\theta \right] \quad (6.26)$$

By integrating term by term the radiation pressure equation on the cylinder surface (see Eq. 6.11) the modulus of the radiation force per unit length can be deduced as:

$$F_{rad} = -\frac{\pi \rho_0}{4a} \left[ 2(R_0 R_1 + S_0 S_1) \alpha^2 + (R_1 R_2 + S_1 S_2) (\alpha^2 - 2 + 2\eta) + \sum_{n=2}^{\infty} (R_n R_{n+1} + S_n S_{n+1}) (\alpha^2 - n(n+1)) \right] \quad (6.27)$$

### 6.3.1.3 Coefficients of the Expressions for Standing and Progressive Waves

#### Standing wave

For a standing wave:

$$K_n = \cos(n\pi/2 + kh) \quad (6.28)$$

Here  $h$  is the distance in the  $y$ -direction between the center of any cylinder cross-section and a fixed plane of reference in the acoustic field. The real parts of  $U$  and  $\phi$  can thus be written as:

$$ReU = \frac{\eta}{a}(R_1 \sin \omega t + S_1 \cos \omega t) \quad (6.29)$$

$$Re\phi = \sum_{n=0}^{\infty} (R_n \sin \omega t + S_n \cos \omega t) \cos n\theta \quad (6.30)$$

with:

$$R_n = -\frac{2A\alpha e_n}{\pi\Omega_n} \cos(n\frac{\pi}{2} + kh) \cos \epsilon_n \quad S_n = -\frac{2A\alpha e_n}{\pi\Omega_n} \cos(n\frac{\pi}{2} + kh) \sin \epsilon_n \quad (6.31)$$

#### Progressive wave

For a progressive wave:

$$K_n = \cos n\frac{\pi}{2} + i \sin n\frac{\pi}{2} \quad (6.32)$$

The real parts of  $U$  and  $\phi$  assume the forms:

$$ReU = \frac{\eta}{a}(R_1 \cos \omega t + S_1 \sin \omega t) \quad (6.33)$$

$$Re\phi = \sum_{n=0}^{\infty} (R_n \cos \omega t + S_n \sin \omega t) \cos n\theta \quad (6.34)$$

with:

$$R_n = -\frac{2Ae_n\alpha}{\pi\Omega_n} \cos[(n+1)\frac{\pi}{2} - \epsilon_n] \quad S_n = -\frac{2Ae_n\alpha}{\pi\Omega_n} \sin[(n+1)\frac{\pi}{2} - \epsilon_n] \quad (6.35)$$

Here  $R_n$  and  $S_n$  do not depend on  $h$ , the position of the center of the cylinder cross-section in the acoustic field. In both cases of standing and progressive fields the coefficients  $\Omega_n$

and  $\epsilon_n$  are calculated with the following expressions:

$$\Omega_n^2 = F_n^2(\alpha) + G_n^2(\alpha) \quad \cos \epsilon_n = \frac{F_n(\alpha)}{\Omega_n} \quad \sin \epsilon_n = \frac{G_n(\alpha)}{\Omega_n} \quad (6.36)$$

It can be noticed that only in the case of a standing wave field the expressions of  $p_{rad}$  and  $F_{rad}$  depend on the position  $h$  of the object in the acoustic field.

#### 6.3.1.4 Dimensionless Expressions

The expressions derived in the previous section can be reduced by factoring the term  $\bar{P}$  which is given by:

$$\bar{P} = \frac{p_a^2}{\rho_0 c_0^2} \quad (6.37)$$

The selected normalizing factor has the same unit of a pressure, but can be also interpreted as the mean acoustic energy per unit volume carried by a standing wave propagating in an environment free from any obstacles. This dual interpretation perfectly highlights the quality of the radiation pressure. The dimensionless function  $p^*(\alpha, \eta, \theta, h)$  is then defined as  $p^* = p_{rad}/\bar{P}$ . The radiation force per unit length can be also rendered dimensionless through the factor  $\bar{P}$ . In this case the dimensionless force  $F^*(\alpha, \eta)$  is defined as  $F^*(\alpha, \eta) = F_{rad}/a\bar{P}$ .

Eq. 6.23 to 6.27 can be written in their dimensionless forms as:

$$p_\zeta^* = \frac{\eta^2}{2}(R_1'^2 + S_1'^2) \cos^2 \theta + \frac{\eta}{2} \left[ \sum_{n=1}^{\infty} n(R_1' R_n' + S_1' S_n') \sin n\theta \right] \sin \theta \quad (6.38)$$

$$p_\phi^* = -\frac{1}{2} \left[ \frac{\eta^2}{2}(R_1'^2 + S_1'^2) \cos^2 \theta + \frac{1}{2} \left( \sum_{n=1}^{\infty} n^2 (R_n'^2 + S_n'^2) \sin^2 n\theta \right. \right. \\ \left. \left. + 2 \sum_{1 \leq n < m \leq \infty} nm (R_n' R_m' + S_n' S_m') \sin n\theta \sin m\theta \right) \right] \quad (6.39)$$

$$p_q^* = \frac{\alpha^2}{4} \left[ \sum_{n=0}^{\infty} (R_n'^2 + S_n'^2) \cos^2 n\theta + 2 \sum_{0 \leq n < m \leq \infty} (R_n' R_m' + S_n' S_m') \cos n\theta \cos m\theta \right] \quad (6.40)$$

The dimensionless radiation pressure  $p^*$  is now given by  $p^* = p_\zeta^* + p_\phi^* + p_q^*$ , whereas the

dimensionless radiation force can be written as:

$$F^* = -\frac{\pi}{4} \left[ 2(R'_0 R'_1 + S'_0 S'_1) \alpha^2 + (R'_1 R'_2 + S'_1 S'_2) (\alpha^2 - 2 + 2\eta) + \sum_{n=2}^{\infty} (R'_n R'_{n+1} + S'_n S'_{n+1}) (\alpha^2 - n(n+1)) \right] \quad (6.41)$$

The coefficients  $R'_n$  and  $S'_n$  assume the forms reported in Table 6.1.

Standing wave	Progressive wave
$R'_n = -\frac{2e_n}{\pi\Omega_n} \cos(n\frac{\pi}{2} + kh) \cos \epsilon_n$	$R'_n = -\frac{2e_n}{\pi\Omega_n} \cos[(n+1)\frac{\pi}{2} - \epsilon_n]$
$S'_n = -\frac{2e_n}{\pi\Omega_n} \cos(n\frac{\pi}{2} + kh) \sin \epsilon_n$	$S'_n = -\frac{2e_n}{\pi\Omega_n} \sin[(n+1)\frac{\pi}{2} - \epsilon_n]$
$\Omega_n^2 = F_n^2(\alpha) + G_n^2(\alpha)$	$\cos \epsilon_n = \frac{F_n(\alpha)}{\Omega_n} \quad \sin \epsilon_n = \frac{G_n(\alpha)}{\Omega_n}$

Table 6.1: Coefficients  $R'_n$  and  $S'_n$  for both standing and progressive waves.

In the following dimensionless expressions are used to investigate the convergence of the infinite sum, and the dependence on the parameters  $\alpha$  and  $\eta$ . Particular attention will be paid to the cases  $\eta = 0.0013$  and  $\eta = 7$ . The first case is representative of the experimental conditions considered here, i.e heavy object (water jet) in a light gas environment (air). The second case corresponds to the case of a light gaseous jet in a heavier surrounding gas.

### 6.3.2 Convergence Analysis: Truncated Expressions of the Radiation Pressure and Resulting Force

Expressions derived in the previous section are given by the sum of an infinite number of terms  $s$ . When the infinite sum is approximated by a finite sum a truncation error is caused. In the following, for the standing wave, three specific classed of positions inside the acoustic field are considered: the pressure anti-nodes PAN, for  $h = c_0 j \pi / \omega = j \lambda / 2$  (e.g.  $h = 0, \lambda/2$ , etc.); the velocity anti-nodes VAN, for  $h = c_0 (2j + 1) \pi / 2 \omega = \lambda (2j + 1) / 4$  (e.g.  $h = \lambda/4, 3\lambda/4$ , etc.); the intensity anti-nodes IAN, for  $h = c_0 (4j \mp 1) \pi / 4 \omega = \lambda (4j \mp 1) / 8$  (e.g.  $h = \lambda/8, 3\lambda/8$ , etc.), with  $j \in \mathbb{Z}$  where  $\lambda = c_0 / f$  is the wavelength. The analysis of the convergence is carried out in a  $(\alpha, \eta)$  domain centered around the conditions of the experimental investigation, namely  $\alpha = 0.055$  and  $\eta = 0.0013$ .

### Truncation Error for $\alpha = 0.055$ and $\eta = 0.0013$

We define the maximum truncation error between to consecutive finite sums as:

$$err(\alpha, \eta) = \max(p^*(s+1) - p^*(s)) \quad (s = 1, 2, 3\dots) \quad (6.42)$$

where  $s$  is number of terms kept in a truncated sum. Figure 6.2 shows how the maximum truncation error varies as a function of  $s$ . Here,  $\alpha = 0.055$  and  $\eta = 0.0013$  corresponding to experimental conditions investigated serve as the reference case. Results for the three positions PAN, VAN and IAN for a standing wave are reported as well as results for a progressive wave. Calculations indicate that with one term ( $s = 1$ )  $err \approx 0.002$ , and for  $s > 1$   $err < 0.002$ . The only exception is represented by IAN, in which case for  $s = 1$   $err \approx 0.02$ . For  $s = 2$  the error between the sums with 2 and 3 terms is  $err \approx 10^{-4}$ , and  $s \geq 3$  the error is practically zero  $err \approx 10^{-6}$  whatever the types of waves. In order to fix a criterion which is valid for both waves, a sum of three terms must be considered to minimize the truncation error.

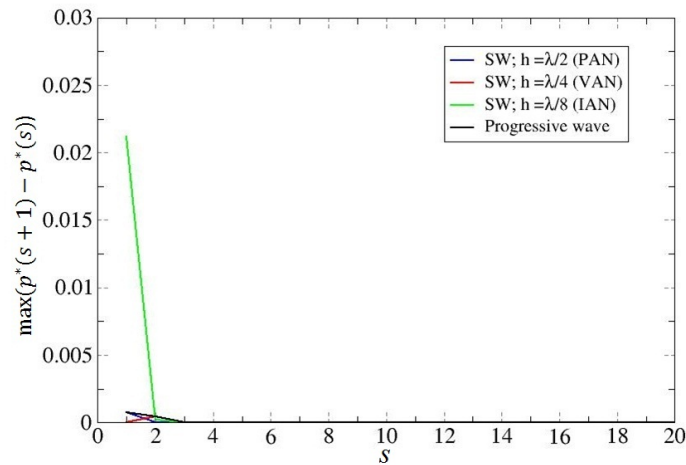


Figure 6.2: Truncation error as a function of the number  $s$  of terms considered in the sum of  $p^*$  ( $\alpha = 0.055$ ;  $\eta = 0.0013$ ;  $f = 1000$  Hz;  $c_0 = 340$  m/s). SW: Standing Wave; PW: Progressive Wave.

### Approximation Error as a Function of $\alpha$ and $\eta$

In the previous section the truncation error has been evaluated by considering a fixed value of  $\alpha$  and  $\eta$ . The effects of these two parameters on the approximation of the infinite sum by a sum of  $s = 3$  terms is studied hereafter. The sum calculated with  $s = 20$  is considered as representative of the infinite sum and is compared with the sum  $s = 3$  by

means of the percentage error defined by:

$$p_{err}^*(\alpha, \eta) = \frac{stdev(p^*(s=20) - p^*(s=3))}{max(|p^*(s=20)|)} \quad (6.43)$$

Figure 6.3 shows  $p_{err}^*$  as a function of the Helmholtz number  $\alpha = ka$  for  $\eta = 0.0013$  (representative of the configuration of a water jet in ambient air) for the progressive and standing waves at the three positions VAN, PAN and IAN. The percentage error between  $p_{err}^*$  is less than 4 % for both standing and progressive waves. No significant difference is found between the errors calculated at the locations in the field (even if the largest error is at PAN). Let us note that in the specific experimental configurations studied in the previous chapters for which  $\alpha = 0.055$ , the error in the truncation is less than 1 %. In the case of the progressive wave, the error can be considered as negligible, remaining lower than 0.2 %.

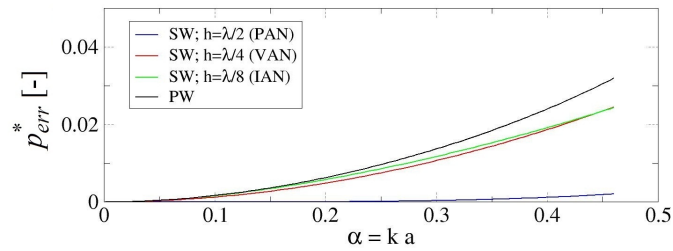


Figure 6.3: Percentage difference  $p_{err}^*$  between  $p^*(s=3)$  and  $p^*(s=20)$  as a function of  $\alpha$  ( $\eta = 0.0013$ ;  $f = 1000 \text{ Hz}$ ;  $c_0 = 340 \text{ m/s}$ ). SW: Standing Wave; PW: Progressive Wave.

The densities ratio parameter  $\eta$  can vary in a large range. Figure 6.4 reports the percentage error  $p_{err}^*$  between  $p^*(s=20)$  and  $p^*(s=3)$  as a function of  $\eta$  for the case of  $\alpha = 0.055$ . Two peaks can be observed at around  $\eta = 0.15$  and  $\eta = 0.4$  (see Figure 6.4) which are due to the definition of  $p_{err}^*$ <sup>b</sup>. However, the error is always less than 0.2 % whatever  $\eta$ . Even for very large  $\eta$ , the error which is the same for all the configurations, is truly negligible (lower than 0.05 %).

It can be concluded that whatever  $\eta$ , and particularly in the case  $\alpha = 0.055$ , the finite sum for  $s = 3$  is an accurate approximation of the infinite sum for both standing and progressive waves, whatever the positions in the acoustic field for the former one.

<sup>b</sup>The  $max(|p^*(s=20)|)$  at the denominator of Eq. 6.43 has a minimum, for which  $p_{err}^*(\alpha, \eta)$  is maximum.

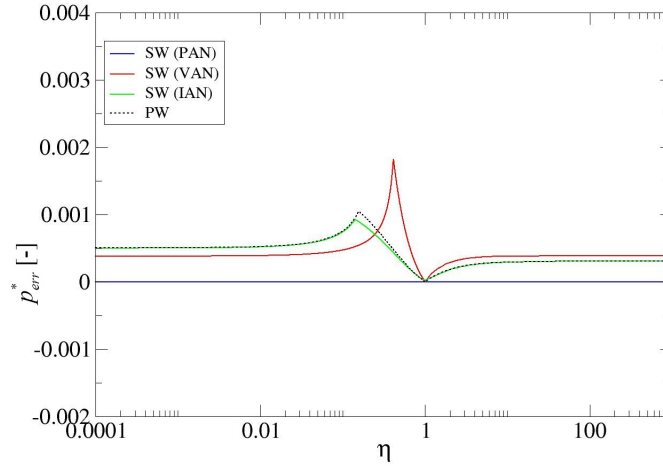


Figure 6.4: Percentage difference  $p_{err}^*$  between  $p^*(s = 3)$  and  $p^*(s = 20)$  as a function of  $\eta$  ( $\alpha = 0.055$ ;  $f = 1000$  Hz;  $c_0 = 340$  m/s).

### Distributions of $p^*$ at PAN, VAN and IAN

For  $\alpha = 0.055$  the previous results are illustrated by comparing the radiation pressure distribution  $p^*$  versus  $\theta$  for the three specific positions investigated experimentally in the standing wave field for  $s = 1 - 3 - 10 - 20$ . The profiles are shown in Figures 6.5-6.6-6.7 at PAN, VAN and IAN respectively. As expected at the three positions curves merge quasi-perfectly for all  $n$ , no significant differences can be noted, except at IAN for which the profile obtained with  $s = 1$  slightly differs from that calculated with  $s = 3 - 10 - 20$  (maximum difference 2%). The largest discrepancy is observed in the vicinity of the two poles on the cylinder.

The distribution of  $p^*$  for a progressive wave  $PW$  is shown in Figure 6.8 for  $s = 1 - 3 - 10 - 20$ . As already observed in the previous section the expressions of radiation pressure and radiation force in the case of a progressive wave field do not depend on the position  $h$  inside the acoustic axis. No differences between the different calculations can be noticed.

### 6.3.3 Small Objects Approximation ( $\alpha \ll 1$ )

In the previous section it has been demonstrated that for small values of the Helmholtz number  $\alpha$  the truncation error caused by approximating the infinite sum, giving the radiation pressure, by the three first terms of the series is negligible  $\forall \eta$ . These summations limited to 3 terms are now simplified under the approximation of small objects ( $\alpha \ll 1$ ).

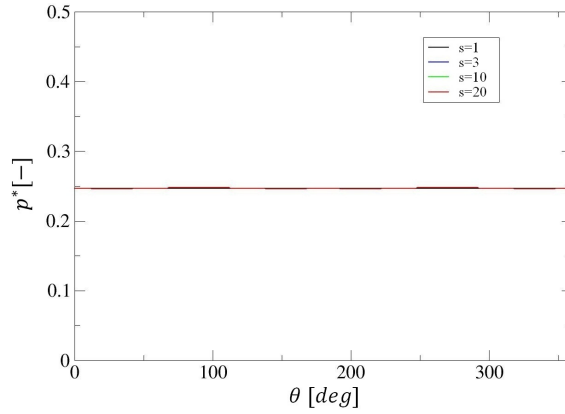


Figure 6.5: Comparison of  $p^*$  distribution at PAN for  $s = 1 - 3 - 10 - 20$  in the case of a standing wave field ( $h = \lambda/2$ ;  $\alpha = 0.055$ ;  $\eta = 0.0013$ ;  $f = 1000 \text{ Hz}$ ;  $c_0 = 340 \text{ m/s}$ ).

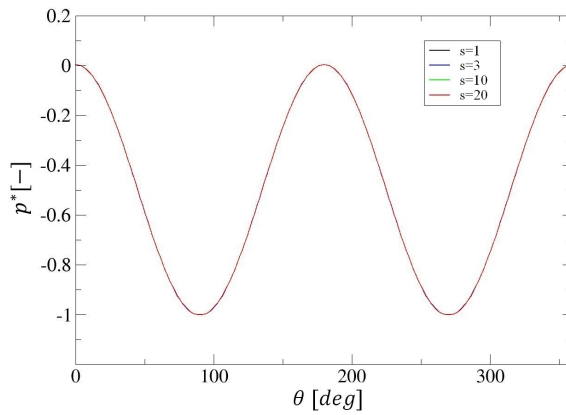


Figure 6.6: Comparison of  $p^*$  distribution at VAN for  $s = 1 - 3 - 10 - 20$  in the case of a standing wave field ( $h = \lambda/4$ ;  $\alpha = 0.055$ ;  $\eta = 0.0013$ ;  $f = 1000 \text{ Hz}$ ;  $c_0 = 340 \text{ m/s}$ ).

The Bessel's functions  $J_n(\alpha)$  and  $Y_n(\alpha)$  are approached by their asymptotic expressions:

$$J_n(\alpha) \approx \frac{1}{n!} \left(\frac{\alpha}{2}\right)^n \tag{6.44}$$

$$Y_n(\alpha) \approx \frac{-(n-1)!}{\pi} \left(\frac{\alpha}{2}\right)^{-n} \tag{6.45}$$

This provides the following expressions:

$$J_0 \approx 1 \quad J_1 \approx \frac{\alpha}{2} \quad J_2 \approx \frac{\alpha^2}{8} \quad J_3 \approx \frac{\alpha^3}{48} \tag{6.46}$$

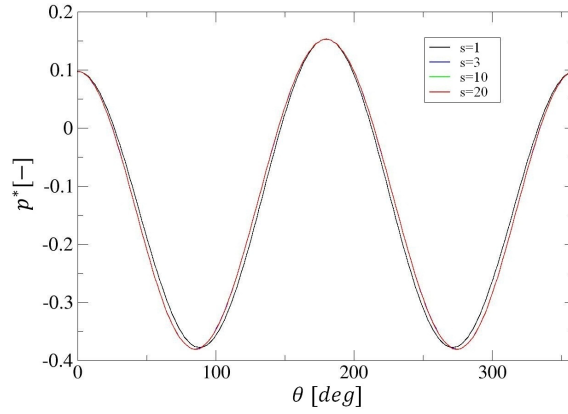


Figure 6.7: Comparison of  $p^*$  distribution at IAN for  $s = 1 - 3 - 10 - 20$  in the case of a standing wave field ( $h = \lambda/8$ ;  $\alpha = 0.055$ ;  $\eta = 0.0013$ ;  $f = 1000\text{Hz}$ ;  $c_0 = 340\text{ m/s}$ ).

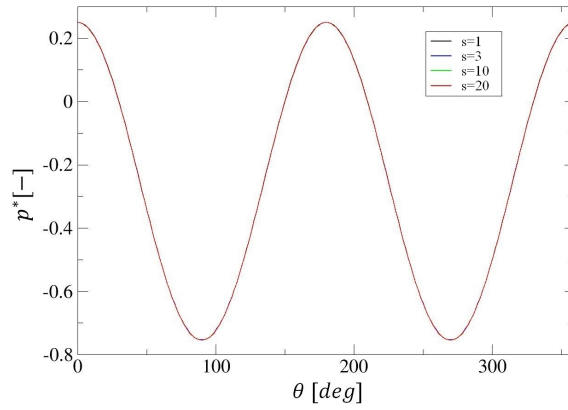


Figure 6.8: Comparison of  $p^*$  distribution for  $s = 1 - 3 - 10 - 20$  in the case of a progressive wave field ( $\alpha = 0.055$ ;  $\eta = 0.0013$ ;  $f = 1000\text{Hz}$ ;  $c_0 = 340\text{ m/s}$ ).

$$Y_0 \approx \frac{2}{\pi} \ln \frac{\alpha}{2} \quad Y_1 \approx -\frac{2}{\pi\alpha} \quad Y_2 \approx -\frac{4}{\pi\alpha^2} \quad Y_3 \approx -\frac{16}{\pi\alpha^3} \quad (6.47)$$

From them the functions  $F_n(\alpha)$ ,  $G_n(\alpha)$  and  $\Omega_n(\alpha)$  can be computed:

$$F_0 \approx \frac{\alpha^3}{2} \quad F_1 \approx \frac{\alpha^4}{8} - (1 - \eta) \frac{\alpha^2}{2} \quad F_2 \approx \frac{\alpha^5}{48} - \frac{\alpha^3}{4} \quad (6.48)$$

$$G_0 \approx -\frac{2\alpha}{\pi} \quad G_1 \approx \frac{1}{\pi}(-2 - 2\eta) \quad G_2 \approx \frac{8}{\pi\alpha} \quad (6.49)$$

$$\Omega_0 \approx -\frac{4\alpha^2}{\pi^2} \quad \Omega_1 \approx \frac{4}{\pi^2}(1+\eta)^2 \quad \Omega_2 \approx \frac{64}{\pi^2\alpha^2} \quad (6.50)$$

Finally, the  $R'_n$  and  $S'_n$  coefficients reported in Table 6.1 can be written as:

**Standing wave**

$$R'_0 = \frac{\pi^3}{16\alpha} \cos(kh) \quad R'_1 = -\frac{\alpha^2\pi^3(1-\eta)}{8(1+\eta)^4} \sin(kh) \quad (6.51)$$

$$S'_0 = \frac{\pi^2}{4\alpha^3} \cos(kh) \quad S'_1 = -\frac{\sin(kh)}{2(1+\eta)^3} \quad (6.52)$$

**Progressive wave**

$$R'_0 = \frac{\pi^2}{4\alpha^3} \quad R'_1 = -\frac{\alpha^2\pi^3(1-\eta)}{8(1+\eta)^4} \quad (6.53)$$

$$S'_0 = -\frac{\pi^3}{16\alpha} \quad S'_1 = -\frac{\pi^2}{2(1+\eta)^3} \quad (6.54)$$

**6.3.3.1 Approximate Expressions for a Standing Wave**

By means of the coefficients calculated above under the hypothesis of  $\alpha \ll 1$ , the analytical expressions of the dimensionless radiation pressure and its three constitutive terms are deduced at any positions  $h$  of the cylinder along a.a.:

$$\tilde{p}_\zeta^* = \frac{2}{(1+\eta)} \left[ \frac{\eta^2}{(1+\eta)} \sin^2 kh \cos^2 \theta + \frac{\eta}{(1+\eta)} \sin^2 kh \sin^2 \theta + \frac{\alpha}{4} \eta \sin 2kh \sin \theta \sin 2\theta \right] \quad (6.55)$$

$$\tilde{p}_\phi^* = -\frac{1}{(1+\eta)} \left[ \frac{\eta^2}{(1+\eta)} \sin^2 kh \cos^2 \theta + \frac{1}{(1+\eta)} \sin^2 kh \sin^2 \theta + \frac{\alpha}{2} \sin 2kh \sin \theta \sin 2\theta \right] \quad (6.56)$$

$$\tilde{p}_q^* = \frac{1}{2} \left[ \frac{1}{2} \cos^2 kh - \frac{\alpha}{(1+\eta)} \cos \theta \sin 2kh \right] \quad (6.57)$$

$$\tilde{p}^* = \left[ \frac{\cos^2 kh}{4} + \frac{\sin^2 kh}{(1+\eta)^2} (\eta^2 \cos^2 \theta + (2\eta - 1) \sin^2 \theta) - \frac{\alpha \sin 2kh}{2(1+\eta)} [(\sin \theta \sin 2\theta)(1-\eta) + \cos \theta] \right] \quad (6.58)$$

The dimensionless radiation force is obtained by simply integrating the analytical expression giving  $\tilde{p}^*$ :

$$\tilde{F}^* = \frac{\pi\alpha(3-\eta)}{4(1+\eta)} \sin 2kh \quad (6.59)$$

The expressions of  $\tilde{p}^*$ ,  $\tilde{p}_\zeta^*$ ,  $\tilde{p}_\phi^*$  and  $\tilde{p}_q^*$  are calculated at the three positions, namely PAN, VAN and IAN. Resulting relationships are summarized in Table 6.2.

<b>PAN</b>	$\tilde{p}_\zeta^* = 0, \tilde{p}_\phi^* = 0$ $\tilde{p}_q^* = \frac{1}{4}$ $\tilde{p}^*(kh = j\pi) = \tilde{p}_{PAN}^* = \frac{1}{4}$
<b>VAN</b>	$\tilde{p}_\zeta^* = \frac{2}{(1+\eta)^2} [(\eta^2 - \eta) \cos^2 \theta + \eta]$ $\tilde{p}_\phi^* = -\frac{1}{(1+\eta)^2} [(\eta^2 - 1) \cos^2 \theta + 1]$ $\tilde{p}_q^* = 0$ $\tilde{p}^*(kh = \frac{(2j+1)\pi}{2}) = \tilde{p}_{VAN}^* = \frac{1}{(1+\eta)^2} [(\eta - 1)^2 \cos^2 \theta + (2\eta - 1)]$
<b>IAN</b>	$\tilde{p}_\zeta^* = \frac{\eta}{(1+\eta)} \left[ \frac{\eta}{(1+\eta)} \cos^2 \theta + \frac{1}{(1+\eta)} \sin^2 \theta + \frac{\alpha}{2} \sin \theta \sin 2\theta \right]$ $\tilde{p}_\phi^* = -\frac{1}{2(1+\eta)} \left[ \frac{\eta^2}{(1+\eta)} \cos^2 \theta + \frac{1}{(1+\eta)} \sin^2 \theta + \alpha \sin \theta \sin 2\theta \right]$ $\tilde{p}_q^* = \frac{1}{8} - \frac{\alpha}{2(1+\eta)} \cos \theta$ $\tilde{p}^*(kh = \frac{(4j\mp 1)\pi}{4}) = \frac{1}{2} (\tilde{p}_{PAN}^* + \tilde{p}_{VAN}^*) \mp \frac{\alpha}{2(1+\eta)} [(\sin \theta \sin 2\theta)(1 - \eta) + \cos \theta]$

Table 6.2: Approximate expressions  $\tilde{p}^*$  calculated from the truncated solutions  $p^*$  for  $\alpha \ll 1$  at four classes of locations inside the standing wave (with  $j \in \mathbb{Z}$ )

Two expressions of  $\tilde{p}^*$  can be obtained for IAN, depending on the specific positions with respect to PAN. The expression with  $(4j - 1)$  must be considered for positive gradients of the acoustic pressure, whereas the one with  $(4j + 1)$  must be considered for negative gradients. This takes into account the fact that the direction of the resulting radiation force changes in sign across PAN and VAN.

### 6.3.3.2 Approximate Expressions for a Progressive Wave

Approximate expressions for  $\alpha \ll 1$  can be also derived for progressive waves. They are written as follows:

$$\tilde{p}_\zeta^* = \frac{2\eta^2}{(1+\eta)^2} \cos^2 \theta + \frac{\eta}{2} \left[ \frac{4}{(1+\eta)^2} \sin^2 \theta + \frac{\pi\alpha^3(1-\eta)}{2(1+\eta)^2} \sin \theta \sin 2\theta \right] \quad (6.60)$$

$$\tilde{p}_\phi^* = -\frac{1}{2} \left[ \frac{2\eta^2}{(1+\eta)^2} \cos^2 \theta + \frac{2}{(1+\eta)^2} \sin^2 \theta + \frac{\alpha^2}{2} \sin^2 2\theta + \frac{\pi\alpha^3(1-\eta)}{2(1+\eta)^2} \sin \theta \sin 2\theta \right] \quad (6.61)$$

$$\tilde{p}_q^* = \frac{1}{2} \left[ \frac{1}{2} + \frac{2\alpha^2}{(1+\eta)^2} \cos^2 \theta - \frac{\alpha^2}{2} \cos 2\theta - \frac{\pi\alpha^3}{(1+\eta)^2} \cos \theta \right] \quad (6.62)$$

$$\tilde{p}^* = \frac{1}{4} \left[ 1 + \frac{4\eta^2}{(1+\eta)^2} \cos^2 \theta + \frac{4(2\eta-1)}{(1+\eta)^2} \sin^2 \theta \right] + \frac{\alpha^2}{4} \left[ \frac{4}{(1+\eta)^2} \cos^2 \theta - \cos 2\theta \right] - \frac{\alpha^3}{4(1+\eta)^2} \left[ (1-\eta)^2 \sin 2\theta \sin \theta + 2 \cos \theta \right] \quad (6.63)$$

The terms of the radiation pressure have the same dominant order of magnitude ( $\alpha^0$ ). The resulting radiation force is given by:

$$\tilde{F}^* = \frac{\pi^2 \alpha^3}{8(1+\eta)^2} [4 + (1-\eta)^2] \quad (6.64)$$

It must be noticed that the leading term of the dimensionless expression of the radiation force is of order  $\alpha^3$  for a progressive wave, which is much lower than the one obtained for a standing wave which is of order of  $\alpha$ .

### 6.3.3.3 Comparison Between General Expressions $p^*$ and $F^*$ and Approximate Solutions $\tilde{p}^*$ and $\tilde{F}^*$

In order to verify the range of validity of the approximate expressions for  $\alpha \ll 1$  they are compared with the general expressions (sum for  $s = 20$ ). The percentage difference defined by Eq. 6.65 is reported in Figure 6.9 as a function of  $\alpha$ . For a progressive wave field  $\tilde{p}_{err}^*$  is always lower than 6 % in the range of  $\alpha$  considered.

$$\tilde{p}_{err}^* = \frac{stdev(p^*(s=20) - \tilde{p}^*)}{max(|p^*(s=20)|)} \quad (6.65)$$

For a progressive wave  $\tilde{p}_{err}^*$  is always lower than 6 % in the range of  $\alpha$  considered. For a standing wave  $\tilde{p}_{err}^*$  is lower than 10 % at VAN and IAN, whereas it reaches the 15 % at PAN for  $\alpha$  reaching values of 0.4.

Figure 6.10 shows  $\tilde{p}_{err}^*$  as a function of  $\eta$  for  $\alpha = 0.055$ . The error is independent of  $\eta$  at PAN and keeps the value of 0.25 %. A maximum error of 0.9 % is calculated at VAN when  $\eta$  approaches the value of 0.4. At IAN and for the progressive wave, the error is lower than 0.6 %. For all the conditions, the error after reaching a minimum of order of 0.05 % tends asymptotically to an error lower than 0.4 %. To conclude the approximate expressions can be considered good approximations of the general solutions, especially for the conditions representative of the experiments investigated here, namely of a water jet

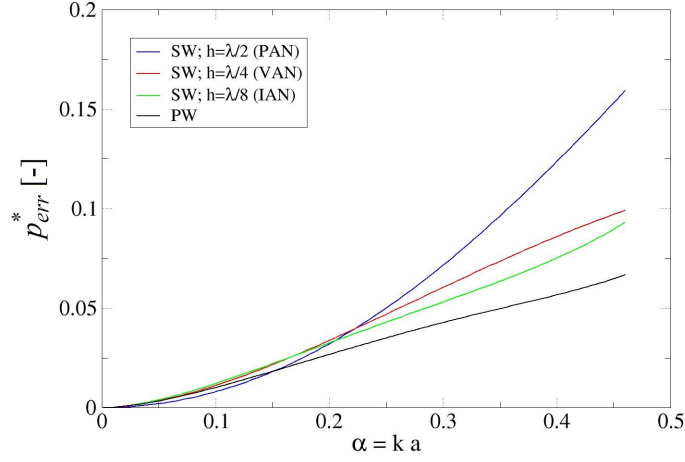


Figure 6.9: Percentage difference  $\tilde{p}_{err}^*$  between  $p^*(s = 20)$  and  $\tilde{p}^*$  as a function of  $\alpha$  ( $\eta = 0.0013$ ).

in a gaseous environment ( $\alpha = 0.055$  and  $\eta = 0.0013$ ).

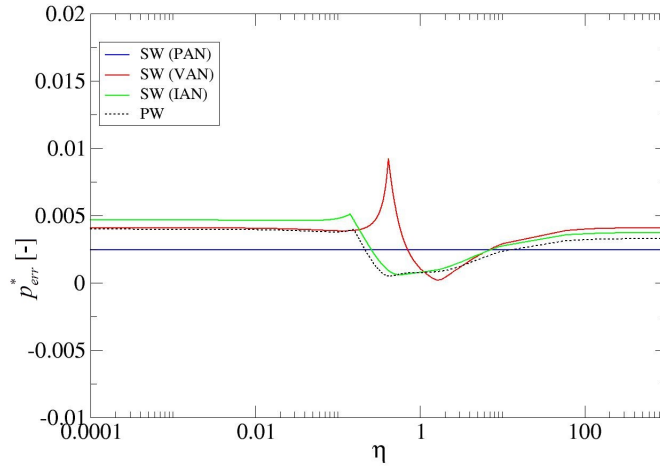


Figure 6.10: Percentage difference  $\tilde{p}_{err}^*$  between  $p^*(s = 20)$  and  $\tilde{p}^*$  as a function of  $\eta$  ( $\alpha = 0.055$ ).

### 6.3.3.4 Contribution of $\tilde{p}_\zeta^*$ , $\tilde{p}_\phi^*$ and $\tilde{p}_q^*$ to $\tilde{p}^*$ for both waves

The dimensionless radiation pressure  $\tilde{p}^*$  is composed of three terms: the dimensionless volumetric kinetic energy ( $\tilde{p}_\phi^*$ ), volumetric potential energy density ( $\tilde{p}_q^*$ ) and the term due to the motion of the object ( $\tilde{p}_\zeta^*$ ). The distributions of the three terms are compared in order to quantify how they contribute in the calculation of  $\tilde{p}^*$ . In the figures presented

hereafter,  $\tilde{p}^*$  will be reported as a continuous line and the three terms with symbol markers ( $\tilde{p}_\zeta^* = \circ$ ;  $\tilde{p}_\phi^* = \Delta$ ;  $\tilde{p}_q^* = \times$ ). The chosen conditions are  $\alpha = 0.055$  and  $\eta = 0.0013$  to illustrate their different weights.

**Standing wave**

**PAN** - The distribution of  $\tilde{p}^*$  around an object of cylindrical shape at PAN is reported in Figure 6.11 along with the three terms composing it. The terms  $\tilde{p}_\phi^*$  and  $\tilde{p}_\zeta^*$  are close to zero and the only contribution to  $\tilde{p}^*$  comes from the time-average volumetric potential acoustic energy density term,  $\tilde{p}_q^*$ . The distribution of  $\tilde{p}^*$  is uniform around the object, which corresponds to a uniform compression:  $\tilde{p}^* = \tilde{p}_q^* = \frac{1}{4}$ . In practice, the dimensional radiation pressure  $\tilde{p} = \tilde{p}_q$  is equal to  $\frac{\bar{P}}{4} = \frac{p_a^2}{4\rho_0 c_0^2}$ . It corresponds to the time-average acoustic energy per volume carried by the standing wave in an environment free from any obstacles. The integral of  $\tilde{p}^*$  around the object surface is null and thus also the dimensionless resulting radiation force  $\tilde{F}^*$ .

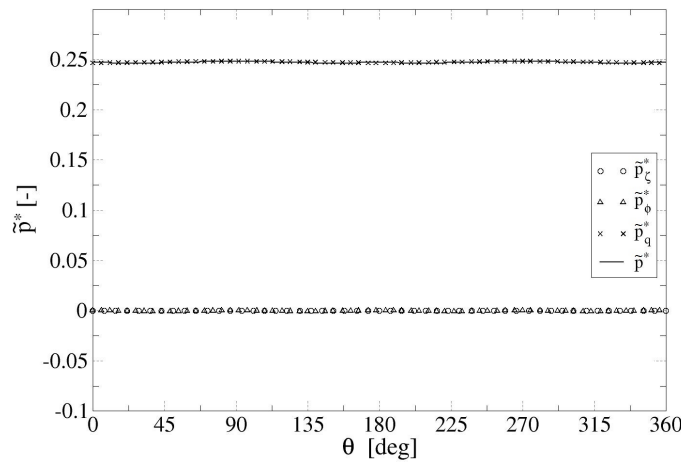


Figure 6.11: Comparison between  $\tilde{p}^*$  and  $\tilde{p}_\zeta^*$ ,  $\tilde{p}_\phi^*$  and  $\tilde{p}_q^*$  at PAN ( $h = \lambda/2$ ;  $\alpha = 0.055$ ;  $\eta = 0.0013$ ;  $f = 1000 \text{ Hz}$ ;  $c_0 = 340 \text{ m/s}$ ).

**VAN** - When the object is placed at VAN the radiation pressure distribution is that reported in Figure 6.12. At this location the object is submitted to the maximum amplitude of the acoustic velocity fluctuations and the only term contributing to  $\tilde{p}^*$  is that corresponding to the time-averaged volumetric kinetic acoustic energy  $\tilde{p}_\phi^*$ . The resulting distribution of  $\tilde{p}^*$  is negative with two minima corresponding to the two pole points at  $\theta = 90^\circ$  and  $\theta = 270^\circ$  (see Figure 6.1;  $\tilde{p}^*$  is null at the two equatorial points ( $\theta = 0^\circ$  and  $\theta = 180^\circ$ )). The distribution produces a suction effect which is maximum in the direction perpendicular to the acoustic axis. Jointly, the integral of  $\tilde{p}^*$  leads to a zero resulting

radiation force.

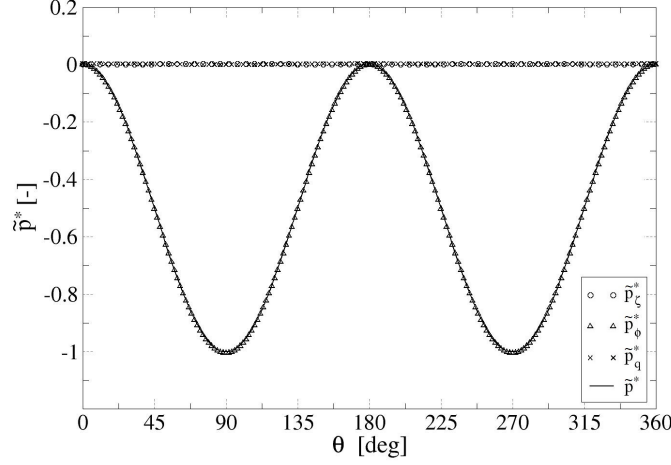


Figure 6.12: Comparison between  $\tilde{p}^*$  and  $\tilde{p}_\zeta^*$ ,  $\tilde{p}_\phi^*$  and  $\tilde{p}_q^*$  at VAN ( $h = \lambda/4$ ;  $\alpha = 0.055$ ;  $\eta = 0.0013$ ;  $f = 1000$  Hz;  $c_0 = 340$  m/s).

**IAN** - The distributions of  $\tilde{p}^*$  when the object is placed at IAN is reported in Figure 6.13. At this location, where both acoustic velocity and pressure fluctuations present important amplitudes, two terms are revealed to contribute to the final distribution of  $\tilde{p}^*$ ;  $\tilde{p}_\phi^*$  corresponding to the time-averaged volumetric kinetic acoustic energy and  $\tilde{p}_q^*$  that corresponding to the time-averaged volumetric potential energy density. The term  $\tilde{p}_\zeta^*$  is close to zero. The evolution is similar to that obtained at VAN, producing a suction effect around the cross section with a maximum action near the pole points ( $\theta = 90^\circ$  and  $\theta = 270^\circ$ ). The quantity  $\tilde{p}_q^*$  gives rise to a compression effect (positive values) with a maximum at the position  $\theta = 180^\circ$  and a minimum at the position  $\theta = 0^\circ$ , corresponding to the two equatorial points where additionally  $\tilde{p}_\phi^*$  is zero. This difference of  $\approx 36\%$  in the local compression action leads to a non-symmetric distribution of  $\tilde{p}^*$  around the cross-section. Consequently it produces a non-null integral of the radiation pressure leading to a non-zero resulting force modulus  $\tilde{F}^*$ . As  $\tilde{F}^* > 0$ , the force is pointed in the y-direction toward VAN. Moreover, by comparing the areas under the curve  $\tilde{p}^*(\theta)$ , it is clearly highlighted that the suction phenomenon strongly dominates against the compression one.

Figure 6.14 reports the maximum and minimum values extracted from the profile  $\tilde{p}^*(\theta)$  as functions of the position  $h$  in the acoustic field, for  $\alpha = 0.055$  and  $\eta = 0.0013$ . Compression effect (positive values) is maximum at PAN ( $|\tilde{p}^*| \approx 0.25$ ) and zero at VAN, whereas the suction has a maximum at VAN ( $|\tilde{p}^*| \approx 1$ ) and is zero in between IAN and PAN. Moving from VAN to PAN the suction effect decreases and the compression one

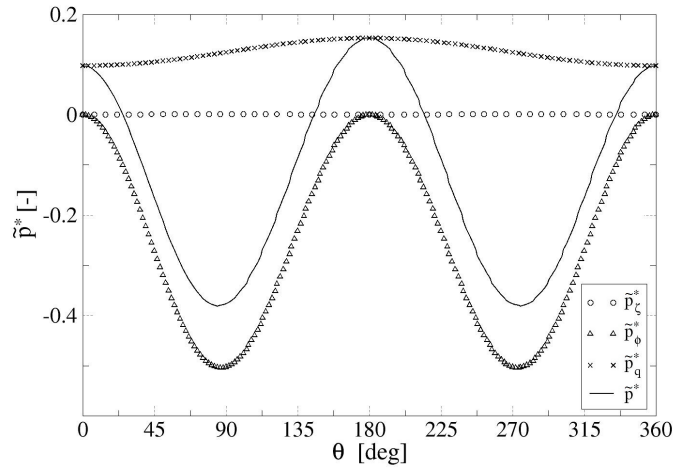


Figure 6.13: Comparison between  $\tilde{p}^*$  and  $\tilde{p}_\zeta^*$ ,  $\tilde{p}_\phi^*$  and  $\tilde{p}_q^*$  at IAN ( $h = \lambda/8$ ;  $\alpha = 0.055$ ;  $\eta = 0.0013$ ;  $f = 1000 \text{ Hz}$ ;  $c_0 = 340 \text{ m/s}$ ).

increases until counterbalance the suction action in a zone located between IAN and PAN, close to the position where the suction effects become zero. In the region near PAN only compression effects are present.

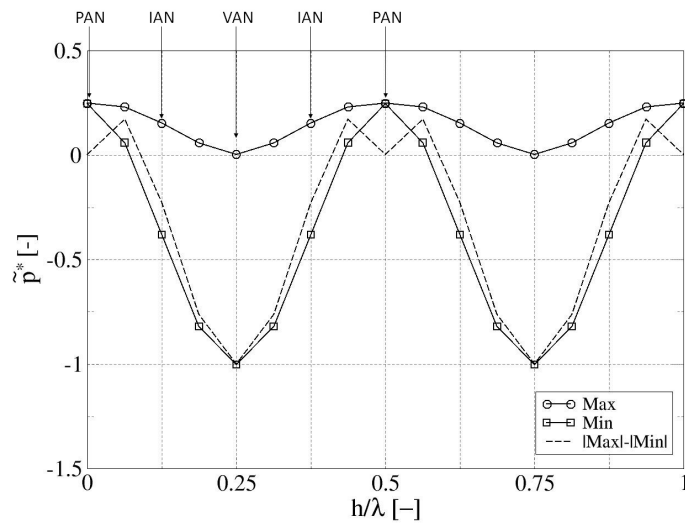


Figure 6.14: Comparison between the dimensionless radiation pressure maximum and minimum values and their difference, on a cylindrical object in a standing wave field as a function of  $h$  ( $\alpha = 0.055$ ,  $\eta = 0.0013$ ).

### Progressive wave

The distribution of  $\tilde{p}^*$  for the progressive wave, and of the three terms composing it, is reported in Figure 6.15. The situation is similar to that observed at an intermediate point

in between VAN and PAN. Here,  $\tilde{p}_q^*$  appears to vary as a positive constant, which induces a translation of the distribution without any modification of the shape of  $\tilde{p}_\phi^*$ . Actually, the asymmetry of  $\tilde{p}_q^*$  is so small that it cannot be visible at naked eye on the diagram. The dimensionless resulting radiation force  $\tilde{F}^*$  seems zero, which is consistent with its expression given in Eq. 6.64 whose order of magnitude is very small ( $\alpha^3$ ).

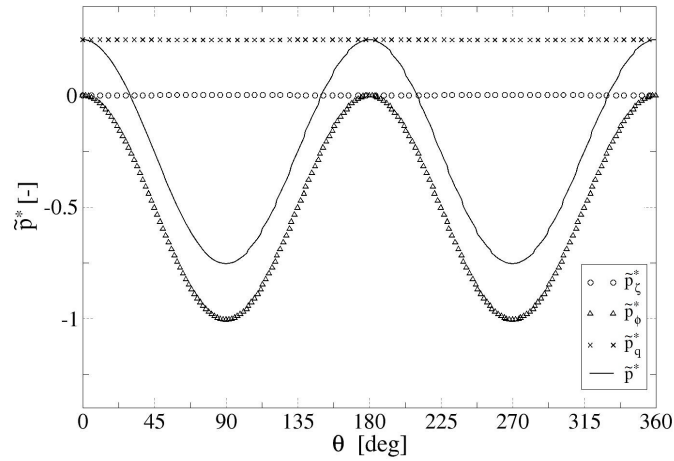


Figure 6.15: Comparison between  $\tilde{p}^*$  and  $\tilde{p}_\zeta^*$ ,  $\tilde{p}_\phi^*$  and  $\tilde{p}_q^*$  in a progressive wave field ( $\alpha = 0.055$ ;  $\eta = 0.0013$ ;  $f = 1000$  Hz;  $c_0 = 340$  m/s).

### 6.3.3.5 Asymptotic Approximate Expressions for both Standing and Progressive Waves

For a fixed value of  $\alpha$  the dimensionless approximate radiation pressure distributions  $\tilde{p}^*$  evolve with  $\eta$ . The only exception is represented by PAN for which  $\tilde{p}^* = 1/4$  for all values of  $\alpha$  and  $\eta$  (see Figure 6.11). In all other positions, expressions can be further simplified by considering the limits for  $\eta \rightarrow 0$  and  $\eta \rightarrow \infty$ .

The asymptotic expressions for  $\eta \rightarrow 0$  and  $\eta \rightarrow \infty$  of dimensionless radiation pressure  $\tilde{p}^*$ , of the three terms ( $\tilde{p}_\zeta$ ,  $\tilde{p}_\phi$  and  $\tilde{p}_q$ ) and also of the radiation force per unit length ( $\tilde{F}^*$ ) are summarized in Tables 6.3 and 6.4 for standing and progressive waves respectively.

Asymptotic expressions for SW		
$\eta \rightarrow 0$	$\tilde{p}_\zeta \rightarrow 0$ $\tilde{p}_\phi \rightarrow -\sin^2 \theta$ $\tilde{p}_q \rightarrow \frac{1}{4} \cos^2 kh$	$\tilde{p}^* \rightarrow \frac{\cos^2 kh}{4} - \sin^2 kh \sin^2 \theta$ $\tilde{F}^* \rightarrow \frac{3\pi\alpha}{4} \sin 2kh$
$\eta \rightarrow \infty$	$\tilde{p}_\zeta \rightarrow 2 \sin^2 kh \cos^2 \theta$ $\tilde{p}_\phi \rightarrow -\sin^2 kh \cos^2 \theta$ $\tilde{p}_q \rightarrow \frac{1}{4} \cos^2 kh$	$\tilde{p}^* \rightarrow \frac{\cos^2 kh}{4} + \sin^2 kh \cos^2 \theta$ $\tilde{F}^* \rightarrow \frac{-\pi\alpha}{4} \sin 2kh$

Table 6.3: Asymptotic approximate expressions of the dimensionless radiation pressure, of its three contributions and of the modulus of the radiation force per unit length for a standing wave.

Asymptotic expressions for PW		
$\eta \rightarrow 0$	$\tilde{p}_\zeta^* \rightarrow 0$ $\tilde{p}_\phi^* \rightarrow -\sin^2 \theta$ $\tilde{p}_q^* \rightarrow \frac{1}{4}$	$\tilde{p}^* \rightarrow \frac{1}{4} - \sin^2 \theta$ $\tilde{F}^* \rightarrow \frac{5\pi^2\alpha^3}{8}$
$\eta \rightarrow \infty$	$\tilde{p}_\zeta^* \rightarrow 2 \cos^2 \theta$ $\tilde{p}_\phi^* \rightarrow -\cos^2 \theta$ $\tilde{p}_q^* \rightarrow \frac{1}{4}$	$\tilde{p}^* \rightarrow \frac{1}{4} + \cos^2 \theta$ $\tilde{F}^* \rightarrow \frac{\pi^2\alpha^3}{8}$

Table 6.4: Asymptotic approximate expressions of the dimensionless radiation pressure, of its three contributions and of the modulus of the radiation force per unit length for a progressive wave.

### 6.3.3.6 Influence of $\eta$

In this section the asymptotic expressions of  $\tilde{p}^*$  are compared with the two cases:  $\eta = 0.0013$ , corresponding to a liquid cylinder in the air, and  $\eta = 7$ , corresponding to a warm

gas cylinder in a colder gaseous environment. Solutions calculated for  $\eta = 0.5$  and  $\eta = 3$  are also considered.

### Standing wave

**VAN** - For a cylindrical object placed at VAN the spatial distribution of the acoustic radiation pressure with respect to  $\theta$  and for the different values of  $\eta$  is reported in Figure 6.16(a). Figure 6.16(b) shows how the maximum and minimum values of  $\tilde{p}^*$  varies with  $\eta$ , as well as their difference. Whatever  $\eta$  the distribution of  $\tilde{p}^*$  is always non-uniform and symmetrical, which implies that  $\tilde{F}^* = 0$ . The distribution for  $\eta = 0.0013$  is always negative and is the same as that of the asymptotic distribution for  $\eta \rightarrow 0$ . The object is submitted to a suction effect mainly in the direction perpendicular to the acoustic axis. By increasing  $\eta$  the suction decreases and the compression in the direction of the acoustic axis increases (see Figure 6.16(b)). For  $\eta \geq 0.5$  the distribution of  $\tilde{p}^*$  is positive at any values of  $\theta$ . There the object is submitted to a compression effect in all the directions around the cylinder, but stronger in the direction parallel to the acoustic axis. In the limit case  $\eta \rightarrow \infty$  the object is submitted only to a large compression, mainly in the direction parallel to a.a., and the difference between the maximum and minimum values of  $\tilde{p}^*$  tends to 1. This distribution is anti-symmetric with respect to that noted with  $\eta \rightarrow 0$  in which the object is submitted only to a large suction effect in the direction perpendicular to a.a..

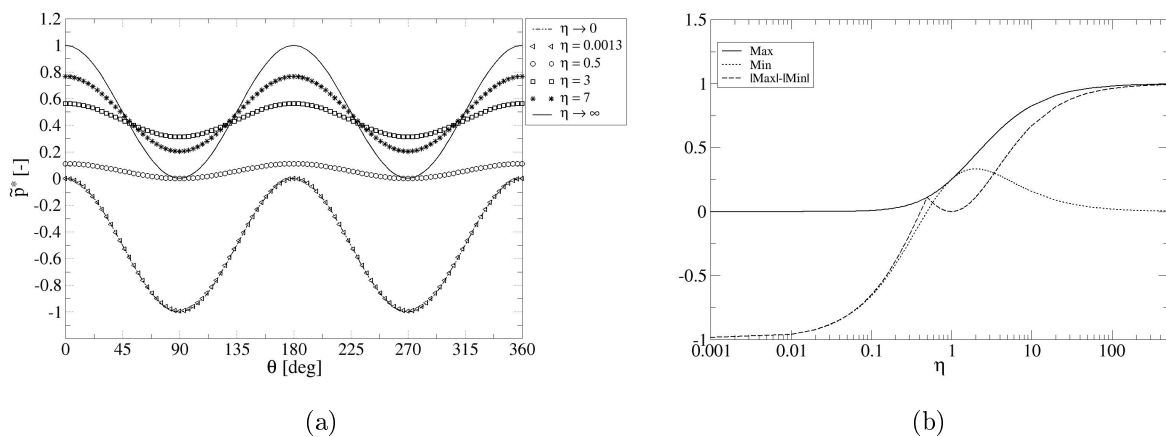


Figure 6.16: (a) Radiation pressure distribution at VAN around a cylindrical object in a standing wave field as a function of  $\eta$  ( $\alpha \ll 1$ ). (b) Comparison between the radiation pressure distribution  $\tilde{p}^*$  maximum, minimum and their difference at VAN around a cylindrical object in a standing wave field as a function of  $\eta$  ( $h = \lambda/4$ ;  $\alpha \ll 1$ ;  $f = 1000$  Hz).

**IAN** - The distribution of  $\tilde{p}^*$  at IAN is shown in Figure 6.17(a). Similarly to what

observed at VAN the distribution for  $\eta = 0.0013$  is the same as for  $\eta \rightarrow 0$ . For  $\eta \leq 3$  the (absolute) maximum of  $\tilde{p}^*$  is at  $\theta = 180^\circ$ , but for  $\eta \geq 3$  it is at  $\theta = 0$  (or  $\theta = 360^\circ$ ). Figure 6.17(b) shows the maximum and minimum values of  $\tilde{p}^*$  as functions of  $\eta$ , along with their difference. For  $\eta \rightarrow 0$  suction is stronger than compression. For  $\eta \rightarrow \infty$  only compression is present, and the difference between the maximum and minimum values of  $\tilde{p}^*$  tends to 0.5.

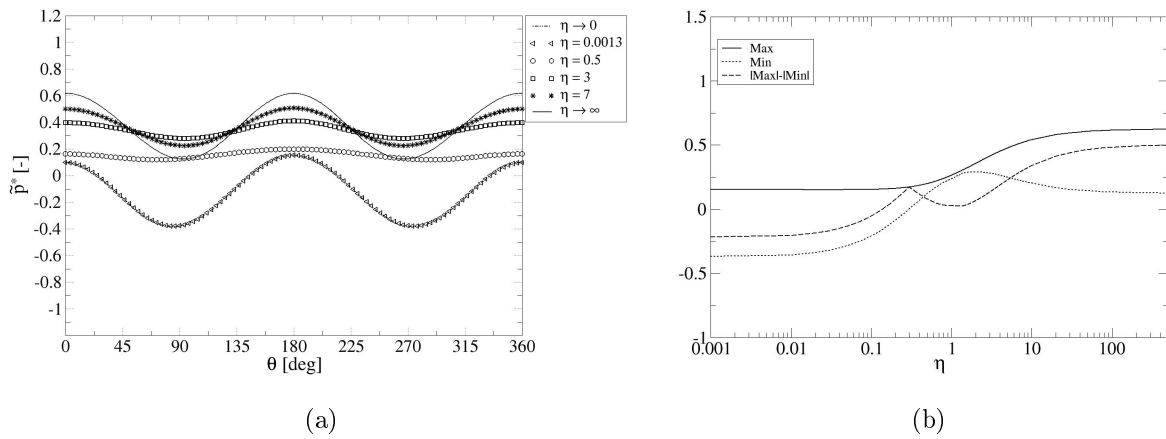


Figure 6.17: (a) Radiation pressure distribution at IAN around a cylindrical object in a standing wave field as a function of  $\eta$  ( $\alpha \ll 1$ ). (b) Comparison between the radiation pressure distribution  $\tilde{p}^*$  maximum, minimum and their difference at IAN around a cylindrical object in a standing wave field as a function of  $\eta$  ( $h = \lambda/4$ ;  $\alpha \ll 1$ ;  $f = 1000$  Hz).

Figure 6.18(a) shows  $\tilde{F}^*$  at IAN as a function of  $\eta$ . The force changes its sign at  $\eta = 3$  and for  $\eta \rightarrow 0$  force tends to maximum value  $\tilde{F}^* \approx 0.13$ , whereas for  $\eta \rightarrow \infty$   $\tilde{F}^* \rightarrow -0.048$ .

In Figure 6.18(b) the variation of  $\tilde{F}^*$  is reported as a function of the object position  $h$  in the acoustic field for the different values  $\eta$ . For  $\eta = 3$   $\tilde{F}^* = 0$  and across  $\eta = 3$  the force changes its sign with  $h$ . For  $\eta < 3$   $\tilde{F}^*$  is directed toward the closest velocity anti-node whereas for  $\eta > 3$  it is toward the closest pressure anti-node (see Figure 6.18(b)).

### Progressive wave

The distributions of  $\tilde{p}^*$  in the case of a progressive wave field for the different values of  $\eta$  are reported in Figure 6.19(a). The maximum and minimum values of  $\tilde{p}^*$ , as well as their difference, are reported in Figure 6.19(b) as functions of  $\eta$ . As for the standing wave, suction effect is stronger for small values of  $\eta$ . Indeed, for  $\eta \rightarrow 0$   $\max|\tilde{p}^*| - \min|\tilde{p}^*|$  tends to -0.5. By increasing  $\eta$  only compression is observed, and  $\max|\tilde{p}^*| - \min|\tilde{p}^*|$  tends to 1. The radiation force (see Figure 6.20) in this case present a minimum value  $\tilde{F}^* = 0.000105$

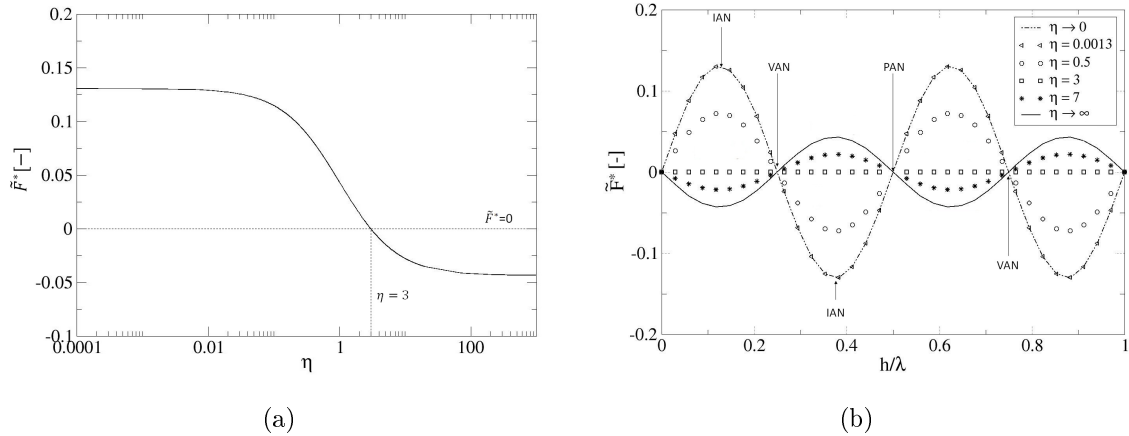


Figure 6.18: (a) Dimensionless radiation force per unit length  $\tilde{F}^*$  at IAN ( $h = \lambda/8$ ) acting on a cylindrical object placed in a standing wave field as a function of  $\eta$  ( $\alpha \ll 1$ ). (b) Dimensionless radiation force per unit length  $\tilde{F}^*$  around a cylindrical object in a standing wave field as a function of  $h$  and  $\eta$  ( $\alpha \ll 1$ ). For  $\eta < 3$   $\tilde{F}^*$  is directed toward the nearest VAN, whereas for  $\eta > 3$  it is directed toward the nearest PAN.

for  $\eta = 3$ . For any value of  $\eta$  is always at least 2 order of magnitude lower than the radiation force in the case of a standing wave. For  $\eta \rightarrow 0$   $\tilde{F}^* \rightarrow 0.00105$ , whereas for  $\eta \rightarrow \infty$   $\tilde{F}^* \rightarrow 0.000209$ .

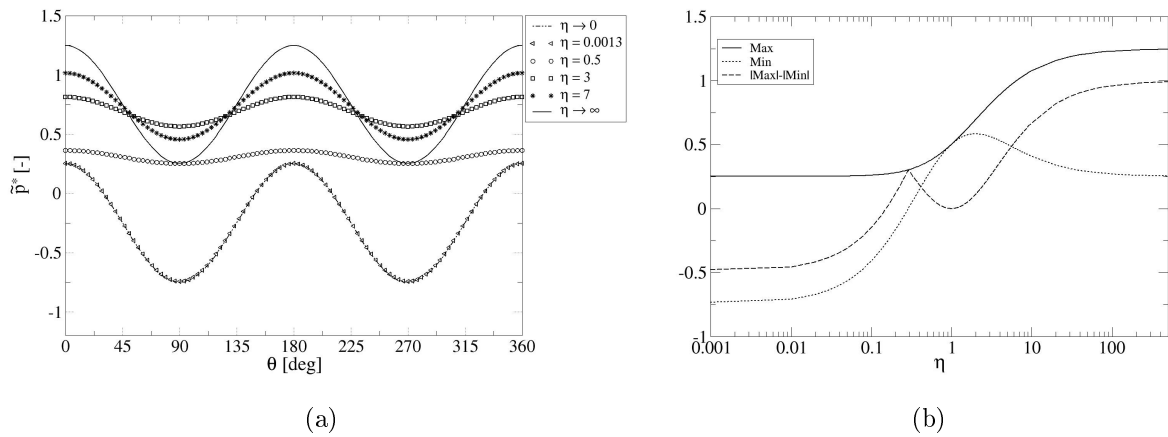


Figure 6.19: (a) Radiation pressure distribution around a cylindrical object in a progressive wave field as a function of  $\eta$  ( $\alpha \ll 1$ ). (b) Comparison between the radiation pressure distribution  $\tilde{p}^*$  maximum, minimum and their difference around a cylindrical object in a progressive wave field as a function of  $\eta$  ( $h = \lambda/4$ ;  $\alpha \ll 1$ ;  $f = 1000$  Hz).

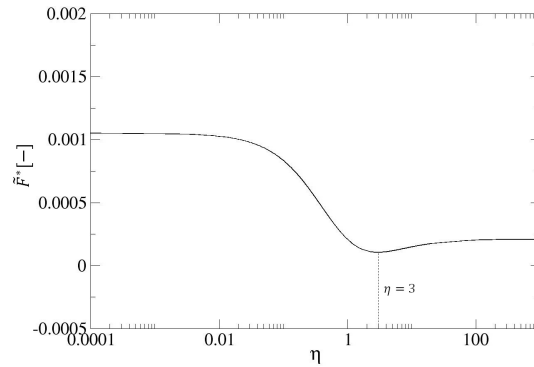


Figure 6.20: Dimensionless radiation force per unit length  $\tilde{F}^*$  around a cylindrical object in a progressive wave field as a function of  $\eta$  ( $\alpha \ll 1$ ).

## 6.4 Spherical Objects

In section 6.3 the expressions of radiation pressure and force have been derived for the case of a cylindrical object. Following a similar procedure the expressions for spherical objects submitted to acoustic nonlinear effects are developed in this section. This case, of great interest in the field of microgravity, especially for applications concerning the *acoustic levitation*, usually focuses on the analytical determination of the radiation force which can counterbalance gravity. However, in our study, the radiation pressure is also an important quantity since its distribution can justify deformation of the particles, and even secondary atomization. Hereafter, we will use the classical approach used by King [93] to set the equations for both acoustic radiation pressure and force. At first, but limited, calculation was also given in Baillot *et al.* [90, 89]. A fine and systematic analysis is proposed in the following.

Let consider the case of a rigid sphere of radius  $a$  placed in an ideal fluid and subjected to an harmonic acoustic field. According to King the velocity potential, the sum of incident and scattered velocity potentials, can be expressed as:

$$\phi = \phi_i + \phi_r = \cos \omega t \sum_{n=0}^{\infty} R_n P_n(\nu) + \sin \omega t \sum_{n=0}^{\infty} S_n P_n(\nu) \quad (6.66)$$

where  $P_n(\nu)$  is the Legendre polynomial of order  $n$  and  $\nu = \cos \theta$ , with  $\theta$  denoting the angle with respect to the acoustic axis. The  $R_n$  and  $S_n$  coefficients are characteristic functions of the acoustic field and their general expressions are given by:

$$R_n = \frac{|A_n|}{H_n(\alpha)} \frac{\cos(\beta_n + \epsilon_n)}{\alpha^{n+1}} \quad (6.67)$$

$$S_n = -\frac{|A_n|}{H_n(\alpha)} \frac{\sin(\beta_n + \epsilon_n)}{\alpha^{n+1}} \quad (6.68)$$

Here again  $\alpha = ka$  with  $k = \omega/c_0$  the wave number,  $A_n$  is the coefficient of the incident radiation field  $\phi_i$ . Factors  $\beta_n$  depend on the nature of the acoustic wave (standing or progressive), they are defined in the next sections.  $H_n$  and  $\epsilon_n$  are combinations of spherical wave functions with:

$$H_n^2 = F_n^2 + G_n^2 \quad \cos \epsilon_n = \frac{F_n}{H_n} \quad \sin \epsilon_n = \frac{G_n}{H_n} \quad (6.69)$$

Referring to an origin at the center of the sphere moving under the action of the acoustic field we can write  $\dot{\phi}$  as:

$$\dot{\phi} = \frac{D\phi}{Dt} - \dot{\zeta} \cos \theta \frac{\partial \phi}{\partial r} + \dot{\zeta} \frac{\sin \theta}{r} \frac{\partial \phi}{\partial \theta} \quad (6.70)$$

where  $\dot{\zeta}$  is the velocity of the center of the sphere along the y-axis, which is given by:

$$\dot{\zeta} = -k\eta \frac{1}{\alpha} (R_1 \cos \omega t + S_1 \sin \omega t) \quad (6.71)$$

Parameter  $\eta$  is the ratio of the density of the fluid  $\rho_0$  over the density of the sphere  $\rho_1$  ( $\eta = \rho_0/\rho_1$ ). Since the fluid must remain in contact with the sphere the following boundary condition ( $r = a$ ) must be also satisfied:

$$-\left(\frac{\partial \phi}{\partial r}\right)_{r=a} = \dot{\zeta} \cos \theta \quad (6.72)$$

### 6.4.1 General Expressions

Eq. 6.8 indicates that the radiation pressure is composed of three terms. The first time-average contribution on the sphere ( $r = a$ ) is given by the sphere displacement:

$$p_\zeta = \frac{1}{T} \int_0^T \rho_0 \dot{\phi} dt \quad (6.73)$$

Considering Eq. 6.70 and taking the time average over the period  $T$  we obtain that the first term is null while the expressions of the two others terms can be calculated as:

$$\left[ -\dot{\zeta} \cos \theta \frac{\partial \phi}{\partial r} + \dot{\zeta} \frac{\sin \theta}{r} \frac{\partial \phi}{\partial \theta} \right]_{r=a} = \dot{\zeta}^2 \cos^2 \theta + \dot{\zeta} \frac{\sin \theta}{a} \frac{\partial \phi}{\partial \theta} \quad (6.74)$$

where

$$\zeta^2 = k^2 \eta^2 \frac{1}{\alpha^2} (R_1^2 \cos^2 \omega t + S_1 \sin^2 \omega t + 2R_1 S_1 \cos \omega t \sin \omega t) \quad (6.75)$$

and

$$\frac{\partial \phi}{\partial \theta} = \frac{\partial \phi}{\partial \nu} \frac{\partial \nu}{\partial \theta} = - \left[ \cos \omega t \sum_{n=0}^{\infty} R_n P_n'(\nu) + \sin \omega t \sum_{n=0}^{\infty} S_n P_n'(\nu) \right] \sin \theta \quad (6.76)$$

Quantity  $(P_n'(\nu))$  is the derivative of Legendre polynomial of order  $n$ .  $\phi$  is obtained from Eq. 6.70 by substituting Eq. 6.75 and 6.76 into Eq. 6.74. Finally  $p_\zeta$  at  $r = a$  is deduced from Eq. 6.73:

$$p_\zeta = \rho_0 \frac{1}{2} \frac{k^2}{\alpha^2} \eta^2 (R_1^2 + S_1^2) \cos^2 \theta + \frac{k\eta\rho_0}{2a\alpha} \left[ R_1 \sum_{n=0}^{\infty} R_n P_n' + S_1 \sum_{n=0}^{\infty} S_n P_n' \right] \sin^2 \theta \quad (6.77)$$

Term by term integration of Eq. 6.77 over the sphere surface gives the contribution of  $p_\zeta$ . The second contribution to the radiation pressure at  $r = a$  is given by time averaging the potential acoustic energy per unit volume:

$$p_\phi = \frac{1}{T} \int_0^T \frac{1}{2} \frac{\rho_0}{c_0^2} \dot{\phi}^2 dt \quad (6.78)$$

The preceding calculations give:

$$\dot{\phi} = -\omega \left( \sin \omega t \sum_{n=0}^{\infty} R_n P_n(\nu) - \cos \omega t \sum_{n=0}^{\infty} S_n P_n(\nu) \right) \quad (6.79)$$

and

$$\begin{aligned} \dot{\phi}^2 = \omega^2 \left[ \sin^2 \omega t \left( \sum_{n=0}^{\infty} R_n P_n(\nu) \right)^2 + \cos^2 \omega t \left( \sum_{n=0}^{\infty} S_n P_n(\nu) \right)^2 \right. \\ \left. - \sin \omega t \cos \omega t \sum_{n=0}^{\infty} R_n P_n(\nu) \sum_{n=0}^{\infty} S_n P_n(\nu) \right] \end{aligned} \quad (6.80)$$

The time average of Eq. 6.80 provides the expression of  $p_\phi$ :

$$p_\phi = \frac{1}{4} \frac{\omega^2}{c_0^2} \rho_0 \left[ \left( \sum_{n=0}^{\infty} R_n P_n(\nu) \right)^2 + \left( \sum_{n=0}^{\infty} S_n P_n(\nu) \right)^2 \right] \quad (6.81)$$

The last contribution to the radiation pressure at  $r = a$  is given by the time average

of the kinetic acoustic energy per unit volume:

$$p_q = \frac{1}{T} \int_0^T [-\frac{1}{2}\rho_0(\vec{\nabla}\phi)^2] dt \quad (6.82)$$

Considering the boundary condition given by Eq. 6.72 and the fact that  $\phi$  only depends on  $\theta$  and  $r$  we can express the square of the gradient of  $\phi$  as follows:

$$(\vec{\nabla}\phi)^2 = \left[ \zeta^2 \cos^2 \theta + \frac{1}{a^2} \left( \frac{\partial\phi}{\partial\theta} \right)^2 \right]_{r=a} \quad (6.83)$$

The first term of the previous equation has already been treated in the calculation of  $p_\zeta$ , while the second one can be easily obtained by taking the time average of the square of Eq.6.76. The sum of the 2 terms gives rise to:

$$p_q = -\rho_0 \frac{1}{4} \frac{k^2}{\alpha^2} \eta^2 (R_1^2 + S_1^2) \cos^2 \theta - \frac{\rho_0}{4a^2} \left[ \left( \sum_{n=0}^{\infty} R_n P'_n \right)^2 + \left( \sum_{n=0}^{\infty} S_n P'_n \right)^2 \right] \sin^2 \theta \quad (6.84)$$

Adding the three contributions calculated above leads to a general form for the acoustic radiation pressure, expressed by:

$$\begin{aligned} p_{rad} = & -\frac{\rho_0}{4a^2} \underbrace{\left[ \left( \sum_{n=0}^{\infty} R_n P'_n(\nu) \right)^2 + \left( \sum_{n=0}^{\infty} S_n P'_n(\nu) \right)^2 \right]}_{\text{Baillot et al.}} \sin^2 \theta + \\ & \frac{\rho_0}{4a^2} k^2 \underbrace{\left[ \left( \sum_{n=0}^{\infty} R_n P_n(\nu) \right)^2 + \left( \sum_{n=0}^{\infty} S_n P_n(\nu) \right)^2 \right]}_{\text{Baillot et al.}} + \\ & \frac{\rho_0}{2a^2} \eta \left[ R_1 \sum_{n=0}^{\infty} R_n P'_n(\nu) + S_1 \sum_{n=0}^{\infty} S_n P'_n(\nu) \right] \sin^2 \theta + \\ & \frac{\rho_0}{4a^2} \eta^2 (R_1^2 + S_1^2) \cos^2 \theta \end{aligned} \quad (6.85)$$

The first two terms represent the  $p_{rad}$  expression already found by Baillot *et al.* [90, 89] for the case  $\eta \ll 1$ . The coefficients  $R_n$  and  $S_n$  depends on the kind of wave considered.

### Standing wave

For a standing wave  $|A_n| = |A| (2n + 1) \cos(kh + \frac{1}{2}n\pi)$  and  $\beta_n = 0$ . The coefficients  $R_n$  and  $S_n$  are then rewritten as:

$$R_n = \frac{F_n |A|}{H_n^2 \alpha^{n+1}} (2n + 1) \cos(kh + \frac{1}{2}n\pi) \quad (6.86)$$

$$S_n = -\frac{G_n |A|}{H_n^2 \alpha^{n+1}} (2n+1) \cos(kh + \frac{1}{2}n\pi) \quad (6.87)$$

### Progressive wave

In the case of a progressive wave  $|A_n| = |A|(2n+1)$  and  $\beta_n = -\frac{1}{2}n\pi$ , thus the coefficients  $R_n$  and  $S_n$  can be written as:

$$R_n = \frac{|A|}{H_n \alpha^{n+1}} (2n+1) \cos(\beta_n + \varepsilon_n) \quad (6.88)$$

$$S_n = -\frac{|A|}{H_n \alpha^{n+1}} (2n+1) \sin(\beta_n + \varepsilon_n) \quad (6.89)$$

## 6.4.2 Truncated expressions

We assume that the convergence of the series could be approximated by keeping the terms until  $n = 2$  as demonstrated in section 6.3 for the cylinder. Expanding the summations until  $n = 2$  and rearranging the terms in Eq. 6.85 lead to the following truncated relationship for  $p_{rad}$ :

$$p_{rad} = -\frac{\rho_0}{4a^2} \left[ (R_1^2 + S_1^2)B_1 + (R_2^2 + S_2^2)B_2 - \alpha^2 \left( (R_0^2 + S_0^2) + 2(R_0R_1 + S_0S_1)B_{01} + (R_0R_2 + S_0S_2)B_{02} \right) \right] \quad (6.90)$$

with

$$B_1 = -\eta^2 \cos^2 \theta + (1 - 2\eta) \sin^2 \theta - \alpha^2 \quad (6.91)$$

$$B_2 = 9 \cos^2 \theta \sin^2 \theta - \frac{\alpha^2}{4} (3 \cos^2 \theta - 1)^2 \quad (6.92)$$

$$B_{01} = \cos \theta \quad (6.93)$$

$$B_{02} = 3 \cos^2 \theta - 1 \quad (6.94)$$

The same procedure is carried out to calculate the truncated expression of the resulting radiation force. First, expanding the sum in Eq. 6.77 up to  $n = 2$  and integrating over the sphere surface provides the contribution of  $p_\zeta$  to the radiation force:

$$F_\zeta = -2\pi a^2 \int_0^\pi p_\zeta \sin \theta \cos \theta d\theta = -\frac{4}{5} \pi \eta \rho_0 (R_1R_2 + S_1S_2) \quad (6.95)$$

Similarly expanding the sum in Eq. 6.81 up to  $n = 2$  and integrating over the sphere

surface provides the contribution of  $p_\phi$  to the radiation force:

$$F_\phi = -\frac{2}{3}\pi\rho_0\alpha^2\left[(R_0R_1 + S_0S_1) + \frac{2}{5}(R_1R_2 + S_1S_2)\right] \quad (6.96)$$

Finally the contribution of  $p_q$  to the radiation force expression is obtained from Eq. 6.84 :

$$F_q = \frac{4}{5}\pi\rho_0(R_1R_2 + S_1S_2) \quad (6.97)$$

The truncated expression of the radiation force is then deduced by adding the three contributions:

$$F_{rad} = \pi\rho_0\left[\frac{4}{5}(R_1R_2 + S_1S_2)\left(1 - \eta - \frac{\alpha^2}{3}\right) - \frac{2}{3}\alpha^2(R_0R_1 + S_0S_1)\right] \quad (6.98)$$

Equations 6.90 and 6.98 depend on the coefficients  $R_n$  and  $S_n$  which in turns, depend on the acoustic wave characteristics (e.g. standing or progressive acoustic waves).

### 6.4.3 Small Objects Approximation ( $\alpha \ll 1$ )

Under the small objects hypothesis ( $\alpha = ka \ll 1$ ), the coefficients  $F_n$ ,  $G_n$ ,  $H_n$ , the Legendre polynomials  $P_0(\nu)$  and their derivatives  $P'_0(\nu)$  can be expressed as follows:

n	0	1	2	3
$F_n$	$1/\alpha$	$(2 + \eta)/\alpha^3$	$9/\alpha^5$	$60\alpha^7$
$G_n$	$\alpha^2/3$	$\alpha^2/15 - (1 - \eta)/3$	$\alpha^2/105 - 2/15$	$\alpha^2/945 - 3/105$
$H_n$	$(1 + \alpha^2)/\alpha^2$	$(2 + \eta)^2/\alpha^6$	$81/\alpha^{10}$	$3600/\alpha^{14}$
$P_0(\nu)$	1	$\nu$	$(3\nu^2 - 1)/2$	
$P'_0(\nu)$	0	1	$3\nu$	

Table 6.5: Coefficients defining the acoustic field for a spherical object under the hypothesis  $\alpha \ll 1$ .

For  $\alpha \ll 1$  King [93] demonstrated that  $F_{n+1}F_n \gg G_{n+1}G_n$ . The expressions of the radiation pressure and force can be thus simplified and approximate expressions can be obtained for both standing and progressive waves.

### 6.4.3.1 Approximate Expressions for a Standing Wave

In the case of a standing wave for  $\alpha \ll 1$ , and for  $n = 0, 1$  and  $2$  the following expressions for the coefficients  $R_n$  and  $S_n$  are deduced:

$$R_0 = \frac{|A|}{(1 + \alpha^2)} \cos(kh) \quad R_1 = -\frac{3|A|\alpha}{(2 + \eta)} \sin(kh) \quad R_2 = -\frac{5}{9} |A| \alpha^2 \cos(kh) \quad (6.99)$$

$$S_0 = -\frac{|A|\alpha^3}{3(1 + \alpha^2)} \cos(kh) \quad S_1 = -\frac{(1 - \eta)|A|\alpha^4}{(2 + \eta)^2} \sin(kh) \quad S_2 = -\frac{2|A|\alpha^7}{243} \cos(kh) \quad (6.100)$$

with

$$R_0^2 + S_0^2 = \frac{|A|^2}{(1 + \alpha^2)^2} \cos^2(kh) \quad (6.101)$$

$$R_1^2 + S_1^2 = 9 \frac{|A|^2}{(2 + \eta)^2} \alpha^2 \sin^2(kh) \quad (6.102)$$

$$R_2^2 + S_2^2 = \frac{25}{81} |A|^2 \alpha^4 \cos^2(kh) \quad (6.103)$$

By considering the conditions  $F_{n+1}F_n \gg G_{n+1}G_n$  [93], we also have

$$R_0R_1 + S_0S_1 = -\frac{3}{2} |A|^2 \sin(2kh) \frac{\alpha}{(1 + \alpha^2)(2 + \eta)} \quad (6.104)$$

$$R_1R_2 + S_1S_2 = \frac{5}{6} |A|^2 \sin(2kh) \frac{\alpha^3}{(2 + \eta)} \quad (6.105)$$

$$R_0R_2 + S_0S_2 = -\frac{5}{9} |A|^2 \cos^2(kh) \frac{\alpha^2}{(1 + \alpha^2)} \quad (6.106)$$

The approximate expressions of the acoustic radiation pressure and force are thus given by:

$$\tilde{p}_{rad} = -\frac{\rho_0}{4a^2} |A|^2 \alpha^2 \left[ \frac{9 \sin^2(kh)}{(2 + \eta)^2} [-\eta^2 \cos^2 \theta + (1 - 2\eta) \sin^2 \theta] - \cos^2(kh) \right] + O(\alpha^3) \quad (6.107)$$

$$\tilde{F}_{rad} = \pi \rho_0 |A|^2 \frac{\sin 2kh}{(2 + \eta)} \alpha^3 \left[ 1 + \frac{2}{3}(1 - \eta) \right] + O(\alpha^4) \quad (6.108)$$

### 6.4.3.2 Approximate Expressions for a Progressive Wave

For a progressive wave, and for  $n = 0, 1, 2$  we obtain:

$$R_0 = \frac{|A|}{(1 + \alpha^2)} \quad R_1 = -\frac{(1 - \eta)^2 |A| \alpha^4}{(2 + \eta)} \quad R_2 = -\frac{5}{9} |A| \alpha^2 \quad (6.109)$$

$$S_0 = -\frac{|A| \alpha^3}{3(1 + \alpha^2)} \quad S_1 = \frac{3 |A| \alpha}{(2 + \eta)} \quad S_2 = -\frac{2 |A| \alpha^7}{243} \quad (6.110)$$

And also

$$R_0^2 + S_0^2 = \frac{|A|^2}{(1 + \alpha^2)^2} \quad (6.111)$$

$$R_1^2 + S_1^2 = 9 \frac{|A|^2}{(2 + \eta)^2} \alpha^2 \quad (6.112)$$

$$R_2^2 + S_2^2 = \frac{25}{81} |A|^2 \alpha^4 \quad (6.113)$$

By considering that  $F_{n+1}F_n \gg G_{n+1}G_n$  [93], we finally obtain:

$$R_0R_1 + S_0S_1 = -\frac{3 |A|^2 \alpha^4}{(1 + \alpha^2)(2 + \eta)^2} \quad (6.114)$$

$$R_1R_2 + S_1S_2 = \frac{5}{9} \frac{|A|^2 \alpha^6}{(2 + \eta)^2} (1 - \eta) \quad (6.115)$$

$$R_0R_2 + S_0S_2 = -\frac{5}{9} \frac{|A|^2 \alpha^2}{(1 + \alpha^2)} \quad (6.116)$$

The approximate expression of the acoustic radiation pressure equation in this case is:

$$\tilde{p}_{rad} = -\frac{\rho_0}{4\alpha^2} |A|^2 \alpha^2 \left[ \frac{9}{(2+\eta)^2} [-\eta^2 \cos^2 \theta + (1 - 2\eta) \sin^2 \theta] - 1 \right] + O(\alpha^3) \quad (6.117)$$

while approximate expression of the radiation force can be written as:

$$\tilde{F}_{rad} = 2\pi\rho_0 |A|^2 \alpha^6 \frac{[1 + \frac{2}{9}(1 - \eta)^2]}{(2 + \eta)^2} + O(\alpha^8) \quad (6.118)$$

### 6.4.3.3 Dimensionless Expressions Analysis

As for the cylindrical object (see section 6.3), the expressions presented in the previous section are now normalized by the factor:

$$\bar{P} = \frac{p_a^2}{\rho_0 c_0^2} \quad (6.119)$$

In the following the dimensionless functions are specified by the superscript \* yet. On the basis of the approximate functions  $\tilde{p}(\alpha, \eta, \theta, h)$  and  $\tilde{F}(\alpha, \eta, \theta, h)$  obtained under the assumption  $\alpha = ka \ll 1$ , the dimensionless functions  $\tilde{p}^*(\alpha, \eta, \theta, h)$  and  $\tilde{F}^*(\alpha, \eta, \theta, h)$  are then defined by  $\tilde{p}^* = p_{rad}/\bar{P}$  and  $\tilde{F}^* = F_{rad}/a^2\bar{P}$ .

### Standing wave

$$\tilde{p}_\zeta^* = \frac{9}{2(2+\eta)^2}(\eta^2 \cos^2 \theta \sin^2(kh) + \eta \sin^2 \theta \sin^2(kh)) + \frac{5\alpha\eta}{4(2+\eta)} \sin 2kh \cos \theta \sin^2 \theta \quad (6.120)$$

$$\tilde{p}_q^* = \frac{1}{4} \cos^2(kh) - \frac{3\alpha}{4(2+\eta)} \cos \theta \sin 2kh \quad (6.121)$$

$$\tilde{p}_\phi^* = -\frac{9}{4(2+\eta)^2}(\eta^2 \cos^2 \theta \sin^2(kh) + \sin^2 \theta \sin^2(kh)) - \frac{5\alpha}{4(2+\eta)} \sin 2kh \cos \theta \sin^2 \theta \quad (6.122)$$

The sum of the three terms provides:

$$\begin{aligned} \tilde{p}^* = & -\frac{1}{4} \left[ \frac{9 \sin^2(kh)}{(2+\eta)^2} [-\eta^2 \cos^2 \theta + (1-2\eta) \sin^2 \theta] - \cos^2(kh) \right] \\ & + \frac{\alpha}{4(2+\eta)} [5\eta \sin^2 \theta - 3 - 5 \sin^2 \theta] \cos \theta \sin 2kh \end{aligned} \quad (6.123)$$

The resulting radiation force is defined as:

$$\tilde{F}^* = \frac{\pi\alpha}{(2+\eta)} \sin 2kh \left[ 1 + \frac{2}{3}(1-\eta) \right] \quad (6.124)$$

### Progressive wave

The expressions of the three terms for a progressive wave are independent of  $h$ , and are given by:

$$\tilde{p}_\zeta^* = \frac{9}{2(2+\eta)^2}(\eta^2 \cos^2 \theta + \eta \sin^2 \theta) - \frac{3\eta}{2(2+\eta)^2} \alpha^2 \sin^2 \theta + \frac{5\eta(1-\eta)}{6(2+\eta)^2} \alpha^4 \cos \theta \sin^2 \theta \quad (6.125)$$

$$\tilde{p}_q^* = \frac{1}{4} - \frac{5}{36}(3 \cos^2 \theta - 1) \alpha^2 - \frac{3\alpha^4}{2(2+\eta)^2} \cos \theta + \frac{25\alpha^4}{81} \frac{(3 \cos^2 \theta - 1)}{8} \quad (6.126)$$

$$\tilde{p}_\phi^* = -\frac{9}{4(2+\eta)^2}(\eta^2 \cos^2 \theta + \sin^2 \theta) - \frac{225}{324} \alpha^2 \cos^2 \theta \sin^2 \theta - \frac{15(1-\eta)}{18(2+\eta)^2} \alpha^4 \cos \theta \sin^2 \theta \quad (6.127)$$

The expression of  $\tilde{p}^*$  obtained by adding the three terms is:

$$\tilde{p}^* = -\frac{1}{4} \left[ \frac{9}{(2+\eta)^2} [-\eta^2 \cos^2 \theta + (1-2\eta) \sin^2 \theta] - 1 \right] \quad (6.128)$$

and the resulting radiation force becomes:

$$\tilde{F}^* = 2\pi\alpha^4 \frac{[1 + \frac{2}{9}(1-\eta)^2]}{(2+\eta)^2} \quad (6.129)$$

#### 6.4.3.4 Contribution of $\tilde{p}_\zeta^*$ , $\tilde{p}_\phi^*$ and $\tilde{p}_q^*$ to $\tilde{p}^*$ for both waves

##### Standing wave

The different quantities are first studied as spatial functions of the angle  $\theta$  around the sphere surface, for  $\eta = 0.0013$ . As for the cylinder, when the sphere is placed at PAN the radiation pressure distribution is constant,  $\tilde{p}^* = \tilde{p}_q^*/4$ . Its constant value corresponds to the time-average acoustic energy per volume carried by the standing wave in an environment free from any obstacles:  $\tilde{p} = \tilde{p}_q = \frac{\bar{P}}{4} = \frac{p_a^2}{4\rho_0 c_0^2}$ . The integral of  $\tilde{p}^*$  around the object surface is null and thus also the dimensionless resulting radiation force  $\tilde{F}^*$ . The distribution of  $\tilde{p}^*$  at VAN is shown in Figure 6.21 with distributions of  $\tilde{p}_\zeta^*$ ,  $\tilde{p}_\phi^*$  and  $\tilde{p}_q^*$ . Only the term corresponding to the volumetric acoustic kinetic energy  $\tilde{p}_q^*$  contributes to  $\tilde{p}^*$ .

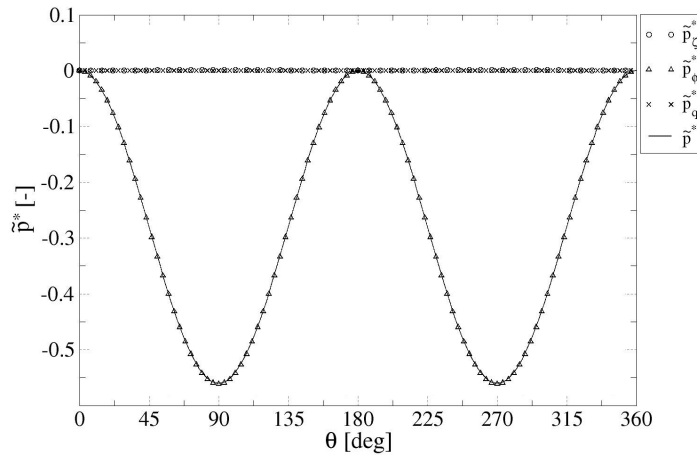


Figure 6.21: Comparison between  $\tilde{p}^*$  and  $\tilde{p}_\zeta^*$ ,  $\tilde{p}_\phi^*$  and  $\tilde{p}_q^*$  at VAN ( $h = \lambda/4$ ;  $\alpha = 0.055$ ;  $\eta = 0.0013$ ;  $f = 1000$  Hz;  $c_0 = 340$  m/s).

The situation is more complicated at IAN where the two terms corresponding to  $\tilde{p}_q^*$  and  $\tilde{p}_\phi^*$  contribute to the final distribution of  $\tilde{p}^*$  (see Figure 6.22). By comparing the areas

under the curve  $\tilde{p}^*(\theta)$ , the suction effect appears globally to be slightly stronger than the compression effect. The two phenomena counterbalance at  $\theta = 45^\circ$  modulo  $90^\circ$  ( $\tilde{p}^* = 0$ ). Similarly to the cylinder, the distribution of  $\tilde{p}^*(\theta)$  is not symmetric according to the plane perpendicular to a.a. which contains the two poles, since the maxima at the equatorial points ( $\theta = 0^\circ$  and  $\theta = 180^\circ$ ) differ from 0.05%. This gives rise to a net resulting force  $\tilde{F}^* \neq 0$ .

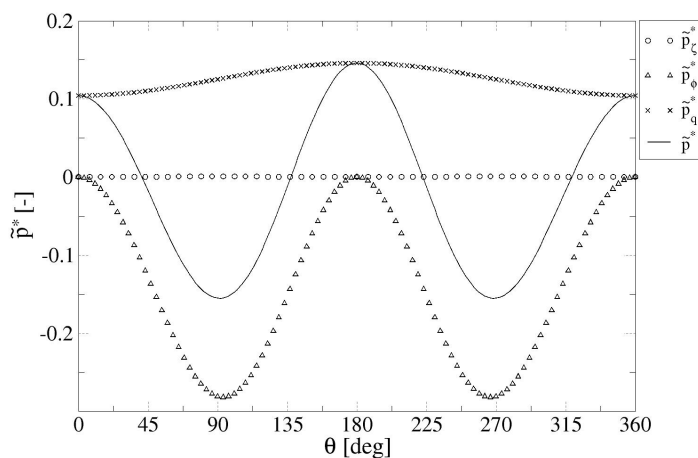


Figure 6.22: Comparison between  $\tilde{p}^*$  and  $\tilde{p}_\zeta^*$ ,  $\tilde{p}_\phi^*$  and  $\tilde{p}_q^*$  at IAN ( $h = \lambda/8$ ;  $\alpha = 0.055$ ;  $\eta = 0.0013$ ;  $f = 1000 \text{ Hz}$ ;  $c_0 = 340 \text{ m/s}$ ).

As carried out for the cylinder, the (absolute) maximum and minimum values of  $\tilde{p}^*$  are investigated as functions of the position  $h$  in the acoustic field (see Figure 6.23). Compression effect ( $\tilde{p}^* > 0$ ) is maximum at PAN ( $|\tilde{p}^*| \approx 0.25$ ) and zero at VAN, whereas suction ( $\tilde{p}^* < 0$ ) is maximum at VAN ( $|\tilde{p}^*| \approx 0.55$ ) and zero in between IAN and PAN. The values of the two extrema counterbalance at IAN.

### Progressive wave

The distribution of  $\tilde{p}^*$  in this case is reported in Figure 6.24, along with the contribution of the three terms  $\tilde{p}_\zeta^*$ ,  $\tilde{p}_\phi^*$  and  $\tilde{p}_q^*$ . In practice, only  $\tilde{p}_\phi^*$  and  $\tilde{p}_q^*$  have a non-negligible contribution.  $\tilde{p}_\phi^*$  acts as a constant compression effect on the sphere, whereas  $\tilde{p}_q^*$  evolves as a spatially modulated suction effect. By comparing the areas under the curve  $\tilde{p}_\theta^*$ , the suction effect appears to slightly exceed the compression effect. They counterbalance their action at  $\theta = 45^\circ$  modulo  $90^\circ$  ( $\tilde{p}^* = 0$ ).

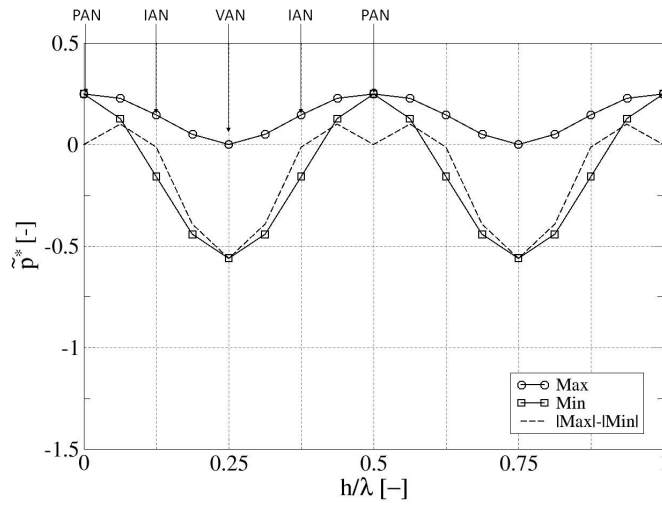


Figure 6.23: Comparison between the dimensionless radiation pressure maximum and minimum values and their difference, on a spherical object in a standing wave field as a function of  $h$  ( $\alpha \ll 1$ ).

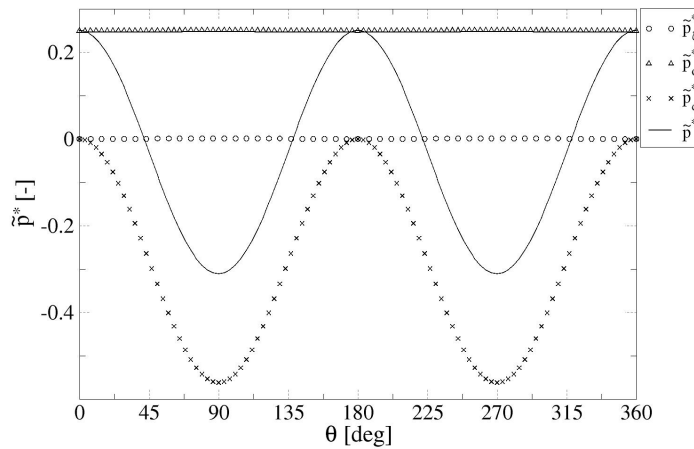


Figure 6.24: Comparison between  $\tilde{p}^*$  and  $\tilde{p}_c^*$ ,  $\tilde{p}_\phi^*$  and  $\tilde{p}_q^*$  in the case of a progressive wave field ( $\alpha = 0.055$ ;  $\eta = 0.0013$ ;  $f = 1000 \text{ Hz}$ ;  $c_0 = 340 \text{ m/s}$ ).

### 6.4.3.5 Asymptotic Approximate Expressions for $\eta \rightarrow 0$ and $\eta \rightarrow \infty$

The dimensionless asymptotic expressions for  $\eta \rightarrow 0$  and  $\eta \rightarrow \infty$  are reported in Tables 6.6 and 6.7 for standing and progressive waves respectively.

Asymptotic expressions for SW		
$\eta \rightarrow 0$	$\tilde{p}_\zeta \rightarrow 0$ $\tilde{p}_\phi \rightarrow -\frac{9}{16} \sin^2 kh \sin^2 \theta$ $\tilde{p}_q \rightarrow \frac{1}{4} \cos^2 kh$	$\tilde{p}^* \rightarrow \frac{1}{4} \cos^2 kh - \frac{9}{16} \sin^2 kh \sin^2 \theta$ $\tilde{F}^* \rightarrow \frac{5}{6} \pi \alpha \sin 2kh$
$\eta \rightarrow \infty$	$\tilde{p}_\zeta \rightarrow \frac{9}{2} \sin^2 kh \cos^2 \theta$ $\tilde{p}_\phi \rightarrow -\frac{9}{4} \sin^2 kh \cos^2 \theta$ $\tilde{p}_q \rightarrow \frac{1}{4} \cos^2 kh$	$\tilde{p}^* \rightarrow \frac{1}{4} \cos^2 kh + \frac{9}{4} \sin^2 kh \cos^2 \theta$ $\tilde{F}^* \rightarrow -\frac{2}{3} \pi \alpha \sin kh$

Table 6.6: Asymptotic dimensionless expressions of the radiation pressure, its three contributions and the modulus of the radiation force for a standing wave under the approximation  $\alpha \ll 1$ .

Asymptotic expressions for PW		
$\eta \rightarrow 0$	$\tilde{p}_\zeta \rightarrow 0$ $\tilde{p}_\phi \rightarrow -\frac{9}{16} \sin^2 \theta$ $\tilde{p}_q \rightarrow \frac{1}{4}$	$\tilde{p}^* \rightarrow \frac{1}{4} - \frac{9}{16} \sin^2 \theta$ $\tilde{F}^* \rightarrow \frac{11}{18} \pi \alpha^4$
$\eta \rightarrow \infty$	$\tilde{p}_\zeta \rightarrow \frac{9}{2} \cos^2 \theta$ $\tilde{p}_\phi \rightarrow -\frac{9}{4} \cos^2 \theta$ $\tilde{p}_q \rightarrow \frac{1}{4}$	$\tilde{p}^* \rightarrow \frac{1}{4} + \frac{9}{4} \cos^2 \theta$ $\tilde{F}^* \rightarrow \frac{4}{9} \pi \alpha^4$

Table 6.7: Asymptotic dimensionless expressions of the radiation pressure, its three contributions and the modulus of the radiation force for a progressive wave under the approximation  $\alpha \ll 1$ .

### 6.4.3.6 Influence of $\eta$

In this section the asymptotic expressions of  $\tilde{p}^*$  are compared with the two cases of  $\eta = 0.0013$  (corresponding to the case of a liquid cylinder in air) and  $\eta = 7$  (corresponding to that of a warm gas in a colder gaseous environment). Solutions obtained for  $\eta = 0.5$  and  $\eta = 2.5$  are also considered.

#### Standing wave

As for the cylinder  $\tilde{p}^*$  at PAN is constant and does not depend on  $\eta$ .

**VAN** - Whatever  $\eta$  the distribution of  $\tilde{p}^*$  at VAN is non-uniform, but the locations of the extrema are independent of  $\eta$ . The profile of  $\tilde{p}^*(\theta)$  is symmetric according to the plane perpendicular to a.a. containing the points  $\theta = 90^\circ$  and  $\theta = 180^\circ$ . This implies that  $\tilde{F}^*$  is always zero (see Figure 6.25(a)). Figure 6.25(b) shows how the maximum and minimum values of  $\tilde{p}^*$  vary with  $\eta$  as well as their difference. For  $\eta < 0.5$  the difference results in a suction effect in the direction perpendicular to the acoustic axis. For  $\eta > 0.5$  only compression is noted at any positions. However, the non-uniformity leads to a predominant compression in the direction parallel to the acoustic axis. For

$\eta \rightarrow \infty \max|\tilde{p}^*|$  tends to 2.25 and  $\min|\tilde{p}^*|$  to 0.25, so  $\max|\tilde{p}^*| - \min|\tilde{p}^*|$  tends 2, a value which is twice the asymptotic value in the case of the cylinder.

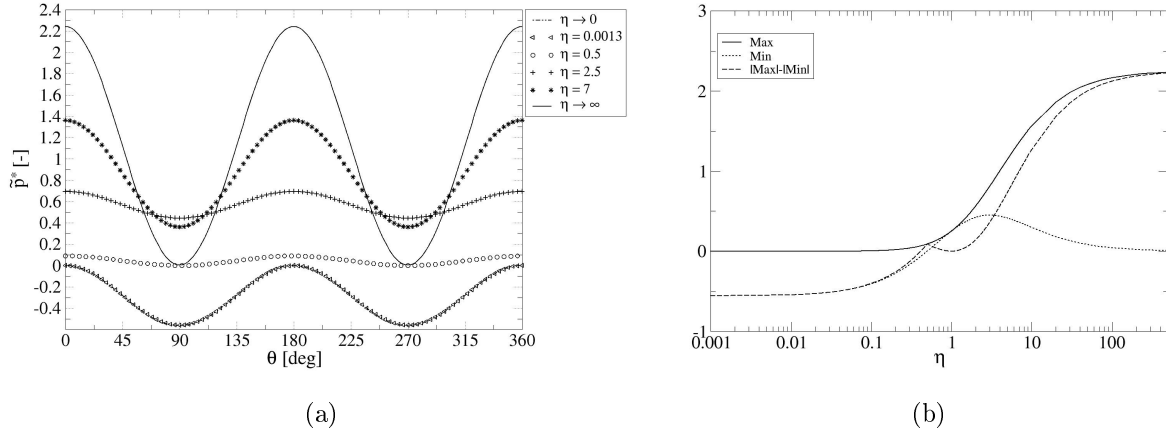


Figure 6.25: (a) Radiation pressure distribution at VAN around a spherical object in a standing wave field as a function of  $\eta$  ( $\alpha \ll 1$ ). (b) Comparison between the radiation pressure distribution  $\tilde{p}^*$  maximum, minimum and their difference at VAN around a spherical object in a standing wave field as a function of  $\eta$  ( $h = \lambda/4$ ;  $\alpha \ll 1$ ;  $f = 1000$  Hz).

**IAN** - Similar distributions of  $\tilde{p}^*$  are observed at IAN, as reported in Figure 6.26(a). The same kind of spatial distribution with  $\theta$  is noted between compression and suction effects. But the amplitude of the extrema is divided by 2, compared to what is obtained at VAN. Figure 6.26(b) gives a clear illustration of this whatever  $\eta$  by reporting  $\max|\tilde{p}^*|$ ,  $\min|\tilde{p}^*|$  and  $\max|\tilde{p}^*| - \min|\tilde{p}^*|$  with respect to  $\eta$ . The convergence of the difference toward 1 as  $\eta$  increases, is less rapid than what is noted at VAN. The distributions are slightly non-symmetric with respect to  $\theta = 90^\circ$ . This induces a resulting radiation non-null force  $\tilde{F}^*$ . Figure 6.27(a) shows the evolution of  $\tilde{F}^*$  with respect to  $\eta$ . Across  $\eta = 2.5$ , for which  $\tilde{F}^* = 0$ , the force changes its sign. For  $\eta < 2.5$  it is directed toward the nearest VAN whereas for  $\eta > 2.5$  it is directed toward the nearest PAN. This is illustrated in Figure 6.27(b) which shows  $\tilde{F}^*$  as a function of the object position  $h$  and  $\eta$ . The asymptotic value of the force for  $\eta \rightarrow 0$  is 0.145, whereas for  $\eta \rightarrow \infty \tilde{F}^* \rightarrow -0.116$ .

### Progressive wave

Figure 6.28(a) shows the distribution of  $\tilde{p}^*$  for a spherical object in a progressive wave field. The maximum and minimum values of  $\tilde{p}^*$ , as well as their difference, are shown in Figure 6.30, with respect to  $\eta$ . Distributions of  $\tilde{p}^*$  are similar to the ones observed for a standing wave at VAN. For  $\eta \rightarrow \infty \max|\tilde{p}^*| - \min|\tilde{p}^*| \rightarrow 2$ , the asymptotic value is the same as that obtained at VAN for the standing wave. However the slighter asymmetry

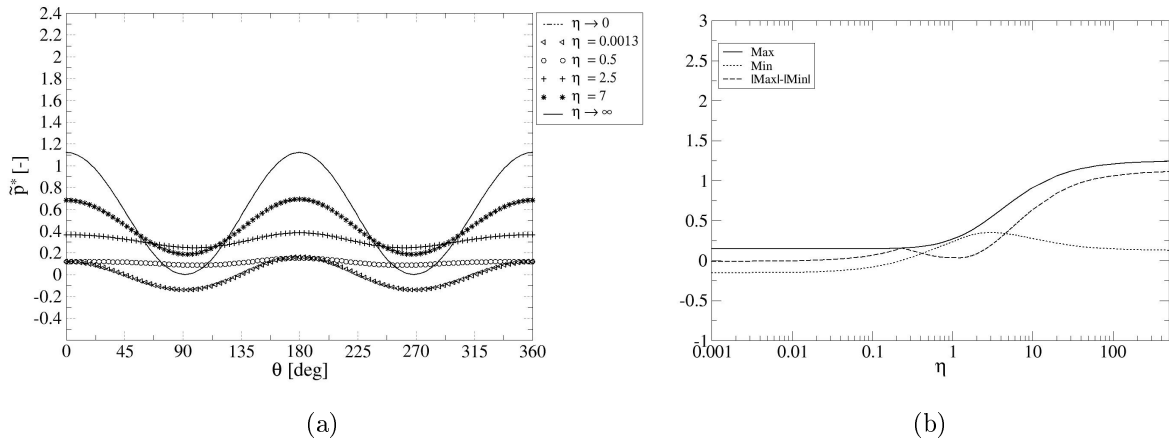


Figure 6.26: (a) Radiation pressure distribution at IAN around a spherical object in a standing wave field as a function of  $\eta$  ( $\alpha \ll 1$ ). (b) Comparison between the radiation pressure distribution  $\hat{p}^*$  maximum, minimum and their difference at IAN around a spherical object in a standing wave field as a function of  $\eta$  ( $h = \lambda/4$ ;  $\alpha \ll 1$ ;  $f = 1000$  Hz).

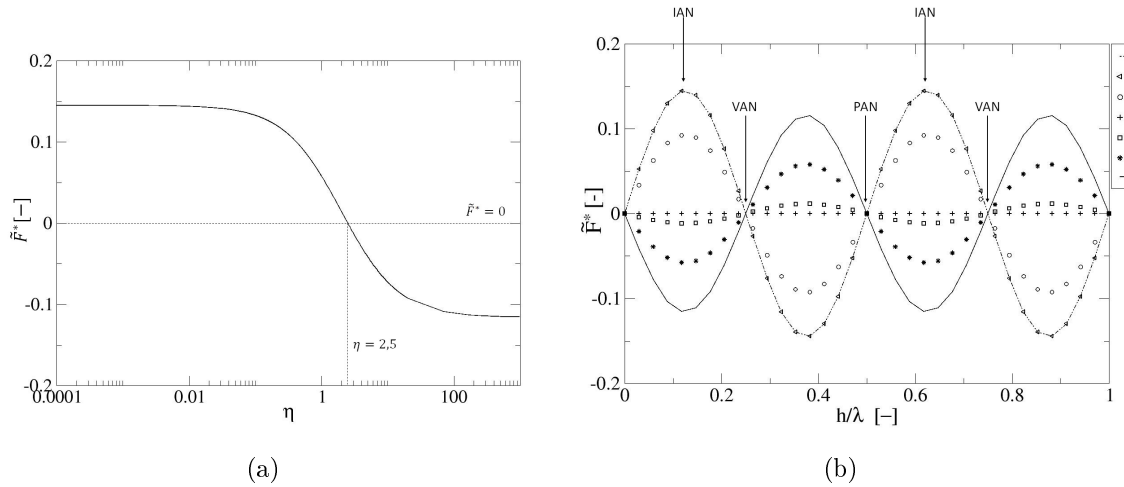


Figure 6.27: (a) Dimensionless radiation force  $\tilde{F}^*$  at IAN ( $h = \lambda/8$ ) acting on a spherical object placed in a standing wave field as a function of  $\eta$  ( $\alpha \ll 1$ ). (b) Dimensionless radiation force  $\tilde{F}^*$  around a spherical object in a standing wave field as a function of  $h$  and  $\eta$  ( $\alpha \ll 1$ ). For  $\eta < 3$   $\tilde{F}^*$  is directed toward the nearest VAN, whereas for  $\eta > 3$  it is directed toward the nearest PAN.

leads to a smaller force, a result which is reinforced by the fact that  $\tilde{F}^*$  varies as  $\alpha^4$  instead of  $\alpha$ . The force never changes its sign; it is always oriented in the way of the wave propagation as shown in Figure 6.29. It is maximum ( $1.81 \cdot 10^{-5}$ ) at  $\eta = 0$  and decreases up to a minimum for  $\eta = 2.5$ , before increasing again asymptotically for  $\eta \rightarrow \infty$  toward a constant value which is about  $1.31 \cdot 10^{-5}$  the value of the maximum at  $\eta = 0$ .

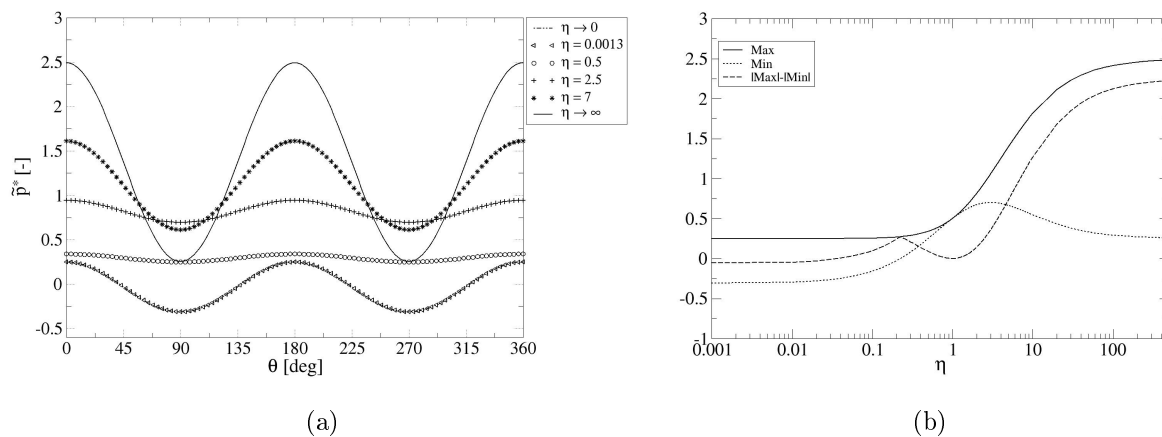


Figure 6.28: (a) Radiation pressure distribution  $\tilde{p}^*$  around a spherical object in a progressive wave field as a function of  $\eta$  ( $\alpha \ll 1$ ). (b) Comparison between the radiation pressure distribution  $\tilde{p}^*$  maximum, minimum and their difference around a spherical object in a progressive wave field as a function of  $\eta$  ( $\alpha \ll 1$ ;  $f = 1000 \text{ Hz}$ ).

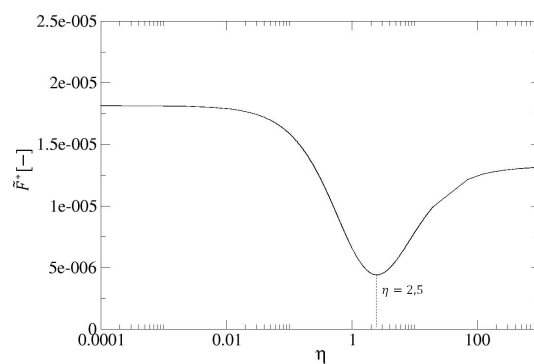


Figure 6.29: Dimensionless radiation force  $\tilde{F}^*$  around a spherical object in a progressive wave field as a function of  $\eta$  ( $\alpha \ll 1$ ).

## 6.5 Most important equations

In this section are summarized the dimensionless expressions of radiation pressure  $\tilde{p}^*$  and force  $\tilde{F}^*$  obtained for cylindrical and spherical objects (small objects approximation  $\alpha \ll 1$ ) in standing and progressive wave fields.

### CYLINDRICAL OBJECTS

#### STANDING WAVE

$$\tilde{p}^* = \left[ \frac{\cos^2 kh}{4} + \frac{\sin^2 kh}{(1+\eta)^2} (\eta^2 \cos^2 \theta + (2\eta - 1) \sin^2 \theta) - \frac{\alpha \sin 2kh}{2(1+\eta)} [(\sin \theta \sin 2\theta)(1-\eta) + \cos \theta] \right] \quad (6.130)$$

$$\tilde{F}^* = \frac{\pi\alpha(3-\eta)}{4(1+\eta)} \sin 2kh \quad (6.131)$$

#### PROGRESSIVE WAVE

$$\tilde{p}^* = \frac{1}{4} \left[ 1 + \frac{4\eta^2}{(1+\eta)^2} \cos^2 \theta + \frac{4(2\eta-1)}{(1+\eta)^2} \sin^2 \theta \right] + \frac{\alpha^2}{4} \left[ \frac{4}{(1+\eta)^2} \cos^2 \theta - \cos 2\theta \right] - \frac{\alpha^3}{4(1+\eta)^2} [(1-\eta)^2 \sin 2\theta \sin \theta + 2 \cos \theta] \quad (6.132)$$

$$\tilde{F}^* = \frac{\pi^2 \alpha^3}{8(1+\eta)^2} [4 + (1-\eta)^2] \quad (6.133)$$

### SPHERICAL OBJECTS

#### STANDING WAVE

$$\tilde{p}^* = -\frac{1}{4} \left[ \frac{9 \sin^2(kh)}{(2+\eta)^2} [-\eta^2 \cos^2 \theta + (1-2\eta) \sin^2 \theta] - \cos^2(kh) \right] + \frac{\alpha}{4(2+\eta)} [5\eta \sin^2 \theta - 3 - 5 \sin^2 \theta] \cos \theta \sin 2kh \quad (6.134)$$

$$\tilde{F}^* = \frac{\pi\alpha}{(2+\eta)} \sin 2kh \left[ 1 + \frac{2}{3}(1-\eta) \right] \quad (6.135)$$

#### PROGRESSIVE WAVE

$$\tilde{p}^* = -\frac{1}{4} \left[ \frac{9}{(2+\eta)^2} [-\eta^2 \cos^2 \theta + (1-2\eta) \sin^2 \theta] - 1 \right] \quad (6.136)$$

$$\tilde{F}^* = 2\pi\alpha^4 \frac{[1 + \frac{2}{9}(1-\eta)^2]}{(2+\eta)^2} \quad (6.137)$$

## 6.6 Comparison Between the Nonlinear Quantities in the Presence of Cylindrical and Spherical Objects

In this chapter the relationship giving the *acoustic radiation pressure* distribution and the resulting *radiation force* have been derived for standing and progressive waves around objects of cylindrical and spherical shapes. Dimensionless expressions have been defined by introducing the normalizing factor  $\bar{P} = p_a^2/\rho_0 c_0^2$  such as  $p^* = p_{rad}/\bar{P}$  and  $F^* = F_{rad}/a\bar{P}$  for cylinders and  $F^* = F_{rad}/a^2\bar{P}$  for spheres. *This factor has the same unit of a pressure and can be also interpreted as the mean acoustic energy per unit volume of a standing wave.* Analytical approximate and asymptotic expressions have been then derived under the hypothesis of  $\alpha \ll 1$ . The approximate expressions of  $\tilde{p}^*$  are reported in Table 6.8 for the cylinder and the sphere, for both waves waves.

Wave	Geometry	$\tilde{p}^*$
SW	Cylinder	$\frac{1}{4} \cos^2(kh) + \frac{1}{(1+\eta)^2} [(2\eta - 1) \sin^2 \theta + \eta^2 \cos^2 \theta] \sin^2(kh)$
	Sphere	$\frac{1}{4} \cos^2(kh) + \frac{9}{4(2+\eta)^2} [(2\eta - 1) \sin^2 \theta + \eta^2 \cos^2 \theta] \sin^2(kh)$
PW	Cylinder	$\frac{1}{4} + \frac{1}{(1+\eta)^2} [(2\eta - 1) \sin^2 \theta + \eta^2 \cos^2 \theta]$
	Sphere	$\frac{1}{4} + \frac{9}{4(2+\eta)^2} [(2\eta - 1) \sin^2 \theta + \eta^2 \cos^2 \theta]$

Table 6.8: Approximate expressions of the radiation pressure  $\tilde{p}^*$  with  $\alpha \ll 1$ .

Expressions reported in Tables 6.8 depend strongly on the density ratio parameter  $\eta = \rho_0/\rho_1$ . They lead to similar distributions of  $\tilde{p}^*$  which result for both types of objects from the two energetic terms:  $\tilde{p}_q^*$ , the time-average volumetric potential energy density, and  $\tilde{p}_\phi^*$ , the time-average volumetric kinetic energy density. The contribution due to the motion of objects  $\tilde{p}_\zeta^*$  is noted negligible whatever the studied configurations. For  $\eta = 1$  the profiles of the radiation pressure exerted on cylinders and spheres are identical for standing waves as well as for progressive waves. Such identical profiles are also noted whatever  $\eta$  when cylinders and spheres are positioned at PAN. By comparing the expressions of  $\tilde{p}^*$  in Table 6.8 for cylinders and spheres, it appears that whatever the points located on the objects' surfaces,  $\tilde{p}^*(\theta)$  on cylinders is always greater than  $\tilde{p}^*(\theta)$  on spheres provided that  $\eta < 1$ . It is verified for the two classes of waves. For  $\eta < 0.5$  local compression ( $\tilde{p}^* > 0$ ) and suction ( $\tilde{p}^* < 0$ ) act on the surface of both types of objects, whereas for  $\eta > 0.5$  only compression is noted. Nevertheless the resulting effects can be seen as a traction in the direction perpendicular to the acoustic axis.

The dimensional approximate radiation force can be expressed as follows:  $\tilde{F}_{rad} = \Theta(\alpha)G\bar{P}\psi(\eta)$ . Parameter  $G$  represents the object surface:  $G = 4\pi a^2$  for spheres and

$G = 2\pi a$  for cylinders of unit length. The expressions of the functions  $\Theta(\alpha)$  and  $\psi(\eta)$  are reported in Table 6.9 and in Figure 6.30. In the case of standing waves,  $|\psi(\eta)|$  for the cylinder is always greater than for the sphere, except in a near vicinity where the radiation force exerted on the cylinder is zero, namely  $\frac{3+\sqrt{124}}{5} < \eta < \sqrt{13}$ . But even in that latter case, the force with the sphere stays very small since this zone is not far from the domain where it is zero, namely  $\eta = 2.5$ . For progressive waves,  $|\psi(\eta)|$  for the cylinder is always greater than for the sphere without any condition.

Geometry	Wave	$\Theta$	$\psi(\eta)$
SW	Cylinder	$\frac{\alpha}{8} \sin(2kh)$	$\frac{3-\eta}{1+\eta}$
	Sphere	$\frac{\alpha}{4} \sin(2kh)$	$\frac{1+2/3(1-\eta)}{2+\eta}$
PW	Cylinder	$\frac{\pi}{16} \alpha^3$	$\frac{4+(1-\eta)^2}{(1+\eta)^2}$
	Sphere	$\frac{\alpha^4}{2}$	$\frac{1+2/9(1-\eta)^2}{(2+\eta)^2}$

Table 6.9: Approximate expressions of radiation force functions  $\Theta$  and  $\psi$  with  $\alpha \ll 1$ . SW: Standing Wave; PW: Progressive Wave.

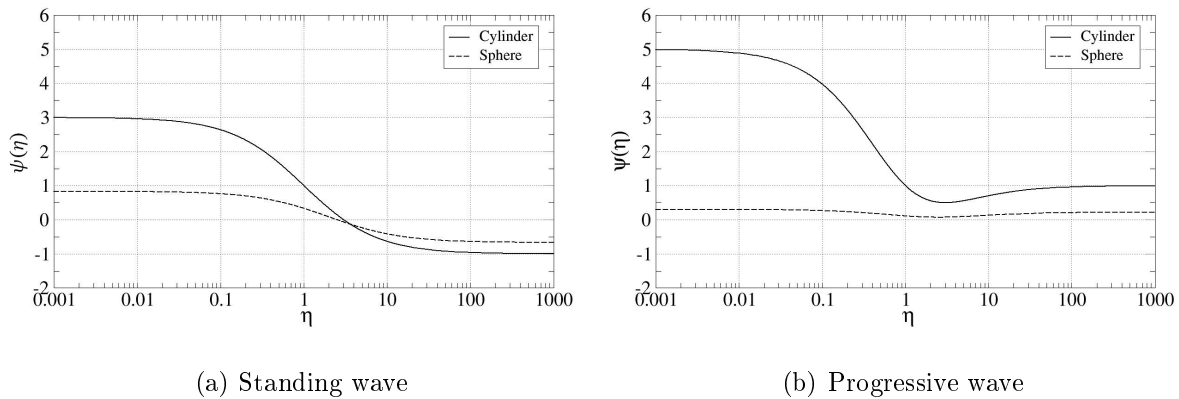


Figure 6.30: Comparison between the  $\psi(\eta)$  functions for cylinder and sphere as functions of  $\eta$  for: (a) standing; (b) progressive wave.



# Chapter 7

## Analysis of Observed Phenomena on the Basis of the Theoretical Model

*The nonlinear theory presented in Chapter 6 is used in this chapter to interpret and explain experimental observations. Section 7.1 introduces the analysis and provides basic concepts of the nonlinear acoustics model. Section 7.2 focuses on the experiments presented in Chapter 5 in the liquid/gas configuration. Section 7.3 is dedicated to the generalization of the model on the basis of results found in literature for configurations different from the liquid/gas one. A trans-critical/super-critical configuration is discussed in section 7.3.1, whereas section 7.3.2 is dedicated to gas/gas configuration. Section 7.4 provides the concluding remarks.*

### 7.1 Introduction

In Chapter 6 some basic elements of nonlinear acoustic theory were given in order to introduce the concept of acoustic radiation pressure. It was explained how the distribution of the radiation pressure around an object of cylindrical or spherical shape could induce a suction effect in the direction perpendicular to the acoustic axis, or produce a net resulting force directed along the acoustic axis. Such a model is used in this chapter to interpret and explain experimental results. In the first part, the experimental results presented in Chapter 5 concerning the response of an air-assisted liquid jet submitted to transverse acoustic are considered. Jet flattening and deviation are quantified by introducing two models based on radiation pressure and resulting radiation force. Results found in literature concerning the presence of flattening and deviation in trans-critical/super-critical and gas/gas configurations, are discussed in the second part. These results are used to

prove the general validity of the model.

An illustration of the radiation pressure distributions around the circular cross-section of a cylinder or sphere, for  $\eta \ll 1$ , is presented in Figure 7.1. Although it is a simplification of the real distribution, it is a quite powerful instrument to explain experimental observations based on previous calculations. When the object is placed at **VAN** the radi-

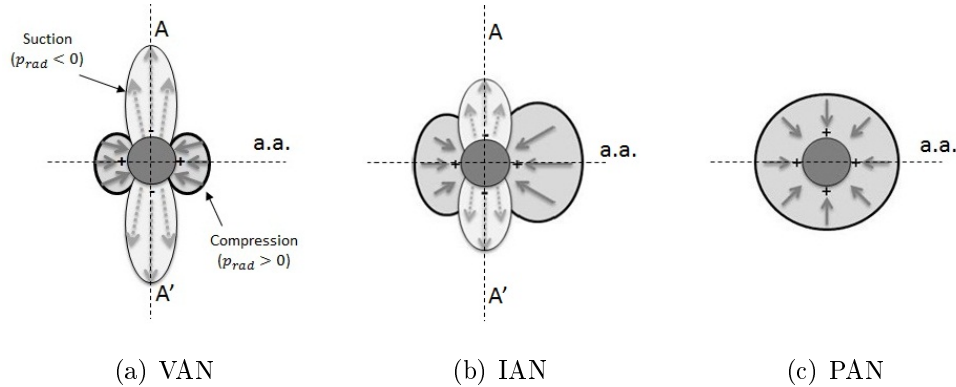


Figure 7.1: A qualitative illustration of radiation pressure distribution around a circular cross-section of a heavy object in a lighter environment ( $\eta \ll 1$ ) placed at: (a) VAN, (b) IAN and (c) PAN.

ation pressure distribution is non-uniform. In particular the radiation pressure is positive along the acoustic axis and negative in the perpendicular direction. Thus, two axes of symmetry AA' and a.a. can be identified. This implies that the resulting radiation force is necessarily zero. No deviation of the jet can exist. An efficient suction effect in the direction perpendicular to the acoustic axis may be obtained (see Fig.7.1(a)). The object is thus deformed, resulting in the jet flattening. The radiation pressure presents an absolute maximum value at a velocity anti-node, so the flattening phenomenon is first observable at this location. In between VAN and PAN the radiation pressure is still non-uniform. The flattening phenomenon may be observed also in between these two locations.

When the object is located at **IAN** the distribution of  $p_{rad}$  is non-uniform as mentioned above, but in addition it is no longer symmetric with respect to AA' (see Figure 7.1(b)). Contrarily to the former case for which the radiation force  $\vec{F}_{rad}$  was zero, at IAN  $\vec{F}_{rad} \neq \vec{0}$ . The jet is thus deviated (see section 5.2.3). The radiation force is maximum at IAN and in the case illustrated in Figure 7.1(b) for  $\eta \ll 1$  it is oriented toward the nearest VAN. It is worth noting that for  $\eta > 3$  ( $\eta > 2.5$ ) for the cylinder (sphere), the radiation force is directed toward the nearest PAN (this has been demonstrated in Chapter 6).

When the object is at **PAN** the radiation pressure distribution is again uniform all around the object (see Fig.7.1(c)) acting as a supplementary constant pressure added to

the atmospheric pressure, like a pressurized environment. Thus, flattening and deviation cannot be observable at this position. Continuous modification of  $p_{rad}$  distribution is found between the three positions presented in Figure 7.1, where compression and traction effects compete.

## 7.2 Interpretation of the Liquid/Gas Results by Means of the Nonlinear Acoustic Model

In this section the nonlinear acoustic model is shown to be at the basis of the two main phenomena described in Chapter 5, namely flattening (see section 5.2.1) and deviation (see section 5.2.3). Figure 7.2 shows three round jets without acoustics (see Figure 7.2(a)) in the multi-injection configuration discussed in section 5.3 (injection conditions:  $We_g = 9$ ;  $Re_l = 2000$ , without domes). They are placed (from left to right) at VAN, IAN and PAN (see Figure 7.2(b)). The experimental jet deformation (flattening and deviation)

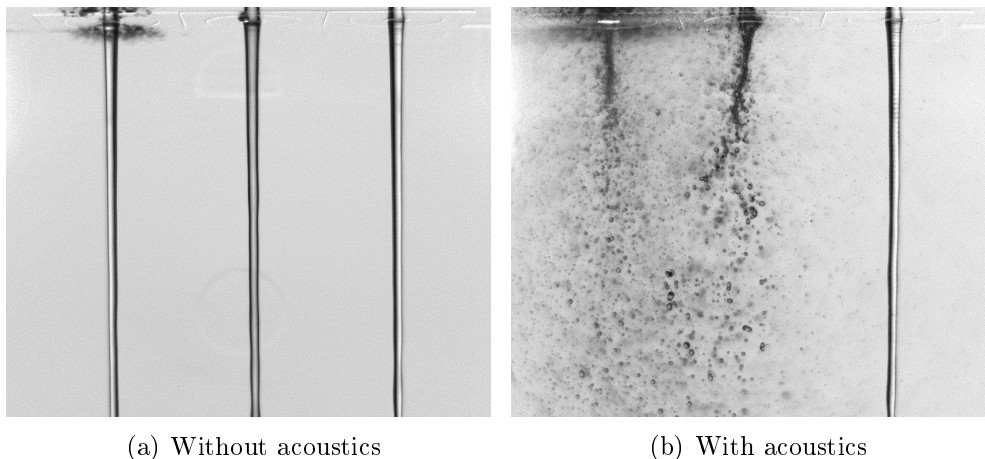


Figure 7.2: Effects of a transverse acoustic field on three jets placed at a pressure anti-node (left), an intensity anti-node (middle) and a velocity anti-node (right).  $We_g = 9$ ;  $Re_l = 2000$ ;  $p_{a,pp} \approx 12 \text{ kPa}$  at 1 kHz.

can be first justified by the qualitative sketch drawn in Figure 7.2(b). The jet placed at PAN is not modified as results from the uniform distribution of  $p_{rad}$  around its cross-section (see Figure 7.1(c)). The two jets at VAN and IAN are flattened and atomized. The jet at IAN is deviated in the direction of VAN. Moreover, in section 6.3.3.6 it was shown (see Figure 6.18(b) in section 6.3.3.6) that, the sign of the radiation force changes across VAN and IAN. This has been observed experimentally as shown in Figure 7.3.

Figure 7.3(a) shows the multi-injection configuration with the three injectors placed at IAN, VAN and IAN, respectively. Figure 7.3(b) shows the multi-injection configuration with the three injectors placed at IAN, PAN and IAN, respectively. In both cases, the jets are deviated toward the nearest velocity anti-node, and across VAN or PAN the direction of the deviation changes in sign. The jets at VAN and PAN are not deviated.

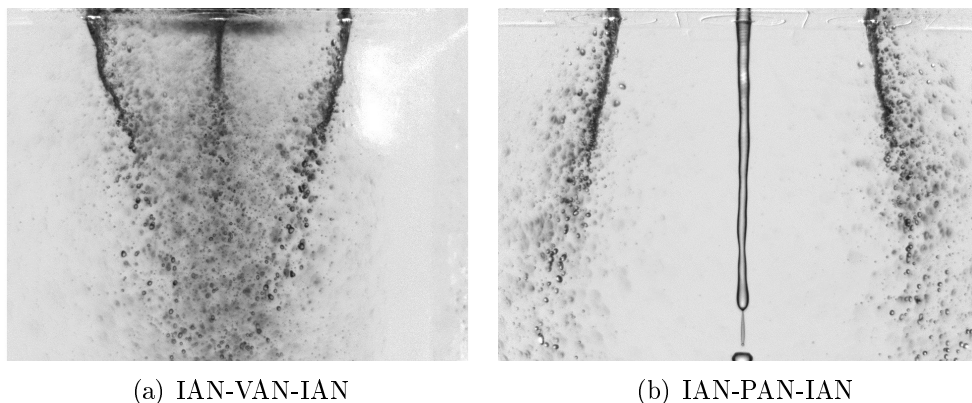


Figure 7.3: Effects of a transverse acoustic field on three jets placed at: (a) IAN - VAN- IAN; (b) IAN - PAN - IAN.  $We_g = 9$ ;  $Re_l = 2000$ ;  $p_{a,pp} \approx 12 \text{ kPa}$  at 1 kHz.

### 7.2.1 Flattening Onset Threshold

In this section two models based on  $p_{rad}$  and  $F_{rad}$  are introduced to calculate: the threshold for the flattening onset; the deviation angle. The validation of those models is made by considering experimental results concerning the Rayleigh axi-symmetric regime. Such an atomization regime better lends itself to the comparison with the theory since the jet can be considered at first approximation as cylindrical. The liquid jet flattening into a sheet perpendicular to the acoustic axis can be explained by considering the radiation pressure distribution (see Figure 7.1). The positive values along the acoustic axis create a compression and the strong negative values in the perpendicular direction induce a suction effect. Under suitable conditions, the combination of these two contributions can provoke the jet flattening. These suitable conditions are related to the amplitude of the acoustic field, thus of the radiation pressure.

In section 5.2.1.2 it was shown that, in those cases in which the flattening took place without deviation, an average acoustic pressure threshold of around 2700 Pa could be identified. To explain the flattening phenomenon it is hypothesized that the jet deformation occurs when the non-uniform radiation pressure distribution around the jet is able to overcome interfacial forces that tend to maintain the jet cylindrical shape. The inter-

facial coherence is represented by the Laplace pressure drop  $\Delta p_{Lap}$  which, in the case of a cylinder, is expressed as:

$$\Delta p_{Lap} = \sigma/r_o \quad (7.1)$$

Here  $\sigma$  is the surface tension and  $r_o$  the initial jet radius at the measurement location. The Laplace pressure drop must be then compared with the radiation pressure in order to obtain a theoretical threshold  $p_{th}$  to be compared with the experimental values of  $p_{10\%}$ . The comparison with the Laplace pressure drop needs to choose a representative value of the radiation pressure distribution. The specified amplitude of the non-uniform radiation pressure distribution is defined as the radiation pressure drop  $\Delta p_{rad}$ :

$$\Delta p_{rad} = |p_{rad}(\theta = 0) - p_{rad}(\theta = \pi/2)| \quad (7.2)$$

with  $\theta$  being the angular coordinate in the reference system presented in Figure 6.1. The radiation pressure drop introduced through Eq. 7.2 corresponds to the absolute value of the dimensionless difference  $max(\tilde{p}^*) - min(\tilde{p}^*)$ .

The equality  $\Delta p_{rad} = \Delta p_{Lap}$  gives a threshold condition for the flattening onset which can be converted in terms of acoustic pressure field amplitude  $p_a$ , and referred as  $p_a = p_{th}$ . A similar approach was introduced by Baillot *et al.* [90, 89] considering the  $p_{rad}$  distribution around an object of spherical shape. The deformation of the jet into a liquid sheet was observed at that time to take place suddenly because of the relatively short signal ramp duration considered (60 *ms*). To follow the deformation occurring at the threshold, a longer ramp duration (300 *ms*) has been chosen. Moreover, the radiation pressure distribution considered is that for a cylindrical object, more representative of the liquid jet than a spherical one.

As already discussed in section 5.2.1.2, for a flattening leading to a diminishing of 10% of the jet thickness, the jet can still be considered cylindrical, thus equations introduced in section 6.3 for the calculation of  $p_{rad}$  can be considered. The theoretical values of the threshold  $p_{th}$  are compared here with the experimental values of the acoustic pressure threshold, which was referred to  $p_{10\%}$ . Tests considered in section 5.2.1.2 will be used for the calculation of  $p_{th}$  and  $\Delta p_{rad}$ . They are summarized again in Table 7.1, for the sake of clarity, where  $r_o$  is the jet radius measured at  $\tilde{z} = 3.33$  and  $\tilde{z} = 5.85$  (see section 5.2.1.2). The maximum acoustic pressure at PAN ( $p_a$ ) is also reported. The comparison between the values of  $p_{th}$  and  $p_{10\%}$  are reported in Figure 7.4, whereas Figure 7.5 shows the ratio between  $\Delta p_{rad}^{10\%}$  and  $\Delta p_{Lap}$  as a function of the test cases. Good agreement is found between  $p_{th}$  and  $p_{10\%}$ , for all tests at VAN and IAN-VAN (labeled from 1 to 7

Test number	Position	$r_o(\tilde{z} = 3.33)/r_{inj}$	$r_o(\tilde{z} = 5.85)/r_{inj}$	$p_{a,pp}$ [Pa] <sup>a</sup>
1	VAN	0.48	0.42	6124
2	VAN	0.50	0.44	8379
3	VAN	0.72	0.68	10096
4	VAN	0.65	0.63	11396
5	VAN	0.54	0.48	12277
6	IAN-VAN	0.53	0.46	7110
7	IAN-VAN	0.54	0.48	12281
8	IAN	0.50	0.46	8842
9	IAN	0.52	0.48	12283
	PAN-IAN	No flattening		
	PAN	No flattening		

Table 7.1: Flattening analysis: summary of test case conditions at  $\tilde{z} = 3.33$  and  $\tilde{z} = 5.85$  (<sup>a</sup>Maximum peak-to-peak acoustic pressure amplitude measured at PAN.).

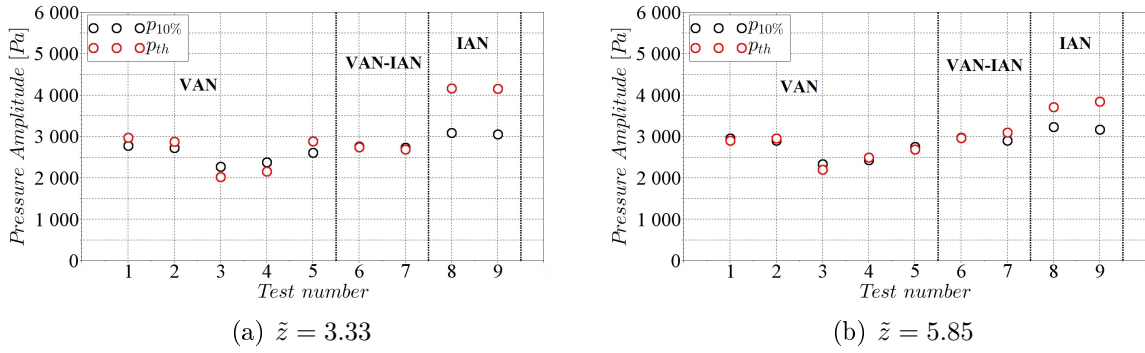


Figure 7.4: Comparison between  $p_{th}$  and  $p_{10\%}$  for the test cases indicated in Table 7.1 at: (a)  $\tilde{z} = 3.33$  and (b)  $\tilde{z} = 5.85$ .

in Table 7.1 and Figure 7.4), and for both locations considered along  $\tilde{z}$ . This concerns also tests 3 and 4, for which the theory predicts a lower values due to a bigger initial jet radius  $r_o$ <sup>a</sup>, which implies a smaller value of  $\Delta p_{Lap}$ . Figure 7.5 shows that, at these positions, the ratio between  $\Delta p_{Lap}$  and  $\Delta p_{rad}$  is around 1. Results confirm that the competition between  $\Delta p_{Lap}$  and  $\Delta p_{rad}$  is the driving mechanism in the flattening process whatever the positions between VAN and IAN-VAN. The model based on the radiation pressure distribution around a heavy object of cylindrical shape correctly predicts the threshold value above which acoustics induces flattening onset. The dependence with the jet radius is also correctly predicted. When the injector is placed at IAN (tests 8 and 9)  $p_{10\%}$  is higher than  $p_{th}$ . As already discussed in the section dedicated to experimental results (see Chapter 5) this is due to jet deviation that takes place simultaneously to

<sup>a</sup>The larger jet radius is due to the higher value of the Reynolds number (see section 5.2.1).

flattening. Indeed, flattening and deviation compete for the acoustic energy distribution: the acoustic energy is only partially dedicated to the flattening phenomenon, while the rest is transferred into the deviation process.

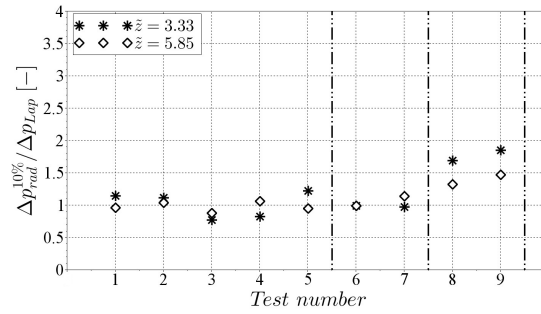


Figure 7.5: Ratio between  $\Delta p_{rad}^{10\%}$  and  $\Delta p_{Lap}$  for the test cases indicated in Table 7.1 at  $\tilde{z} = 3.33$  and  $\tilde{z} = 5.85$ .

We now introduce the dimensionless Laplace’s pressure drop, reduced by the coefficient  $\bar{P} = p_a^2 / \rho_0 c_0^2$  (see section 6.3.1.4. Figure 7.6 shows  $|max(\tilde{p}^*) - min(\tilde{p}^*)|$  and the dimensionless Laplace’s pressure drop for two dimensionless jet radii ( $r_0/r_{inj} = 1; 0.5$ ) as functions of the position  $h$  in the acoustic field. It can be seen that in certain regions in the acoustic

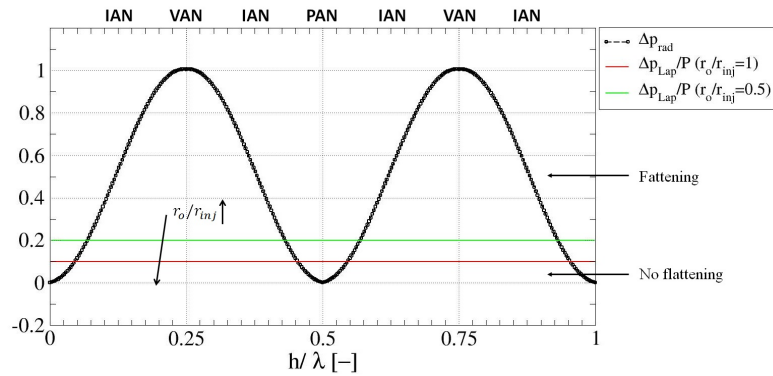


Figure 7.6: Comparison between  $|max(\tilde{p}^*) - min(\tilde{p}^*)|$  and the dimensionless Laplace’s pressure drop as function of  $h$  for a cylindrical object.

field the dimensionless Laplace’s pressure drop is higher than  $|max(\tilde{p}^*) - min(\tilde{p}^*)|$ . Here, the acoustic energy cannot overcome the interfacial force and the jet is not deformed. The smaller the jet radius, the larger the spatial region where the jet is not deformed. This is exemplified by the region centered around the pressure anti-nodes. On the contrary, in the region around the velocity anti-nodes  $|max(\tilde{p}^*) - min(\tilde{p}^*)|$  is higher than the dimensionless Laplace’s pressure drop, leading to a possible jet deformation.

## 7.2.2 Deviation Angle

The second phenomenon that can also be explained by means of nonlinear acoustics is the jet deviation. As observed in the previous chapter, around IAN the distribution of the acoustic radiation pressure is non-uniform and non-symmetric, which induces a non-null force contribution  $\vec{F}_{rad}$ , the direction of which depends on the parameter  $\eta$ . Experiments indicate that the liquid system not in the near vicinity of VAN and PAN is deviated by the acoustic field toward the nearest VAN (see section 5.2.3), which was carried out for  $\eta = 0.0013$ . Calculations performed with this experimental  $\eta$  confirm that the direction of the resulting radiation force is the same as that found experimentally.

Figure 7.7 represents a simplified model for the calculation of the deviation angle  $\gamma$ . It is based on the balance between the liquid column weight  $\vec{W}$  and the radiation force

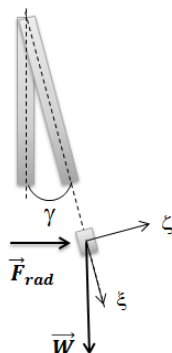


Figure 7.7: Sketch of the simplified model force diagram for  $\gamma$  calculation.

$\vec{F}_{rad}$  along the direction  $\vec{\zeta}$ , where  $\zeta$  is the local coordinate perpendicular to the displaced jet axis. The radiation force  $\vec{F}_{rad}$  for a cylindrical object is expressed by Eq. 6.59. The present experiments have been carried out for a small Helmholtz number ( $\alpha = 0.055$ ), and displacements resulting from the deviation are of the same order of magnitude of the jet diameter. Thus radiation force variation, due to the displacement<sup>b</sup> is considered to be negligible.

The theoretical deviation angles (represented as continuous lines) are compared to measured values in Figure 7.8 and Figure 7.9. Experimental values of the deviation angle  $\gamma$  are those reported in section 5.2.3.

<sup>b</sup>It has been demonstrated in Chapter 6 that  $\vec{F}_{rad}$ , in a standing wave field, depends on the object position  $h$  in the acoustic field.

### Deviation without flattening

Experiments indicate that at some positions in the acoustic field, e.g. PAN-IAN the jet is deviated without being flattened. In these cases the jet remains cylindrical and deviation angle is constant through all the jet length. Figure 7.8 shows the experimental evolution of  $\gamma$  compared with the theoretical deviation angle for two test cases, test " $p_{a,pp} = 11870 Pa$ " and test " $p_{a,pp} = 6000 Pa$ ". Tests are indicated by their respective maximum peak-to-peak acoustic pressure values measured at PAN, once the signal plateau is reached. For each test, the acoustic values refers to the maximum peak-to-peak acoustic pressure measured at PAN. In both cases the theoretical angle is in good agreement with the experiments. The model accurately reproduces the increasing part (due to the signal ramp) and provides a good prediction of the final deviation angle attained during the plateau of the acoustic signal. At this position in the acoustic field (PAN-IAN) all the acoustic energy is used to deviate the jet, since flattening is absent; thus it is correct to assume that all the acoustic energy is used to deviate the jet.

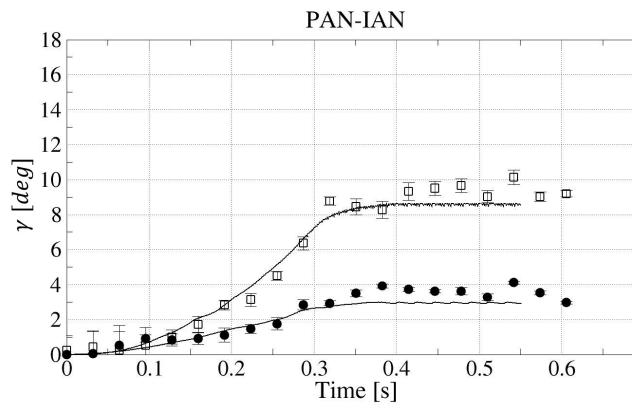
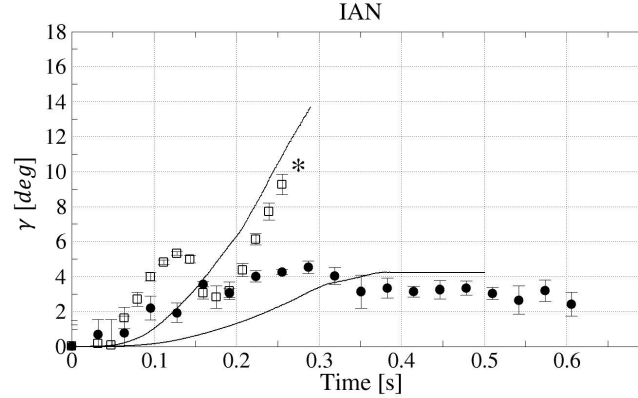


Figure 7.8: Comparison between experimental and calculated deviation angle  $\gamma$  at PAN-IAN for:  $\square$ , test " $p_{a,pp} = 11870 Pa$ ";  $\bullet$ , test " $p_{a,pp} = 6000 Pa$ ". Continuous lines: simplified approach.

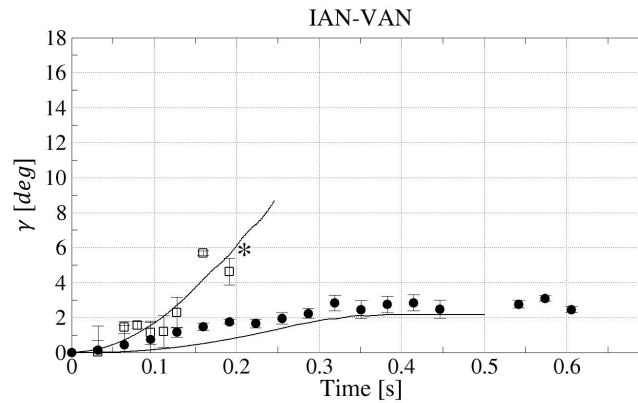
### Deviation attenuated by flattening

At IAN and IAN-VAN, experimental deviation and flattening appear simultaneously, and liquid sheet atomization occurs for acoustic levels  $p_{a,pp}$ , measured at PAN, higher than about 5500 Pa. At these locations, a part of the acoustic energy is used to flatten the jet, and the liquid surface on which the radiation pressure acts is deformed. Due to the liquid surface deformation, the radiation force changes along the jet axis and the deviation is no longer uniform.

Fig. 7.9 shows the experimental evolution of  $\gamma$  when the injector is placed at IAN (see Figure 7.9(a)) and IAN-VAN (see Figure 7.9(b)) compared with the calculation of  $\gamma$  based on the simplified approach which are represented as continuous lines. The stars \* represent the instants of atomization.



(a)



(b)

Figure 7.9: Comparison between experimental and calculated deviation angle  $\gamma$  at: (a) IAN for  $\square$ , test " $p_{a,pp} = 11870 Pa$ ";  $\bullet$ , test " $p_{a,pp} = 3660 Pa$ " and (b) IAN-VAN for  $\square$ , test " $p_{a,pp} = 12180 Pa$ ";  $\bullet$ , test " $p_{a,pp} = 5015 Pa$ ". Continuous lines: simplified approach; \*: jet atomization.

For sufficiently high values of the acoustic field the jet is deviated and a total jet flattening is achieved, leading to the atomization of the liquid sheet (i.e. test " $p_{a,pp} = 11870 Pa$ " at IAN and test " $p_{a,pp} = 12180 Pa$ " at IAN-VAN). A transition phase is observed, during which the jet is also flattening, and  $\gamma$  does not increase continuously. The calculated values of  $\gamma$  do not agree with experiments in the transition phase.

For lower values of the amplitude of the acoustic field (i.e. test " $p_{a,pp} = 3660 Pa$ " at IAN and test " $p_{a,pp} = 5015 Pa$ " at IAN-VAN), the jet is deviated, but during the ramp

the jet begins to flatten without being totally spread. So, a smoother transition in  $\gamma$  behavior is detected:  $\gamma$  monotonically increases as a function of time with the ramp, and reaches a constant value once the plateau is reached. During this transition, discrepancies between the theoretical and experimental values of  $\gamma$  are observed. Once the transition is finished the theoretical values of  $\gamma$  follow the same trend as the experimental ones.

The nonlinear acoustic model indicates that, at these locations in the acoustic field, the object is submitted to the simultaneous action of compression and suction. Flattening and deviation are superimposed, and compete for the acoustic energy distribution. We can conclude that the simplified approach, based on nonlinear acoustic theory, provides a good prediction of the deviation angle when the acoustic levels are relatively low, such that the jet is deviated and no flattening occurs. Discrepancies between the prediction and experiments are observed during the transition, when the liquid jet is not only deviated but is also flattening.

### 7.2.3 Unsteady Jet Displacement

The nonlinear model derived in Chapter 6 is based on the consideration that the cylinder is free to move under the action of the acoustic field. A complementary unsteady displacement can be superimposed to the nonlinear time average properties. This theoretical displacement  $\zeta$  of the liquid jet submitted to acoustics can be thus estimated from the model by integrating in time the cylinder displacement velocity  $\vec{U}$ :

$$\zeta \vec{y} = \int U \vec{y} dt \tag{7.3}$$

The displacement velocity  $\vec{U}$  has been obtained in section 6.3.1, by applying the momentum equation to the cylinder (see Eq. 6.15 in section 6.3.1). For the calculation of  $\zeta$  only the real part of  $\vec{U}$  is considered:

$$ReU = \frac{\eta}{a} (R_1 \sin \omega t + S_1 \cos \omega t) \tag{7.4}$$

where  $a$  is the cylinder radius. The coefficients  $R_1$  and  $S_1$  introduced in section 6.3.1 are given by:

$$R_1 = -\frac{4A\alpha}{\pi\Omega_1^2} F_1 \sin(kh) \qquad S_1 = -\frac{4A\alpha}{\pi\Omega_1^2} G_1 \sin(kh) \tag{7.5}$$

where  $A = p_a/\omega\rho_0$ ,  $\Omega_1 \approx 4(1 + \eta)^2/\pi^2$ ,  $F_1 \approx \alpha^4/8 - (1 - \eta)\alpha^2/2$  and  $G_1 \approx -2(1 + \eta)/\pi$  (see section 6.3.2).

Even though the experimental jet is fixed at the top of the cavity, this calculation gives a good estimation of the experimental oscillation displacement along the acoustic axis. Indeed, by considering the experimental conditions  $\alpha = 0.055$  and  $\eta = 0.0013$ , we obtain  $R_1 \approx 2.8 \cdot 10^{-3} \sin(kh)$  and  $S_1 \approx 1.9 \cdot 10^{-1} \sin(kh)$ . Since  $0 < |\sin(kh)| < 1$  we can neglect  $R_1$  with respect to  $S_1$ . By using Eq. 7.4, and neglecting the term  $R_1 \sin \omega t$ , the integral of Eq. 7.3 becomes:

$$\zeta \vec{y} = \int \frac{\eta}{a} (S_1 \cos \omega t) \vec{y} dt = \frac{\eta}{a\omega} (S_1 \sin \omega t) \vec{y} \quad (7.6)$$

For a frequency of 1000 Hz, the maximum dimensionless jet displacement modulus is  $\zeta/a = 0.0046 \sin \omega t$ . This means that the maximum displacement of the jet is of about 0.5% of the jet radius. Such a theoretical displacement is too small to be detected in our experiments. This is consistent with the fact that no unsteady displacements were measured on the experimental jets studied here.

### 7.3 Generalization of the model in the absence of surface tension phenomena

The nonlinear acoustic theoretical model developed in Chapter 6 has revealed the importance of the two dimensionless quantities, whatever the kinds of the acoustic waves used:  $\alpha$  characterizing the acoustic field, and  $\eta$  characterizing the two media. It has been used to interpret the phenomena, flattening and deviation, highlighted in the experiments presented in Chapter 5 in liquid/gas configuration for  $\eta = 0.0013$ , in which the surface tension is involved. The question is to know if such nonlinear phenomena can be observed without the implication of the surface tension. It would mean that the driving feature is the existence of a density difference between the two media, specified by  $\eta$ . When it is localized in space, the layer separating the two media is seen as an interface. In such an approach the interface does not need to be restricted only to a liquid/gas interface. The model shows that the nonlinear quantities (radiation pressure and resulting force) responsible of the phenomena are all the greatest as  $\eta$  is very large or very small. In the literature, both phenomena were indeed observed in trans-critical/super-critical conditions [42, 43, 87, 88, 86], but also in gas/gas configurations [95] at ambient pressure. In the following we are going to show how the nonlinear model is able to explain the results mentioned above.

### 7.3.1 Trans-critical/super-critical conditions (small $\eta$ )

Gonzalez-Flesca *et al.* [86] observed a turbulent round jet flattened in the presence of transverse acoustic modulations in LES simulations. Simulations concerned a trans-critical nitrogen jet ( $\rho_{inj} = 717 \text{ kg/m}^3$ ,  $T_{inj} = 100 \text{ K}$ ) surrounded by the same fluid in super-critical conditions ( $\rho_{\infty} = 16.5 \text{ kg/m}^3$ ,  $T_{\infty} = 1200 \text{ K}$ ), for which  $\eta = 0.023$ . These authors linked the jet spreading with dynamical effects resulting from the reduction of the pressure in the transverse direction in relation with increased velocities on the two sides of the jet.

#### Jet flattening

In the case of a *standing wave* the phenomenon was noted at the velocity anti-node for large acoustic velocity amplitudes  $v(t) = v_0 \cos(2\pi ft)$ . To physically explain the reduction of the pressure on both sides of the jet, they proposed to estimate it by applying the unsteady Bernoulli theorem at constant density:

$$\frac{\partial \phi}{\partial t} + \frac{p}{\rho} + \frac{v^2}{2} = 0 \quad (7.7)$$

where  $\phi$  is the velocity potential of the light surrounding fluid,  $\rho$  its density and  $v$  its velocity. The velocity potential existing around the heavy jet is expressed in cylindrical coordinates  $(r, \theta)$  by the solution of an incompressible and irrotational flow around a cylindrical solid:

$$\phi(r, \theta, t) = v(t) \left( r + \frac{R^2}{r} \right) \cos \theta \quad (7.8)$$

where  $R$  is the initial jet radius. On the jet surface ( $r = R$ ) the radial velocity component is zero and the tangential is give by:

$$v_{\theta} = \frac{1}{2} \frac{\partial \phi}{\partial \theta} = -2v(t) \sin \theta \quad (7.9)$$

The pressure distribution around the jet was finally given by:

$$p(\theta, t) = 2\rho_0 R v_0 \omega \sin \omega t \cos \theta - 2\rho_0 v_0^2 \cos^2 \omega t \sin^2 \theta \quad (7.10)$$

The time average pressure drop calculated between the two points  $\theta = \pi/2$  and  $\theta = 0$  leads to  $-\rho_0 v_0^2$ . By considering an iso-density surface where  $\rho_0 = 100 \text{ kg/m}^3$  and  $v_0 = 25 \text{ m/s}$  they estimated a pressure drop of 62500 Pa.

Now, we are going to compare their results with the nonlinear acoustic model we have developed in Chapter 6. From our model it is possible to derive an expression for the

pressure  $p(\theta, t)$  around the object at  $r = R = a$ , to compare with that of Eq. 7.10. For this purpose, we start from the general expression of  $p(\theta, t)$  defined in Eq. 6.6 where the total velocity potential ( $\phi = \phi_i + \phi_r$ ) is obtained from nonlinear quantities (Eq. 6.30). In the configuration presented by Gonzalez-Flesca *et al.*  $\alpha \approx 0.046$ , we will thus consider the approximate coefficients for  $\alpha \ll 1$ . From the  $S_n$  and  $R_n$  coefficients presented in section 6.3.3 for a standing wave, our calculations at VAN ( $kh = \pi/2$ ) for  $\alpha \ll 1$  and  $n = 2$  (three terms) gives:  $S_0 = R_0 = S_2 = R_2 = 0$  and  $R_1 \ll S_1$ . Thus, we can write:

$$p(\theta, t) = \rho_0 \omega S_1 \sin \omega t \cos \theta + \frac{1}{2} \frac{\rho_0}{c_0^2} (\omega^2 S_1^2 \sin^2 \omega t \cos^2 \theta) - \frac{1}{2} \rho_0 \left[ \frac{\eta^2}{a^2} S_1^2 \cos^2 \omega t \cos^2 \theta + \frac{1}{a^2} S_1^2 \cos^2 \omega t \sin^2 \theta \right] \quad (7.11)$$

The coefficient  $S_1$  is given by  $S_1 = -2v_a a / (1 + \eta)^2$ , and  $v_a$  is the acoustic velocity. By considering  $\eta \ll 1$  Eq. 7.11 can be thus approximated and rewritten as:

$$p(\theta, t) = -2\rho_0 \omega v_a a \sin \omega t \cos \theta - 2\rho_0 v_a^2 \cos^2 \omega t \sin^2 \theta \quad (7.12)$$

This approximate expression of the pressure is the same as Eq. 7.10 obtained by Gonzalez-Flesca *et al.*. The time average of Eq. 7.12 gives the expression of the radiation pressure, i.e.  $\Delta p_{rad} = -\rho_0 v_0^2$ . Obviously, if we consider for  $\rho_0$  the value of  $100 \text{ kg/m}^3$  given by Gonzalez-Flesca *et al.* we obtain the same value of the radiation pressure drop  $\Delta p_{rad} = 62500 \text{ Pa}$ . But, in such conditions  $\eta = 0.14$  and the approximation  $\eta \ll 1$  is no longer valid. All the terms in Eq. 7.11 must be thus considered for the calculation  $p(\theta, t)$  and  $\Delta p_{rad}$ , which leads to  $\Delta p_{rad} = \rho_0 v_a^2 (1 - \alpha^2 + \eta^2) / (1 + \eta)^2 = 48932.6 \text{ Pa}^c$ .

The expression of their pressure can be thus interpreted as a particular case of our model at VAN, in its approximate formulation with  $\alpha \ll 1$  and  $\eta \ll 1$ . We have demonstrated that the expression of  $p(\theta, t)$  is derived from nonlinear quantities, which means that the pressure drop  $-\rho v_0^2$  obtained by Gonzalez-Flesca *et al.* is actually a radiation pressure drop. The analysis of the radiation pressure has shown that at VAN the radiation pressure is provided only by the term of acoustic kinetic energy per unit volume  $p_\phi$  (the term  $p_\zeta$  is negligible), which creates suction at the pole points  $\theta = \pi/2$  and  $\theta = 3\pi/2$ , and practically no action at the equatorial points  $\theta = 0$  and  $\theta = \pi$ . Contrarily to the approach chosen by Gonzalez-Flesca *et al.* to interpret their results, the nonlinear acoustic model we have derived has the great advantage to be general in its application.

---

<sup>c</sup>By considering for the value  $\rho_0 = 16.5 \text{ kg/m}^3$ , the density of the external media, and  $\eta \ll 1$  the radiation pressure drop is about  $10300 \text{ Pa}$

This means, that it can be applied at any positions ( $\forall h$ ) of the acoustic field, and for any values of  $\eta$ , and can be used to explain the observed nonlinear acoustic phenomena at these positions. This represents an important asset for the model, if we consider its potential application. Indeed, in liquid rocket engines, where hundreds of jets are present in the acoustic field, it is necessary to know the response in any location, and not only at VAN. The method presented here could be used to derive low order models which could be implemented in simulations concerning thermoacoustic instabilities. The validity of their model does not extend to PAN, IAN or any other intermediate locations since the second order term corresponding to the volumetric potential energy density ( $p_q$ ) is not considered (see section 6.2).

### Jet deviation

In the case of a *progressive wave* they observed a jet spreading similar to that observed in the standing wave, but the pressure drop being not estimated by their simplified model no comparison can be made. In addition, a bending of the jet was observed in the wave propagation direction. The bending may be interpreted as the deviation highlighted in our nonlinear acoustics model. This is explained by the existence of a non-zero radiation force in section 6.3.3.6 for a progressive wave, due to a non-symmetric radiation pressure distribution (see Figure 6.19). This force has been demonstrated to always keep the direction of the propagation of the traveling wave (see Figure 6.20), independently of the position in the acoustic field, contrarily to the standing wave. It is possible to conclude that also this phenomenon, shown in simulations, as the jet spreading discussed above, must be ascribed to nonlinear acoustic effects.

### Unsteady jet displacement

In addition to flattening and deviation an oscillation of the jet around the mean position was observed from the simulations performed by Gonzalez-Flesca *et al.* in both standing and progressive wave. In order to interpret the phenomenon they proposed another model in which the jet displacement is composed of two terms. The first term is due to the acoustic field. It is obtained by time-averaging the acoustic velocity, the second one is given by the hydrodynamic jet response. Only the term due to the acoustic field, represented by Eq. 7.13 is considered here for comparison with our model:

$$y_c^{ac}(t) = \frac{v_a}{\omega} t_{12} \sin(\omega t) \quad (7.13)$$

Here  $t_{12} = 2\rho_1 c_1 / (\rho_1 c_1 + \rho_2 c_2)$  represents the transmission coefficient from the outer medium (region 1) to the inner jet (region 2). By introducing the transmission coefficient

$t_{12}$  in Eq. 7.13 and rearranging we obtain:

$$y_c^{ac}(t) = \frac{2v_a}{\omega} \frac{\eta'}{(1 + \eta')} \sin(\omega t) \quad (7.14)$$

where  $\eta' = \eta c_1/c_2$  can be seen as a modified density ratio. The maximum dimensionless (reduced with the jet diameter  $d$ ) value of the displacement for  $t_{12} \approx 0.77$  is:  $y_c^{ac}/d = 0.15$ . This calculation is carried out for the test case indicated as  $VA_{12,5}^{0,8}$  in Gonzalez-Flesca *et al.* ( $f^{ac} = 2000$  Hz, and  $v_a = 12.5$  m/s).

As already stated in section 7.2.3 our general model is based on the consideration that the cylinder is free to move under the action of the acoustic field. Indeed, by integrating the jet displacement velocity over time, the jet displacement is obtained. By using their conditions in our model ( $d = 0.005$ ,  $\rho_0 = 100$  kg/m<sup>3</sup>,  $\alpha = 0.046$ ,  $v_a = 12.5$  m/s,  $\omega = 12566.4$  rad/s) we obtain  $R_1$  and  $S_1$  introduced in section 6.3.1:  $R_1 = 4.6 \cdot 10^{-4}$  and  $S_1 = 2.9 \cdot 10^{-1}$ . The term  $R_1 \sin \omega t$  is seen to be neglected in Eq. 7.4 and we obtain for the displacement:

$$\zeta(t) = \frac{2v_a}{\omega} \frac{\eta}{(1 + \eta)} \frac{\pi^2}{4(1 + \eta)^2} \sin(\omega t) \quad (7.15)$$

Eq. 7.15 is similar to that of Eq. 7.14 with a supplementary co-factor  $\pi^2/4(1 + \eta)^2$ . For  $\eta = \eta' = 0.626$  the resulting dimensionless maximum jet displacement is of about  $0.14d$ , which is in agreement with the one obtained by Gonzalez-Flesca *et al.*. Similarly to the spreading and the bending, also the unsteady jet displacement can be interpreted as nonlinear acoustic effect. Once again, this highlights the general validity of the nonlinear acoustic theory presented in Chapter 6.1 which takes into account all observed phenomena and do not need supplementary models.

### 7.3.2 Gas/gas conditions (large $\eta$ )

Nonlinear acoustics phenomena, due to the presence of a heavy/light interface, were also observed in configurations in which the density ratio was reversed, namely for  $\eta > 1$ . Indeed, in parallel research activities carried out at CORIA [95] showed that hot gases and laminar, conical or inverted-conical, flames with  $\eta = 6$ , were deviated under the action of a transverse acoustic field. Figure 7.11 shows two images of an inverted-conical premixed flame without acoustics (see Figure 7.10(a)) and with acoustics (see Figure 7.10(b)). In the latter case, the hot gases and the flame were deviated toward the pressure anti-node, in agreement with calculations presented in section 6.3 for a cylindrical object, indicating that the direction of  $F_{rad}$  changes in sign for  $\eta > 3$ . Similarly, an helium jet issuing into

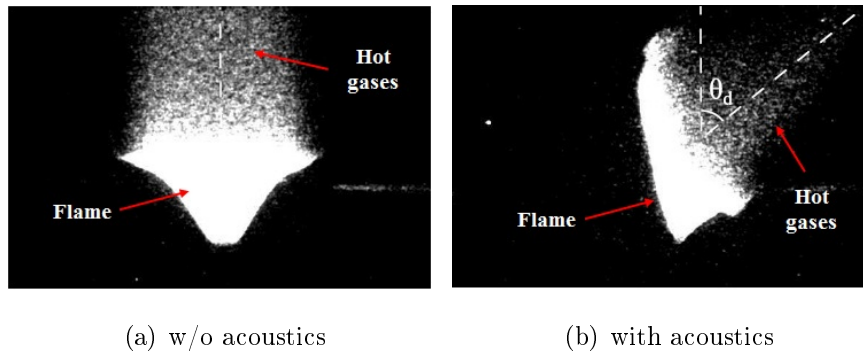


Figure 7.10: Premixed flame direct light emission images: (a) without acoustics; (b) with acoustics;  $f = 1010 \text{ Hz}$  [95].

the ambient air, for which  $\eta = 7$ , was deviated in the direction of the pressure anti-node. The density difference between the (hot or cold) light jets and the (heavy) ambient air, characterized by  $\eta$ , leads there to the presence of an interface between the heavy and light media on which the nonlinear effects can act. Therefore for a sufficient level, nonlinear phenomena can be observed.

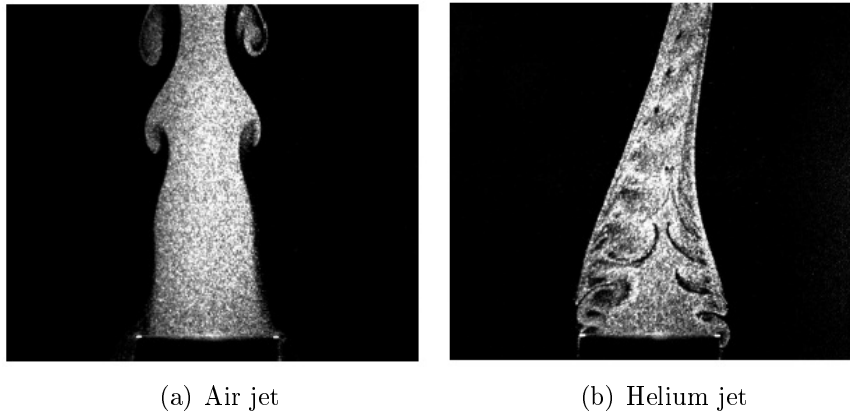


Figure 7.11: Tomographic view of jets submitted to a transverse acoustic field;  $f = 1010 \text{ Hz}$ : (a) air jet; (b) helium jet. [95]

In addition, it was also shown that an air jet issuing into the ambient air was not deviated when the same transverse acoustic field was active, see Figure 7.11(a). This configuration corresponds to  $\eta = 1$ . Well, calculations presented in Chapter 6 indicate that for  $\eta = 1$  the radiation force is not null. This question was raised by Gor'kov [119] which proposed a correction factor  $C(\eta)$ , for the radiation force exerted on spherical objects, in order to take into account compressibility effects. This coefficient is given by  $C(\eta) = -1/3\chi_1/\chi_2 = -\eta/3c_0^2/c_1^2$ , where  $\chi = 1/\rho(\partial\rho/\partial P)$  is the isentropic coefficient of compressibility. A similar coefficient was introduced by Lespinasse [95]:  $C(\eta) = -\chi_1/\chi_2 = -\eta c_0^2/c_1^2$

to modify the resulting radiation force exerted on cylinder objects. With the addition of these coefficients in the expressions of  $F_{rad}$  presented in section 6.6, the radiation force becomes null for an object placed in an environment of the same kind, at the same thermodynamic conditions. This modification of the radiation force exerted on compressible systems is consistent with experiments with systems for any value  $\eta^d$ . Thus, by considering the hot gases as a cylinder separated from the ambient air by an interface on which the modified nonlinear radiation force acts, they proposed a simplified approach which allowed to justify and estimate the deviation of the inverted-conical flame.

## 7.4 Concluding Remarks

The model developed in Chapter 6 has been used in this chapter to interpret experimental phenomena that have been described in Chapter 5. It has been shown that the response of jets submitted to acoustic perturbations can be explained by considering the distribution of the radiation pressure around the object surface, and the resulting radiation force. Two simplified approaches have been derived from the general equations to quantify the observed phenomena. In the first application the competition between the radiation pressure and Laplace pressure drops has been used to quantify the threshold for the flattening onset. In the second one, the competition between the radiation force and the object weight has been used to calculate the deviation angle. In both cases theoretical results are in good agreement with experiments, especially when flattening does not take place simultaneously with deviation.

It has been shown that flattening and deviation observed in trans-critical/super-critical and gas/gas configurations can be explained by the nonlinear model developed here. In general, these phenomena are interpreted individually in literature: each phenomenon is interpreted by means of a specific approach. For the trans-critical/super-critical configuration, we have shown that these approaches can be considered as specific cases of our nonlinear acoustic model. Indeed, each phenomenon can be explained by recurring to the distribution of the radiation pressure and resulting radiation force. This confirms, the general validity of our model, and that phenomena observed in trans-critical/super-critical (and gas/gas) configuration are actually nonlinear acoustic phenomena. From experiments based on systems for which  $\eta = 1$ , a supplementary coefficient taking into account compressibility effects in the radiation force is an interesting way to improve the model in the configuration of light gases surrounding by heavy gases [119, 95]. Whatever, all these

---

<sup>d</sup>In particular for  $\eta$  small this supplementary term is negligible.

comparisons experiments/theory lead to the conclusion that the presence of a heavy/light, but not necessarily liquid/gas, interface between the jet and the surrounding environment is crucial for the observed phenomena to be revealed. This means that the model can be applied to any position ( $\forall h$ ) in the acoustic field and value of  $\eta$ . The generality of the expressions derived here represents a great advantage, compared to models whose validity is restricted to a specific location in the acoustic field or to some particular condition in terms of  $\eta$ . This is an important asset of the model, if we consider its potential application. Indeed, in liquid rocket engines, where hundreds of jets are present in the acoustic field, it is necessary to know the response in any locations. The formulation presented here could be used to derive low order model which can be implemented in simulations concerning thermoacoustic instabilities.



## Part IV

# Conclusion and Perspectives



# Chapter 8

## Conclusion and Perspectives

### 8.1 General Conclusions

The objective of this research was to provide a better insight into one of the critical mechanisms involved in thermoacoustic instabilities observed in liquid rocket engines: the interaction between the injection and the acoustic field, in particular the atomization response and the acoustic coupling between injection domes and main cavity.

Among the different types of combustion instabilities, high frequency azimuthal (spinning or standing) mode instabilities are considered as the most harmful for the operations of liquid rocket engines. An experimental and theoretical study is proposed here to investigate the effects of transverse acoustic field on air-assisted liquid jets. The experimental setup is composed of a main resonant cavity in which the transverse acoustic field (corresponding to the 2T mode of the main cavity) is excited by means of four compression drivers. The setup has been optimized in order to produce acoustic pressure peak-to-peak amplitudes that can be as high as 12000 Pa at the frequency of 1 kHz. One up to three (multi-injection configuration) coaxial jets can be placed in the acoustic field excited in the resonant cavity. Atomization regimes ranging from the Rayleigh axi-symmetric ( $We_g \approx 9$ ,  $Re_l = 2000$ ), to the fiber one ( $We_g > 400$ ,  $Re_l > 2000$ ) have been investigated. In the multi-injection configuration the three injectors can be fed through out three separate lines, or connected with two injections domes, one for the gas and one for the liquid. The two injection domes were designed during this work<sup>a</sup> in order to experimentally investigate the acoustic coupling between the main resonant cavity and the injection system. Their conception allows to submit them to several acoustic conditions depending on the

---

<sup>a</sup>Numerical simulations performed with the acoustic module of COMSOL Multiphysics for the design and the acoustic characterization of the domes provided the necessary complement to the investigation.

position of the injectors in the acoustic field. Several resonant conditions can be obtained according to dome and connecting elements sizes.

In order to have a complete characterization of the air-assisted jet response to the transverse acoustic field, five characteristic positions along the acoustic axis, representative of what occurs in such a transverse acoustic field have been investigated: the pressure anti-node (PAN); the intensity anti-node (IAN), the velocity anti-node (VAN); the position PAN-IAN at equal distances between the pressure and intensity anti-nodes, and the position IAN-VAN between the intensity and velocity anti-nodes.

Experimental activities have been carried out in parallel with a theoretical study aiming to model the behavior of jets submitted to high-amplitude acoustic fields by means of nonlinear acoustics. Such a model has been developed for standing and progressive waves, and for cylindrical and spherical objects. The general expressions for the radiation pressure  $p_{rad}$  and the resulting radiation force  $F_{rad}$  have been derived. It has been shown that the radiation pressure is composed of three terms: the time-average volumetric potential energy density  $p_q$ ; the time-average volumetric kinetic energy density  $p_\phi$  and the contribution due to the motion of the object  $p_\zeta$ . The sum of these three terms provides the shape of the radiation pressure distribution around the object surface (as a function of the angular coordinate  $\theta$ ). The term corresponding to the time-average volumetric potential energy density  $p_q$  is non-symmetric with respect to the axis AA' perpendicular to the acoustic axis (a.a.), giving rise to the resulting radiation force. The analytical study of  $p_{rad}$  and  $F_{rad}$  revealed the importance of two parameters: the Helmholtz number  $\alpha$  characterizing the acoustic field, and the ratio  $\eta$  of the jet and the surrounding. The model has been used to interpret and explain experimental observations in the liquid/gas configuration  $\eta \ll 1$  investigated here, but also in trans-critical and gas/gas configurations. This leads to the important conclusion that the jet responses observed (in experiments and simulations) can be actually interpreted as resulting from nonlinear acoustic effects.

For what concerns the *acoustic coupling* between the main resonant cavity and the injection domes, experimental results indicated that both liquid and gas domes presented a strong response to the acoustic field to which they were submitted. All tests have been performed at  $p_{a,pp} = 12000 Pa$  (peak-to-peak pressure measured at PAN) at  $f=1000$  Hz. Depending on the position of the injectors in the acoustic field three configurations have been investigated: IAN-PAN-IAN, IAN-VAN-IAN, and PAN-IAN-VAN. The gas dome presented a well defined response as a function of the parameters investigated, whereas the liquid dome response did not show a uniform trend. Experiments demonstrated that boundary conditions in terms of phase shift at the injectors' exit plane have a predominant

role in the acoustic coupling. Indeed, the most important acoustic response of the gas dome has been observed when the three injectors were placed in the section of the cavity around the velocity anti-node (configuration denominated as IAN-VAN-IAN). In this configuration injectors were submitted to acoustic fluctuations presenting a phase shift which matched the resonant mode of the injection system consisting of the dome and the injectors. The acoustic characteristics of the injection system must be carefully considered with respect to the acoustic characteristics of the combustion chamber (resonant frequency and mode-shape).

Concerning the investigation of the liquid/gas jets' response to the transverse acoustic fields, single injector and multi-injector configurations have been investigated. In addition the single injector investigation has been the object of the theoretical analysis, in which phenomena observed experimentally have been interpreted via the nonlinear quantities derived from the theoretical model. The experiments have been carried out for atomization regimes ranging from the Rayleigh axi-symmetric to the fiber one, at the five characteristic locations mentioned above, and for several acoustic levels up to  $p_{a,pp} = 12000 Pa$  ( $f=1000$  Hz). Experimental results demonstrate that a high-amplitude (high-frequency) acoustic field may drastically affect the atomization of air-assisted liquid jets (for all regimes) by inducing a non-uniform spatial distribution of the droplets inside the combustion chamber. The experimental response of the jet has been classified into three main phenomena: flattening, atomization improvement and deviation.

The *flattening* consists in the spreading of the jet in the direction perpendicular to the acoustic axis. It mainly depends on the position in the acoustic field and on the acoustic levels. It takes place at all positions from VAN to the vicinity of IAN. Its intensity is maximum at VAN and decreases toward IAN. Experimentally, flattening has been observed in low (quasi-cylindrical jet shape) and high Weber number atomization regimes (liquid spray). Flattening appears when a certain acoustic pressure threshold is attained, and it is achieved when high values of the acoustic field are reached. A fine investigation of the phenomenon has been performed at VAN, where its intensity is maximum. First, the theoretical model indicates that at VAN the distribution of the radiation pressure around an object of cylindrical shape is given by the time-average volumetric kinetic energy density  $p_\phi$ . The distribution of  $p_{rad}$  is non-uniform, but remains symmetrical relatively to the acoustic axis and the axis perpendicular to it (the resulting radiation force is zero). The object is thus submitted to a suction effect in the direction perpendicular to the acoustic axis. Thanks to a fine experimental investigation concerning jets at low Weber numbers, as well as a fine theoretical analysis, it has been shown that the threshold for

the flattening onset corresponds to a balance between the radiation pressure drop and the Laplace's pressure drop of about 1. This means that in our specific case, in which a liquid jet is placed in an air environment  $\eta \ll 1$ , the competition between the radiation pressure drop and the Laplace's pressure drop is the driving mechanism explaining why the flattening is possible.

Obviously, a totally achieved flattening leads to an *improvement of the atomization process* of jets at low Weber numbers. The improvement of the atomization process has been also observed for sprays at high Weber number atomization regimes, and it can be suggested that it come from the flattening phenomenon exerted on the droplets<sup>b</sup>. Indeed, the nonlinear acoustic model indicates that radiation pressure distribution and the resulting radiation force acting on spherical objects present similar features to those acting on cylindrical objects: droplets submitted to a suction effect are then deformed. When acoustic levels are sufficiently high, droplets can be broken into smaller ones as soon as the balance between the pressure radiation and the Laplace's pressure drop is broken to the advantage of the nonlinear effects. For very high Weber number atomization regimes droplets are very small and difficult to be broken; thus more acoustic energy is required to modify the atomization regime. The phenomenon is maximum at VAN and is no longer observed at PAN, in between them the higher the acoustic amplitude the wider the distance from VAN to PAN in which the phenomenon is observed.

Another important phenomenon observed experimentally is the jet *deviation*. It takes place in all positions in between VAN and PAN (these two excluded). The spatial region in which deviation can be observed is all the wider as the amplitude levels are higher. Depending on the position in the acoustic field it has been observed with or without flattening. Since the phenomenon is maximum at IAN, this position has been investigated in detail. The theoretical model indicates that the radiation pressure distribution is due to the presence of the term corresponding to the time-average volumetric potential energy density  $p_q$ . The distribution of  $p_{rad}$  is thus non-uniform, and non-symmetric relatively to the axis perpendicular to a.a.. The asymmetry gives rise to a non-null resulting radiation pressure force exerted on the object. In the case of a liquid/gas system ( $\eta \ll 1$ ), the radiation force is directed toward the nearest velocity anti-node, which agrees with experimental observations. For high Weber number regimes deviation is found to increase non-linearly with the amplitude of the acoustic field. By introducing the acoustic Froude number (defined as the square root of the ratio of the mean acoustic energy of a standing wave per unit mass over the gravitational potential energy of the liquid system per

---

<sup>b</sup>Boisdron [89] visualized a flattening phenomenon exerted on droplets which led to their atomization

unit mass) it has been shown that deviation is possible as soon as the acoustic potential energy becomes high enough to counterbalance the gravitational energy. In order to quantify the deviation phenomenon, jets at low Weber number regimes have been chosen. The deviation angle has been calculated by using the nonlinear acoustic model relying on the counterbalance between the radiation force and the object weight. The agreement between the calculations of the deviation angles, by using the nonlinear model, and experimental angles shows the validity of the model in the interpretation of the phenomenon on the basis of nonlinear acoustic effects.

A *droplet clustering* phenomenon in the spatial region between IAN and VAN has been highlighted in multi-injection configuration, in all atomization regimes. This phenomenon has been visualized and quantified by means of the experimental droplet spatial distributions. It results from the combination of the three nonlinear acoustic phenomenon described above: flattening, atomization improvement and deviation. In a real combustor hundreds of injectors are submitted to the acoustic field, and droplet clustering phenomenon may induce a non-uniform spatial distribution of droplets in the combustion chamber. Moreover, each injector may be submitted to a different acoustic condition, and it is necessary to know the response in any locations. The advantage of the nonlinear acoustic model derived here is its validity in each position of the acoustic field and for each value of  $\eta$ .

As discussed above, the nonlinear acoustic model can explain the phenomena observed in the present experimental liquid/gas configuration for which  $\eta \ll 1$ . But, it was also shown how it can explain flattening and deviation which are observed in trans-critical/super-critical or gas/gas configurations, in both experiments and simulations. This leads to two fundamental conclusions. The first one is that phenomena observed in trans-critical/super-critical and gas/gas configurations can be interpreted as actually resulting from nonlinear acoustics. The second one is that the driving feature is the existence of a density difference between the jet and the surrounding environment. When localized in space, the layer separating the two media is seen as an interface. In such an approach the interface does not need to be restricted only to a liquid/gas interface. The general validity of the nonlinear acoustic model is an important asset, if we consider its potential application. This means that such a model could be adopted to derive low order models which might be used in the development of numerical tools for engines combustion instability prediction in liquid rocket engines. Results of the study presented here can be used to interpret jet's response during the start-up transient phase in which propellants may remain in the liquid/gas state, but also to interpret physical behaviors

of trans-critical/super-critical jets.

## 8.2 Perspectives

Future development concerns both modeling and experimental aspects. For what concerns the modeling, more complicated object shapes (e.g. elliptical shapes in order to represent the liquid sheet or particle cluster for the spray) should be taken into account in order to further generalize the model. However, it will not be possible to obtain a complete analytical solution for any geometries, so numerical tools will be necessary in the case of these more complicated object shapes. An important aspect that should be taken into account in the model concerns compressibility effects in the formulation of the radiation pressure and the resulting radiation force, as suggested by Gor'kov [119] and Lespinasse [95]. It would be also interesting to further develop the model in order to consider different thermodynamic conditions for the two media.

For what concerns the experimental part, preliminary experimental results concerning both droplet size and gas velocity field measurements have been discussed here to demonstrate the feasibility of the application of the two measurements techniques in our experimental setup. They serve mainly as a starting point for future investigations. In order to enhance the knowledge of the nonlinear phenomena discussed in this work, it would be also interesting to investigate them at pressure levels higher than the atmospheric pressure.

Multi-point injection tests have also pointed out that the combination of nonlinear effects is able to induce a non-uniform distribution of the spray in the chamber. From the analysis of domes' acoustic response it can be inferred that the effects of the acoustic coupling could be greater by increasing the connecting elements (number of injectors). It could be then useful to consider more than three injectors, not aligned, in order to have a three-dimensional characterization of the droplet spatial distribution. This would lead to a new injection system concept, a configuration with 5 or more injectors with two cylindrical domes whose volume could be changed by varying the insert structures. For a more distant future the cylindrical injection system could be also connected with a combustion chamber of circular section.

# Bibliography

- [1] F. Culick, “Combustion instabilities in liquid-fueled propulsion system - an overview,” *AGARD conf. Proceedings*, no. 450, 1988.
- [2] L. Crocco and S. I. Cheng, *Theory of Combustion Instability in Liquid Propellant Rocket Motors*, vol. 8. London: Butterworths, 1956.
- [3] T. C. Lieuwen and V. Yang, *Combustion Instabilities in Gas Turbine Engines, Progress in Astronautics and Aeronautics*, vol. 210. Washington, DC: AIAA, 2005.
- [4] J. Oefelein and V. Yang, “Comprehensive review of liquid-propellant combustion instabilities in f-1 engines,” *Journal of Propulsion and Power*, 1993.
- [5] D. Harrje and F. Reardon, “Liquid propellant rocket combustion instability,” tech. rep., NASA SP-194, 1972.
- [6] V. Yang and W. Anderson, *Liquid Rocket Engine Combustion Instability, Progress in Astronautics and Aeronautics*, vol. 169. Washington, DC: AIAA, 1995.
- [7] M. L. Dranovsky, V. Yang, F. Culick, and D. G. Talley, *Combustion Instabilities in Liquid Rocket Engines: Testing and Development in Russia, Progress in Astronautics and Aeronautics*, vol. 221. Washington, DC: AIAA, 2007.
- [8] G. Sutton and O. Biblarz, *Rocket Propulsion Elements, 8th edition*. Wiley, 2010.
- [9] M. Barrère and F. Williams, “Comparison of combustion instabilities found in various types of combustion chambers,” pp. 169–1810, 1968.
- [10] F. Reardon, “Combustion stability specification and verification procedure,” CPIA Publication 247, 1973.
- [11] R. Fry and M. Klem, “Guidelines for combustion stability specifications and verification procedures for liquid propellant rocket engines,” (Columbia, Maryland), CPIA, 1997.

- [12] L. Crocco, "Aspects of combustion stability in liquid propellant rocket motors part i: Low frequency instability with monopropellants," *Journal of the American Rocket Society*, vol. 21, no. 6, pp. 163–178, 1951.
- [13] L. Crocco, "Aspects of combustion stability in liquid propellant rocket motors part ii: Low frequency instability with bipropellants," *Journal of the American Rocket Society*, vol. 22, no. 1, pp. 7–16, 1952.
- [14] L. Crocco, "The sensitive time lag theory," *Liquid propellant rocket combustion instability*, eds Harrje, D.T. and Reardon, F.H., NASA, Washington, DC, pp. 170–194, 1972.
- [15] L. Crocco, J. Grey, and D. Harrje, "Theory of liquid propellant rocket combustion instability and its experimental verification," *Journal of the American Rocket Society*, vol. 30, no. 2, pp. 159–168, 1960.
- [16] L. Crocco, D. Harrje, and F. Reardon, "Transverse combustion instability in liquid propellant rocket motors," *Journal of the American Rocket Society*, vol. 32, no. 3, pp. 366–373, 1962.
- [17] J. Hutt and M. Rocker, "High-frequency injection-coupled combustion instability," pp. 345–555, *Liquid Rocket Engine Combustion Instability*, Progress in Astronautics and Aeronautics, AIAA, 1995.
- [18] J. W. S. Rayleigh, "The explanation of certain acoustic phenomena," *Nature (London)* 18, pp. 319–321, 1878.
- [19] S. Candel, C. Huynh, and T. Poinsot, "Unsteady combustion," *Kluwer Academic*, 1996.
- [20] J. Hulka and J. Hutt, "Instability phenomena in liquid oxygen/hydrogen propellant rocket engines," pp. 39–72, *Liquid Rocket Engine Combustion Instability*, Progress in Astronautics and Aeronautics, AIAA, 1995.
- [21] F. D. Matteo, *Modelling and simulation of liquid rocket engine ignition transients*. PhD thesis, Sapienza University of Rome, Italy, 2011.
- [22] F. D. Matteo, M. D. Rosa, and M. Onofri, "Start-up transient simulation of a liquid rocket engine," 47<sup>th</sup> AIAA/SAE/ASEE Joint Propulsion Conference & Exhibit, AIAA Paper No. 2011-6032, 2011.

- [23] M. Frey, T. Aichner, J. Gorgen, B. Ivancic, B. Kniesner, and O. Knab, "Modeling of rocket combustion devices," 10<sup>th</sup> AIAA/ASME Joint Thermophysics and Heat Transfer Conference, AIAA Paper No. 2010-4329, 2010.
- [24] W. A. Sirignano, J. P. Delplanque, C. H. Chiang, and R. Bhatia, "Liquid-propellant droplet vaporization: A rate-controlling process for combustion instability," in *Liquid rocket engine combustion instability* (V. Yang and W. Anderson, eds.), vol. 169, (Washington, DC), pp. 307–343, AIAA, 1995.
- [25] W. A. Sirignano, "Driving mechanisms for combustion instability," in *Combustion Science and Technology*, vol. 187, pp. 162–205, 2015.
- [26] L. Vingert, P. Gicquel, and D. Lourme, "Coaxial injector atomization," in *Liquid rocket engine combustion instability* (V. Yang and W. Anderson, eds.), vol. 169, (Washington, DC), pp. 145–189, AIAA, 1995.
- [27] W. Anderson and S. R. Ryan, H.M., "Impinging jet injector atomization," in *Liquid rocket engine combustion instability* (V. Yang and W. Anderson, eds.), vol. 169, (Washington, DC), pp. 215–246, AIAA, 1995.
- [28] Bremond and E. Villermaux, "Atomization by jet impact," *Journal of Fluid Mechanics*, vol. 549, pp. 273–306, 2006.
- [29] C. Miesse, "The effect of ambient pressure oscillations on the disintegration and dispersion of a liquid jet," *Journal of Jet Propulsion*, vol. 25, no. 10, pp. 525–530, 1955.
- [30] M. Heidmann, "Oscillatory combustion of a liquid-oxygen jet with gaseous hydrogen," NASA TN D-2753, NASA Lewis Research Center, Cleveland, Ohio, 1965.
- [31] M. Heidmann, "Oxygen-jet behavior during combustion instability in a two-dimensional combustor," NASA TN D-2725, NASA Lewis Research Center, Cleveland, Ohio, 1965.
- [32] P. Wieber and W. Mickelsen, "Effect of transverse acoustic oscillations on the vaporization of a liquid-fuel droplet," NASA TN D-287, NASA Lewis Research Center, Cleveland, Ohio, 1960.
- [33] M. Heidmann and P. Wieber, "Analysis of frequency response characteristics of propellant vaporization," NASA TN D-3749, NASA Lewis Research Center, Cleveland, Ohio, 1966.

- [34] R. D.E., "Liquid droplet vaporization and combustion," *Liquid propellant rocket combustion instability*, eds Harrje, D.T. and Reardon, F.H., NASA, Washington, DC, pp. 74–99, 1972.
- [35] C. Feiler and M. Heidmann, "Dynamic response of gaseous-hydrogen flow system and its application to high-frequency combustion instability," NASA TN D-4040, NASA Lewis Research Center, Cleveland, Ohio, 1967.
- [36] M. Heidmann and J. Groeneweg, "Analysis of the dynamic response of liquid jet atomization to acoustic oscillations," NASA TN D-5339, NASA Lewis Research Center, Cleveland, Ohio, 1969.
- [37] Szatkowski, "Advanced launch system (als) space transportation expert system study, ad-a248 708," tech. rep., 1991.
- [38] D. V. Hoover, H. M. Ryan, S. Pal, C. L. Merkie, H. R. Jacobs, and R. J. Santoro, "Pressure oscillations effects on the jet breakup," *Heat Mass Transfer Spray Syst.*, vol. 187, pp. 27–36, 1991.
- [39] B. Chehroudi and D. Talley, "Preliminary visualizations of acoustic waves interacting with subcritical and supercritical cryogenic jets," (Madison, WI), In the 15<sup>th</sup> annual conference on liquid atomization and spray systems (ILASS Americas), 2002.
- [40] B. Chehroudi, D. Davis, and D. Talley, "Initial results from a cryogenic coaxial injector in an acoustic field," (Reno, Nevada), 44<sup>th</sup> Aerospace Sciences Meeting & Exhibit, AIAA, 2003.
- [41] I. Layva, B. Chehroudi, and D. Talley, "Dark core analysis of coaxial injectors at sub-, near-, and supercritical pressures in a transverse acoustic field," (Cincinnati, OH), 43<sup>rd</sup> AIAA/ASME/SAE/ASEE Joint Propulsion Conference & Exhibit, AIAA 2007-5456, 2007.
- [42] J. J. Graham, I. A. Leyva, J. I. Rodriguez, and D. Talley, "On the effect of transverse acoustic field on a flush shear coaxial injector," No. 2009-5142, AIAA.
- [43] D. Davis and B. Chehroudi, "Shear-coaxial jets from a rocekt-like injector in a transverse acoustic field at high pressures," (Reno, Nevada), 44<sup>th</sup> Aerospace Sciences Meeting & Exhibit, AIAA, 2006.

- [44] D. Davis and B. Chehroudi, "Measurements in an acoustically driven coaxial jet under sub-, near-, and supercritical conditions," *Journal of Propulsion and Power*, vol. 23, no. 2, 2007.
- [45] B. Chehroudi, "Physical hypothesis for the combustion instability in cryogenic liquid rocket engines," *Journal of Propulsion and Power*, vol. 26, no. 6, 2010.
- [46] A. Ghosh, Q. Diao, and K. Yu, "Flame-acoustic interaction in gox/gh2 shear-coaxial injector flow-field," (Reno, Nevada), 44<sup>th</sup> Aerospace Sciences Meeting & Exhibit, AIAA, 2006.
- [47] A. Ghosh, Q. Diao, and K. Yu, "Experimental investigation of shear-coaxial injector flame stability on flow parameters," (Cincinnati, Ohio), 43<sup>th</sup> AIAA/ASME/SAE/ASEE Joint Propulsion Conference, AIAA, 2007.
- [48] A. Ghosh, *The role of density gradient in liquid rocket engine combustion instability*. PhD thesis, University of Maryland, USA, 2008.
- [49] K. Miller, J. Sisco, N. Nugent, and W. Anderson, "Experimental study of combustion instabilities in a single-element coaxial swirl injector," 41<sup>th</sup> AIAA/SAE/ASEE Joint Propulsion Conference & Exhibit, AIAA, 2005.
- [50] Y. Yu, L. O'Hara, J. Sisco, and W. Anderson, "Experimental study of high-frequency combustion instability in a continuously variable resonance combustor (cvrc)," 47<sup>th</sup> AIAA Aerospace Sciences Meeting Including the New Horizons Forum and Aerospace Exposition, AIAA Paper No. 2009-234, 2009.
- [51] T. Feldman, *Unstable combustion processes for a Single Element Shear/Coax Injector in a Longitudinal Combustor*. PhD thesis, Purdue University, USA, 2013.
- [52] V. Sankaran, M. Harvazinski, W. Anderson, and D. Talley, "Progress and challenges in liquid rocket combustion stability modeling," Seventh International Conference on Computational Fluid Dynamics (ICCFD7), 2012.
- [53] M. Harvazinski, W. Anderson, and C. Merkle, "Combustion instability diagnostics using the rayleigh index," 47<sup>th</sup> AIAA/SAE/ASEE Joint Propulsion Conference & Exhibit, AIAA, 2011.
- [54] Y. Yu, J. Sisco, and W. Anderson, "Examination of spatial mode shapes and resonant frequencies using linearized euler solutions," 37<sup>th</sup> AIAA Fluid Dynamics Conference and Exhibit, AIAA Paper No. 2009-234, 2007.

- [55] S. Rosen, "Combustion instabilities in the transition region of an unstable model rocket combustor," Master's thesis, Purdue University, USA, 2011.
- [56] A. Ficuciello, "Analysis of combustion instability in a liquid rocket combustor," Master's thesis, University "La Sapienza" of Rome, 2011.
- [57] G. Xia, M. Harvazinski, W. Anderson, and C. Merkle, "Investigation of modeling and physical parameters on instability prediction in a model rocket combustor," 47<sup>th</sup> AIAA/SAE/ASEE Joint Propulsion Conference & Exhibit, AIAA, 2011.
- [58] H. C. S. V. Harvazinski, M.E., T. Feldman, W. Anderson, and C. Merkle, "Coupling between hydrodynamics, acoustics, heat release in self-sustained excited unstable combustor," *Physics of Fluids*, vol. 27, no. 045102, 2015.
- [59] B. Pomeroy, J. Sisco, J. Eckstein, and W. Anderson, "Characterization of gas-centered swirl-coaxial injector stability in a subscale multi-ement combustor," 44<sup>th</sup> AIAA/SAE/ASEE Joint Propulsion Conference & Exhibit, AIAA, 2008.
- [60] M. Wierman, N. Nugent, and W. Anderson, "Characterization of an unstable rocket combustor with the addition," 46<sup>th</sup> AIAA/SAE/ASEE Joint Propulsion Conference & Exhibit, AIAA Paper No. 2010-6895, 2010.
- [61] B. Pomeroy, C. Morgan, and W. Anderson, "Response of a gas-centered swirl coaxial injector to transverse instabilities," 47<sup>th</sup> AIAA/SAE/ASEE Joint Propulsion Conference & Exhibit, AIAA, 2011.
- [62] M. Wierman, N. Nugent, and W. Anderson, "Combustion response of a lox/lch4 element to transverse instabilities," 47<sup>th</sup> AIAA/SAE/ASEE Joint Propulsion Conference & Exhibit, AIAA Paper No. 2011-5549, 2011.
- [63] M. Wierman, W. Hallum, W. Anderson, and B. Austin, "Oxidizer post resonance response of a high pressure combustor," 51<sup>st</sup> AIAA/SAE/ASEE Joint Propulsion Conference, AIAA Paper No. 2015-4228, 2015.
- [64] M. Oswald, A. Schik, M. Klar, and W. Meyer, "Investigation of coaxial ln2-gh2-injection at supercritical pressure by spontaneous raman scattering," 35<sup>th</sup> Joint Propulsion Conference, AIAA, 1999.
- [65] M. Oswald, J. Smith, R. Branam, J. Hussong, and A. Schik, "Injection of fluids into supercritical environments," *Combustion Sci. and Tech.*, vol. 178, pp. 49–100, 2006.

- [66] J. S. Hardi, M. Oswald, C. Webster, S. Gröning, S. Beinke, P. Armbruster, N. Blanco, D. Suslov, and B. Knapp, "High frequency combustion instabilities in liquid propellant rocket engines: research programme at dlr lampoldshausen," In the International Symposium on Thermoacoustic Instabilities in Gas Turbines and Rocket Engines: Industry meets Academia, May 2016.
- [67] S. Koeglmeier, M. Schulze, M. Oswald, and J. Hardi, "Hf combustion stability - research activities in germany," *Space Propulsion*, 2016.
- [68] B. Knapp and M. Oswald, "High speed visualization of flame response in a lox/h<sub>2</sub> combustion chamber during external excitation," 12th International Symposium on Flow Visualization, German Aerospace Centre (DLR), 2006.
- [69] K. B. Sliphorst, M., S. Gröning, and M. Oswald, "Combustion instability-coupling mechanisms between liquid oxygen/methane spray flames and acoustics," *Journal of Propulsion and Power*, vol. 28, no. 6, pp. 1339–1350, 2012.
- [70] M. Oswald, Z. Farago, G. Searby, and F. Cheuret, "Resonance frequencies and damping of a combustor acoustically coupled to an absorber," *Journal of Propulsion and Power*, vol. 24, no. 3, pp. 524–533, 2008.
- [71] M. Sliphorst, S. Gröning, and M. Oswald, "Theoretical and experimental identification of acoustic spinning mode in a cylindrical combustor," *Journal of Propulsion and Power*, vol. 27, no. 1, pp. 182–189, 2011.
- [72] G. Searby, A. Nicole, M. Habiballah, and E. Laroche, "Prediction of the efficiency of acoustic damping cavities," *Journal of Propulsion and Power*, vol. 24, no. 3, pp. 516–523, 2008.
- [73] J. Hardi, M. Oswald, and B. Dally, "Flame response to acoustic excitation in a rectangular rocket combustor with lox/h<sub>2</sub> propellants," *CEAS Space Journal*, Vol. 2, pp. 41-49, 2011.
- [74] J. Hardi, S. Beinke, M. Oswald, and B. Dally, "Coupling behaviour of lox/h<sub>2</sub> flames to longitudinal and transverse acoustic instabilities," 48<sup>th</sup> AIAA/ASME/SAE/ASEE Joint Propulsion Conference & Exhibit, 2012.
- [75] J. Hardi, M. Oswald, and B. Dally, "Acoustic characterisation of a rectangular rocket combustor with lox/ h<sub>2</sub> propellants," 4<sup>th</sup> European Conference for Aerospace Sciences, St. Petersburg, Russia, 4-8 July 2011, 2011.

- [76] J. Hardi, *Experimental Investigation of High Frequency Combustion Instability in Cryogenic Oxygen-Hydrogen Rocket Engines*. PhD thesis, The University of Adelaide, 2012.
- [77] S. Gröning, D. Suslov, M. Oswald, and T. Settlemayer, “Stability behaviour of acylindrical rocket engine combustion chamber operated with liquid hydrogen and liquid oxygen,” 5<sup>th</sup> European Conference for Aerospace Sciences, 2013.
- [78] S. Gröning, J. Hardi, D. Suslov, and M. Oswald, “Injector-driven combustion instabilities in a hydrogen/oxygen rocket combustor,” *Journal of Propulsion and Power*, vol. 32, no. 3, pp. 560–573, 2016.
- [79] A. Urbano, L. Selle, G. Staffelbach, B. Cuenot, T. Schmitt, S. Ducruix, and S. Candel, “Exploration of combustion instability triggering using large eddy simulation of a multiple injector liquid rocket engine,” *Combustion and Flame*, no. 169, pp. 129–140, 2016.
- [80] C. Rey, Ducruix, S., P. Scouffaire, L. Vingert, and S. Candel, “Experimental analysis of high frequency combustion instabilities associatede with collective interactions,” (Chamonix, France), 4th Pacific Symposium on Flow Visualization and Image Processing, Pacific Center of Thermal-Fluids Engineering, 2003.
- [81] C. Rey, Ducruix, F. S., Richecoeur, P. Scouffaire, L. Vingert, and S. Candel, “High frequency combustion instabilities associatede with collective interactions in liquid propulsion,” (Fort Lauderdale, FL), 40<sup>th</sup> AIAA/ASME/SAE/ASEE Joint Propulsion Conference & Exhibit, 2004.
- [82] F. Richecoeur, P. Scouffaire, S. Ducruix, and S. Candel, “High frequency transverse acoustic coupling in a multiple injector cryogenic combustor,” vol. 22, pp. 790–799, 2006.
- [83] F. Richecoeur, P. Scouffaire, S. Ducruix, and S. Candel, “Interactions between propellant jets and acoustic modes in liquid rocket engines: experiments and simulations,” (Sacramento, California), 42<sup>th</sup> AIAA/ASME/SAE/ASEE Joint Propulsion Conference & Exhibit, 2006.
- [84] T. Schmitt, M. Méry, M. Boileau, and S. Candel, “Large-eddy simulation of oxygen/methane flames under transcritical conditions,” *Proc. Combusti. Inst.* 33(1), 1383-1390, 2011.

- [85] L. Hakim, A. Ruiz, T. Schmitt, M. Boileau, G. Staffelbach, S. Ducruix, B. Cuenot, and S. Candel, “Large eddy simulations of multiple transcritical coaxial flames submitted to high-frequency transverse acoustic modulation,” *Proc. Combust. Inst.*, 35(2), 1461-1468, 2015.
- [86] M. Gonzalez-Flesca, T. Schmitt, S. Ducruix, and S. Candel, “Large eddy simulations of a transcritical round jet submitted to transverse acoustic modulation,” *Physics of Fluids*, 28, 055106, 2016.
- [87] Y. Méry, *Mécanismes d’instabilités de combustion haute-frequence et application aux moteurs-fusées*. PhD thesis, École Centrale Paris, EM2C, France, 2010.
- [88] L. Hakim, *Dynamics of transcritical coaxial flames in high-frequency transverse fields: Application to liquid rocket engine instabilities*. PhD thesis, École Centrale Paris, EM2C, France, 2013.
- [89] G. Boisdrón, *Etude de l’atomisation d’un jet liquide assisté par air soumis à une onde acoustique stationnaire transverse haute fréquence*. PhD thesis, University of Rouen, France, 2006.
- [90] F. Baillot, J. B. Blaisot, G. Boisdrón, and C. Dumouchel, “Behavior of an air-assisted jet submitted to a transverse high frequency acoustic field,” *Journal of Fluid Mechanics*, vol. 640, pp. 307–344, 2009.
- [91] F. Baillot, J. B. Blaisot, C. Richard, and M. Théron, “Effects of acoustic radiation on air-assisted jets in a transverse high-frequency acoustic field,” In the ILASS - 25<sup>th</sup> European Conference on Liquid Atomization and Spray Systems, 2013.
- [92] L. Landau and E. Lifchitz, *Mécanique des Fluides*. University Science Books, 1989.
- [93] L. V. King, “On the acoustic radiation on spheres,” vol. 147, (London), pp. 212–240, The Royal Society, 1934.
- [94] F. Baillot and F. Lespinasse, “Response of a laminar premixed v-flame to a high-frequency acoustic field,” *Combustion and Flame*, vol. 161, pp. 1247–1267, 2014.
- [95] F. Lespinasse, *Réponse de la dynamique d’une flamme prémélangée à des modes acoustiques azimutaux*. PhD thesis, University of Rouen, France, 2014.
- [96] J. C. Lasheras and E. J. Hopfinger, “Liquid jet instability and atomization in a coaxial gas stream,” *Annual Review of Fluid Mechanics*, vol. 32, no. 275, 2000.

- [97] E. J. Hopfinger, "Liquid jet instability and atomization in a coaxial gas stream," *Advances in turbulence VII*, U. Frisch eds., pp 69-78, vol. 32, no. 275, 1998.
- [98] Z. Faragó and N. Chigier, "Morphological classification of disintegration of round jets in a coaxial airstream," *Atomisation and sprays 2*, pp. 137-153, 1992.
- [99] Z. Faragó and M. Oswald, "Resonance frequencies and damping in combustion chambers with quarter wave cavities," (Munich), 6th Symposium on Launcher Technologies, 2005.
- [100] N. Fdida, *Developpement d'un systeme de granulometrie par imagerie. Application aux sprays larges et heterogenes*. PhD thesis, University of Rouen, France, 2008.
- [101] H. Malot and J. Blaisot, "Droplet size distribution and sphericity measurements of low-density sprays through image analysis," *Part. Part. Syst. Charact.*, no. 17, pp. 146-158, 2000.
- [102] J. Yon, *Jet diesel haute pression en champe proche et lointain: etude par imagerie*. PhD thesis, University of Rouen, France, 2003.
- [103] J. B. Blaisot and J. Yon, "Droplet size and morphology characterization for dense sprays by image processing: application to the diesel spray," *Experiments in Fluids*, vol. 39, no. 6, pp. 977-994, 2005.
- [104] J. R. Taylor, *An introduction to error analysis*. MIR, 1997.
- [105] J. B. Blaisot, "Drop size and drop size distribution measurements by image analysis," In the ICLASS - 12<sup>th</sup> Triennial International Conference on Liquid Atomization and Spray Systems, 2012.
- [106] J. Goodman, *Introduction to Fourier optics*. New York: McGraw Hill, 1968.
- [107] N. Fdida and J. Blaisot, "Drop size distribution measured by imaging: determination of the measurement volume by the calibration of the point spread function," *Meas. Sci. Technol.*, vol. 21, no. 2, 2010.
- [108] TSI incorporated, *Phase Doppler Particle Analyzer (PDPA)/ Laser Doppler Velocimetry (LDV)*, 2006.
- [109] M. Cáceres, F. Baillot, E. Domingues, J.-B. Blaisot, G. Goddard, and C. Gobin, "New experimental setup for thermoacoustic instabilities investigation in two-phase

- flow swirled combustion,” In the Proc. 8th European Combustion Meeting (EMC), 2017. Dubrovnik, Croatia.
- [110] A. Ficuciello, J. B. Blaisot, F. Baillot, C. Richard, and M. Théron, “Response of coaxial air-assisted liquid jets in an acoustic field: atomization and droplets clustering,” In the 13<sup>th</sup> International Conference on Liquid Atomization and Spray System (ICLASS), 2015.
- [111] A. Ficuciello, J. B. Blaisot, F. Baillot, C. Richard, and M. Théron, “High amplitude acoustic field effects on air-assisted liquid jets,” 52<sup>th</sup> AIAA/SAE/ASEE Joint Propulsion Conference & Exhibit, AIAA Paper No. 2016-5085, 2016.
- [112] P. Marmottant, *Atomisation d’un liquide par un courant gazeux*. PhD thesis, University of Grenoble, France, 2001.
- [113] M. F. Hamilton and D. T. Blackstock, *Nonlinear Acoustics*. Acoustic Society of America, 2008.
- [114] O. V. Rudenko and S. I. Soluyan, *Theoretical Foundations of Nonlinear Acoustics*. Springer, 1977.
- [115] T. G. Wang and C. P. Lee, *Radiation Pressure and Acoustic Levitation*, ch. 6. Acoustic Society of America, 2008.
- [116] P. M. Yarin, A. L. and C. Tropea, “On the acoustic levitation of droplets,” *The Journal of Fluid Mechanics*, 1998.
- [117] A. P. Zhuk, “Radiation force acting on a cylindrical particle in a sound field,” *Prikl. Mekh.*, vol. 22, no. 7, pp. 103–108, 1986.
- [118] J. Wu, G. Du, S. S. Work, and D. M. Warshaw, “Acoustic radiation pressure on a rigid cylinder: An analytical theory and experiments,” *The Journal of the Acoustical Society of America*, 1990.
- [119] L. Gor’kov, “On the forces acting on a small particle in an acoustical field in an ideal fluid,” vol. 6, pp. 773–775, *Sov. Phys. Dokl.*, 1962.

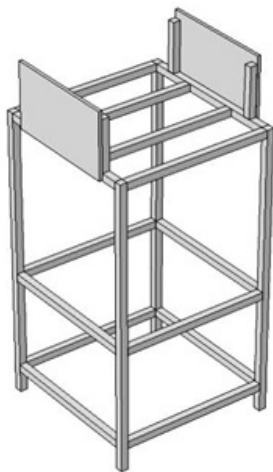


# Appendices



## Appendix A - Vibration Tests

The four compression drivers installed in the main cavity generate a non negligible mechanical vibration which can be transmitted to the domes and affect measurements. A test campaign dedicated to the evaluation of the mechanical vibration has been conducted on a first version of the structure supporting the elements of the experiment. This campaign showed that vibrations of significative levels were transmitted to the domes, particularly in the vertical direction. In order to reduce the mechanical transmission between the cavity and the domes an expressly designed structure has been installed around the main cavity. The structure is shown in the sketch of Figure 1(a) while in Figure 1(b) it is shown the positioning of the injection domes on the structure on the top of the cavity. In this configuration the contact with the main cavity is reduced and mechanical transmission is minimized. Vibration measurements have been performed with a PCB miniature triaxial ICP accelerometers. Results of the test campaigns in terms of measured accelerations are summarized in Figures A2 and A3 for different levels of acoustic solicitation expressed in terms of mVRMS of the signal sent to the compression drivers. For the maximum solicitation conditions, namely 1400 mVRMS (corresponding to  $p_{a,pp} \approx 12 \text{ kPa}$  at PAN in the main cavity) a noticeable reduction of vibration levels has been obtained with the new experimental setup, i.e. 67% for the gas dome and 36% for the liquid dome, as reported in Figure A4.



(a)



(b)

Figure A1: (a) A sketch of the structure designed to support the injection domes, (b) a picture of the injection domes placed on the top of the cavity and sustained by the structure.

VIBRATION PRELIMINARY MEASUREMENTS (old config)									
CAVITY									
Input signal	coord. X (wall to wall)			coord. Y (vertical)			coord. Z (parallel to walls)		
IN mVRMS	RMS [m/s <sup>2</sup> ]	pk [m/s <sup>2</sup> ]	pkpk [m/s <sup>2</sup> ]	RMS [m/s <sup>2</sup> ]	pk [m/s <sup>2</sup> ]	pkpk [m/s <sup>2</sup> ]	RMS [m/s <sup>2</sup> ]	pk [m/s <sup>2</sup> ]	pkpk [m/s <sup>2</sup> ]
200	0.3434	1.255	<b>2.115</b>	0.2565	0.9809	<b>1.715</b>	0.4519	1.532	<b>2.793</b>
400	0.6809	2.429	<b>4.352</b>	0.3587	1.302	<b>2.32</b>	0.6525	2.1	<b>3.796</b>
600	3.024	11.06	<b>19.55</b>	9.298	3.549	<b>5.936</b>	1.789	5.246	<b>10.07</b>
800	4.284	14.44	<b>24.31</b>	1.201	4.11	<b>6.816</b>	2.647	6.847	<b>13.36</b>
1000	5.569	17.32	<b>29.09</b>	1.512	5.038	<b>8.403</b>	3.488	8.044	<b>15.97</b>
1200	6.112	19.59	<b>33.05</b>	1.666	5.651	<b>9.688</b>	3.883	9.316	<b>18.59</b>
1400	7.38	21.9	<b>37.3</b>	2.016	6.428	<b>11.27</b>	4.714	10.62	<b>21.12</b>
GAS DOME									
Input signal	coord. X (wall to wall)			coord. Y (vertical)			coord. Z (parallel to walls)		
IN mVRMS	RMS [m/s <sup>2</sup> ]	pk [m/s <sup>2</sup> ]	pkpk [m/s <sup>2</sup> ]	RMS [m/s <sup>2</sup> ]	pk [m/s <sup>2</sup> ]	pkpk [m/s <sup>2</sup> ]	RMS [m/s <sup>2</sup> ]	pk [m/s <sup>2</sup> ]	pkpk [m/s <sup>2</sup> ]
200	0.2733	1.162	<b>2.136</b>	0.5851	1.922	<b>3.842</b>	0.3556	1.363	<b>2.65</b>
400	0.4941	1.464	<b>2.879</b>	0.986	2.638	<b>5.058</b>	0.6637	1.909	<b>3.613</b>
600	0.8486	2.473	<b>4.685</b>	1.377	3.522	<b>6.621</b>	0.9714	2.547	<b>5.01</b>
800	0.9909	3.124	<b>5.841</b>	1.538	4.78	<b>9.511</b>	1.035	3.039	<b>6.028</b>
1000	1.378	3.791	<b>7.023</b>	2.521	6.736	<b>13.07</b>	1.398	3.753	<b>7.042</b>
1200	1.551	3.952	<b>7.084</b>	3.428	8.806	<b>17.52</b>	1.526	3.698	<b>7.053</b>
1400	1.816	4.368	<b>7.807</b>	4.603	10.71	<b>21.35</b>	1.714	3.938	<b>7.589</b>
LIQUID DOME									
Input signal	coord. X (wall to wall)			coord. Y (vertical)			coord. Z (parallel to walls)		
IN mVRMS	RMS [m/s <sup>2</sup> ]	pk [m/s <sup>2</sup> ]	pkpk [m/s <sup>2</sup> ]	RMS [m/s <sup>2</sup> ]	pk [m/s <sup>2</sup> ]	pkpk [m/s <sup>2</sup> ]	RMS [m/s <sup>2</sup> ]	pk [m/s <sup>2</sup> ]	pkpk [m/s <sup>2</sup> ]
200	0.1345	0.536	<b>0.946</b>	0.296	1.147	<b>2.218</b>	0.1843	0.7104	<b>1.334</b>
400	0.152	0.5442	<b>1.079</b>	0.5083	1.571	<b>3.133</b>	0.2608	1.053	<b>2.05</b>
600	0.1621	0.5946	<b>1.139</b>	0.5611	1.669	<b>3.212</b>	0.3272	1.207	<b>2.355</b>
800	0.1868	0.6861	<b>1.343</b>	0.6421	2.096	<b>3.785</b>	0.3824	1.289	<b>2.461</b>
1000	0.2224	0.9296	<b>1.793</b>	0.8575	2.651	<b>4.66</b>	0.7543	1.428	<b>2.849</b>
1200	0.2208	0.9166	<b>1.811</b>	0.7662	2.8	<b>5.415</b>	0.4265	1.596	<b>3.158</b>
1400	0.3088	1.152	<b>2.169</b>	1.158	2.962	<b>5.79</b>	0.6053	1.674	<b>3.306</b>

Figure A2: Summary of vibration measurements before setup modification.

VIBRATION FINAL MEASUREMENTS (new config)									
CAVITY									
Input signal	coord. X (wall to wall)			coord. Y (vertical)			coord. Z (parallel to walls)		
IN mVRMS	RMS [m/s <sup>2</sup> ]	pk [m/s <sup>2</sup> ]	pkpk [m/s <sup>2</sup> ]	RMS [m/s <sup>2</sup> ]	pk [m/s <sup>2</sup> ]	pkpk [m/s <sup>2</sup> ]	RMS [m/s <sup>2</sup> ]	pk [m/s <sup>2</sup> ]	pkpk [m/s <sup>2</sup> ]
200	1.204	3.041	5.922	0.4569	1.862	3.366	0.4724	1.423	2.773
400	2.502	6.798	13	0.9793	3.217	5.838	0.9161	2.504	4.739
600	3.525	9.619	17.29	1.269	3.708	7.16	1.208	3.036	5.9
800	3.545	11.7	19.97	1.217	4.261	8.473	1.162	3.463	6.549
1000	4.712	13.56	22.22	1.676	5.282	10.11	1.466	3.856	7.274
1200	5.221	15.4	24.36	1.956	6.515	12.25	1.582	4.081	7.672
1400	5.83	17.46	26.59	2.45	7.985	15.31	1.69	4.185	7.908
GAS DOME									
Input signal	coord. X (wall to wall)			coord. Y (vertical)			coord. Z (parallel to walls)		
IN mVRMS	RMS [m/s <sup>2</sup> ]	pk [m/s <sup>2</sup> ]	pkpk [m/s <sup>2</sup> ]	RMS [m/s <sup>2</sup> ]	pk [m/s <sup>2</sup> ]	pkpk [m/s <sup>2</sup> ]	RMS [m/s <sup>2</sup> ]	pk [m/s <sup>2</sup> ]	pkpk [m/s <sup>2</sup> ]
200	0.283	1.004	1.964	0.2969	1.138	2.224	0.1837	0.7147	1.315
400	0.3186	0.9719	1.938	0.3805	1.535	3.01	0.2195	0.9065	1.729
600	0.4304	1.327	2.398	0.3838	1.403	2.614	0.2807	1.015	1.909
800	0.4485	1.322	2.521	0.6493	2.206	4.002	0.3537	1.323	2.429
1000	0.5249	1.553	3.042	1.029	3.229	6.132	0.58	1.915	3.655
1200	0.6864	2.113	3.974	0.9831	3.277	6.161	0.6929	2.233	4.375
1400	0.9463	2.349	4.492	1.444	3.886	7.07	0.9731	2.61	4.995
LIQUID DOME									
Input signal	coord. X (wall to wall)			coord. Y (vertical)			coord. Z (parallel to walls)		
IN mVRMS	RMS [m/s <sup>2</sup> ]	pk [m/s <sup>2</sup> ]	pkpk [m/s <sup>2</sup> ]	RMS [m/s <sup>2</sup> ]	pk [m/s <sup>2</sup> ]	pkpk [m/s <sup>2</sup> ]	RMS [m/s <sup>2</sup> ]	pk [m/s <sup>2</sup> ]	pkpk [m/s <sup>2</sup> ]
200	0.1435	0.5793	1.106	0.2478	0.9026	1.766	0.1657	0.6145	1.134
400	0.1353	0.5629	1.018	0.3349	1.07	2.114	0.1554	0.6878	1.255
600	0.1406	0.531	1.056	0.3507	1.457	2.855	0.1637	0.7343	1.328
800	0.1453	0.7169	1.262	0.5687	1.67	3.285	0.1651	0.6127	1.21
1000	0.148	0.5193	1.019	0.6436	1.733	3.215	0.1716	0.7181	1.329
1200	0.1528	0.579	1.105	0.585	1.881	3.361	0.1743	0.6147	1.196
1400	0.1606	0.6692	1.244	0.7469	2.046	3.695	0.1873	0.8592	1.491

Figure A3: Summary of vibration measurements after setup modification.

	GAS DOME			LIQUI DOME		
	x (wall to wall)	y (vertical)	z (parallel)	x (wall to wall)	y (vertical)	z (parallel)
	pkpk [m/s <sup>2</sup> ]					
Before	7.8	21.4	7.6	2.2	5.8	3.3
After	4.5	7.1	5.0	1.2	3.7	1.5
%	-42	-67	-34	-43	-36	-55

Figure A4: Comparison of vibration levels in gas and liquid domes before and after the experimental setup modification.

## Appendix B - Resonant Cavity Eigenmodes

Simulations presented in the manuscript have been performed with the Acoustics module of COMSOL Multiphysics which is an optional package that extends the COMSOL environment and presents functionality optimized for the analysis of acoustics and vibration problems. In this appendix results concerning the effects of the compression driver (loudspeaker) duct length on the eigenmode of the main resonant cavity are presented. Simulations have been performed with the *Pressure Acoustics, Frequency domains* interface in which the Helmholtz equation is solved in the frequency domain without source terms and the acoustic pressure  $p$  is the only variable of the problem. As described in section 2.1 the acoustic resonant cavity is provided with 4 compression drivers, two on each side. The membrane of the compression drivers is placed at a distance  $l_{ls}$  from the inner cavity surface as indicated in Figure 1(a). The four resulting ducts in between the com-

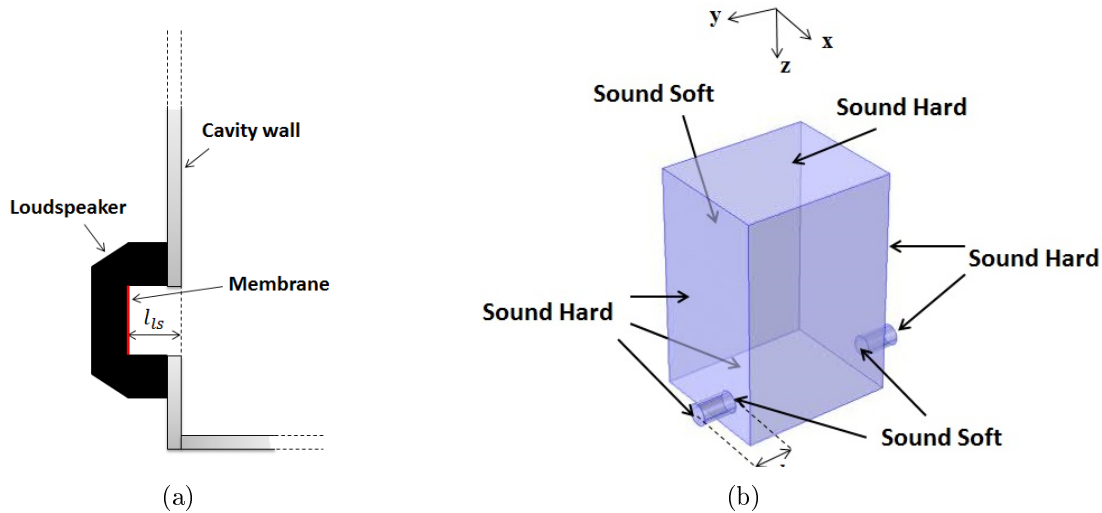


Figure B1: (a) Detail of the cavity/compression driver interface indicating the duct length  $l_{ls}$ . (b) Resonant cavity geometrical domain and boundary conditions for eigenmodes analysis.

pression driver membranes and the cavity inner surface must be taken into account in the geometrical domain considered for the calculation of the cavity eigenmode. Figure 1(b) shows half of the geometrical domain considered in the calculation of the eigenmodes (see Figure 1(b)). Sound hard boundary conditions (i.e. zero normal acoustic-velocity fluctuations) are used for the cavity walls, roof, floor and compression driver membrane surfaces while sound soft boundary conditions ( $p = 0$ ) are used at the open surfaces of the cavity and on interfaces between the compression driver ducts and the cavity .

The 2T resonant mode of the cavity is shown in Figure B2. Only half of the cavity is presented to show the structure of the mode in the central plane in the x-direction which corresponds to the injections plane. Figure 2(a) represents the eigenmode without compression drivers duct, i.e.  $l_{ls} = 0$ . Figure 2(b) to 2(d) presents the mode shape for different duct lengths  $l_{ls}/L_c$  where  $L_c$  is the cavity length. It can be seen that the presence of the compression drivers duct affects the cavity mode shape. The modification of the acoustic field is more evident for short lengths whereas the mode shape assumes the same structure that without compression drivers (Figure 2(a)) when  $l_{ls}/L_c$  approaches 0.222 (Figure 2(d)). In the experiments  $l_{ls}/L_c \approx 0.194$ .

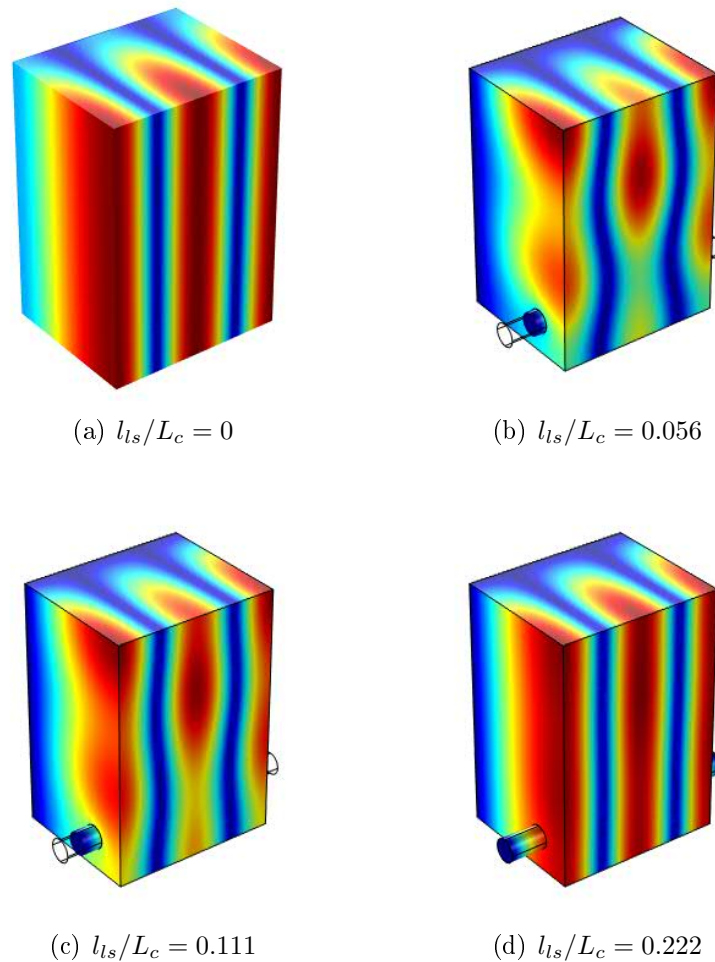


Figure B2: Resonant cavity eigenmodes at 1000 Hz (a) without compression drivers and for different length of the compression driver duct connection  $l_{ls}/L_c$ : (b) 0.056; (c) 0.111; (d) 0.222.

## Appendix C - Injection Domes Technical Sketches

Technical sketches of the two injection domes designed for the investigation of the acoustic response upstream the injection are shown in Figure C1.

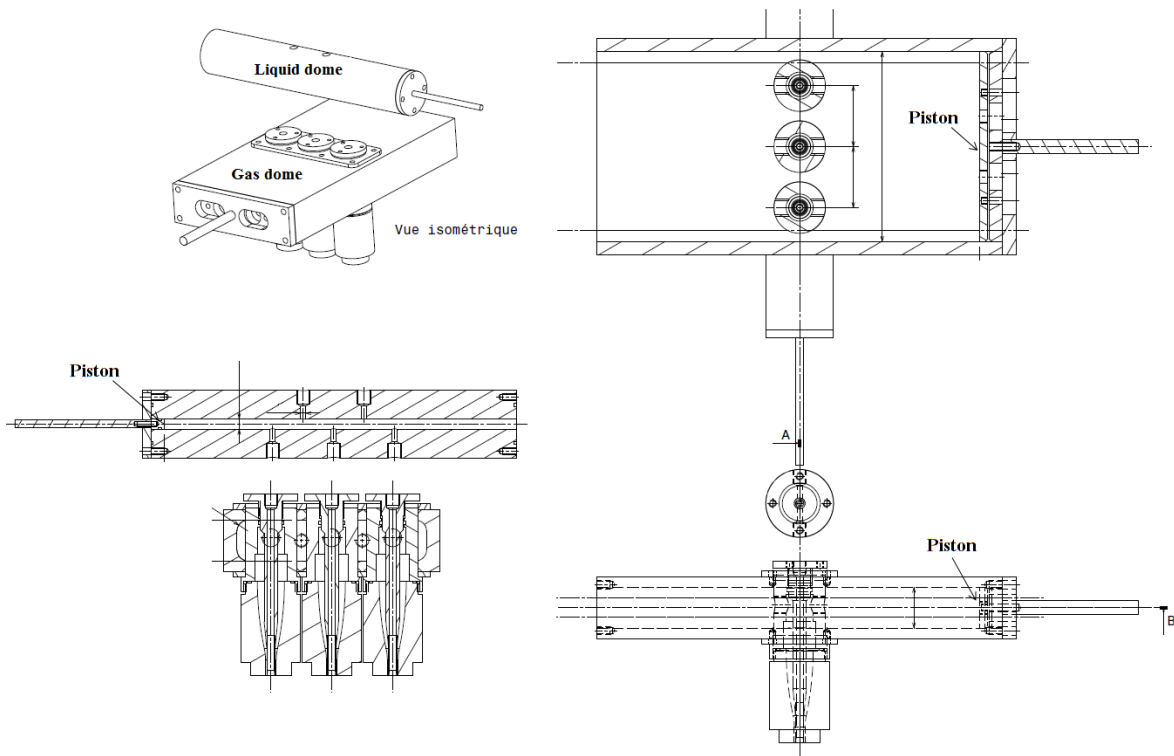


Figure C1: Schematic of injection domes. Dimension are not reported for confidential reason imposed by the partner of this work (CNES).

## Appendix D - Gas Dome Acoustic Pressure Signal Plots

In this section raw acoustic pressure signals measured with pressure transducers  $PT_{l_0}$ ,  $PT_{l_1}$ ,  $PT_{c_0}$  and  $PT_{r_0}$  in the gas dome are shown for the three configurations investigated in Chapter 4. Measurements carried out without flow rate are compared with those with the maximum flow rate, for  $GD0$ ,  $GD4$  and  $GD8$  ( $f = 1000 \text{ Hz}$ ;  $p_{a,pp} \approx 12 \text{ kPa}$  at PAN;  $d_{or} = 1.125$ ). Figure D1 shows acoustic measurements in the IAN-VAN-IAN configuration. The amplitude of fluctuations decreases by increasing the dome size or the mass flow rate.  $PT_{l_0}$ ,  $PT_{r_0}$  and  $PT_{l_1}$  present similar amplitudes of fluctuations, whereas  $PT_{c_0}$  amplitude is always close to zero. Signals measured with  $PT_{l_0}$  and  $PT_{l_1}$  are always in-phase, and both are out-of-phase with  $PT_{r_0}$ .

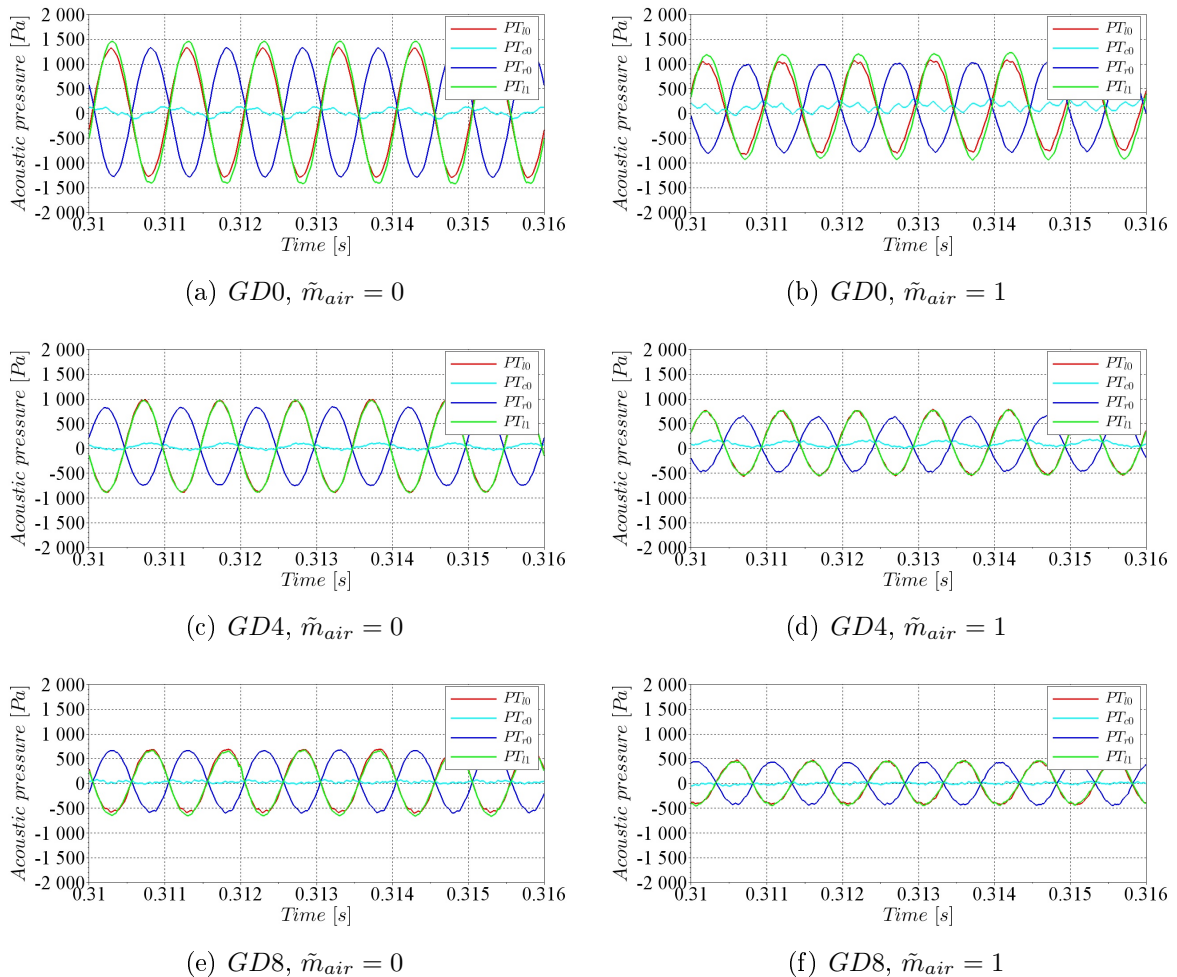


Figure D1: Acoustic pressure signal comparison in the gas dome for IAN-VAN-IAN: (a)  $GD0, \tilde{m}_{air} = 0$ , (b)  $GD0, \tilde{m}_{air} = 1$ ; (c)  $GD4, \tilde{m}_{air} = 0$ ; (d)  $GD4, \tilde{m}_{air} = 1$ ; (e)  $GD8, \tilde{m}_{air} = 0$ ; (f)  $GD8, \tilde{m}_{air} = 1$  ( $f = 1000 \text{ Hz}$ ;  $p_{a,pp} \approx 12 \text{ kPa}$  at PAN;  $d_{or} = 1.125$ ).

Acoustic pressure measurements performed at PAN-IAN-VAN are shown in Figure D2. The amplitude decreases by increasing the dome size and the mass flow rate. Also in this configuration,  $PT_{l0}$ ,  $PT_{r0}$  and  $PT_{l1}$  presents similar amplitudes, which are much higher than for  $PT_{c0}$ .  $PT_{l0}$  and  $PT_{l1}$  are in-phase. Their phase shift with  $PT_{r0}$  varies in between  $120^\circ$  and  $180^\circ$ .

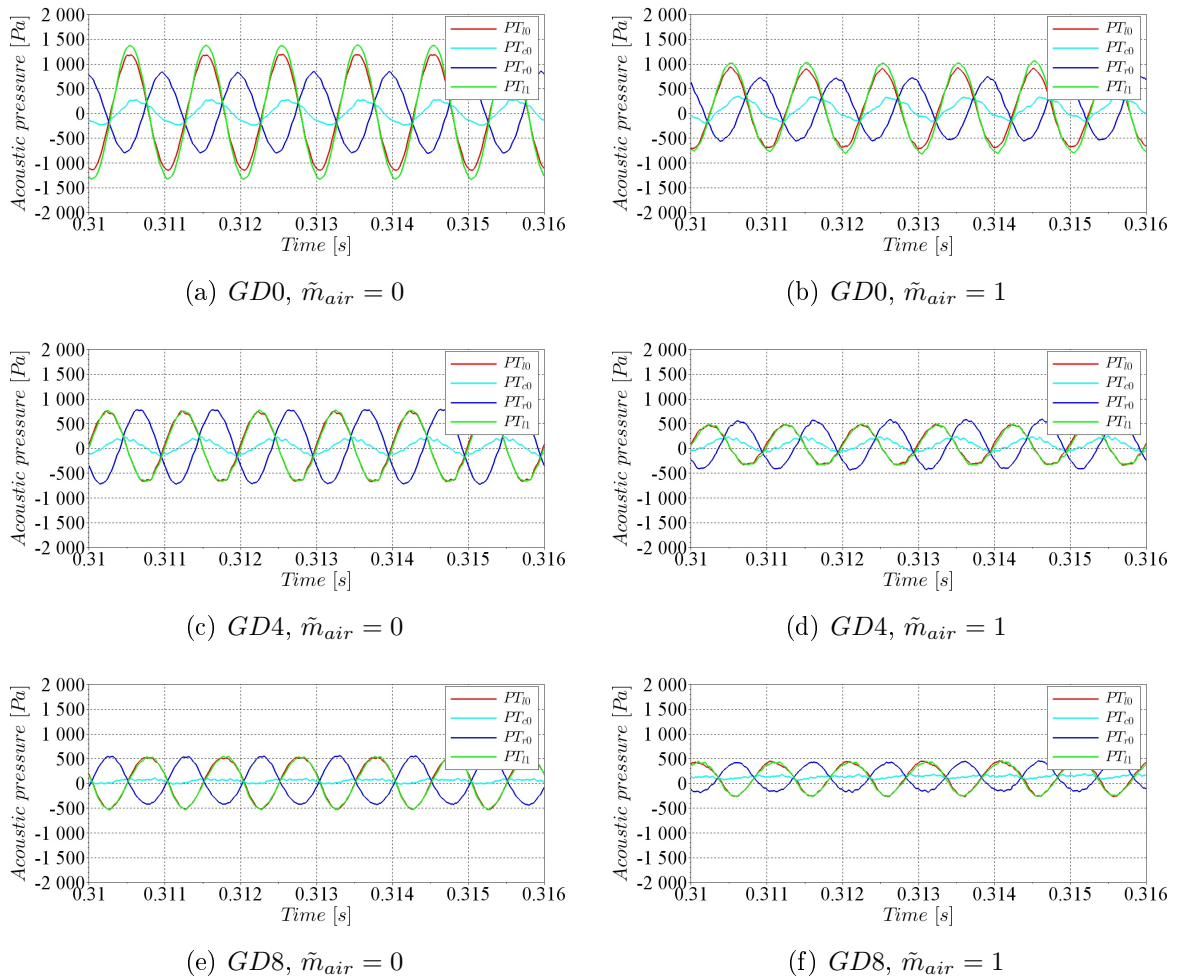
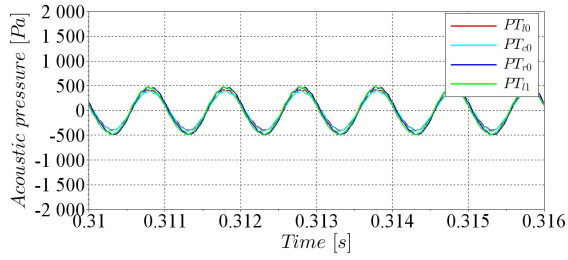
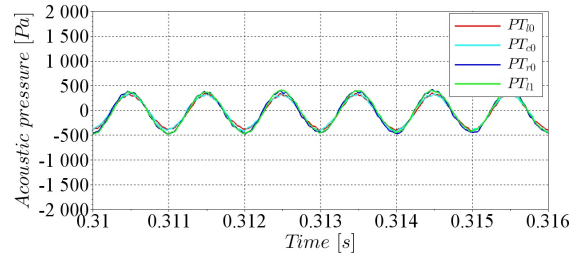


Figure D2: Acoustic pressure signal comparison in the gas dome for PAN-IAN-VAN: (a)  $GD0$ ,  $\tilde{m}_{air} = 0$ ; (b)  $GD0$ ,  $\tilde{m}_{air} = 1$ ; (c)  $GD4$ ,  $\tilde{m}_{air} = 0$ ; (d)  $GD4$ ,  $\tilde{m}_{air} = 1$ ; (e)  $GD8$ ,  $\tilde{m}_{air} = 0$ ; (f)  $GD8$ ,  $\tilde{m}_{air} = 1$  ( $f = 1000 \text{ Hz}$ ;  $p_{a,pp} \approx 12 \text{ kPa}$  at PAN;  $d_{or} = 1.125$ ).

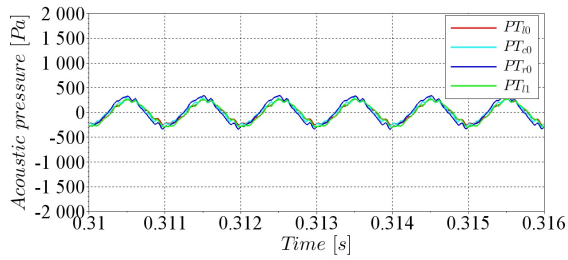
Figure D3 shows acoustic measurements for the IAN-PAN-IAN configuration. The amplitude of fluctuations decreases by increasing the dome size and the mass flow rate, and are much lower than those measured in the two previous configurations. All pressure transducers are in-phase, and present very similar amplitudes of fluctuations.



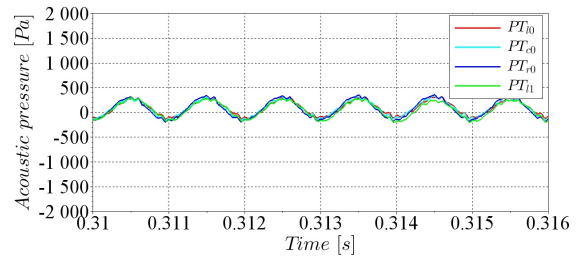
(a)  $GD0, \tilde{m}_{air} = 0$



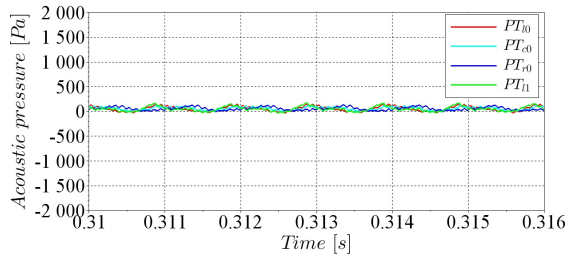
(b)  $GD0, \tilde{m}_{air} = 1$



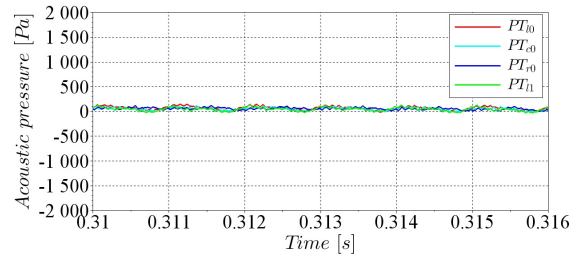
(c)  $GD4, \tilde{m}_{air} = 0$



(d)  $GD4, \tilde{m}_{air} = 1$



(e)  $GD8, \tilde{m}_{air} = 0$



(f)  $GD8, \tilde{m}_{air} = 1$

Figure D3: Acoustic pressure signal comparison in the gas dome for IAN-PAN-IAN: (a)  $GD0, \tilde{m}_{air} = 0$ , (b)  $GD0, \tilde{m}_{air} = 1$ ; (c)  $GD4, \tilde{m}_{air} = 0$ ; (d)  $GD4, \tilde{m}_{air} = 1$ ; (e)  $GD8, \tilde{m}_{air} = 0$ ; (f)  $GD8, \tilde{m}_{air} = 1$  ( $f = 1000 \text{ Hz}$ ;  $p_{a,pp} \approx 12 \text{ kPa}$  at PAN;  $d_{or} = 1.125$ ).

## Appendix E - High Speed Visualization Minimum Images Analysis

In Chapter 3.1 it has been shown how high-speed visualizations can be processed to obtain two-level minimum or average images. Average images, as shown in Figure 3.3(b), are converted here to pseudo-color images to more easily visualize the spray modifications induced by the acoustic field at high Weber. In these images, colors ranging from black to blue, green and red correspond to the probability of finding liquid increasing from zero to 1. Four mean images are computed from four partial image sequences of 200 frames extracted from the entire sequence. These sequences are selected following the timings indicated in Figure E1. Each sequence is composed of 200 images corresponding to a time interval of  $0.032\text{ s}$ . Results are reported in Figure E2 for VAN (a-d), IAN-VAN (e-h), IAN (i-l) and PAN-IAN (m-p). Injection conditions are given by  $We_g = 250$  and  $Re_l = 3200$ . No significant difference can be observed at VAN between the four mean images. On the contrary, the effects of acoustics can be observed at VAN-IAN, IAN and PAN-IAN. In these cases the average images corresponding to  $fr_2$  and  $fr_3$  show a deviation toward the right side side (toward VAN); indicating that the probability to find liquid objects in the right side is higher than that of find them on the left side due to the deviation. On the contrary, images corresponding to  $fr_1$  and  $fr_4$  are more centered and symmetric.

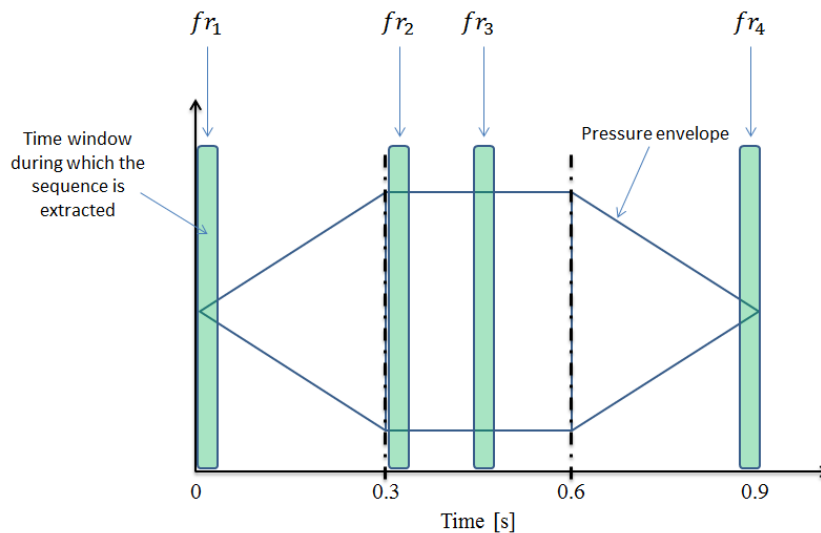


Figure E1: Reference time windows for post-processing with respect to the acoustic signal envelope.

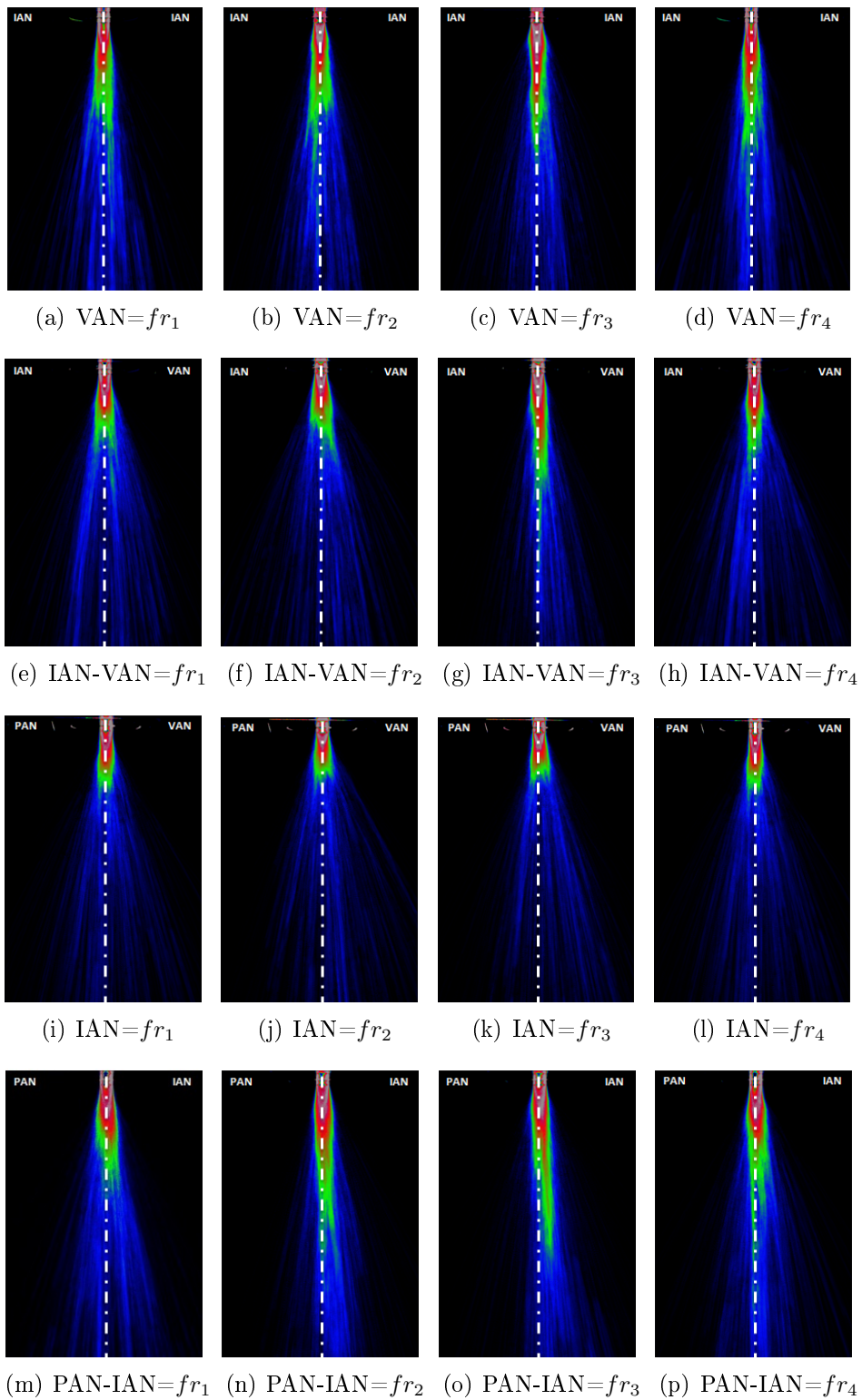


Figure E2: Average images converted to RGB images at: (a-d) VAN; (e-h) IAN-VAN; (i-l) IAN and (m-p) PAN-IAN. Forcing frequency  $f = 1 \text{ kHz}$ ,  $p_{a,pp} = 12 \text{ kPa}$ .

For lower Weber number atomization regimes the effects of the deviation are more clearly visible as shown in Figure E3 for the Rayleigh axi-symmetric ( $We_g = 9$ ;  $Re_l = 2000$ ), Rayleigh non-symmetric ( $We_g = 40$ ;  $Re_l = 3000$ ), shear breakup ( $We_g = 60$ ;  $Re_l = 3900$ ) and membrane ( $We_g = 120$ ;  $Re_l = 2800$ ) regimes. The position considered is IAN and average images are calculated from the  $fr_2$  image sequence.

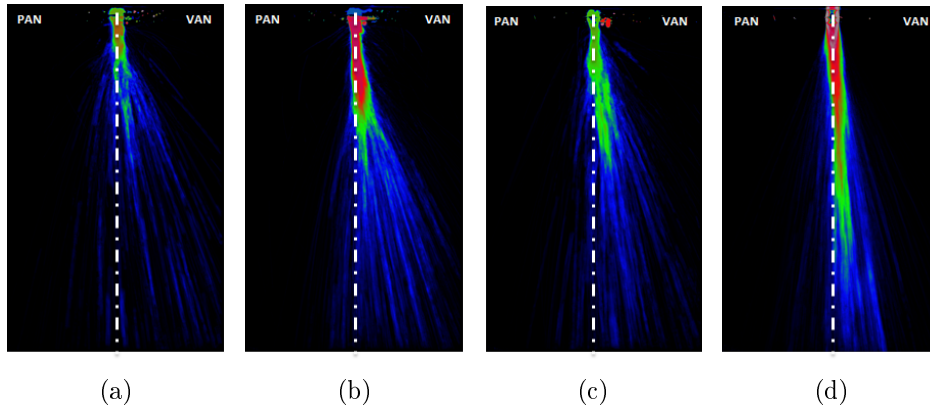


Figure E3: Average images converted to RGB images at IAN for: (a) Rayleigh axi-symmetric ( $We_g = 9$ ;  $Re_l = 2000$ ); (b) Rayleigh non-symmetric ( $We_g = 40$ ;  $Re_l = 3000$ ); (c) shear breakup ( $We_g = 60$ ;  $Re_l = 3900$ ) and (d) membrane ( $We_g = 120$ ;  $Re_l = 2800$ ). Forcing frequency  $f = 1 \text{ kHz}$ ,  $p_{a,pp} = 12 \text{ kPa}$ .